CR 151254

[redacted]

Axiomatix

(NASA-CR-151254) STUDY TO INVESTIGATE AND EVALUATE MEANS OF OPTIMIZING THE KU-BAND COMMUNICATION FUNCTION FOR THE SPACE SHUTTLE Final Report (Axiomatix, Marina del Rey, Calif.) 218 p HC A10/MF A01 CSCL 17B G3/16

N77-21171

Unclas 24336

Marina del Rey • California

STUDY TO INVESTIGATE AND EVALUATE MEANS OF OPTIMIZING THE KU-BAND COMMUNICATION FUNCTION FOR THE SPACE SHUTTLE

FINAL REPORT

Contract No. NAS 9-14614
Exhibit C

Prepared for

NASA Lyndon B. Johnson Space Center
Houston, Texas 77058

Prepared by

Marvin K. Simon
Sergei Udalov
Gaylord K. Huth

Axiomatix
13900 Panay Way, Suite 110M
Marina del Rey, California 90291

Axiomatix Report No. R7703-2
March 31, 1976

TABLE OF CONTENTS

LIST OF TABLES

LIST OF FIGURES

1.0 INTRODUCTION AND OVERVIEW

This is the final report for the "Study to Investigate and Evaluate Means of Optimizing the Ku-Band Communication Function for the Space Shuttle." The objective of the study was to carry out a number of advanced analytical and design tasks for the purpose of optimizing the configuration and the performance of the Ku-band communication system for the Space Shuttle. The communication system is a part of the Ku-Band Integrated Radar and Communication Equipment.

The forward link of the overall communication system consists of the ground-TDRS-Orbiter communication path. Because the last segment of this link is directed towards a relatively low orbiting Shuttle, methods must be provided to reduce the signal spectral density impinging on the earth's surface. Spreading the relatively narrowband data spectrum (32 to 216 kbps) by addition of a pseudo-noise (PN) code is considered to be the simplest method for reducing the spectral density of the forward link. The use of a PN code, however, requires code acquisition and tracking functions to be incorporated into the Orbiter's Ku-band receiver.

The driving parameters for the return link, which consists of the Orbiter-TDRS-ground communication path, include: (1) multiplexing of three independent data streams and (2) the capability to handle the symbol rates of up to 100 Msps, the latter originating from rate 1/2 encoding of data streams of up to 50 Mbps. As the result of previous work, Axiomatix has demonstrated the feasibility of simultaneously combining all three channels by phase multiplexing. One of the analytical tasks included in this report was the optimization of this three-channel multiplexing technique.

Both the forward link receiver and the return link transmitter share a 36-inch diameter parabolic dish antenna. The receive frequency for the Shuttle Ku-band equipment is 13.775 MHz. The return link transmitter operates on 15.0034 GHz and the nominal power supplied by the transmitter tube to the antenna is 50 watts.

The first step in establishing the TDRS/Shuttle Ku-band communication link is the alignment of the antenna directivity patterns along a common line-of-sight (LOS). The alignment of the TDRS antenna is aided by the "wide beam" horn radiator mounted on the Shuttle's high gain antenna. The alignment of the Shuttle antenna with the LOS to TDRS must be performed by scanning the Shuttle antenna across the residual uncertainty volume,

which may be as wide as a 20° cone. For best scan efficiency, a spiral pattern is used to search out the uncertainty volume. Furthermore, in order not to limit the rate at which the uncertainty volume is scanned spatially, the energy detection is used to declare TDRS intercept by the main beam of the Shuttle antenna. Other phases of TDRS signal acquisition include PN code acquisition, carrier search and acquisition, and bit synchronization. After the acquisition phases of all receiver subunits are completed, the system goes into a track mode.

Because the initial acquisition of the TDRS signal requires frequency search with a Costas loop, which also serves as a data demodulator, the probability of false lock on data rate spectral lines must be kept to a minimum. If special design criteria are not met, the false lock acquisition can present a serious problem, particularly at high signal-to-noise ratios at the Costas loop. Consequently, one of the major analytical tasks of this program was to define the Costas design parameters which result in adequate suppression of the false lock sidebands. The results of this analytical task are not only of extreme value to the specific case of Shuttle communication, but are general enough to be considered a significant contribution to the communication technology. Section 2.0 of this report presents the analysis of the false lock performance of the Costas receivers.

In Section 3.0, the modulation and multiplexing formats are considered for both the forward and return links. Of particular importance to the return link is the analysis of the phase multiplexing technique which permits simultaneous transmission of <u>three</u> independent data streams on a single digitally phase-modulated carrier. The detailed analysis of the three-channel multiplexer design is rather unique and can be considered as another contribution to the communication technology.

The design considerations pertaining to angular search, acquisition and tracking of the TDRS are presented in Section 4.0. Section 5.0 contains analytical examination of the effects of long- and short-term oscillator instabilities on Ku-band system performance.

Section 6.0 presents the estimate of the range of TDRS signal level fluctuations and provides analytical interpretation of the effects of these variations on the Shuttle Ku-band receiver performance.

Signal distortion effects are analyzed in Section 7.0. Particular emphasis is placed on determining the effect of NRZ bit asymmetry on return

link performance at 100 Msps. Conclusions are presented in Section 8.0.

Appendixes A through F contain supporting analysis for Section 2.0. Appendix G presents the analysis of the optimum three-channel multiplexing technique.

2.0 FALSE LOCK PERFORMANCE CONSIDERATIONS FOR SPACE SHUTTLE ORBITER COSTAS LOOP RECEIVERS

2.1 Motivation and Technical Approach

The ability of a Costas loop to lock up on a data sideband (false lock is a phenomenon which has been of major concern in evaluation of the S-band communication system design. Likewise, in the design of the Ku-band communication system, this false lock problem will need to be considered and dealt with. This section presents recent theoretical results on the false lock behavior of a Costas loop and compares them with measured results obtained by TRW in testing the S-band transponder. Since both random and periodic data sequences are of interest, the latter corresponding to the idle patterns of the delta modulators in the S-band transponder, results are presented for both cases. Consideration is then given to the problem of reducing the false lock tendency of the Costas loop. Several modifications of the conventional Costas loop design are suggested and the theoretical false lock performance of each is presented. To aid the system design in making the necessary tradeoffs between false lock improvement and true lock degradation, these new configurations are also analyzed from the standpoint of true lock tracking and acquisition in the presence of frequency uncertainty. Finally, since both false lock and true lock are phenomena associated with the existence of a dc voltage at the lock detector output and since, when carrier sweeping is used as an acquisition aid, this voltage is necessary to kill the sweep, the discussion is completed by presenting an analysis of the lock detector performance.

2.2 Summary of Results

Consider the Costas loop and associated lock detector illustrated in Figure 1. The input signal $s[t,\theta(t)]$ is assumed to be a bi-phase modulated carrier with average power S, nominal carrier frequency ω_0, and received carrier phase $\theta(t) = \theta_0 + \Omega_0 t$. The modulation on this carrier, denoted by $m(t)$, is binary (a ± 1 digital waveform) and has a data (symbol) rate $R_s = 1/T$. The total received signal $x(t)$ is then the sum of $s[t,\theta(t)]$ and $n_i(t)$, where $n_i(t)$ is the additive channel noise which can be expressed in the form of a narrowband process about the actual frequency $\omega_0 + \Omega_0$ of the observed data. Such a representation generates an equivalent pair of quadrature low-pass white Gaussian noise processes $N_c(t)$ and $N_s(t)$ with single-sided noise spectral density N_0 w/Hz and single-sided bandwidth $B_H < \omega_0/2$.

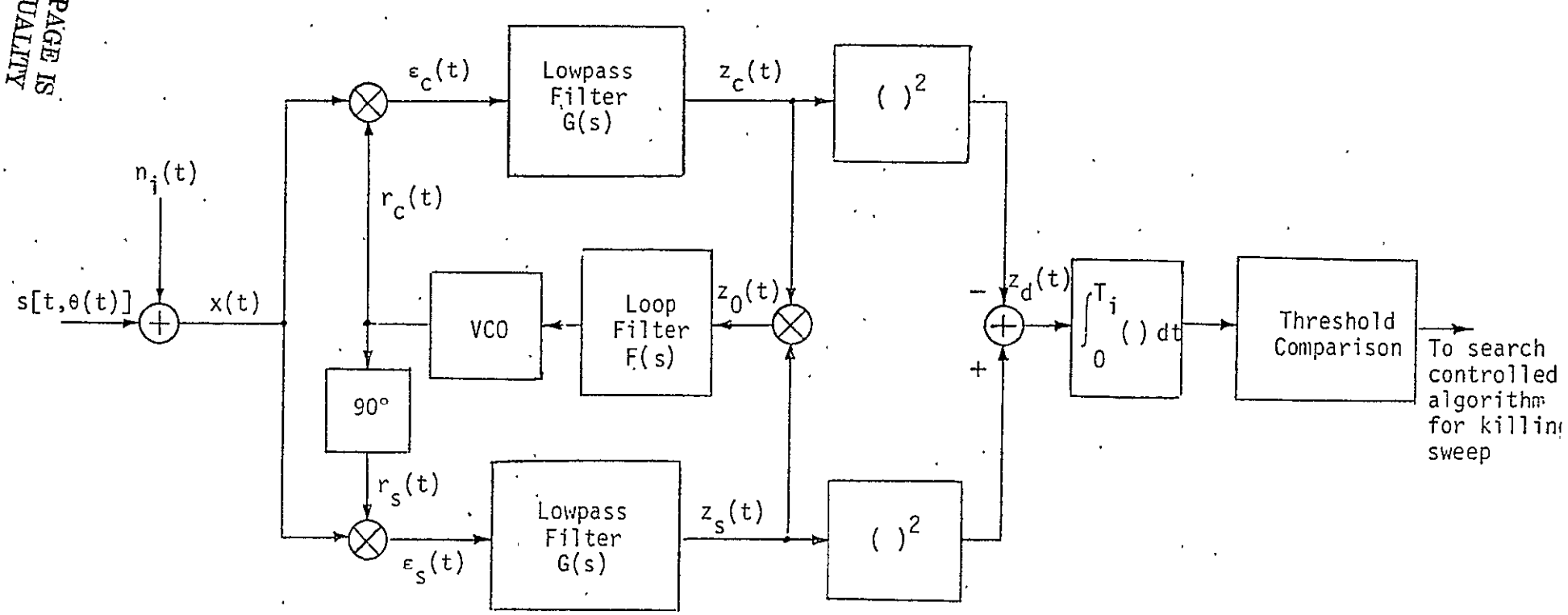

Figure 1. Costas Loop and Associated Lock Detector

When the loop is truly locked, the in-phase and quadrature reference signals $r_s(t)$ and $r_c(t)$, respectively, are expressed as sine and cosine functions of $\omega_0 t + \hat{\theta}(t)$, where $\hat{\theta}(t)$ is the VCO's estimate of $\theta(t)$. When the loop is in a false lock mode, then these same reference signals are now sine and cosine functions of $(\omega_0 - \omega_f)t + \hat{\theta}(t)$, where ω_f is the false lock radian frequency relative to the carrier frequency.

The in-phase and quadrature phase detector outputs, $\varepsilon_s(t)$ and $\varepsilon_c(t)$, respectively, have signal and noise components proportional to sine and cosine of $\omega_f t + \phi(t)$, amplitude modulated by the baseband data modulation $m(t)$ and the low pass noise processes $N_c(t)$ and $N_s(t)$. The process $\phi(t) \triangleq \theta(t) - \hat{\theta}(t)$ in the above is the loop phase error. After low pass filtering with the in-phase and quadrature arm filters $G(s)$, one obtains the signals $z_s(t)$ and $z_c(t)$ which, respectively, have signal components $\hat{m}_c(t;\omega_f,\phi)$ and $\hat{m}_s(t;\omega_f,\phi)$, and noise components $\hat{N}_{ss}(t;\omega_f,\phi)$, $\hat{N}_{cc}(t;\omega_f,\phi)$ and $\hat{N}_{sc}(t;\omega_f,\phi)$, $\hat{N}_{cs}(t;\omega_f,\phi)$. The "hat" is used to denote the filtering by $G(s)$ while the arguments ω_f and ϕ indicate the dependence of these filtered signals and noises on the false lock frequency and the phase error. The loop error signal $z_0(t)$ is formed from the product of $z_s(t)$ and $z_c(t)$, while the lock detector signal is obtained by squaring $z_c(t)$ and $z_s(t)$ and differencing these quantities. In either case, a signal is formed which contains a dc component, V_{dc}, when the frequency difference $\omega_f/2\pi$ between the incoming carrier and the local VCO is other than zero. This is contrary to the usual conclusion that neither the loop error signal nor the lock detector signal contain a dc signal unless $\omega_f = 0$, which is valid only under the assumption that the arm filter distortions can be neglected. Such an assumption is itself valid only in the limit as the bandwidth of these filters becomes very wide with respect to the data rate. A more specific discussion on how wide these filters can be chosen relative to the effect of this choice on tracking threshold will be given shortly.

When the input modulation $m(t)$ is characterized by random data, then in addition to a dc term, both the loop error signal and the lock detector signal contain higher harmonics occurring at multiples of the data rate (i.e., nR_s; $n = 1,2,\ldots$) when the false lock frequency difference $\omega_f/2\pi$ is at multiples of half the data rate (i.e., $nR_s/2$; $n = 1,2,\ldots$). Alternately, when the input modulation is characterized by a periodic data sequence with period p, then the false lock frequencies are at multiples of $R_s/2p$ away from the carrier (i.e., $\omega_f/2\pi = nR_s/2p$; $n = 1,2,\ldots$).

In either the random or periodic data case, the set of dc signal components which occur at the false lock frequencies have the same relative magnitudes for both the loop error signal and the lock detector output. The only difference between the two is that the set of dc components in the loop error signal has a sine dependence on the loop phase error, while those at the lock detector output have a cosine dependence. This statement is also true relative to the dc component which exists when the loop is truly locked.

As an example of the type of results obtained for periodic data sequences, consider the four cases corresponding to the idle patterns in the S-band transponder. The periodic sequences selected are the following:

Number	Data Sequence	Period (p)
(A)	-1,1	2
(B)	-1,-1,1,1	4
(C)	-1,-1,-1,-1,1,1	6
(D)	-1,1,1,1,-1,-1,-1,-1,-1,1,1,1	12

Sequence (A) is clearly the alternating sequence, while sequence (B) also alternates, but at half the rate. Sequences (C) and (D) are actually the rate 1/2 convolutionally encoded sequences of (A) and (B). For a single-pole Butterworth (RC) filter with 3 dB radian cutoff frequency ω_c and Manchester coded data symbols, the set of dc signal component magnitudes $\{|V_{dc}| = |V_n|;\ n = 1,2,3,\ldots\}$, which occur at the false lock frequencies $\omega_f/2\pi = nR_s/2p;\ n = 1,2,3,\ldots$, are only functions of the single parameter $f_cT \triangleq \omega_cT/2\pi$. For $f_cT = 1.4$ (the value corresponding to minimum phase tracking jitter at low symbol signal-to-noise ratio), $|V_n|$ (in dB) is plotted versus $\omega_fT/2\pi = n/2p$ for $n = 0,1,2,\ldots$ in Figure 2. The case $n = 0$ corresponds to the true lock condition. We observe from Figure 2 for sequence (A), the alternating data case, that the strength of the false lock components falls away monotonically as a function of increasing false lock frequency. This observation can be verified from the specific theoretical results given in Appendix B. Furthermore, as the period of the sequences increases, the strong false lock components which remain occur at multiples of half the data rate. In the limit as the period goes to infinity, only these components would remain and would correspond in magnitude to those obtained for a random data sequence (see Appendix A). As a final word of clarification, Figure 2 is not to be interpreted as

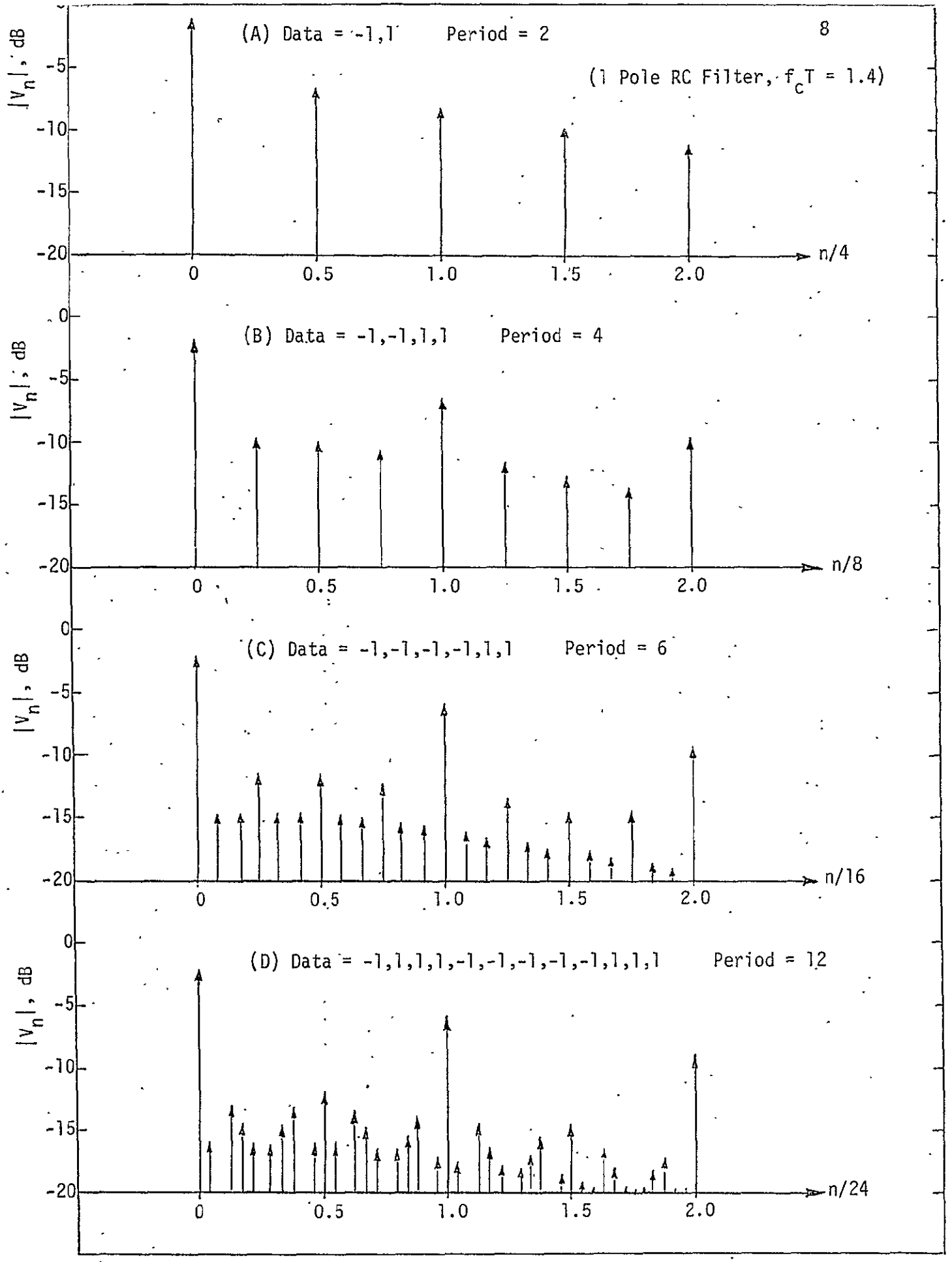

Figure 2. Amplitude of DC Component in Costas Error Signal (or Lock Detector Signal)

a line frequency spectrum and thus should not be confused with the actual line frequency spectrum of the error signal which, coincidentally, has contributions at the same set of frequencies. In Figure 2, each line corresponds, for a given data sequence, to the amplitude of the dc component magnitude in the Costas loop error signal or lock detector output signal at a particular false lock frequency. Since the Costas loop false locks to only one of these frequencies at any given time, then only the particular dc amplitude corresponding to that false lock frequency has any meaning at that time.

Periodic PN sequences of periods 7 and 31 have also been investigated as to their tendency to produce false locks. The resulting sets of dc components in the Costas loop error signal are illustrated in Figure 3 for the same value of f_cT as in Figure 2. Here again, notice that, as the PN code period gets larger, the dominant false lock frequencies occur at multiples of the data rate and in the limit as the period goes to infinity, we again get the results for a random data sequence [see Figure 3(c)]. From this figure and the theoretical results given in Appendix A, we observe that, for the random data case, the set of amplitudes at odd multiples of the half data rate and likewise the set at even multiples of the half data rate are monotonically decreasing with the two sets interleaved in amplitude. Thus, the largest false lock spur occurs at the data rate. This spur is about 4.6 dB below the true lock dc magnitude at $\omega_f = 0$. The S-band transponder test results showed that false lock occurred at the data rate (96 kbps) when the carrier-to-noise ratio (C/N_0) was increased by 3 dB above true lock acquisition threshold (see line 2 of Table 1). The false lock spur at one half the data rate as shown in Figure 3(c) is 8 dB below the true lock point and this was verified by the S-band transponder test (see line 1 of Table 1).

Widening the arm filter bandwidth beyond $f_cT = 1.4$ increases the separation between the true lock voltage $|V_0|$ and the false lock voltages. Figure 4 plots the false lock voltages $|V_k|$ for the false lock frequencies at $k/2T$; $k = 1,2,3,4$ versus f_cT for alternating data [sequence (A)]. Figure 5 illustrates the corresponding behavior of the false lock voltages which, for random data, also occur at $k/2T$, $k = 1,2,\ldots$. Note that, for the alternating data case, the worst false lock point is at one half the data rate where the false lock voltage $|V_1|$ is only 5.83 dB below the true

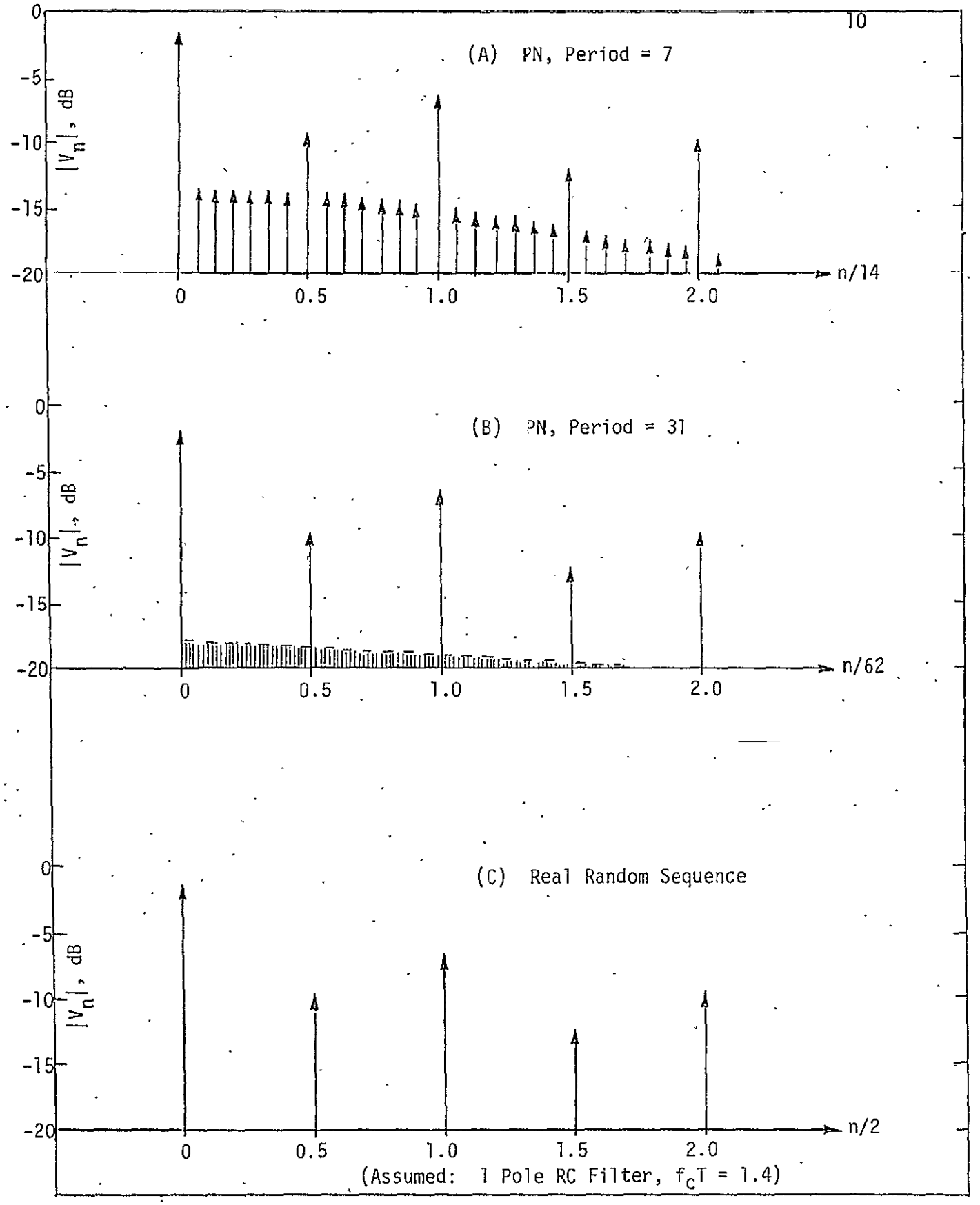

Figure 3. Amplitude of DC Component in Costas Error Signal (or Lock Detector Signal)

Table 1. PSK Modulated Data False Lock Test Results

Arm Filter Bandwidth (kHz)	Static Doppler Shift (kHz)	Data Rate (kbps)	Acquisition Threshold C/N_0 (dB)	False Lock Offset From True Lock (kHz)	False Lock C/N_0 (dB)	Ratio of True Lock to False Lock Threshold (dB)
134	0	96	47.6	±48	55.6	8
134	-60	96	47.6*	+96	50.6	3
308	-60	96	48.0*	+96	54.6	6.6
308	0	216	49.0	None	----	----
308	-60	216	49.0*	+108	55.6	6.6
134	0	72	46.6	-72	50.6	4
308	0	72	47.0	-72	55.6	8.6
308	0	32	47.0*	±32	64.6	17.6

*Not actually measured.

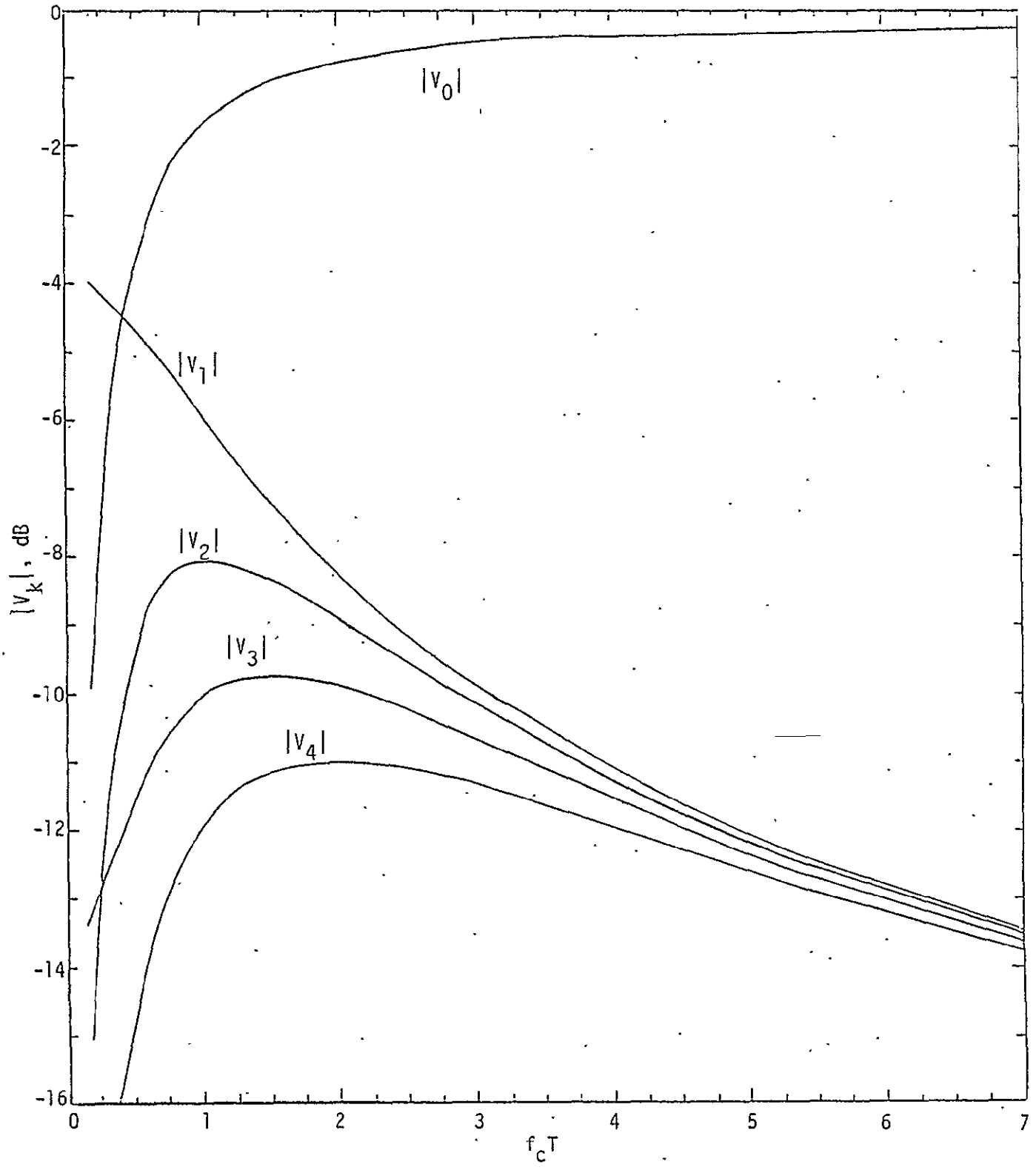

Figure 4. Alternating Data - Manchester Code, RC Filter

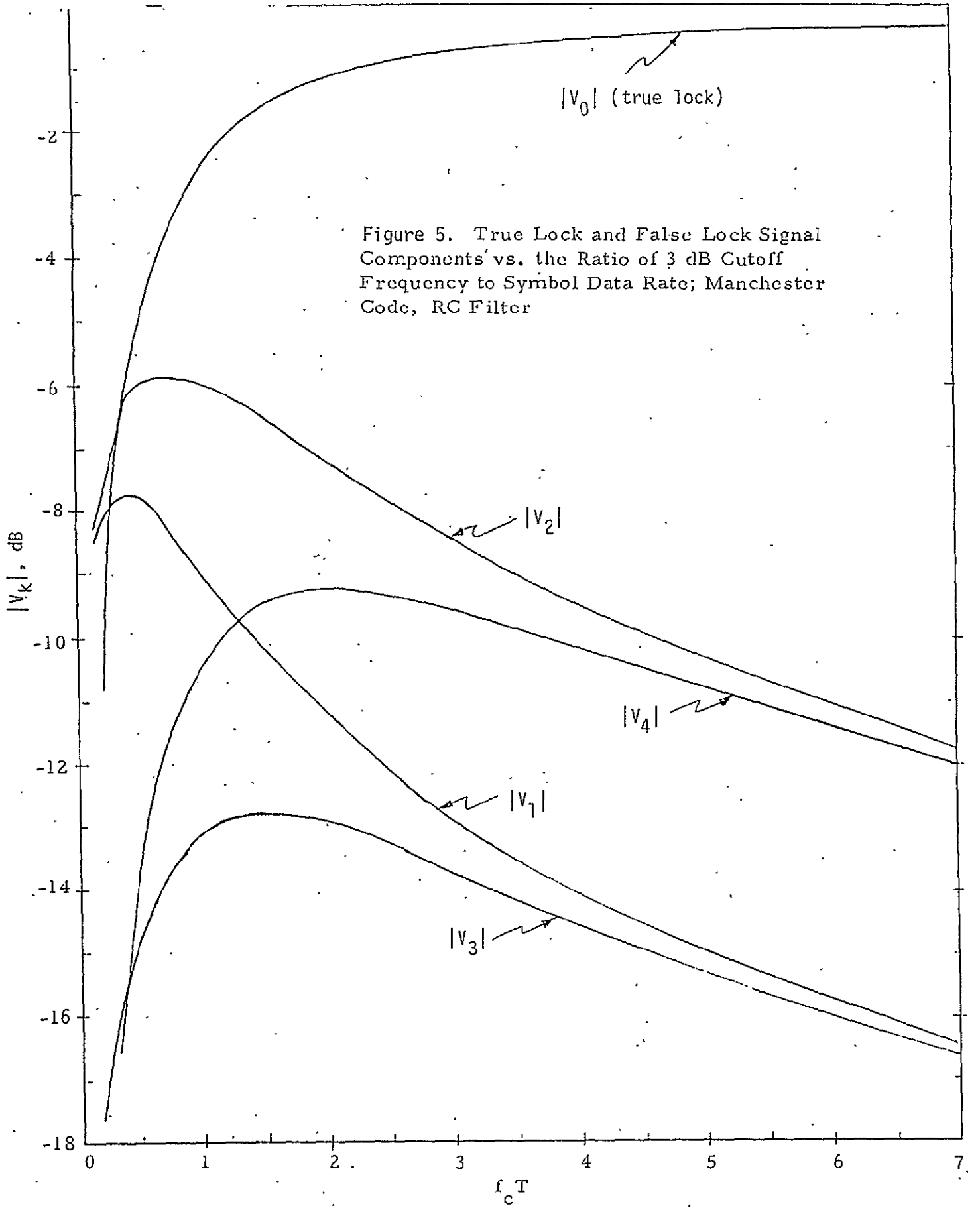

Figure 5. True Lock and False Lock Signal Components vs. the Ratio of 3 dB Cutoff Frequency to Symbol Data Rate; Manchester Code, RC Filter

lock voltage $|V_0|$ at $f_cT = 1.4$. For $f_cT = 7$, all the false lock voltages are about 13 dB below $|V_0|$. For the random data case, the worst false lock point occurs at the data rate ($k = 2$). With $f_cT = 1.4$, $|V_2|$ is 4.6 dB below $|V_0|$. As f_cT is increased to 7, $|V_2|$ decreases to about 11 dB below $|V_0|$. Thus, by continuing to widen the arm filter bandwidth beyond the optimum value which yields minimum tracking threshold loss, the separation between $|V_0|$ and the false lock values continues to increase. This property is desirable from the standpoint of distinguishing false lock from true lock. However, widening the arm filter bandwidth also allows more noise to pass through, thus degrading the tracking threshold.

In order to determine how wide the arm filters can be made to decrease the chance of false lock, the effect on tracking threshold must be assessed. The variance of the phase error is given by

$$\sigma_{2\phi}^2 = \frac{4}{S_L \rho} , \qquad (1)$$

where ρ is the equivalent signal-to-noise ratio in the loop bandwidth of a linear loop and S_L is the squaring loss (i.e., a factor less than 1) incurred in the Costas loop relative to a linear loop, e.g., a phase-locked loop. Therefore, to minimize the phase error variance, S_L must be maximized. Figure 6 presents the ratio of optimum arm filter two-sided noise bandwidth to the symbol rate (B_i/R_s) versus the signal-to-noise ratio (R_d) in the symbol rate bandwidth ($R_s = 1/T$). Note that, for a one-pole filter, the value of $B_i/R_s = 4.4$ for low values of R_d. For a one-pole filter, note also that the two-sided noise bandwidth can be expressed in terms of the 3 dB cutoff frequency by $B_i = \pi f_c$. Therefore, the optimum value of $f_c = 1.4\ R_s$ or $f_cT = 1.4$, as has been previously mentioned.

The variation in squaring loss and hence tracking threshold versus B_i/R_s is presented in Figure 7. Except at very low values of R_d, the variation in S_L is very small for reasonably large changes in B_i/R_s. Thus, the arm filter bandwidths can be increased significantly without having much effect on the tracking threshold. The test results of the S-band transponder shown in Table 1 bear out this conclusion. Note that, for the 96 kbps case, by changing from $f_cT = 1.4$ ($f_c = 134$ kHz) to $f_cT = 3.2$ ($f_c = 308$ kHz), the worst false lock amplitude was decreased by 3.6 dB, while the acquisition threshold was only increased by 0.4 dB. Similarly, for

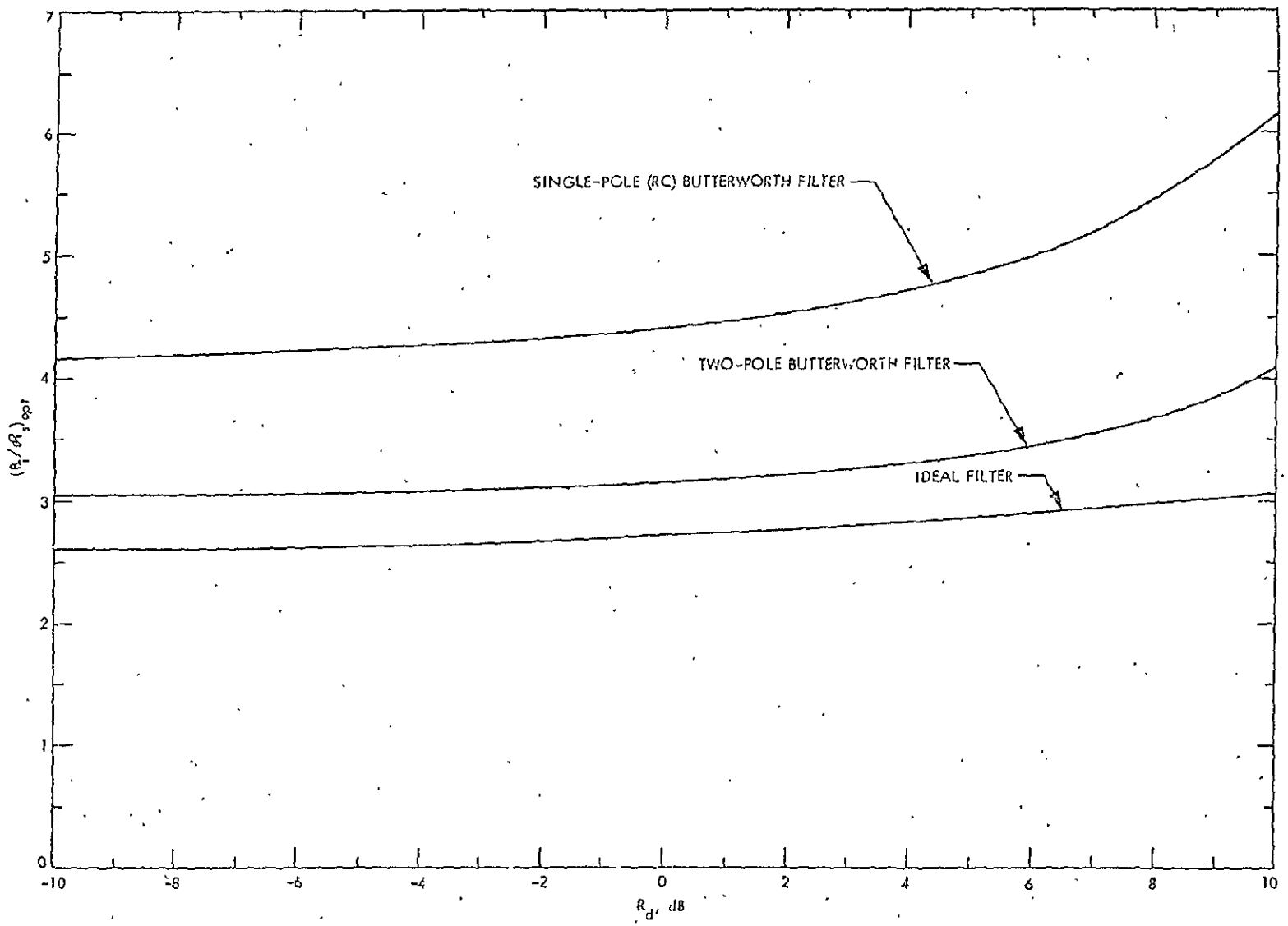

Figure 6. Ratio of Optimum Arm Filter Bandwidth to Symbol Rate versus Symbol Energy to Noise Ratio, R_d

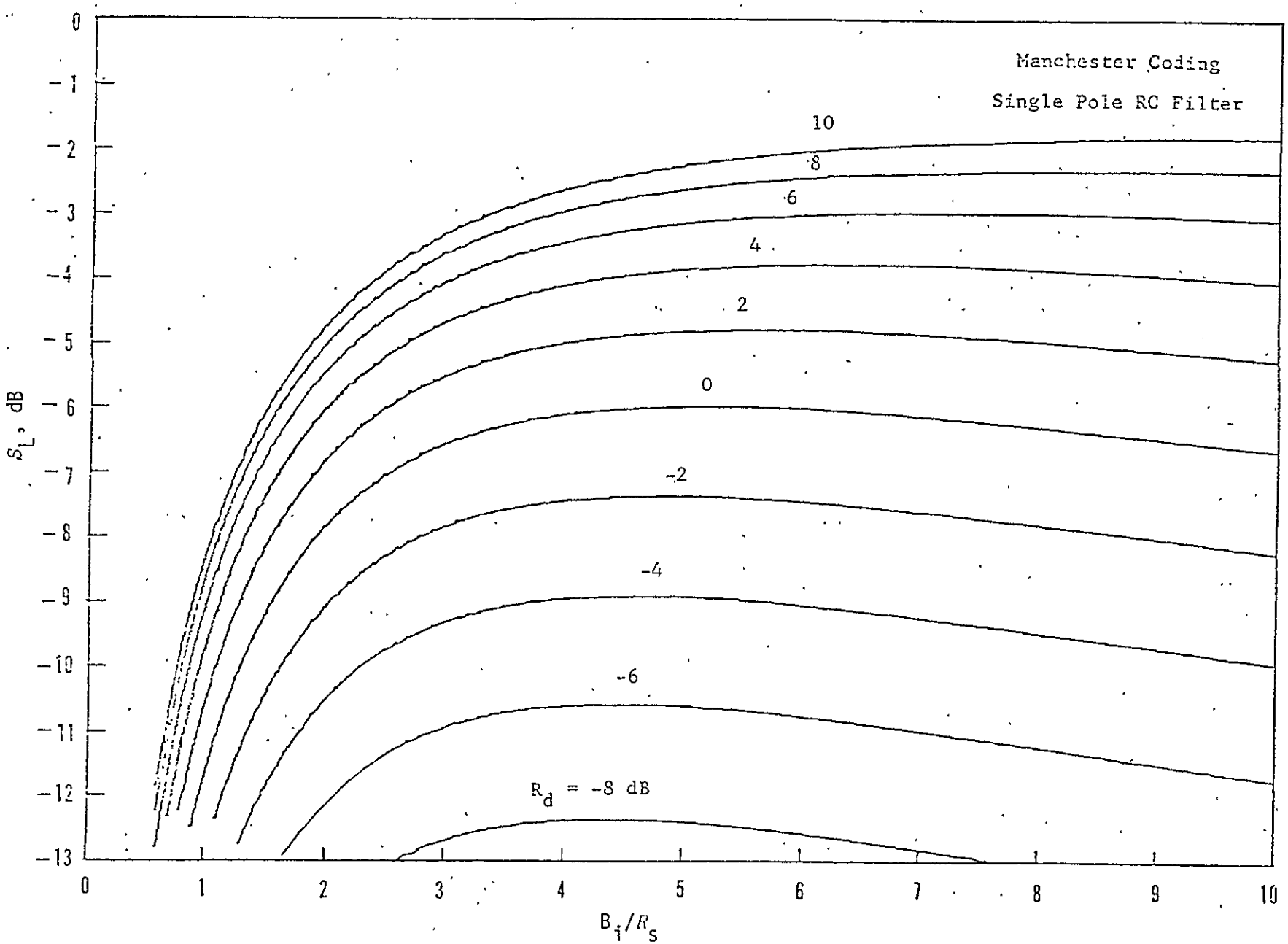

Figure 7. Squaring Loss Variations Versus B_i/R_s for Various Values of R_d

72 kbps, by changing from $f_cT = 1.94$ ($f_c = 134$ kHz) to $f_cT = 4.28$ ($f_c = 308$ kHz), the worst false lock amplitude was decreased by 4.6 dB, while the acquisition threshold only decreased by 0.4 dB. By decreasing the data rate to 32 kbps, $f_cT = 9.6$ ($f_c = 308$ kHz), the worst false lock amplitude decreases by another 11 dB with a 1 dB improvement in acquisition threshold. These test results agree very closely with Figures 5 and 7. The possibility of using wide arm filters in the Costas loop is being investigated for the Ku-band uplink communication system.

Thus far, we have discussed the false lock behavior of a conventional Costas loop in terms of its ability to produce a dc component in the error signal or lock detector output when the frequency difference between the incoming carrier and the local VCO is other than zero. Based upon observation of this dc component alone, we have demonstrated that its magnitude can be significantly reduced by simultaneously increasing the bandwidths of both arm filters at the expense of a small degradation in tracking threshold. The emphasis here has been on a means of reducing the false lock tendency of the loop, rather than detecting its presence.

A method for detecting a false lock condition is based upon the fact that, for random data, there exist strong periodic components (other than the dc component) in the loop error signal when the loop is locked at one of the possible false lock frequencies. These periodic components which occur at integer multiples of the data rate also exist when the loop is truly locked, but are much smaller in amplitude. Because of this fact, true lock and false lock can be differentiated by measuring the amplitudes of these periodic components in the loop error signal using, for example, a bandpass filter centered at the false lock frequency followed by an envelope detector and threshold device.

If one is willing to introduce modifications into the conventional Costas loop design, then several methods are available which virtually eliminate the false lock problem completely. These methods are based upon the principle of frequency discrimination and include augmenting the conventional Costas loop with an automatic frequency control (AFC) loop or modifying the conventional loop to act like an AFC during acquisition. All of these methods have the additional advantage of improving the frequency acquisition capability of the conventional Costas loop at the expense of a degradation in tracking threshold. The exact theoretical

tradeoffs among false lock improvement, acquisition performance improvement, and tracking performance degradation are the subject of Appendices C, D and E, and are briefly summarized here.

The simplest modification is achieved by merely removing the low pass arm filter in the quadrature phase detector channel (see Figure 8). The resultant loop (called a modified Costas loop in [1]) has a frequency restoring force approximately equivalent to that produced by half a balanced frequency discriminator commonly used for AFC. The improved acquisition performance obtained from this simple modification gives a pull-in from initial frequency errors on the order of the in-phase arm filter bandwidth which, for optimum tracking performance design, is on the order of the data rate. Aside from the improvement in acquisition performance, we anticipate from our previous discussion a significant lessening of the false lock tendency of the loop. This reduction in false lock tendency comes about as follows. Removal of the quadrature channel arm filter produces, under false lock conditions, a dc voltage (independent of the loop phase error) which, when added to the sinusoidal restoring force which is normally present, reduces the stability (in noise) of these false lock points. In the true lock condition, this additional phase error independent dc voltage has zero value and thus the stability of the true phase lock points is unaffected. Figure 9 clearly illustrates these points by plotting the modified Costas loop S-curve together with that of the conventional Costas loop for random Manchester coded data, an RC in-phase arm filter with $f_c T = 1.4$, and a false lock frequency equal to half the data rate. The corresponding results for alternating data are illustrated in Figure 10.

Having concluded that the modified Costas loop offers superior acquisition and false lock performance relative to the conventional Costas loop, what remains is to assess the penalty paid in true lock tracking performance. When the signal-to-noise ratio ρ_i in the Costas arm filter bandwidth is small, such as in the S-band transponder (e.g., a C/N_0 = 47.6 dB and an arm filter bandwidth of 134 kHz (51.3 dB) given ρ_i = -3.7 dB), then complete removal of the quadature RC arm filter results in approximately a 3 dB penalty in mean-square tracking jitter or equivalently in tracking threshold (Appendix C). As ρ_i is increased, the tracking performance difference between the modified and conventional Costas loops diminishes.

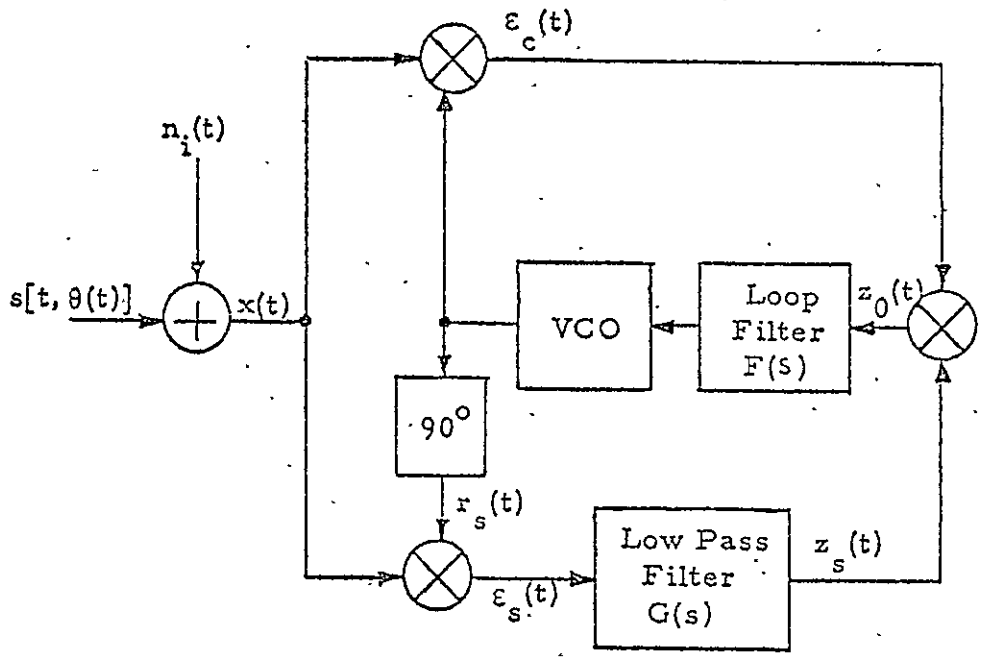

Figure 8. Modified Costas Loop.

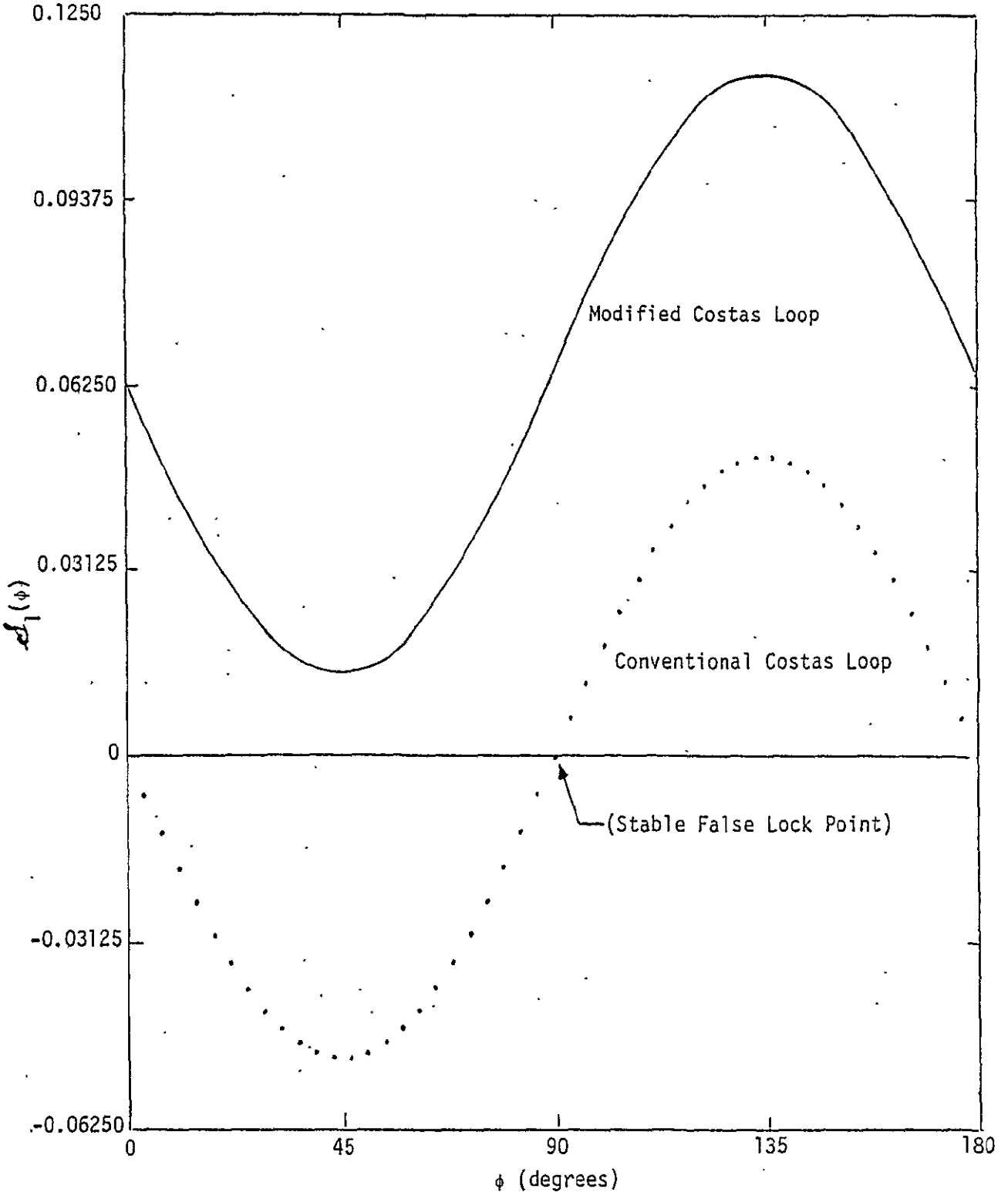

Figure 9. False Lock Error Characteristic for Modified and Conventional Costas Loops; Manchester Code, RC Filter, Random Data; $f_cT = 1.4$

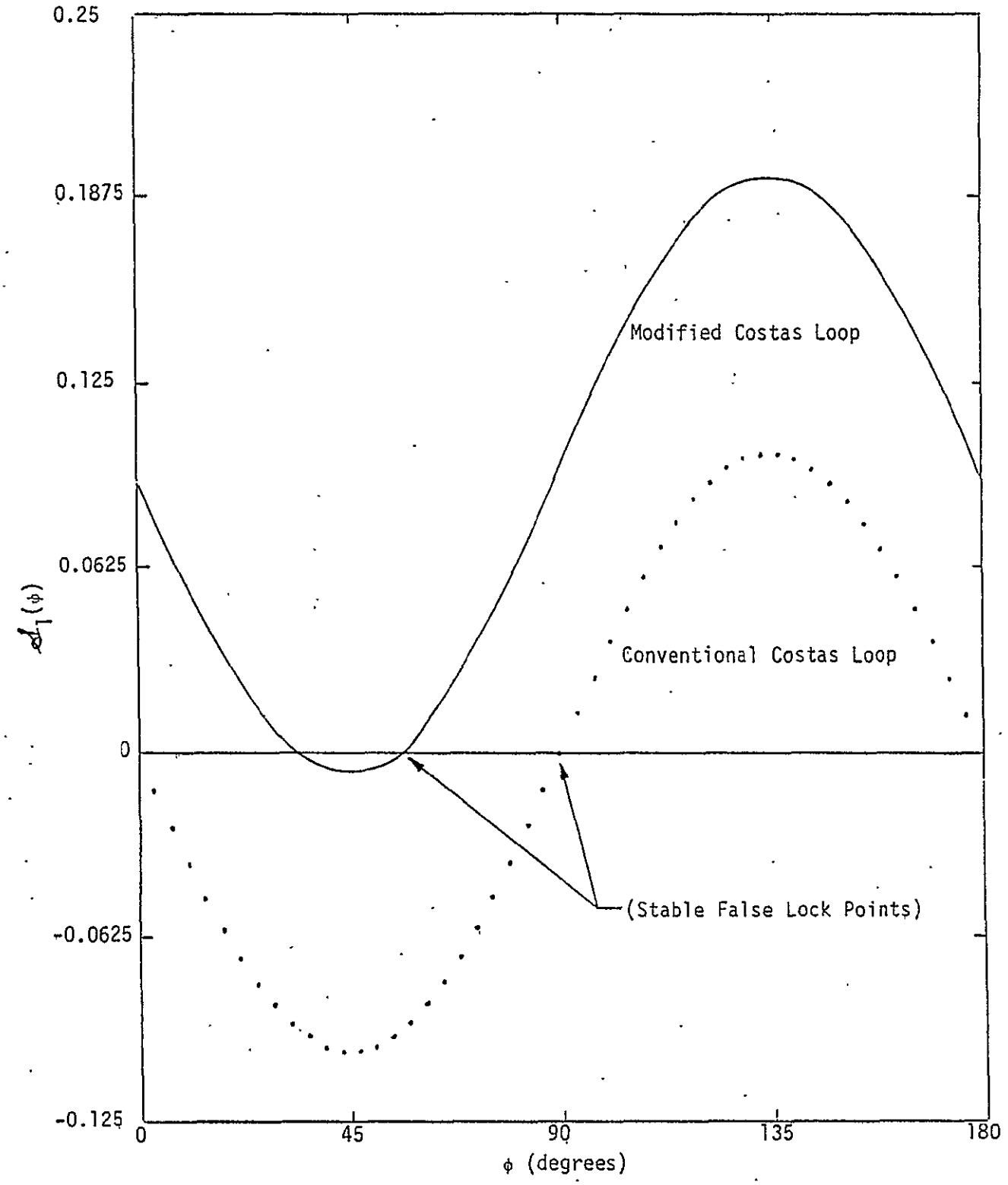

Figure 10. False Lock Error Characteristic for Modified and Conventional Costas Loops; Manchester Code, RC Filter, Alternating Data; $f_cT = 1.4$

A compromise solution to the 3 dB tracking threshold penalty paid at the expense of much improved acquisition and false lock performance is to use a wideband quadrature arm filter as opposed to its complete removal. By continuously varying the ratio of quadrature arm filter bandwidth to in-phase arm filter bandwidth, one can achieve any desired degree of tracking versus false lock performance tradeoff between the two extremes corresponding to the modified Costas loop of above and the conventional Costas loop. One other possibility would be to leave the quadrature arm filter wideband during acquisition and switch its bandwidth during tracking to the optimum bandwidth of the in-phase arm filter.

The next configuration studied was a composite AFC/Costas loop, whose RC arm filters are shared in common between the AFC and Costas loop portions of the overall hybrid configuration. The first case considered was that in which the loop filter was also shared in common (see Figure 11). The results of this study (see Appendix D) reveal that the tracking and false lock performances of this composite AFC/Costas loop are identical to those of the modified Costas loop analyzed in Appendix C. The composite AFC/Costas loop has the advantage, however, of being a balanced configuration and, further, the degree of tradeoff between tracking performance degradation and false lock performance improvement is continuously variable depending on the relative gains of the two error signal components.

The second case considered was a composite AFC/Costas loop with independent AFC and Costas loops in the sense that each has its own loop filter (see Figure 12). By varying the ratio of the two loop bandwidths, one now has an additional degree of freedom available for performing acquisition and tracking tradeoffs. The results of these tradeoff studies are discussed in detail in Appendix E and are briefly summarized as follows.

The AFC discriminator (indicated by dashed lines on Figure 12) has a characteristic (output signal amplitude versus input frequency) illustrated in Figure 13. We note from this figure that both the equivalent linear gain (slope of characteristic at zero frequency) and the approximate region of linearity are functions of the ratio of 3 dB cutoff frequency to data rate. In fact, at the optimum arm filter design point ($f_c T = 1.4$), the normalized linear slope is 0.3535 rather than the more commonly assumed value of unity, which would be the case in the limit of infinite arm filter bandwidth. This reduced value of equivalent linear

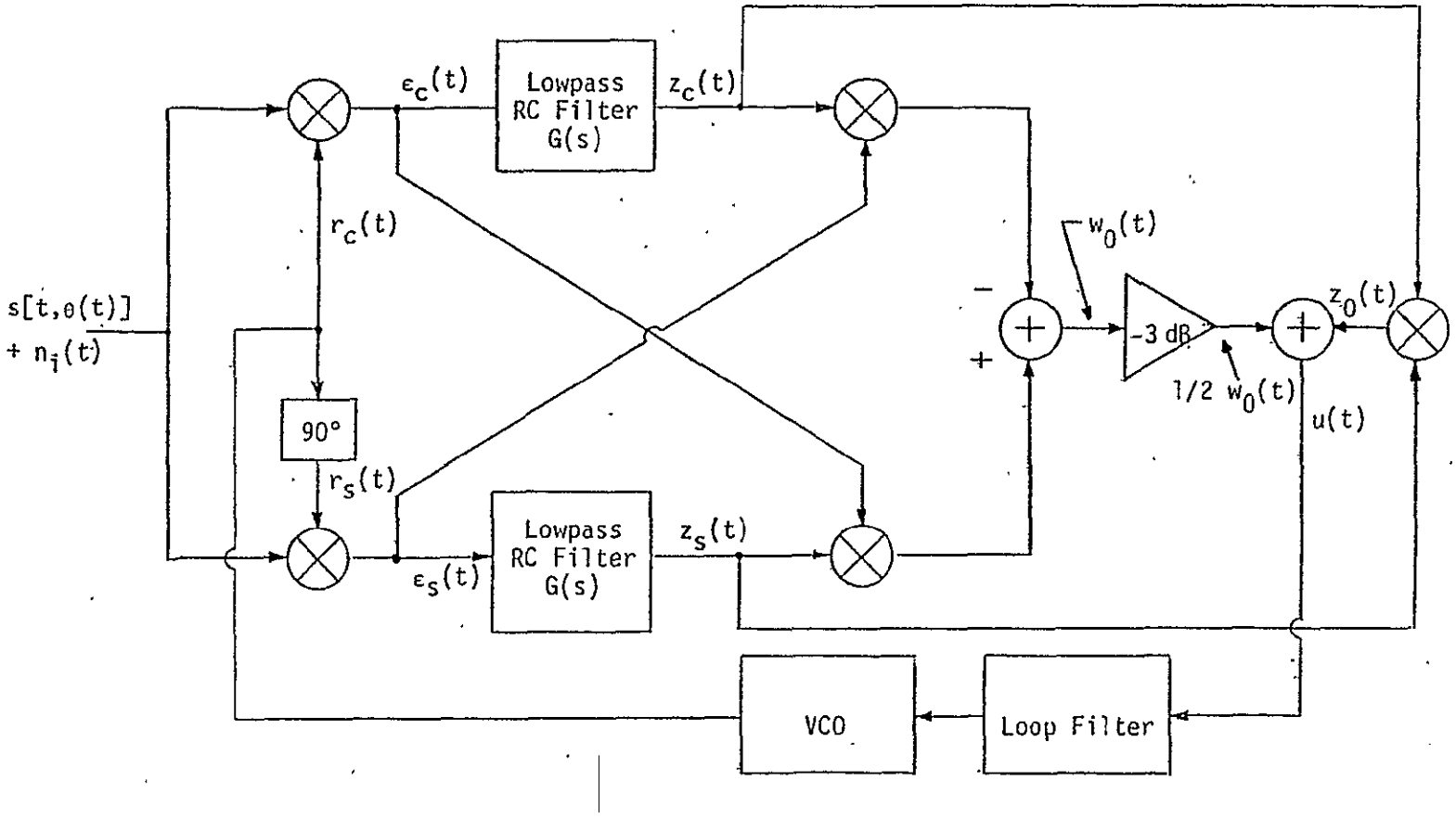

Figure 11. A Composite AFC/Costas Loop

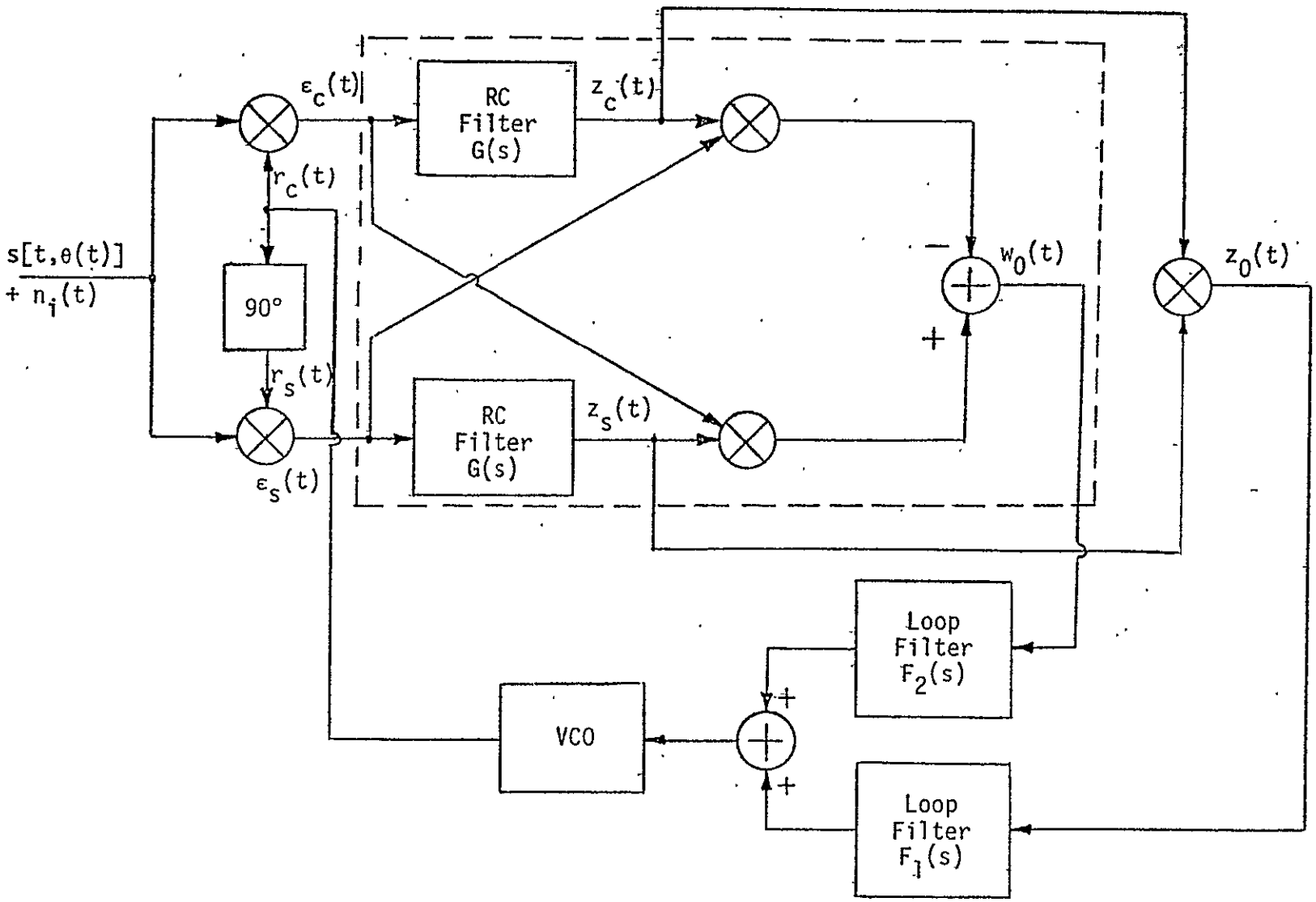

Figure 12. A Composite AFC/Costas Loop

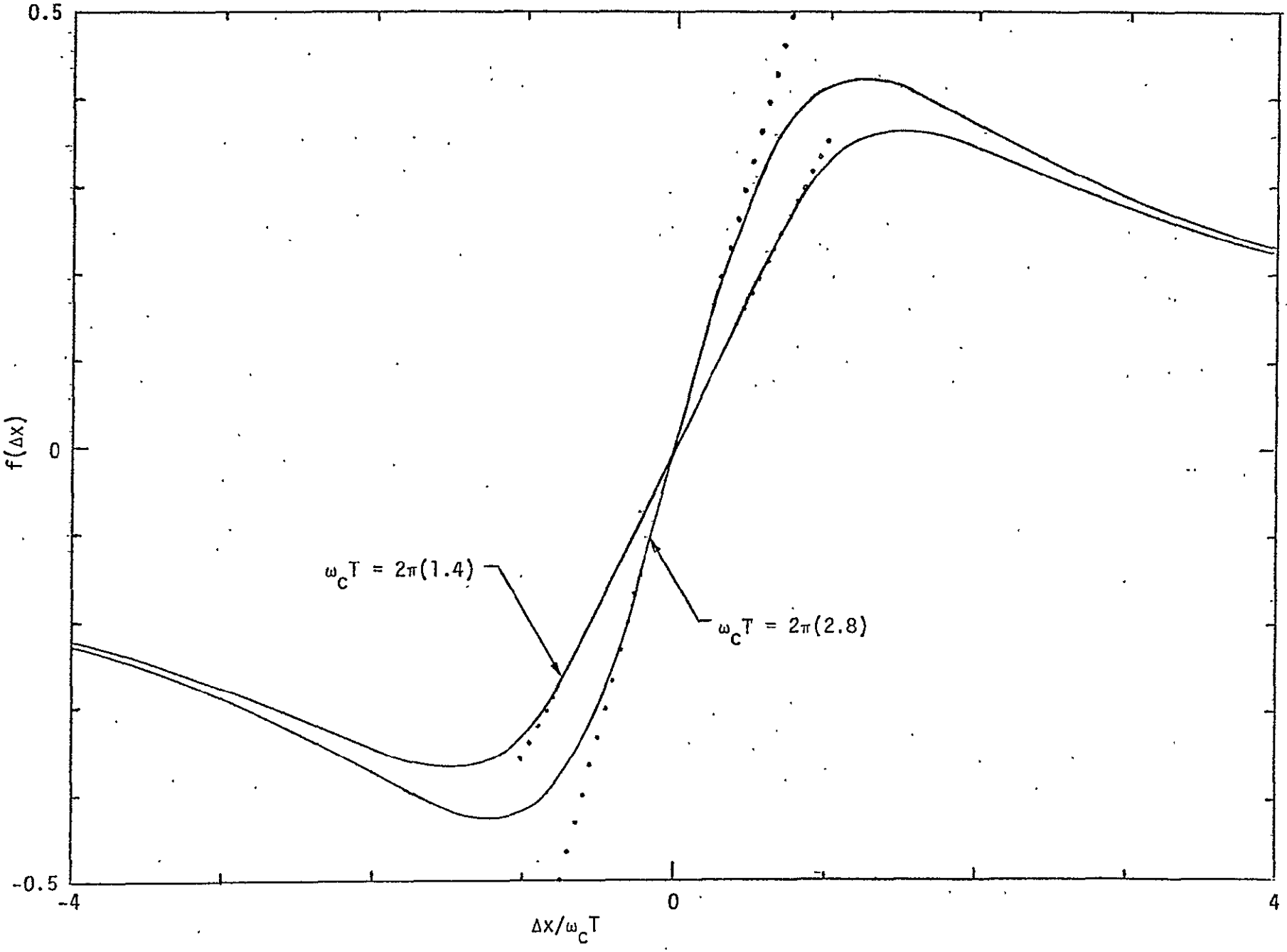

Figure 13. AFC Discriminator Characteristics

gain comes about because of the arm filtering of the data modulation. Thus, in the neighborhood of zero frequency, the discriminator characteristic is given by $f(\omega) = 0.3535\ \omega/\omega_c = 0.3535\ \omega RC$.

The improved acquisition performance of the composite AFC/Costas loop relative to that of a conventional Costas loop is illustrated in Figures 14 and 15. Here, an upper bound on acquisition time T'_{ACQ} (normalized to the Costas loop bandwidth B_{L1}) is plotted versus the ratio of initial frequency offset Δf_0 to Costas loop bandwidth with the ratio of AFC bandwidth B_{LF} to Costas loop bandwidth as a parameter. The two curves are distinguished from one another by the value of the ratio of Costas loop bandwidth to data rate. Also illustrated on these same curves are the corresponding acquisition time (not an upper bound) results for a conventional Costas loop. Clearly, the addition of the AFC increases the acquisition range and reduces the acquisition time. Such improvements, however, do not come without cost. The corresponding degradations in mean-square tracking jitter are illustrated in Figures 16 and 17 for the same loop parameters. The total mean-square tracking jitter of the composite loop is the sum of the Costas jitter and the AFC jitter presented in these figures.

In our discussion of false lock thus far, we have implicitly assumed the presence of frequency uncertainties (due to Doppler shift or oscillator instabilities) of such a magnitude as to cause the carrier acquisition frequency range to include at least one of the false lock frequencies. We have also alluded to the fact that the means by which false lock (or for that matter, true lock) is detected is the presence of a dc voltage at the lock detector output. This identification of the locked state during the carrier acquisition process is the primary purpose of the lock detector associated with the Costas loop. Furthermore, since carrier acquisition in the presence of large frequency uncertainties is commonly achieved by sweeping the carrier VCO (either discretely or continuously) in frequency, a secondary function of the lock detector is to kill this sweep once carrier lock has been detected. By doing this, the Costas loop is not required to track its own sweep, and thus the steady-state tracking peformance is not degraded by the loop stress which would accompany the sweep waveform. Also, killing the sweep serves to minimize the acquisition time.

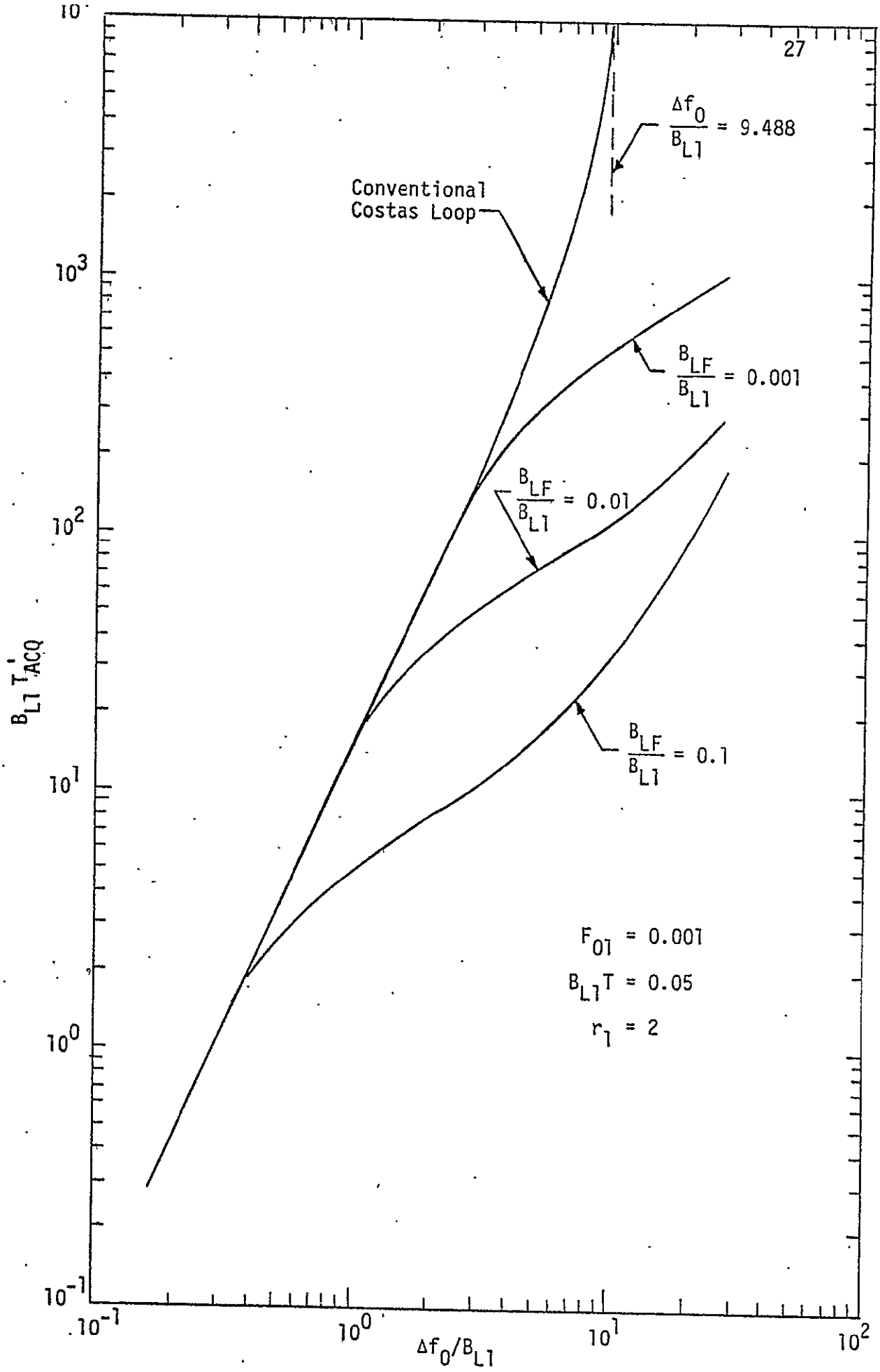

Figure 14. Acquisition Behavior of Composite AFC/Costas Loop

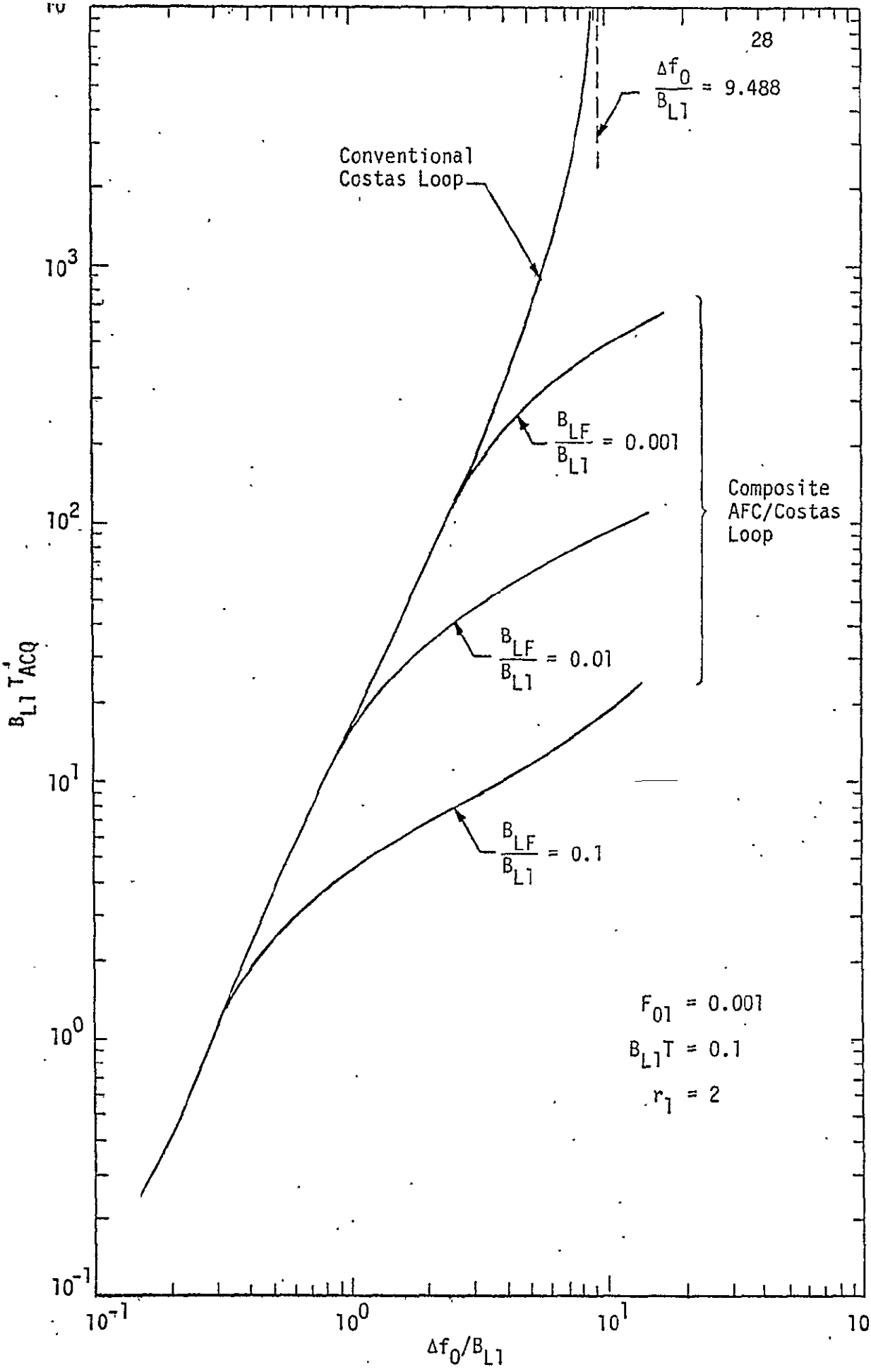

Figure 15. Acquisition Behavior of Composite AFC/Costas Loop

Figure 16. Tracking Jitter Performance Components for Composite AFC/Costas Loop

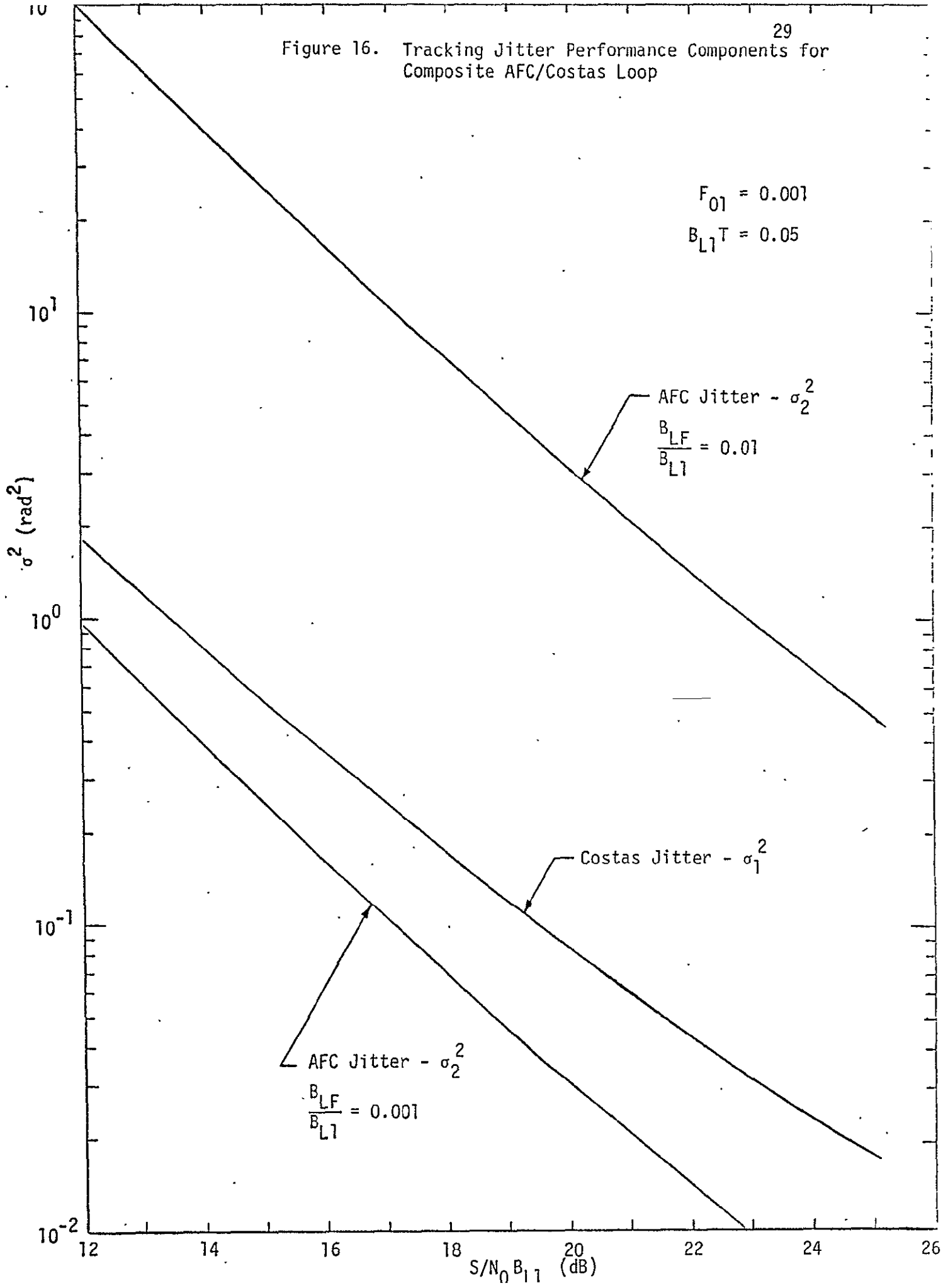

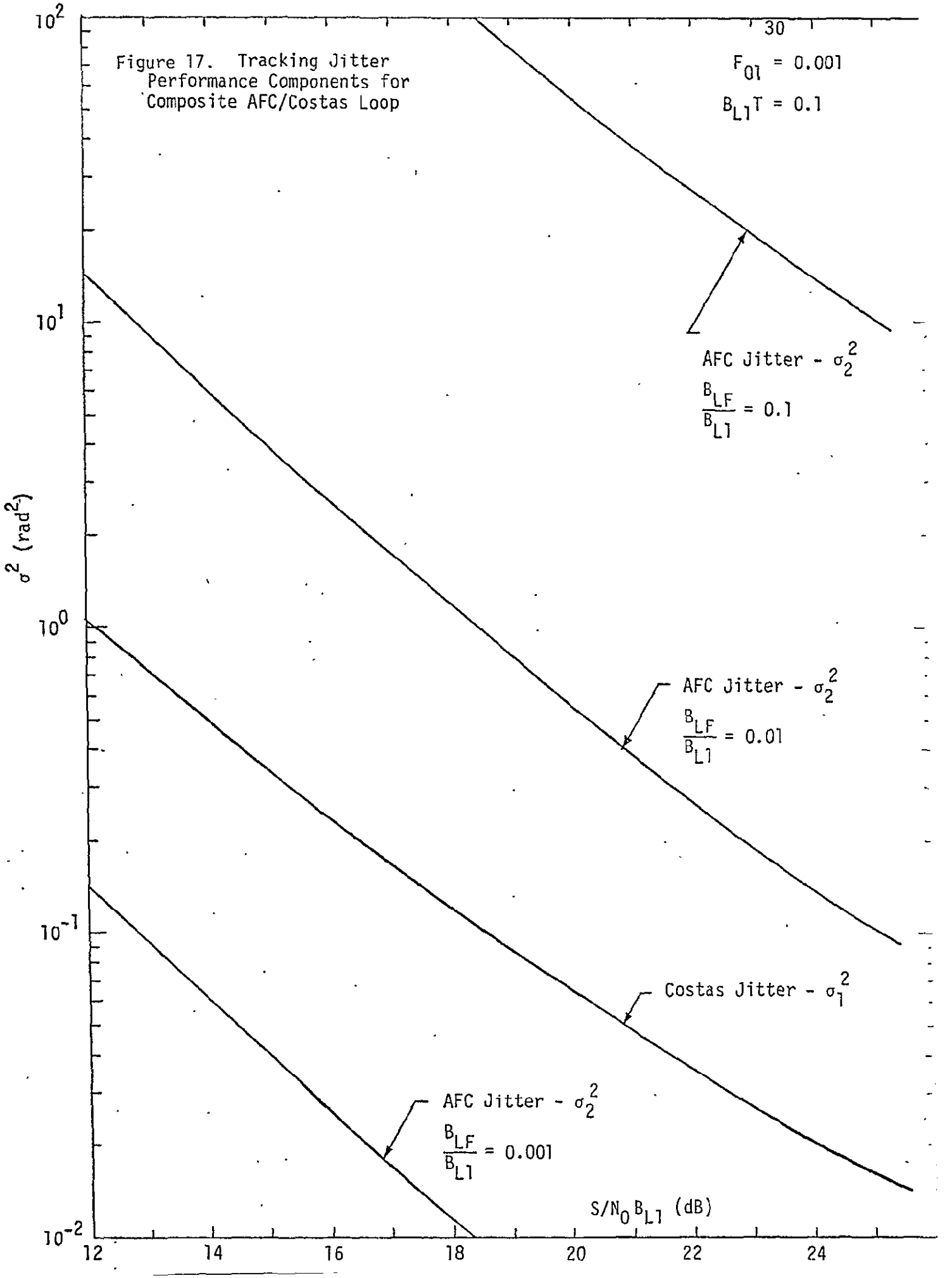
Figure 17. Tracking Jitter Performance Components for Composite AFC/Costas Loop
30
F_{01} = 0.001
$B_{L1}T$ = 0.1
AFC Jitter - σ_2^2
$\frac{B_{LF}}{B_{L1}}$ = 0.1
AFC Jitter - σ_2^2
$\frac{B_{LF}}{B_{L1}}$ = 0.01
Costas Jitter - σ_1^2
AFC Jitter - σ_2^2
$\frac{B_{LF}}{B_{L1}}$ = 0.001
σ^2 (rad^2)
10^2
10^1
10^0
10^{-1}
10^{-2}
12
14
16
18
20
22
24
$S/N_0 B_{L1}$ (dB)

Lock detection in a Costas loop is most readily achieved by nonlinear processing the signals out of the in-phase and quadrature phase channels, differencing the results, and comparing to a preset threshold. The nonlinear processing is customarily accomplished using balanced square-law devices, although an absolute-value type of nonlinearity (e.g., full-wave rectifiers) has advantage when such effects as AGC gain variations, phase detector dc offsets, and arm gain imbalance are other than small. The threshold is fixed by the false alarm probability, i.e., the probability of deciding that the loop has achieved a locked state given that it is in reality out of lock.

When the loop is far out of lock, a double frequency beat note appears at the input to the integrate-and-dump. For a stepped sweep acquisition, the beat note will remain constant in frequency over the duration in time of a single step. As the sweep continues and the loop approaches a locked condition (either true or false lock), a point is reached where the beat note becomes within the pull-in range of the loop, at which time the beat note disappears and a sync pulse whose amplitude is proportional to the steady-state tracking loop jitter appears at the input of the integrate-and-dump. As soon as the sync pulse is sensed by the lock detector, an action is taken to kill the sweep; however, until such time, the sweep continues to step along and, depending on the sweep rate, the loop may break lock and resume beating. It is shown in Appendix F that, for a fixed data rate, signal power to noise spectral density ratio, and specified probabilities of false alarm and false detection, the integration time of the integrate-and-dump is determined, and thus the sweep rate is also set by these same quantities. The results which characterize this interrelationship are illustrated in Figure 18, where the false detection probability β is plotted versus $R_d = ST/N_0$ in dB for fixed false alarm probability α and T_i/T varying between 50 and 500. The ratio T_i/T is the number of symbol intervals in the integration time of the integrate-and-dump. The specific numerical results given in this figure are again for the case of an RC arm filter with optimally designed bandwidth and Manchester coded data.

In order to explain the significance of the dotted curves which also appear on Figure 18, we must first understand the significance of the so-called "beat-note noise" and the effect of the beat note frequency on the setting of the lock detector threshold.

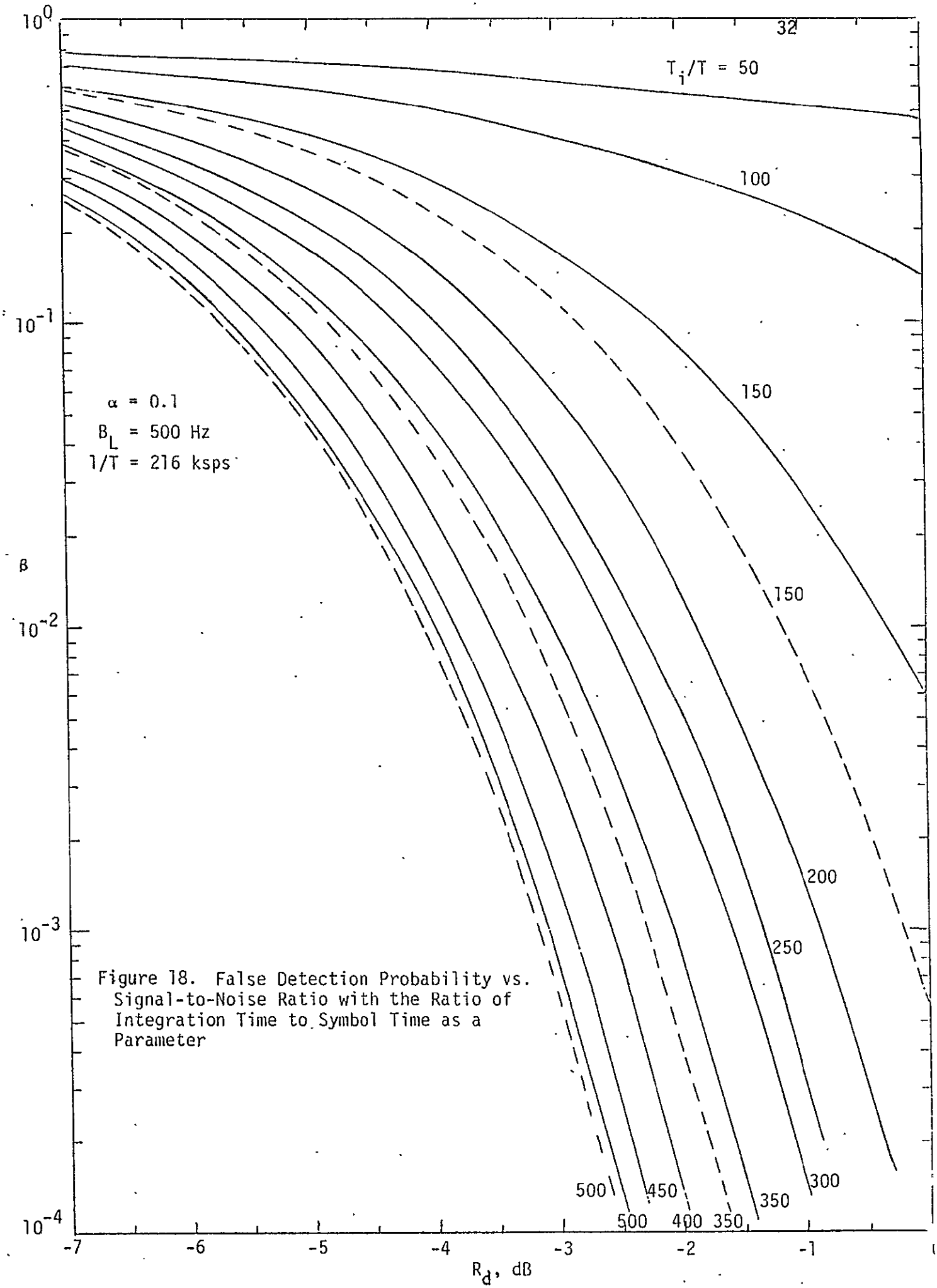

Figure 18. False Detection Probability vs. Signal-to-Noise Ratio with the Ratio of Integration Time to Symbol Time as a Parameter

The total noise out of the integrate-and-dump consists of three components: one due to the total signal × noise and noise × noise terms, a second due to the self-noise of the modulation, and a third which, when the loop is out of lock, is referred to as "beat-note noise" and, when the loop is in lock, is proportional to the loop tracking jitter. The beat-note noise is caused by the lack of coherence between the beat note and the integrate-and-dump timing instants. In general, this noise is a function of the beat note frequency. As the loop approaches true lock, the beat note frequency becomes small with respect to the data rate and the dependence of the beat note noise on this frequency behaves like a $(\sin x/x)^2$ function.

As discussed above, when the loop is out of lock, the total noise is a function of the beat note frequency. The question arises as to the value of this frequency at which to set the lock detector threshold for a given false alarm probability. If the threshold is set based upon the total integrate-and-dump output noise when the loop is far out of lock, i.e., the beat-note noise is neglected, then as the loop approaches lock, the actual integrate-and-dump output noise increases (due to the presence of the beat-note noise) and the lock detector is likely to kill the sweep before lock is fully achieved. In practice, a more reasonable compromise would be to set the threshold based on a value of total integrate-and-dump output noise corresponding to a beat note on the order of the radian pull-in frequency of the loop. Since, for a conventional Costas loop, this pull-in range is typically on the order of the loop bandwidth, the results illustrated as solid curves in Figure 18 were computed on the further assumption that the beat note frequency was set equal to the loop bandwidth B_L. The dotted curves in Figure 18 correspond to selection of the lock detector threshold based upon the loop being far out of lock. This is equivalent to ignoring the beat-note noise and assuming that the total variance of the integrate-and-dump output is identical both under lock and out-of-lock conditions. Clearly, the significance of the beat-note noise diminishes as the integration time T_i increases. This fact bears out on Figure 18 by comparing the solid and dashed curves corresponding to the same value of T_i/T.

2.3 Application to Ku-Band Costas Receiver

Earlier, we presented some false lock test results for the S-band transponder and compared them with the equivalent theoretical results given in Appendix A. To conclude this summary, we discuss the application of the theoretical results to the design of the 216 kbps Ku-band forward link. This link must acquire the carrier over a frequency uncertainty (due to local oscillator instabilities) range of ±150 kHz.

One consideration would be to demodulate the carrier before despreading the 3 Mchip/sec PN sequence. Since this sequence has a period of 1023 chips, then from Figure 3, we observe that the first false lock frequency which yields a significant dc component in the Costas error signal occurs at half the data rate, which in this case, would be approximately half the chip rate, viz., 1.5 MHz. Since this false lock point is at a frequency which is a factor of 10 outside the frequency range over which the loop must be acquired, we can safely say that false lock to a data sideband would not occur. The disadvantage of demodulating the carrier before despreading is that the arm filter bandwidth must be chosen relative to the bandwidth of the power spectrum of the combined 216 kbps data stream and 3 Mchip/sec PN sequence, which is approximately that of the PN sequence alone. Choosing an arm filter bandwidth to accommodate the PN sequence, i.e., one on the order of 10 times that which would be required if the PN were first despread, approximately introduces an additional 0.5 dB squaring loss or equivalent reduction in tracking threshold. Since, however, the forward link is a strong link (C/N_0 > 66.3 dB-Hz at a bit error rate of 10^{-6}) and since the single-sided loop bandwidth B_L is on the order of 3 kHz (34.8 dB-Hz), the loop signal-to-noise ratio is large enough that this additional squaring loss degradation might well be tolerated.

The other alternative, which is the more common, is to despread the PN sequence before reconstructing the carrier. Here, the first false lock at half the data rate, i.e., 108 kHz, is clearly within the sweep acquisition range of the loop. However, the next false lock at the data rate (i.e., 216 kHz) is well outside this range. Thus, we must examine the false lock C/N_0 at half the data rate over the complete range of true lock C/N_0 specified for this link. The zero link margin values of true

lock C/N_0 are 60.2 dB-Hz at a bit error rate of 10^{-2} and 66.3 dB-Hz at a bit error rate of 10^{-6}. Nominally, the link is required to operate with a margin of 8.5 dB while the maximum value of C/N_0 is another 5.5 dB higher. Thus, if the lock detector threshold is set based upon a true lock C/N_0 of 60.2 dB-Hz, then at the maximum value of C/N_0 = 80.3 dB-Hz, the loop will false lock unless the false lock dc component relative to the true lock component is more than 20.1 dB down. By an extension of Figure 5, one can show that, to achieve a separation between $|V_0|$ and $|V_1|$ of about 20 dB, one must widen the arm filter bandwidth so that the ratio of 3 dB cutoff frequency to data rate, f_cT, is approximately nine. This is only a factor of 9/1.4 = 6.4 greater than the optimum choice of arm filter bandwidth and hence produces little additional squaring loss degradation.

3.0 MODULATION/MULTIPLEXING FORMAT CONSIDERATIONS

3.1 General

The forward link consists of the ground-TDRS-Orbiter communication path. Because the last segment of this link is directed towards a relatively low orbiting Shuttle, methods must be provided to reduce the signal spectral density impinging on the earth's surface. Spreading the relatively narrowband data spectrum (32 to 216 kbps) by addition of a pseudo-noise (PN) code is considered to be the simplest method for reducing the spectral density of the forward link. The use of a PN code, however, requires code acquisition and tracking functions to be incorporated into the Orbiter's Ku-band receiver. The performance characterizing these functions is described in Section 3.3.2.

The driving parameters for the return link, which consists of the Orbiter-TDRS-ground communication path, include: (1) multiplexing of three independent data streams and (2) the capability to handle the symbol rates of up to 100 Msps, the latter originating from rate 1/2 encoding of data streams of up to 50 Mbps. As the result of previous work, Axiomatix has demonstrated the feasibility of simultaneously combining all three channels by phase multiplexing. In Section 3.2, we summarize the salient features of this multiplexing method.

3.2 Return Link Implementation

3.2.1 Parameters Summary

The return link has to accommodate simultaneously three independent data channels in two different modes. In Mode 1, all three channels carry digital data and the ultimate output is a phase-modulated carrier. In Mode 2, one of the three channels can be analog and thus the carrier is frequency-modulated by the composite signal, consisting of the three information inputs.

Table 2 presents the detailed summary of the return link data parameters. It is important to point out that the channel numbering shown in the table is consistent with the latest NASA and RI/SD convention. According to this convention, the channels are numbered in the order of the increasing data rates. Thus, because the 192 kbps channel rate is the lowest, this channel is referred to as #1. In Appendix G of this

Table 2. Return Link Data Parameters Summary

Channel Number	Mode 1		Mode 2	
	Rates	Modulation Type	Rates	Modulation Type
1 (See text)	192 kbps (Must also handle 96, 288 and 576 kbps)	Bi-phase on Q-phase of 8.5 MHz subcarrier	Same as Mode 1	Same as Mode 1
2	16 kbps to 2 Mbps	Digital or equivalent analog. Bi-phase on I-component of 8.4 MHz subcarrier	Same as Mode 1	Same as Mode 1
3 (See text)	2 Mbps to 50 Mbps	Rate 1/2 convolutionally encoded. Transmit rate of 4 Mbps to 100 Mbps, bi-phase on carrier.	Up to 4 Mbps digital or analog data compatible with 4.5 MHz bandwidth	Direct FM modulation of carrier.
Comments	The 8.5 MHz subcarrier (composite of channels 1 and 2) and channel 3 modulation result in QPSK signal.		The 8.5 MHz subcarrier (composite of channels 1 and 2) and channel 3 are combined to FM modulate the carrier.	

NOTE: All return link data is superimposed on Orbiter transmitter frequency f_{tx} = 15.0034 GHz.

report, however, we are using an arbitrarily selected notation which reverses the numbering order of the channels. According to our notation, the 192 kbps channel is No. 3 and the wideband (up to 50 Mbps) channel is No. 1. This notation is a carry-over of our previous work and will be rectified in the future.

3.2.2 Multiplexer/Modulator Implementation

The implementation of the multiplexer/modulator for both Mode 1 and Mode 2 is shown in Figure 19. Note that, for both modes, data channels 1 and 2 are placed, respectively, on the Q and I components of an 8.5 MHz subcarrier. The power division between channel 1 and channel 2 is 80% and 20%, respectively.

In Mode 1, the quadriphase-modulated 8.5 MHz is superimposed on the Q component of an L-band carrier. The modulation is bi-phase. Simultaneously, the convolutionally-encoded channel 3 data is bi-phase modulated on the I component of the L-band carrier. The modulated I and Q components are then combined in the ratio of 80% to 20%, respectively, thus forming a quadriphase phase-shifted carrier (QPSK). The QPSK signal is then passed through an amplitude limiter and is up-converted to the 15 GHz transmitter frequency. The function of the amplitude limiter is to remove any RF envelope fluctuations which may result from the simultaneous phase multiplexing of the data streams on the subcarrier and then multiplexing the subcarrier with the channel 3 component.

The detailed analysis of the power allocation required to achieve the specified ratio of 80/16/4 (by percent) between channels 3, 2, and 1, respectively, is given in Appendix G. Included there is also a supplementary analysis which considers the case where the 8.5 MHz subcarrier is a sinusoid instead of a square wave. The results of this analysis support the empirical data [2] which indicates that the use of a sinusoidal subcarrier eliminates the 1.2 to 1.4 dB small signal suppression of the low power channel (192 kbps) encountered with a square-wave subcarrier.

Referring to Figure 19, one can see that, when Mode 2 is activated, channels 1 and 2 are still combined as a quadriphase modulation on the 8.5 MHz subcarrier. Channel 3, however, is linearly summed with the subcarrier and the composite signal then modulates the frequency of an L-band VCO. The L-band output of the VCO is then up-converted to the 15 GHz

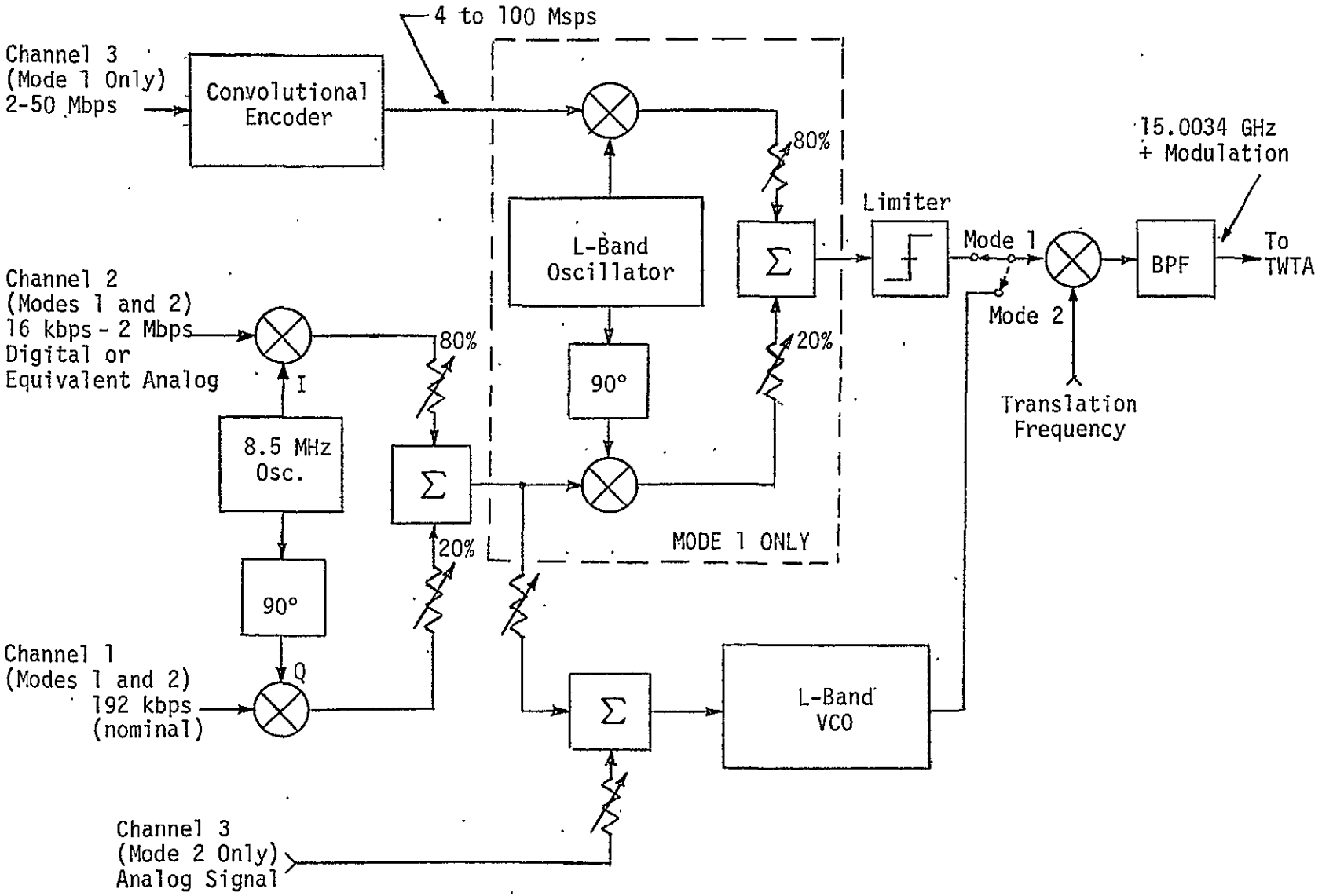

Figure 19. Return Link Multiplexer/Modulator Configuration for Modes 1 and 2

Orbiter transmitter frequency. The magnitude of the composite signal applied to the VCO is set at a level which limits the bandwidth of the modulated carrier to 50 MHz. This bandwidth is well within the bandwidth required to accommodate the 100 Msps rate 1/2 encoded channel 3 data in Mode 1.

3.3 Forward Link Considerations

3.3.1 Link Parameters and Performance Estimates

The forward link carries the data from the ground, via TDRS, to the Orbiter. The salient parameters of this link are summarized in Table 3. The primary operating mode is Mode 1 which employs a 216 kbps Bi-ϕ-L encoded data stream composed of (a) 72 kbps operational data, (b) 128 kbps scientific and instrument data, and (c) 16 kbps overhead. Because these data streams are time-division-multiplexed (TDM), a demultiplexer is employed at the Orbiter. The demultiplexer separates the 72 kbps data stream and applies it to the Network Signal Processor (NSP), which is not a part of the Ku-band equipment. The recovered 128 kbps stream may be routed either to an attached payload or to other equipment onboard the Orbiter.

In Mode 2, a selectable data configuration is available. Because no TDM is used, the demultiplexer is bypassed and any one of the data streams (32 kbps or 72 kbps or 96 kbps or 216 kbps) are applied directly to the NSP.

In both modes, the forward link data spectrum is widened by superimposing a PN code on the data-modulated carrier. The clock rate of the code is approximately 3.03 Mcps. The code length is 1023 chips.

The performance of the forward link can be estimated by considering the C/N_0 values available at the receiver output during the worst-case condition. The worst-case condition will exist when the TDRS EIRP is at its lowest point, i.e., 36.6 dBw, and the Orbiter's antenna has not fully acquired (i.e., centered on) the TDRS. As shown in Table 4, the worst-case condition may occur when the positioning of the antenna is performed by the General Purpose Computer (GPC) and the TDRS is at the edge of the 3 dB beamwidth of the antenna. The estimated C/N_0 at this point is 60.4 dB-Hz.

Table 3. Forward Link Data Parameter

Channel Number	Mode 1		Mode 2	
	Rates	Modulation Type	Rates	Modulation Type
Single Channel Only	216 kbps (Composite, see Comments)	Bi-phase on carrier. Data format Bi-ϕ-L	32 kbps or 72 kbps or 96 kbps or 216 kbps	Bi-phase on carrier.
Comments	1. 216 kbps is composed of: 72 kbps OPS data 128 kbps scientific and instrument data 16 kbps overhead All three are time-division-multiplexed (TDM). 2. PN code superimposed on carrier to reduce spectral density.		1. PN code superimposed on carrier to reduce spectral density.	

NOTES:

1. Orbiter receives forward link data on carrier frequency of f_{RX} = 13.775 GHz.
2. PN code clock = 3.028 Mcps, code length = 1023 chips.

Table 4. Calculation of C/N_0 for Worst Case TDRS Acquisition and for Lowest Acceptable* Forward Link Performance

Part A - TDRS Acquisition

Signal Calculation

TDRS EIRP	+ 36.6 dBW
Path Loss (Maximum)	-208.5 dB
Polarization Loss	- 0.3 dB
Antenna Gain	+ 38.9 dB
C (exclusive of antenna pointing loss, APL)	-133.3 dBW

Noise Density Calculation

Boltzman Constant	-228.6 dBW/°K/Hz
System Noise Temperature (T_s = 1563°K)	+ 31.9 dB-°K
N_0	-196.7 dBW/Hz

Therefore,

$$C/N_0 \text{ (scan)} = -133.3 \text{ dBW} - \underset{\text{(APL)}}{0.6 \text{ dB}} - (-196.7 \text{ dBW/Hz}) = 62.8 \text{ dB-Hz}$$

$$C/N_0 \text{ (GPC design)} = -133.3 \text{ dBW} - \underset{\text{(APL)}}{3.0 \text{ dB}} - (-196.7 \text{ dBW/Hz}) = 60.4 \text{ dB-Hz}$$

Part B - Lowest Acceptable Link Performance

E_b/N_0 for BER = 10^{-2} (From standard BER curve)	+ 4.4 dB
Correlation and Sync Loss	+ 2.5 dB
Bit Rate Bandwidth (10 log 216 kbps)	+53.3 dB-Hz
Required C/N_0	60.2 dB-Hz

*This definition is arbitrary and is used here only for identification purposes.

The comparison of this value with $C/N_0 = 60.2$ dB-Hz, which is considered by NASA as the nominal forward link acquisition threshold, indicates that the bit error rate (BER) should not be greater than 10^{-2} at C/N_0 of 60.4 dB-Hz. This bit error rate will permit the delta-modulated voice links (contained in the 72 kbps rate) to be operational during the initial phase of the TDRS acquisition.

When the TDRS EIRP is at its nominal value of 48 dBw and the antenna is tracking the TDRS, the expected C/N_0 will increase as follows:

$$\begin{aligned} C/N_0\,(\text{nominal}) &= 62.8\ \text{dB-Hz} + 0.3\ \text{dB (APL)} + 11.4\ \text{dB}\ (\Delta\ \text{EIRP}) \\ &= 74.5\ \text{dB-Hz}\ . \end{aligned} \tag{2}$$

This value is for the worst-case path loss of 208.5 dB and for residual antenna tracking offset equivalent to 0.3 dB antenna pointing loss (APL). For the nominal BER of 10^{-6} for the forward link, the margin is therefore

$$\begin{aligned} \text{Forward Link Margin} &= C/N_0\ (\text{nom}) - E_b/N_0\ (10^{-6})\ \text{dB} \\ &\quad - \text{Loss (correlation and bit sync) dB} - 10 \log (216 \times 10^3) \\ &= 74.5\ \text{dB-Hz} - 10.5\ \text{dB} - 2.5\ \text{dB} - 53.3\ \text{dB-Hz} \\ &= 8.2\ \text{dB}. \end{aligned} \tag{3}$$

Consequently, one concludes that, with TDRS at its nominal value of 48 dBw, an adequate margin exists for the forward data link. The variation of the forward link margin as a function of TDRS EIRP is discussed in Section 6.0 of this report.

3.3.2 PN Code Acquisition and Tracking

The baseline configuration for the forward link was based on the use of a 10.7 Mcps PN code [3] for reduction of spectral density of the forward link. However, in order to make the forward link PN code compatible with the "standard" TDRS users, the code rate was modified accordingly. Specifically, the users other than the Orbiter have the code rate related to the carrier frequency by the following relationship:

$$r_c = \frac{31 \times f_c}{96 \times 1469}\ , \tag{4}$$

where r_c is the code rate and f_c is the carrier frequency. Substituting the forward link frequency of 13,775 MHz (13.775 GHz) into (4), we get for the code rate:

$$r_c = \frac{31 \times 13{,}775\ (\text{MHz})}{96 \times 1469} = 3.028\ \text{Mbps} . \qquad (5)$$

Also, to reduce the PN code and carrier acquisition times, the code length was changed from 2047 chips to 1023 chips, and the carrier shift* correction has been specified for the forward link. Without the correction, the forward link carrier frequency uncertainty was estimated at ±1 MHz. With correction, the residual carrier uncertainty is estimated at ±7.5 kHz. The corresponding residual uncertainty on the code clock frequency r_c is less than 2 Hz for a 3.03 Mcps clock rate. The residual uncertainty of the code rate is then due primarily to code clock VCO drift. The conservative estimate for this drift is ±100 Hz, i.e., less than 5×10^{-5}, which is typical of a voltage-controlled crystal oscillator (VCOX) without an oven over the 0°C to 50°C temperature range. With no oven, the same stability or better can be achieved over the specified temperature range for the equipment.

The initial PN code search and acquisition is performed after the TDRS signal has been detected within the 3 dB beamwidth of the Orbiter's antenna. Figure 20 shows the simplified block diagram for a PN code search implementation. Briefly, the device shown operates in the following manner: The frequency of the code clock is changed from its nominal value of 3.03 MHz and thus the phase of the locally generated code is stepped past the phase of the incoming code. The step increment is assumed to be $\tau/2$, i.e., 1/2 chip width. The actual rate of stepping, or the search rate, is determined by the code clock drift, but does not exceed the lowpass filter bandwidth B_v. The stop search command is generated when the DC value at the LPF output exceeds a predetermined threshold. This increase in DC value is the result of code phases stepping into synchronism.

The important parameters are the IF bandwidth of the post correlation filter B_{IF} and the bandwidth of the post-detection low-pass filter

*The shift includes doppler and carrier frequency drift.

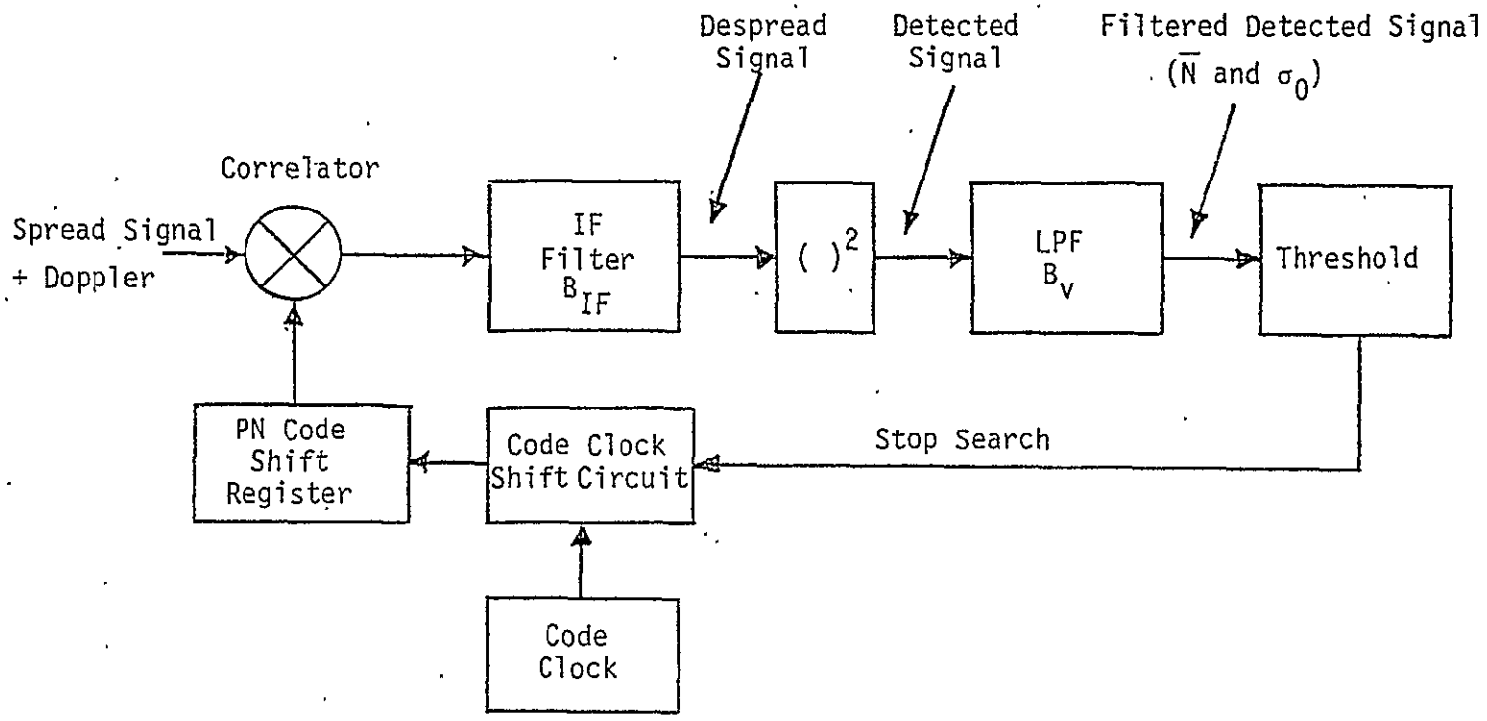

Figure 20. Simplified Block Diagram for PN Code Search Implementation

(LPF) B_v. The selection of B_{IF} is determined by the forward link data spectrum and the residual local oscillator drift in the Orbiter receiver. The current estimate for the residual frequency uncertainty at the Orbiter receiver is ±150 kHz. Allowing twice the data rate bandwidth aperture for passage of the Bi-ϕ-L, 216 kbps signal, the bandwidth of the IF filter for the despread signal is estimated at:

$$B_{IF}\ (\text{despread}) \cong 2\,(|\Delta f_c| + 2 \times \text{Data Rate}) \qquad (6)$$

where Δf_c is the residual carrier uncertainty due to local oscillator drift of the Orbiter's receiver. Substituting the appropriate values into (6), we get

$$B_{IF} = 2\,(150\text{x}10^3 + 2 \times 216\text{x}10^3) = 1.16\text{x}10^6$$

or

$$\cong 1.2 \text{ MHz} . \qquad (7)$$

The selection of B_v is determined by such factors as

(1) specified acquisition time (less than 10 sec)
(2) probability of code lock (≥ 0.99)
(3) code length (N = 1023 chips)
(4) residual code clock uncertainty (±100 Hz).

Considering the code search at the nominal acquisition value of 60.2 dB-Hz, it is shown [4] that, with B_v in the range of 1.5 to 2.5 kHz, the PN code search/acquisition time is between 5.0 and 5.5 seconds for probability of lock of 0.99. These acquisition times are well within the specified 10 seconds PN code acquisition times.

Once the PN code is acquired, the code tracking loop takes over. It then maintains the synchronism between the phases of the incoming and the locally generated codes. Figure 21 shows the block diagram of the delay lock PN code tracking loop. With this loop, the tracking error is generated by comparing the outputs of the A-correlator (local code advanced by $\tau/4$) and the D-correlator (local code delayed by $\tau/4$). A difference in the amplitudes of the two outputs is used to control the frequency, and hence the phase of the local PN code clock.

As shown in Figure 21, the outputs of the A and D correlators are bandpass filtered and then square-law detected. The outputs of the square-law detectors are then passed through zonal filters which pass

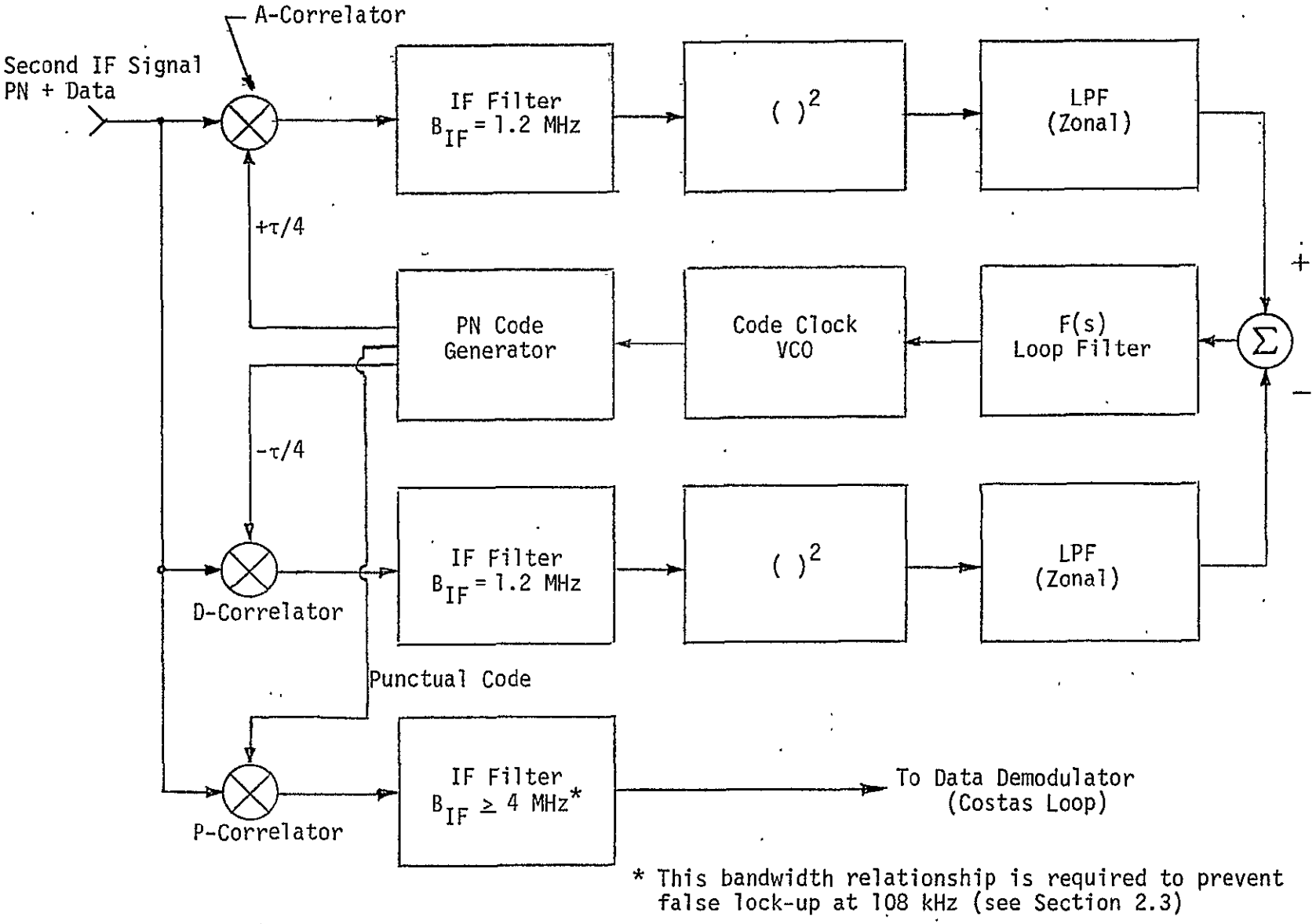

Figure 21. Delay Lock Type PN Code Tracking Loop (DLL)

only the DC-centered components to the difference circuit. The output of the differencer is then applied to the loop filter and finally to the control circuit terminal of the code clock VCO. This closed loop configuration results in an equivalent noise loop bandwidth (one-sided) of B_L.

Figure 22 shows the relationship between the normalized RMS tracking error σ_τ and the tracking loop's one-sided noise bandwidth B_L. The data shown is for $C/N_0 = 60.2$ dB-Hz and the track spacing of $\tau/2$, where τ is the basic code chip length. A typical range of B_L values for this type of function is 100 to 500 Hz during the search and acquisition, with possible narrowing down to 10-20 Hz during tracking. However, if one assumes a baseline value of $B_L = 300$ Hz, the normalized tracking error as shown by Figure 22 is about 1.35% or 0.0135. The corresponding power loss in signal supplied at the output of the punctual correlator is given by [5]:

$$\begin{aligned} L_T \text{ (code)} &= 10 \log (1 - 1.6\ \sigma_\tau) \\ &= 10 \log [1 - (1.6)(0.0135)] \\ &= \underline{0.09 \text{ dB}}. \end{aligned} \tag{8}$$

This is a relatively small loss due to tracking, considering the fact that it is obtained at the acquisition threshold of $C/N_0 = 60.2$ dB-Hz. Reliable tracking can be assumed at this and higher values of C/N_0 without requiring the change of code tracking loop bandwidth.

Tracking performance at lower values of C/N_0 can be estimated from the data shown in Figure 23. From this figure, one can see that, at the nominal tracking threshold value of 57 dB-Hz [4], the rms tracking error for a 300 Hz loop is about 2.6% or 0.026. Applying equation (8), we get the equivalent tracking loss of about 0.18 dB. This is not a significant loss from the standpoint of an impact on the error rate. Consequently, it appears that, at least from the standpoint of the effective signal loss at the tracking threshold, the narrowing of the DLL bandwidth is not required.

3.4 Signal Filtering Considerations

The RF signal filtering considerations for an integrated Ku-band Shuttle radar/communication system are determined primarily by the requirement for minimizing the transmitter-to-receiver interference during the

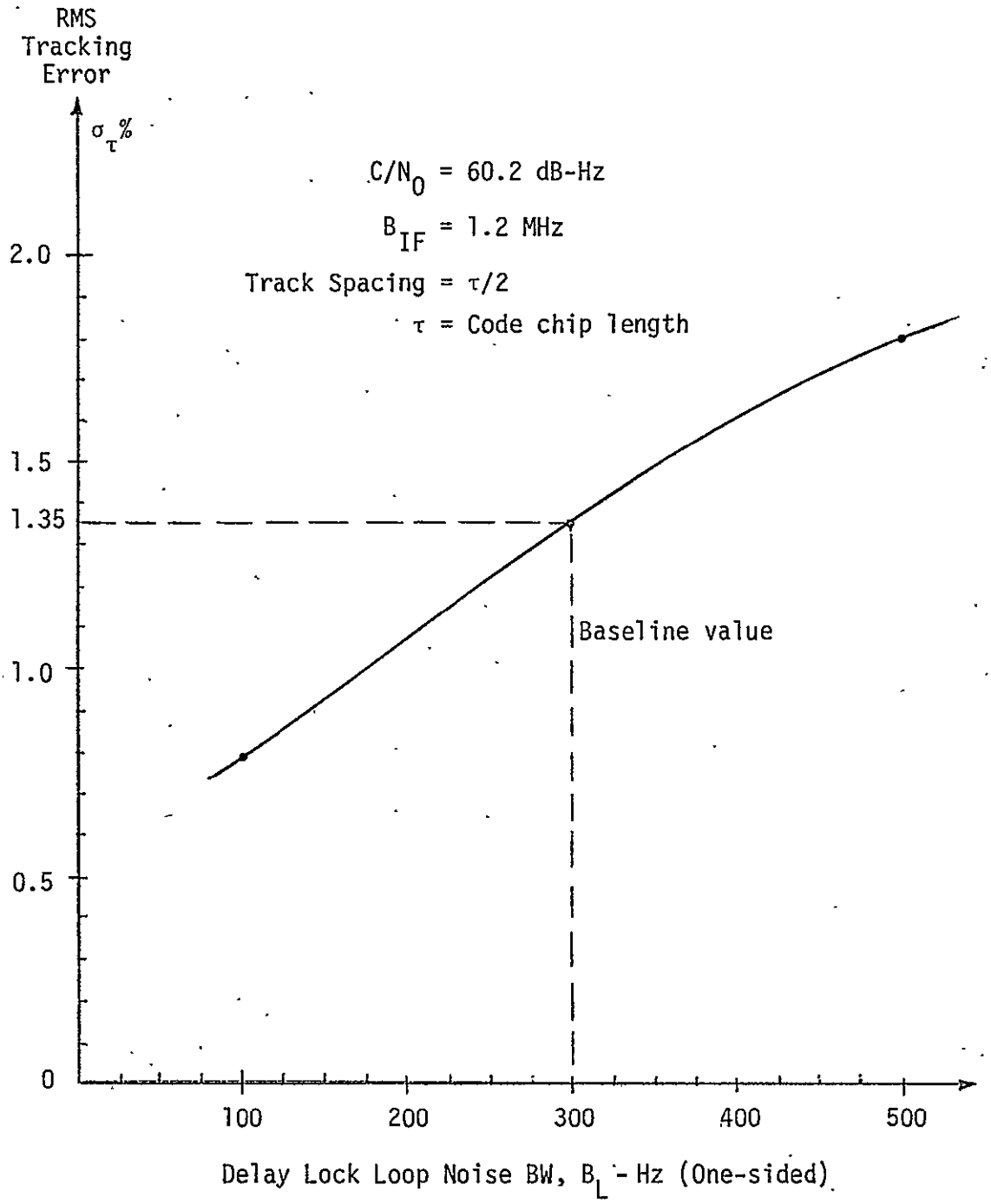

Figure 22. PN Code DLL Tracking Error Versus Loop Noise Bandwidth

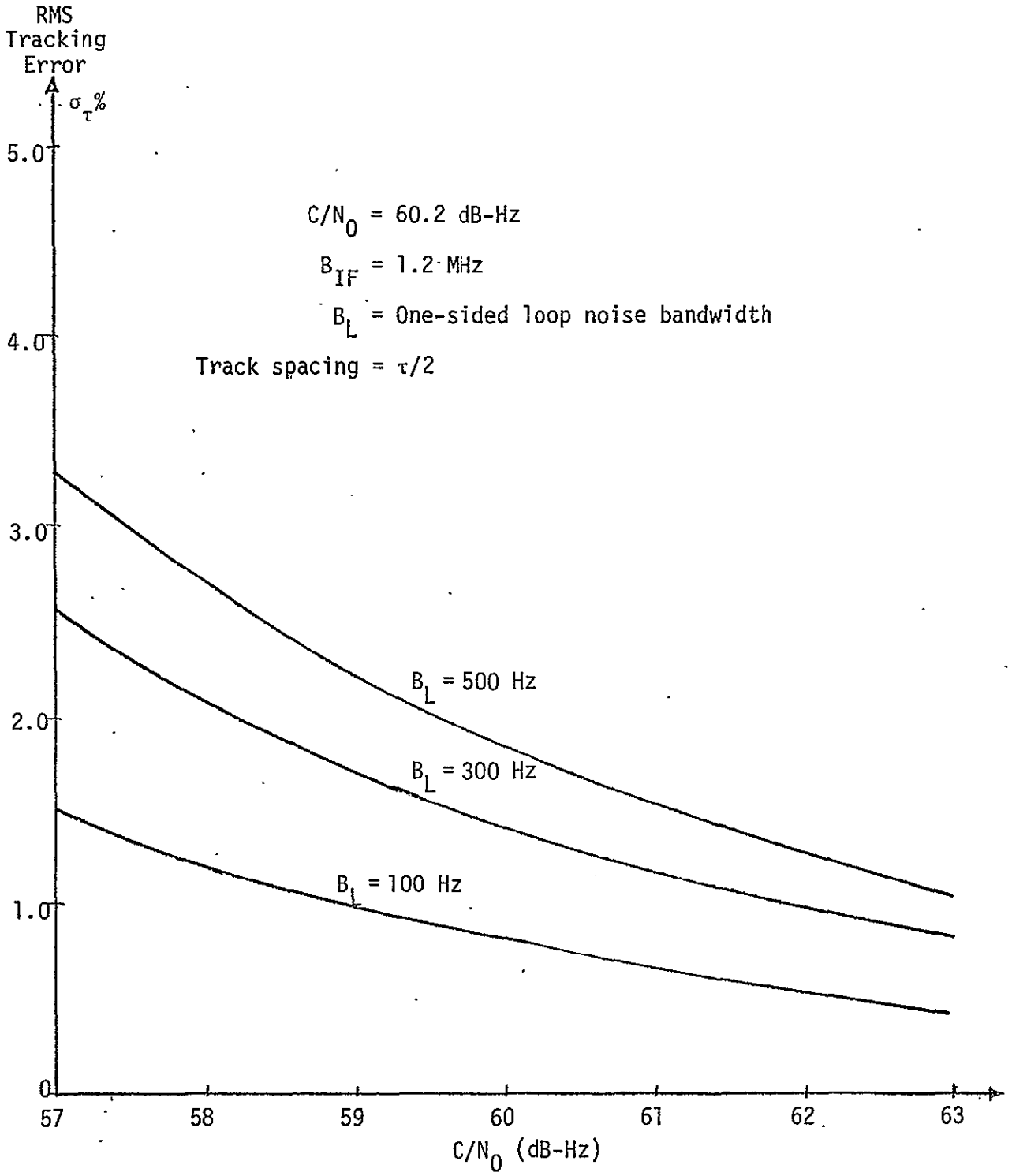

Figure 23. RMS Tracking Error of a DDL Versus C/N_0 and B_L

operation in the communication mode. In this mode, the Shuttle transmitter supplies about +47 dBm (50 watts) CW power to the antenna, while the TDRS signal delivered by the antenna to the receiver is in the order of -110 dBm. The approximate frequencies of the transmit and receive signals are 15 GHz and 13.8 GHz, respectively. Therefore, the frequency separation of about 1.2 GHz provides a guard band across which the required signal isolation must be achieved.

Basically, there are two types of transmitter signal components which are deleterious to receiver operation. These are:

(1) Transmitter output components which fall within the receiver bandwidth, and

(2) Transmitter signal components which, although outside the receive band, are of sufficient level to present a saturation threat to the sum and delta channels of the receiver.

To show how these components can be kept under control, let us consider the RF portion of the integrated radar and communication Ku-band system proposed by the equipment contractor. Figure 24 gives the simplified block diagram for the RF portion of the Ku-band equipment as it is described in [6]. As is shown in Figure 24, the communication transmitter operates at its nominal frequency of about 15.0 GHz. In the radar mode, however, the transmitter operates in the 13.8 GHz range which is compatible with the communication receive bandpass. A common TWT amplifier of sufficient bandwidth (1.2 to 1.5 GHz) is used to accommodate operation in either of the two modes. The placement of the radar frequency in the communication receive band is similar to the approach described in [7] and, therefore, the filtering criteria set in [7] can be applied to the equipment configuration proposed by the Ku-band system contractor.

According to Figure 24, the 15 GHz communication transmit signal passes through three diplexers on its way to the high gain antenna. The diplexers consist of bandpass/band reject filters of multicavity Chebyshev design. Thus, the 15 GHz filter passes the communication transmission band and provides attenuation at the radar/communication receive frequency.

Adequate attenuation at the receive frequency is required to (1) attenuate transmitter signal sidelobes and (2) attenuate transmitter tube noise. Figure 25 shows graphically the attenuation requirements for the transmitter components falling within the communication receive band.

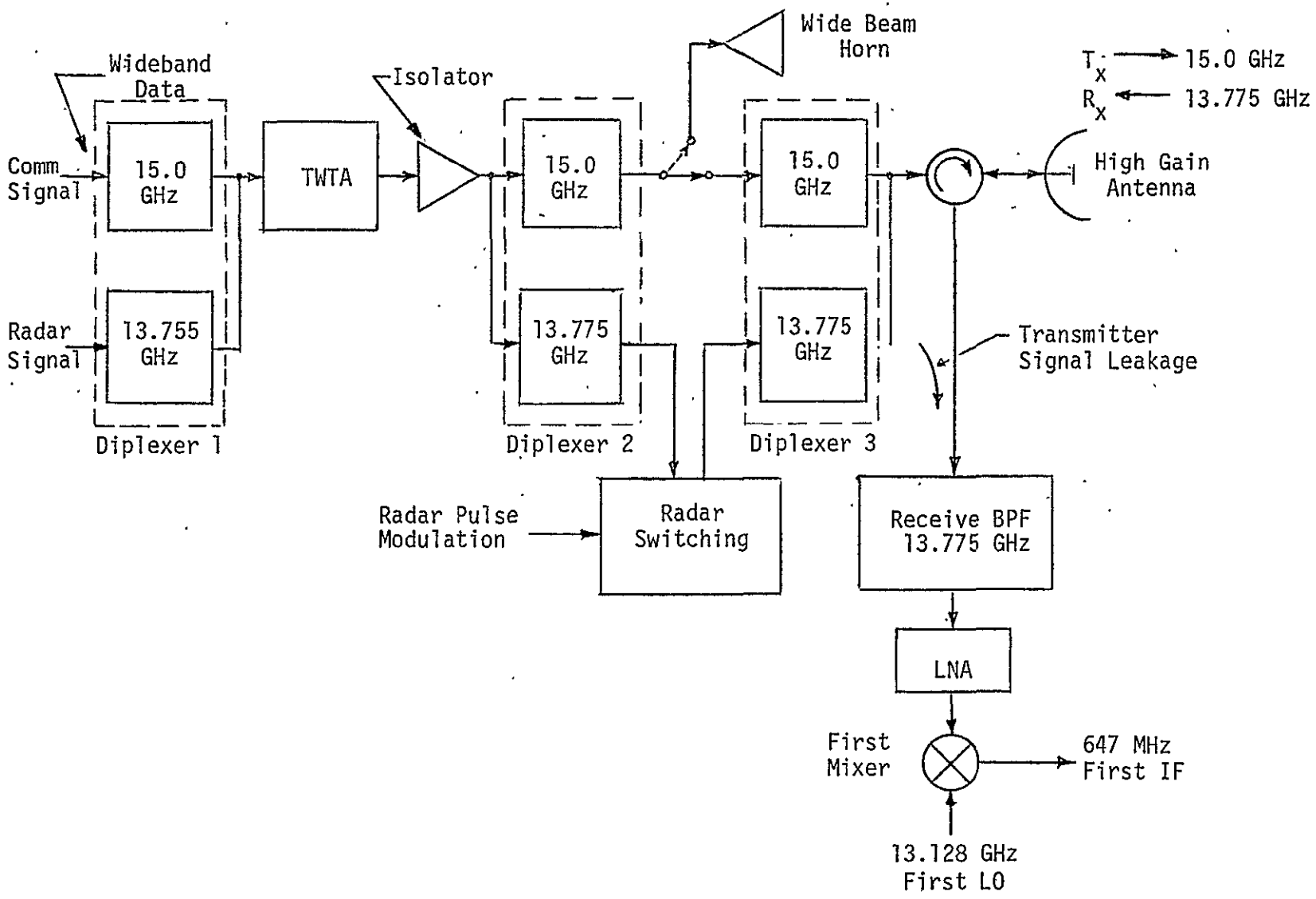

Figure 24. Simplified Block Diagram for the RF Portion of the Integrated Radar and Communication Ku-Band Equipment

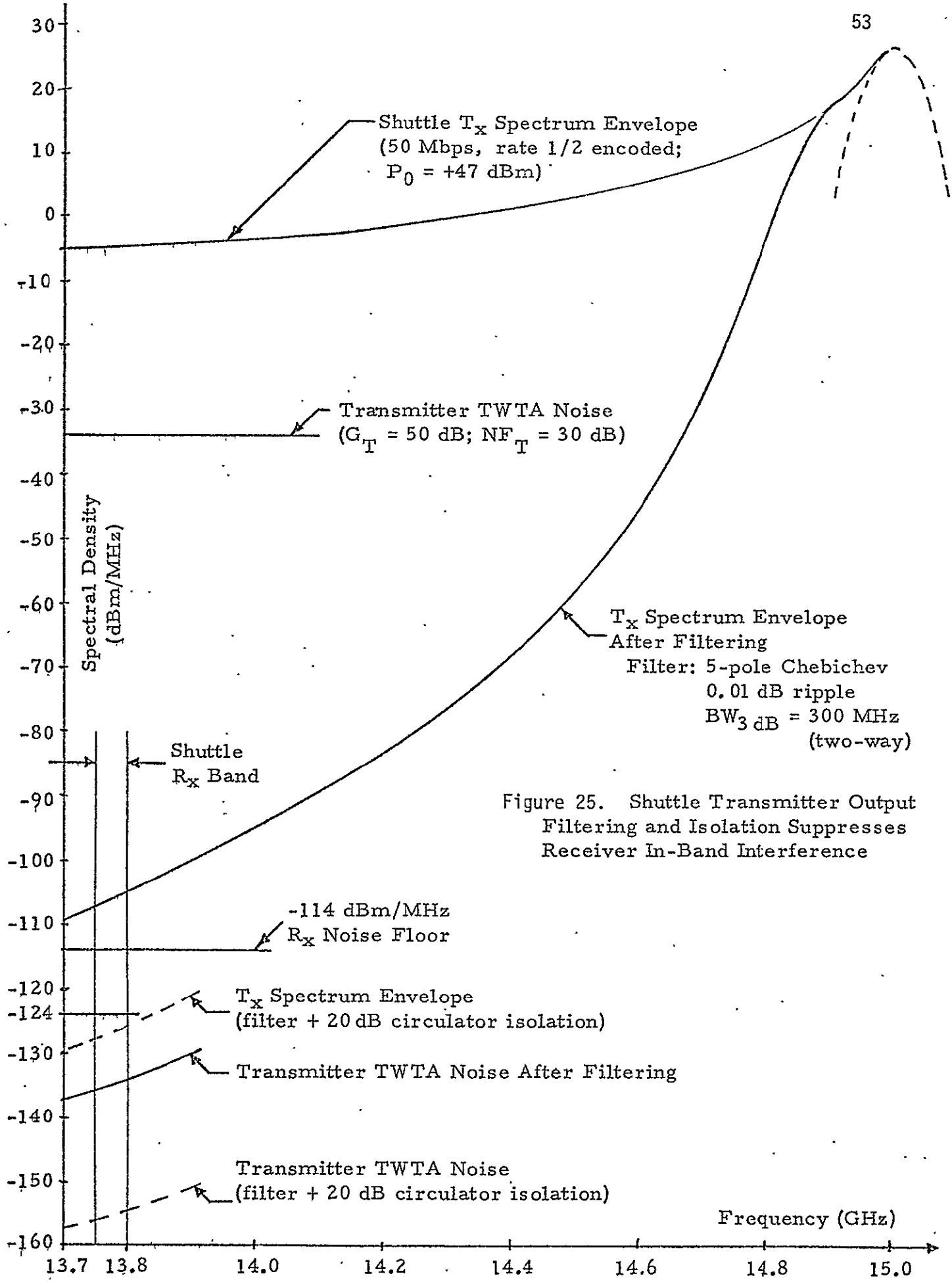

Figure 25. Shuttle Transmitter Output Filtering and Isolation Suppresses Receiver In-Band Interference

Specifically, as shown in Figure 25, the communication transmitter signal is centered at approximately 15 GHz and its maximum power level is about +47 dBm or 50 watts. For a 50 Mbps rate transmission, rate 1/2 encoded, the effective NRZ symbol rate is 100 Mbps. Consequently, the power spectrum has a $(\sin x/x)^2$ envelope with the first nulls at 100 MHz on either side of the nominal 15 GHz carrier frequency. Because the envelope of this spectrum falls off only at a rate of 20 dB/decade, it becomes clear that unless adequate filtering of the transmitter output is provided the sidelobes may cause considerable in-band interference to the receive signal. As shown below, this interference is considerably higher than that caused by the tube noise alone.

For a +47 dB signal and the effective NRZ symbol rate of 100 Mbps, the maximum spectral density of the main lobe is

$$D_m(15) = +47 \text{ dBm} - 20 \text{ dB (100 MHz)} = +27 \text{ dBm/MHz}. \quad (9)$$

According to the $(\sin x/x)^2$ law, this density in the region of the receive band will be reduced by about 31 dB. Thus, the maximum possible interference density in the receive band is:

$$D_m(13.8) = +27 \text{ dBm/MHz} - 31 \text{ dB} = \underline{-4 \text{ dBm/MHz}}. \quad (10)$$

In comparison, based on the assumptions that

G_T = TWT gain = 50 dB at 13.8 GHz

NF_T = TWT noise figure = 30 dB at 13.8 GHz,

we estimate the tube noise density in this region at

$$N_0(13.8) = N_i + NF_T + G_T = -114 \text{ dBm/MHz} + 30 \text{ dB} + 50 \text{ dB}$$

$$= \underline{-34 \text{ dBm/MHz}}. \quad (11)$$

Consequently, it is evident that, unless adequately filtered, the transmitter sidelobe splatter at the maximum transmission rate of 50 Mbps (i.e., 100 Msps) is the primary threat to the communication receiver channel.

If we assume that the antenna terminal circulator provides 20 dB isolation, we can estimate the filter attenuation required to keep the transmitter sidelobe splatter at, say, -124 dBm, which is 10 dB below

the basic noise floor of the receiver:

$$-4 \text{ dBm/MHz} - A - 20 \text{ dB} \leq 124 \text{ dBm/Hz} \qquad (12)$$

or

$$A \geq 100 \text{ dB}.$$

This is a rather stringent requirement but, at least in principle, it can be met with a 5-pole, 0.01 dB ripple Chebychev filter.

However, from the block diagram in Figure 24, it is evident that two bandpass filters are placed at the output of the TWTA (i.e., Diplexers 2 and 3) and one filter at the input of the tube. The input filter may not necessarily be effective in suppressing the spectrum sidelobes, particularly if the TWTA operates in the saturation mode. Thus, we conclude that the attenuation characteristics of Diplexers 2 and 3 must be such as to provide at least 100 dB attenuation (total) at the communication receive frequency of 13.755 GHz. The overall bandwidth centered at 15.0 GHz must be at least 200 MHz to provide minimum attenuation of the wideband signal.

The protection of the receiver is performed by a bandpass filter placed at the input terminal of the receiver. Such a filter must provide 70 to 73 dB of 15.0 GHz signal attenuation [7] in order to tolerate a VSWR of 1.5:1 at the antenna port. The filter(s) proposed [6, Table 3.8-2, page 3-115] by the Ku-band contractor appears to meet the above-stated requirements. Furthermore, the selection of the first IF frequency of 647 MHz permits the receiver filter to provide at least 60 dB attenuation at the image frequency of about 12.48 GHz.

4.0 TDRS ANGULAR SEARCH ACQUISITION AND TRACKING

4.1 Angular Search and TDRS Acquisition

The first step in establishing the two-way Ku-band link between the Shuttle Orbiter and the ground station is to perform the angular search and to acquire the TDRS. Following the initial acquisition, the TDRS is then used as a relay for the forward and return links. The requirements for TDRS signal acquisition as stated in the equipment specification [3] are summarized in Table 5.

Table 5. TDRS Signal Acquisition Requirements Summary

Conical angle uncertainty (maximum)	8°	20°
Maximum search time	1 min	3 min
TDRS signal level	-126.9 dBm/m^2 (EIRP = 36.6 dBW)	
Probability of acquisition (P_D)	0.99	
Probability of false alarm (P_{fa})	10^{-6}	

The requirements listed in Table 5 must also be met under the condition when the TDRS is transmitting a PN code signal to the Shuttle. After correction at TDRS, the total frequency uncertainties, doppler and oscillator drift, of the TDRS signal are reduced to about ±7.5 kHz from the uncompensated uncertainty of ±1 MHz. The compensation reduces the code clock doppler to a negligible value (< 2 Hz), but the frequency uncertainty of the Orbiter receiver's oscillators remains to be dealt with. Thus, the TDRS acquisition has to be performed with a residual frequency uncertainty of about ±150 kHz.

The results of trade-offs carried out by Axiomatix [8], as well as other investigators [6], indicate that, to meet the requirements of Table 5, the presence of TDRS signal within the Shuttle antenna's beamwidth must be based on detection of the energy due to the spread TDRS signal. In other words, the antenna angular search is terminated when the "signal-plus-noise" level within a certain detection bandwidth exceeds the level of the "noise alone" in the same bandwidth. Because the actual signal-to-noise ratio (SNR) may be negative in the IF bandwidth matched to the spread

signal, the signal detection threshold levels are set to the output of the video filter which provides a large amount of post-detection integration.

The typical values for the predetection bandwidth (IF) are in the order of 3 MHz, while the post-detection (video) bandwidth may be only several Hertz. Such a high ratio of IF to video bandwidth insures that the statistical requirements of Table 5, i.e., $P_D = 0.99$ and $P_{fa} = 10^{-6}$, can be met despite negative SNR ratios in the IF bandwidth.

The C/N_0 values at which these acquisition statistics must be met are indicated in Table 4. The two lower acquisition values of C/N_0 are 60.4 dB-Hz and 60.2 dB-Hz. Considering the 60.2 dB-Hz as the acquisition threshold value, the relationship between the acquisition time* and the gimbal rate can be determined. Such a relationship is based on the assumption of constant velocity spiral scan [8,9] and the statistics specified in Table 5. Figure 26 shows the relationships between various parameters which determine the antenna scan performance. The data shown is for an antenna having a 3 dB beamwidth of 1.6° [6] based on a 36-inch diameter antenna. Also, the spiraling out is such that the antenna advances radially 0.72° per revolution and the TDRS signal is never less than 0.6 dB down on the antenna beam shape.

From the data in Figure 26, it is evident that, with the constant frequency spiral scan, the time required to search the 20° uncertainty depends primarily on the gimbal rate. With the nominal communication gimbal rate of 102°/sec [6, Table 3.4-1], the search time is about 50 sec. With the gimbal rate reduced to 90°/sec, the 20° uncertainty can be searched out in 55 sec.

Because the statistical requirements of the TDRS acquisition ($P_D = 0.99$, $P_{fa} = 10^{-6}$) can be met at $C/N_0 = 60.2$ dB-Hz with a low-pass filter bandwidth (B_v) of 20 Hz [4], one is not constrained to using a narrower bandwidth, such as shown in Figure 26. In other words, the search time is determined not by the requirements to keep B_v less than 11 Hz, but by the gimbal rates. The gimbal rate limitation is a fundamental one, and thus one concludes the antenna and the gimbal dynamics are the factors which set the lower limit on the TDRS search time. The 55 seconds, however, are well within the 3 minute (180 sec) specification set by Table 5.

---

*Also referred to as area search time.

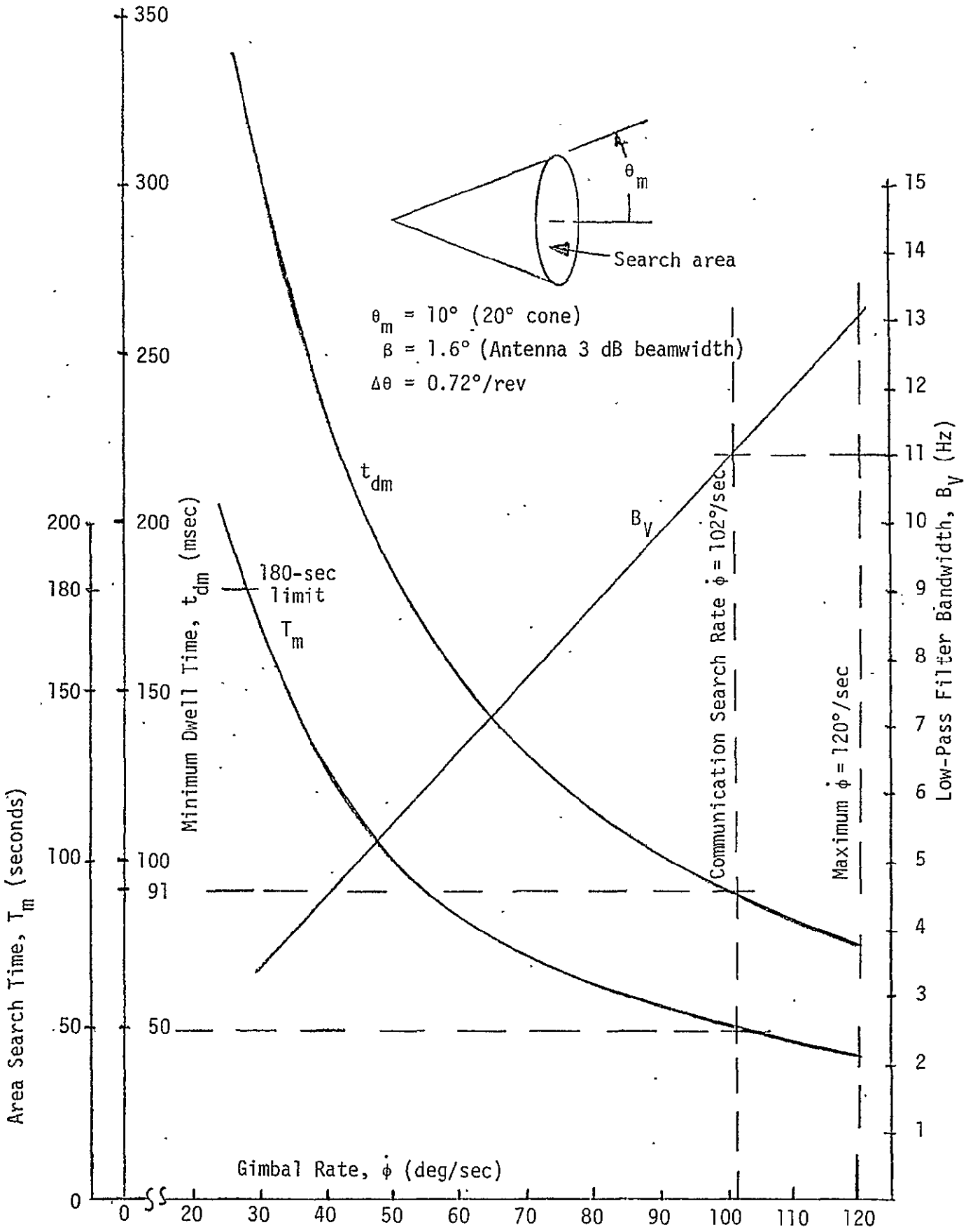

Figure 26. Area Search Time, Minimum Dwell Time, and Low-Pass Filter Bandwidth as Functions of Gimbal Rate (constant frequency spiral scan)

4.2 Angle Tracking

Once the angular acquisition of TDRS is completed, the PN code and carrier acquisition take place (within less than 10 sec at C/N_0 = 60.2 dB-Hz) and the angular tracking of the TDRS commences. The tracking is performed by an amplitude monopulse antenna and the corresponding AZ and EL servo loops. To minimize the number of the receiver channels required to implement the monopulse angle tracking functions, the AZ and EL channels are time-multiplexed. Such multiplexing reduces the number of receiver channels from three to two: one for the sum (Σ) channel and one for the multiplexed ΔAZ/ΔEL channel. The simplified block diagram for implementing such a system is shown in Figure 27.

As shown in Figure 27, the Δ outputs of the monopulse comparator are time-multiplexed prior to first conversion and then applied to the first Δ-channel mixer. Simultaneously, the sum channel undergoes a first conversion in a separate channel. At the second IF, a portion of the sum channel signal is coupled to the Δ-channels, thus providing a carrier on which the multiplexed ΔAZ and ΔEL signal are superimposed. The composite signal, consisting of $\Sigma \pm \Delta AZ \pm \Delta EL$ vectors, is then envelope detected at the first IF frequency. The output of the envelope detector is then applied to a baseband AZ-EL switch, where the two Δ signals are demultiplexed and applied to their respective antenna control loops.

In terms of the pertinent parameters, the expression for the variance of the angle tracking error is

$$\sigma_a^2 = \frac{4\beta^2 B_s A}{K_m^2 \left(\frac{C}{N_0 D}\right)} \times \frac{1 + \frac{B_{IF}(\Delta)}{2\left(\frac{C}{N_0 L_t}\right)}}{1 - \frac{2B_s}{\left(\frac{C}{N_0 D}\right)}} \tag{13}$$

where σ_a = rms value of angle tracking error

β = antenna 3 dB beamwidth

B_s = angle servo loop noise bandwidth

K_m = antenna tracking slope coefficient

A = coupling factor for the monopulse channel

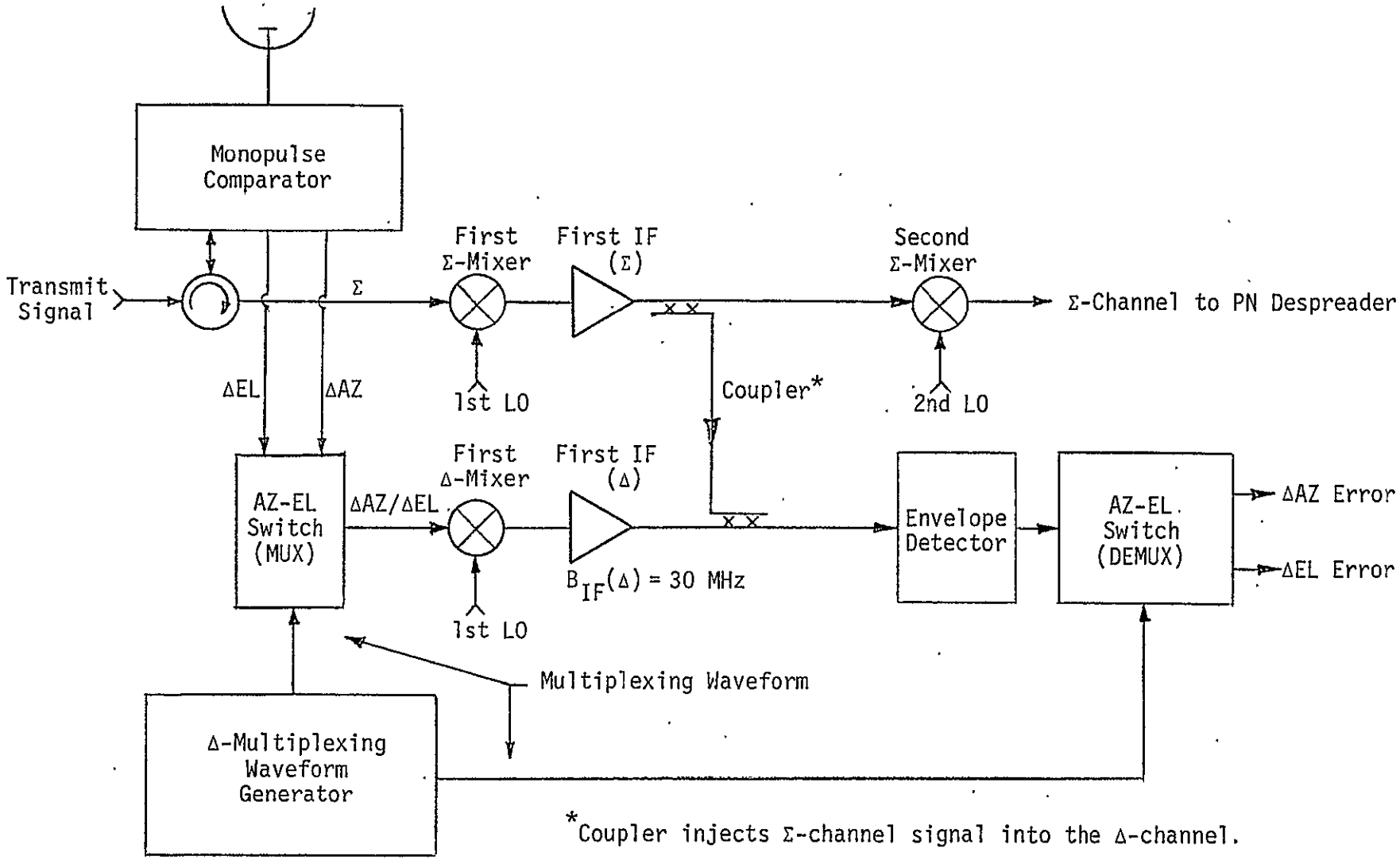

Figure 27. Monopulse Tracking with Time-Multiplexed Δ-Channel

D = effective increase in thermal noise N_0 due to coupling of noise from Δ channel

$B_{IF}(\Delta)$ = IF bandwidth of the angle tracking channel

C/N_0 = carrier-to-noise ratio (dB-Hz) at receiver input.

The angle tracking performance can be estimated using the parameters proposed by the Ku-band equipment contractor [6, p. 3-37]. These parameters are as follows:

$$\beta = 1.6°$$

$$B_s = 1.0 \text{ Hz}$$

$$K_m = 0.5 \text{ (worst case)}$$

$$A = 2 \text{ dB or } 1.585 \text{ numeric}$$

$$D = 2.1 \text{ dB or } 1.622 \text{ numeric}$$

$$B_{IF}(\Delta) = 30 \text{ MHz}.$$

Substituting these values into (13) and solving for σ_a^2 at $C/N_0 = 60.2$ dB-Hz (acquisition threshold), one obtains $\sigma_a^2 = 0.0024$ degrees^2. The corresponding pointing loss due to this random angle error is

$$M(\text{dB}) = \frac{12\,\sigma_a^2}{\beta^2} = \frac{(12)(0.0024)}{(1.6)^2} = 0.01 \text{ dB}. \qquad (14)$$

This loss is negligible compared to RF and servo bias error which may be expected in the system. An estimated pointing loss due to these bias errors is about 0.14 dB [6] and is well within the 0.3 dB pointing loss specification [3]. One therefore concludes that the thermal noise is not a limitation for the angle tracking subsystem if one takes into account the unavoidable bias errors.

5.0 OSCILLATOR FREQUENCY AND PHASE STABILITY CONSIDERATIONS

5.1 General

The oscillators used for generation of the transmit and receive LO carrier frequencies of the Ku-band communication equipment exhibit both the long-term (drift) and short-term (jitter) instabilities. The long-term instability contributes to the frequency uncertainty, which affects the initial carrier frequency search and acquisition performance. Excessive short-term instabilities degrade the performance of the coherent carrier tracking and data demodulator loop and, consequently, the bit error rate is increased. Below, we consider oscillator stability requirements for the Orbiter communication system.

5.2 Long-Term Instabilities

Within the Orbiter receiver, the long-term instabilities affect the frequencies of the local oscillators and, as a consequence, the coherent Costas data demodulator has to be swept over the range of the frequency uncertainties. For the receive frequency of 13.755 GHz and the second IF being less than 55 MHz, the total LO drift can be referred to 13.70 GHz. Using this assumption, one can estimate the total frequency drift budget for the receiver. Based on the estimates provided by the Ku-band equipment contractor [6, p. 3-137], the LO frequency drift budget can be constructed. This budget is shown in Table 6.

Table 6. Orbiter Receiver LO Frequency Drift Estimates

Type of Drift	PPM	Absolute Drift (Referred to 13.7 GHz)
Long-Term	$\pm 5 \times 10^{-6}$ (per year)	± 68.5 kHz
Temperature Range	$\pm 4 \times 10^{-6}$ (0 to 140°F)	± 54.8 kHz
Small Aging Effects	$\pm 1 \times 10^{-6}$	± 13.7 kHz
	Total	±137.0 kHz

The long-term component of the drift can be controlled by proper selection of crystals. Therefore, the actual LO instability may be only about ±70 kHz. To this must be added the drift due to the carrier loop VCO. If a VCXO is used for the carrier tracking loop for a typical stability of 5×10^{-5} and the second IF of 55 MHz, the drift will be only ±2.75 kHz. On the other hand, if one assumes a VCO which is not crystal controlled, the typical stability may be only 1×10^{-3}. The corresponding drift range is ±55 kHz. The comparison is then as follows:

Type	PPM	Drift (Referred to 55 MHz)	Total Drift
VCXO	5×10^{-5}	± 2.75 kHz	± 72.75 kHz
VCO	1×10^{-3}	±55 kHz	±125 kHz

From this comparison, we conclude that, depending on the type of VCO used, the total frequency uncertainty may either exceed or be below the 108 kHz value at which the first false lock occurs. However, as pointed out in Section 2.3, the control over the first false lock-up can be achieved by keeping the bandwidth of the Costas loop arm filters sufficiently wide. Thus, it appears that the expected Ku-band receiver instabilities are within the ±150 kHz estimate used for PN despreader IF bandwidth calculations.

5.3 Short-Term Instability/Oscillator Phase Jitter Considerations

Local oscillator (LO) frequency jitter may degrade the receiver data detection performance significantly if the receiver bandwidths are not chosen appropriately and if the frequency synthesizer design generates excessive phase noise. The following discussion develops the relationship between the LO noise and front end noise, the receiver carrier tracking bandwidth, and the degradation to BER. The conclusion is reached that, for the particular phase noise spectrum considered, there is an optimum bandwidth but the degradation to BER is so small that the bandwidth can be chosen to satisfy other criteria. Furthermore, a frequency synthesizer designed according to good engineering design practice, i.e., crystal oscillators followed by multipliers followed by adequate filtering, will suffice; in other words, synthesizer phase noise is not a critical factor.

The frequency translation scheme being utilized is shown in Figure 28. The phase jitter is introduced by the LOs and causes the

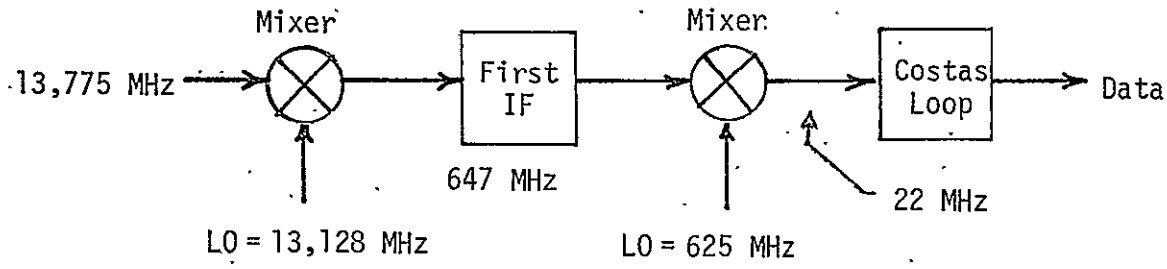

Figure 28. Frequency Translation Scheme

Costas loop to develop a phase error. It can be shown that this phase error is given by

$$\sigma_\psi^2 = \int_0^\infty S_\psi(f)\,|H(j\omega)|^2\,df \tag{15}$$

where

$S_\psi(f)$ = one-sided spectral density of phase noise

$H(j\omega)$ = phase lock loop error transfer function

$$|H(j\omega)|^2 = \frac{(f/f_n)^4}{1 + (f/f_n)^4} \quad \text{for a second-order loop with 0.707 damping.} \tag{16}$$

Typically, the phase noise spectrum can be treated as being composed of several segments,

$$\begin{aligned} S_\psi(f) &= A/f^4 && 0 < f \le f_1 \\ &= B/f^3 && f_1 < f \le f_2 \\ &= C/f^2 && f_2 < f \le f_3 \\ &= D/f && f_3 < f \le f_4 \\ &= E && f_4 < f \end{aligned} \tag{17}$$

where the coefficients A, B, C, D, and E are determined by the particular frequency synthesizer implementation.

The loop mean square phase error due to the receiver front end noise (Gaussian noise) can be shown to be given by

$$\begin{aligned} \sigma_\phi^2 &= 4\frac{B_L N_0}{\alpha S}\left[1 + \frac{N_0 W}{2\alpha S}\right] \\ &= \frac{2 L_s}{S/2 N_0 B_L} \end{aligned} \tag{18}$$

and we define L_s as the squaring loss

$$L_s = \frac{1}{\alpha}\left[1 + \frac{N_0 W}{2\alpha S}\right]. \tag{19}$$

where

W = one-sided arm filter bandwidth = 500 kHz

α = 0.68 for 216 kbps

B_L = $0.53\,\omega_n$.

The total mean square phase jitter in the loop is given by

$$\sigma_T^2 = \sigma_\psi^2 + \sigma_\phi^2 . \tag{20}$$

This has been evaluated as a function of loop bandwidth, with S/N_0 (signal power to front-end noise density) as a parameter.

The phase jitter component σ_ψ^2 was evaluated for the frequency synthesizer implementation shown modeled in Figure 29. The resulting total phase jitter versus loop bandwidth B_L is shown plotted in Figure 30 for $S/N_0 = 64$ dB-Hz and 61 dB-Hz. The crossover point of the two curves can be considered to define an optimum loop bandwidth. This bandwidth is 5 kHz and the corresponding total phase jitter is 6.7 degrees.

The effect of loop phase jitter on the probability of bit error (BEP) has been determined and is plotted in Figure 31 [10]. The curve for $\sigma = 0$ is the case of no loop phase jitter and the case considered ($\sigma = 6.7$) lies between this curve and the $\sigma = 8$ curve. It can be seen that, for the range of BEP = 10^{-2} to 10^{-6}, the degradation is negligible. At the higher values of E_b/N_0, where the phase jitter due to phase noise is the controlling factor, since the loop signal-to-noise ratio is high, the phase jitter does not exceed the 8° shown in Figure 30. Furthermore, if the loop is narrowed, it is seen from Figure 30 that the maximum phase jitter is approximately 7.3 degrees. Thus, it can be concluded that selection of loop bandwidth to accommodate LO phase jitter is not critical. The loop bandwidth can be selected according to other criteria. Such other criteria may be thermal noise performance requirements.

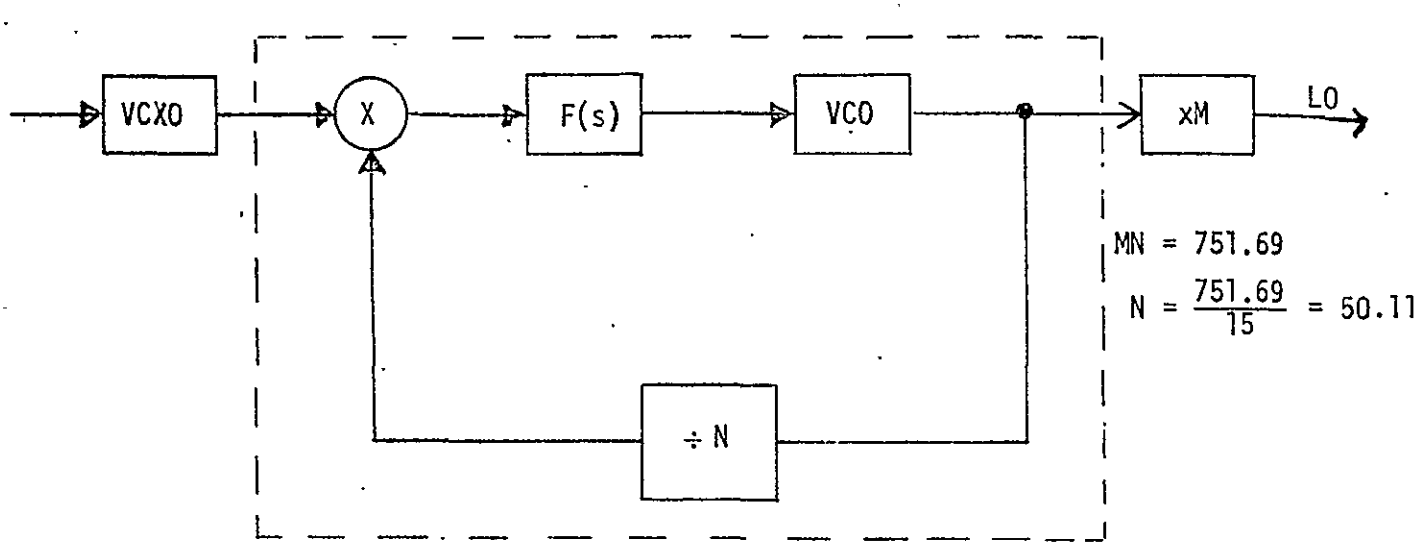

Figure 29. Model of LO Frequency Synthesizer

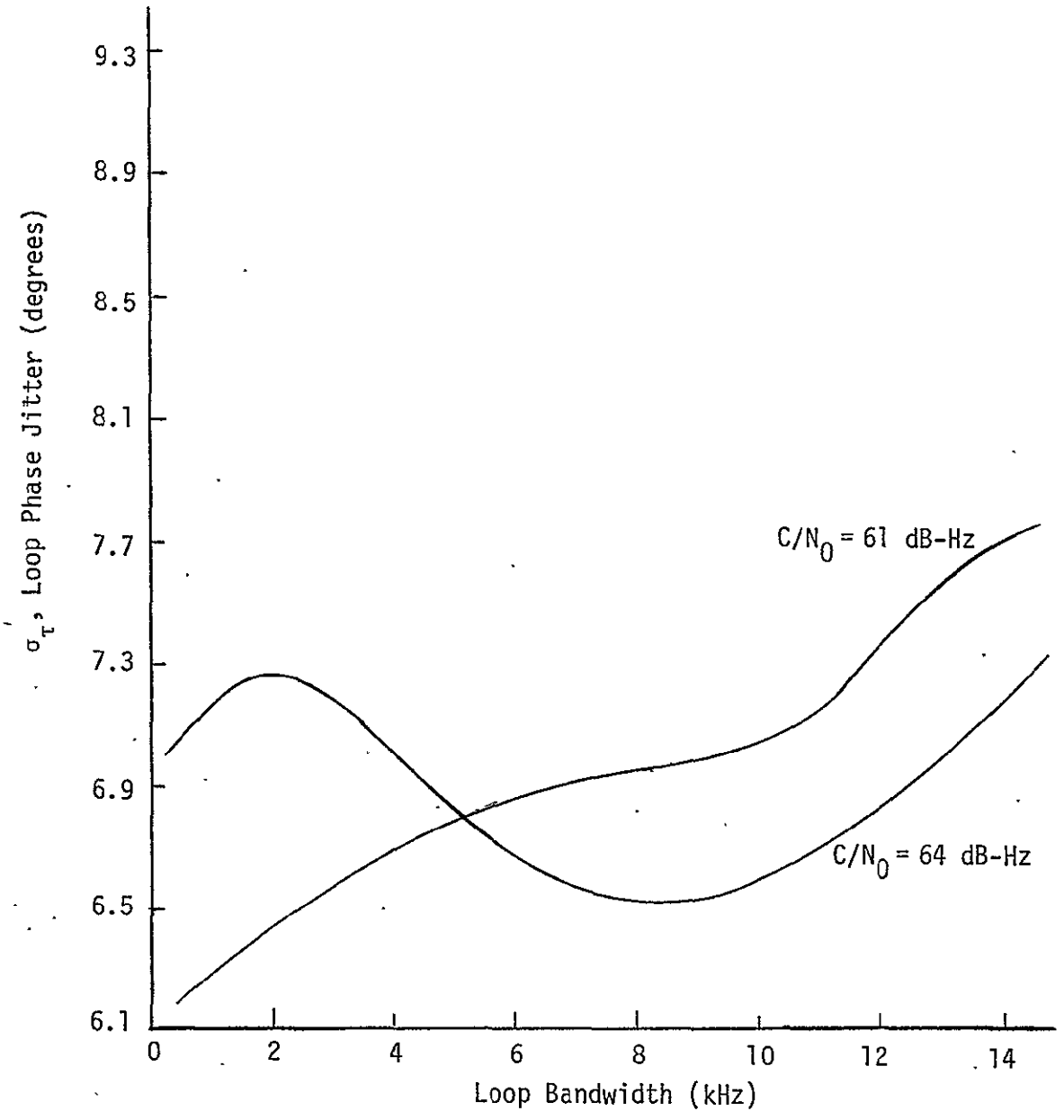

Figure 30. Loop Phase Jitter as a Function of Loop Bandwidth

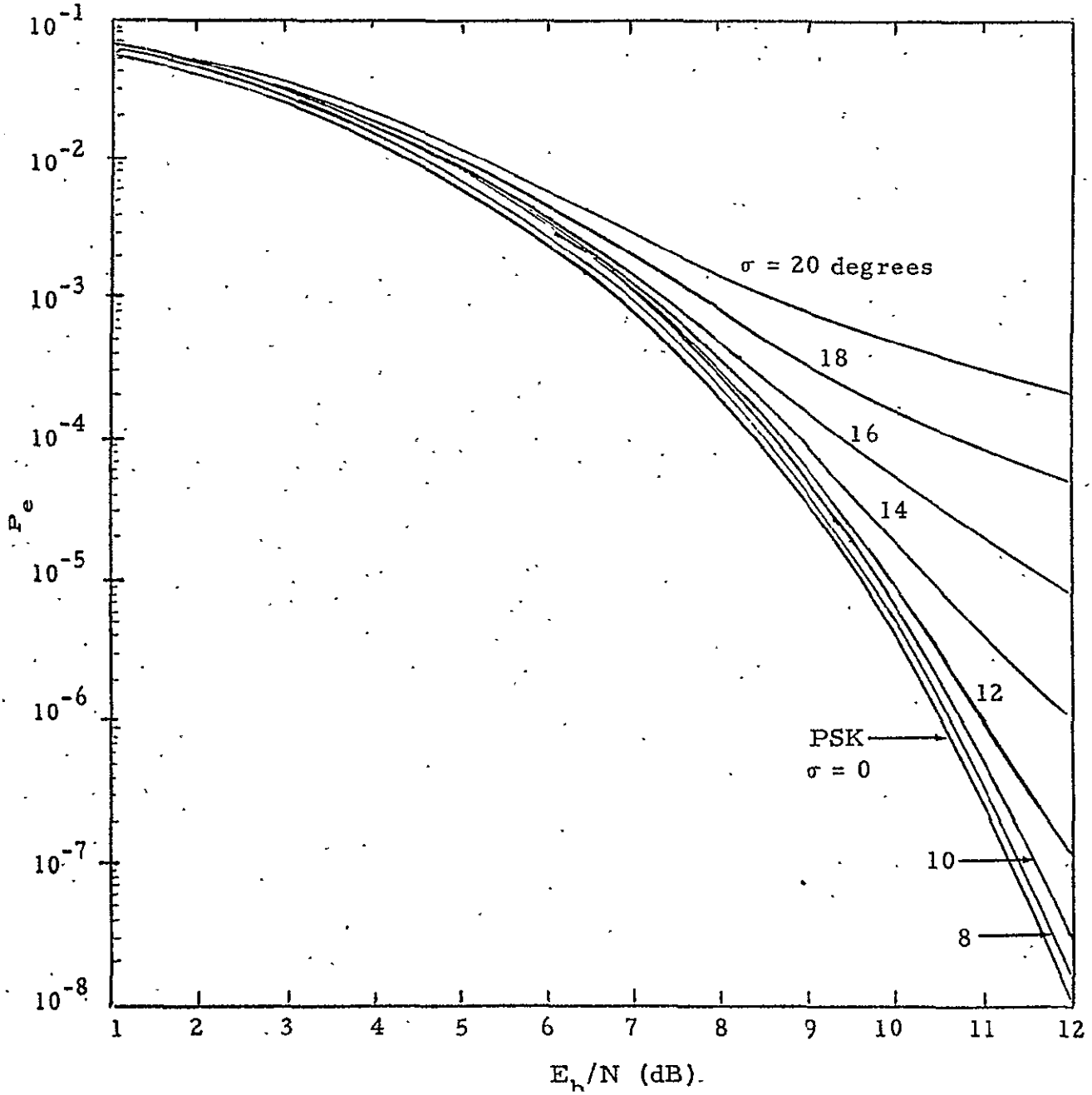

Figure 31. Bit Error Probability for Costas Loop Demodulation with Tracking Jitter, σ

6.0 SIGNAL LEVEL VARIATION EFFECTS

6.1 Sources of Signal Level Variations

Disregarding signal level variations caused by Orbiter maneuvers, the primary source of signal level variation at the Orbiter receiver is expected to be the EIRP of the TDRS. Secondary sources of signal level variation will include the path loss variation and, during the TDRS acquisition, the antenna pointing losses. Thus, for TDRS alone the following range of EIRP is expected:

Nominal: 48.0 dBw
Minimum: 36.6 dBw
Maximum: 53.5 dBw

The terms contributing to the difference between the maximum and nominal levels are estimated as follows:

Life:	1.0 dB	Total of 5.5 dB
High Power:	3.0 dB	
Miscellaneous:	1.5 dB	

Thus, the estimated range of the TDRS EIRP variations is 16.9 dB.

The variation due to path loss is expected to be 2.8 dB (208.5 dB versus 205.7 dB) and the antenna pointing loss variation is estimated at 3 dB.

Another way of looking at the possible level of signal variation is to consider the range of workable C/N_0 and the associated margins. The zero link margin operation occurs at the acquisition threshold C/N_0 of 60.2 dB-Hz and corresponds to a bit error rate (BER) of 10^{-2}. The nominal operating point for the forward link is at 66.3 dB-Hz, which corresponds to a BER of 10^{-6}. Thus, based on the BER curve alone, the difference is 6.1 dB. But, considering a margin of 8.5 dB at the BER = 10^{-6} operating point and the estimated 5.5 dB power variation (upward) from the nominal EIRP value, the maximum expected C/N_0 is:

$$\begin{aligned} C/N_0(\max) &= \underset{\text{(minimum)}}{60.2 \text{ dB-Hz}} + \underset{(10^{-2} \rightarrow 10^{-6})}{6.1 \text{ dB}} + \underset{\text{(margin)}}{8.5 \text{ dB}} + \underset{\text{(power)}}{5.5 \text{ dB}} \\ &= 80.3 \text{ dB-Hz} . \end{aligned} \tag{21}$$

Consequently, the possible variation in C/N_0 over which the Orbiter receiver must operate may be as high as 20.1 dB. As shown in the following section, such a wide range of variation may require special precautions to insure reliable spatial and carrier acquisitions.

6.2 Effects on Spatial and Carrier Acquisition

The spatial search for TDRS is based on detecting the TDRS signal within the main beam of the antenna. The detection, however, must take place at the worst case C/N_0 of 60.2 dB-Hz and, thus, all the acquisition thresholds are set to provide a reliable detection at this value of C/N_0. But if the high level operation is encountered, the antenna's sidelobe suppression may not be adequate and a lock indication may occur within a sidelobe. Table 7 shows the factors which contribute to the degradation of the effective sidelobe degradation.

Table 7. Factors Contributing to Sidelobe Suppression Degradation

Parameter	Maximum	Minimum	Degradation (dB)
TDRS EIRP	48.0 dBw	36.6 dBw	11.4
Path Loss	208.5 dBw	205.7 dBw	2.8
Pointing Loss (GPC designate)	3 dB	0 dB	3.0
		Total Degradation	17.2 dB

Therefore, if the measured sidelobe level of an antenna is 22 dB down (baseline value), the effective level during TDRS acquisition is only

$$\Delta_{eff} = 22 \text{ dB} - 17.2 \text{ dB} = 4.8 \text{ dB}. \qquad (22)$$

Furthermore, if we consider the fact that the TDRS EIRP may be higher by another 5.5 dB, we obtain a negative margin of 0.7 dB for the spatial acquisition!

To offset this margin, the sidelobe suppression must be increased to the goal value of 24 dB. But, even with this sidelobe level, the remaining effective sidelobe suppression is only 1.3 dB. Thus, special methods must be employed to eliminate sidelobe lock-up. Possible methods

include:

(1) Using the wide beam horn in the receive mode during acquisition to provide sidelobe discrimination, and

(2) Carrying out a miniscan at each signal detect point and providing comparisons of amplitudes at various points, thus driving the servo in the direction of the largest signal.

From the standpoint of reducing spatial TDRS acquisition time, the first technique appears more promising, provided that the associated microwave circuitry is not overly complicated.

The problem associated with the carrier acquisition over the 20.1 dB variation in C/N_0 value has been discussed in Section 2.3. There, it was pointed out that, to insure that no false carrier lock occurs at 108 kHz (a subharmonic of the 216 kbps data rate), the bandwidth of the arm filters of the Costas loop must be at least nine times the data rate. This criterion implies the arm filter bandwidth of about 2 MHz for the 216 kbps data. The effect of this requirement on carrier tracking performance is considered in the next section.

6.3 TDRS Signal Variation Effects on Tracking Functions

The variation of TDRS EIRP will result in changes in the effective C/N_0 at the input to the Orbiter Ku-band receiver. Thus, one has to examine the effect of the signal change on various tracking functions of the Ku-band receiver. Of specific interest is the behavior of the tracking functions in the 57 to 63 dB-Hz C/N_0 region, a region within which the acquisition and tracking threshold are located.

Consider first the carrier tracking function. The carrier tracking device is typically a Costas loop which also provides the function of data demodulation. Figure 32 shows the Costas loop signal-to-noise ratio, SNR_L, as the function of the C/N_0 at the system. Note that the data shown includes a 1.5 dB despreader implementation loss. Curve 1 of Figure 32 shows the SNR_L for the arm filter bandwidth of 679 kHz, which is a noise bandwidth of a single RC filter having a cutoff frequency of 412 kHz. Such a bandwidth would be used if there was no threat of a false lock. However, as stated in the previous section, to avoid a false lock at C/N_0 of 80.3 dB-Hz, the arm filter bandwidth must be widened to about 2 MHz.

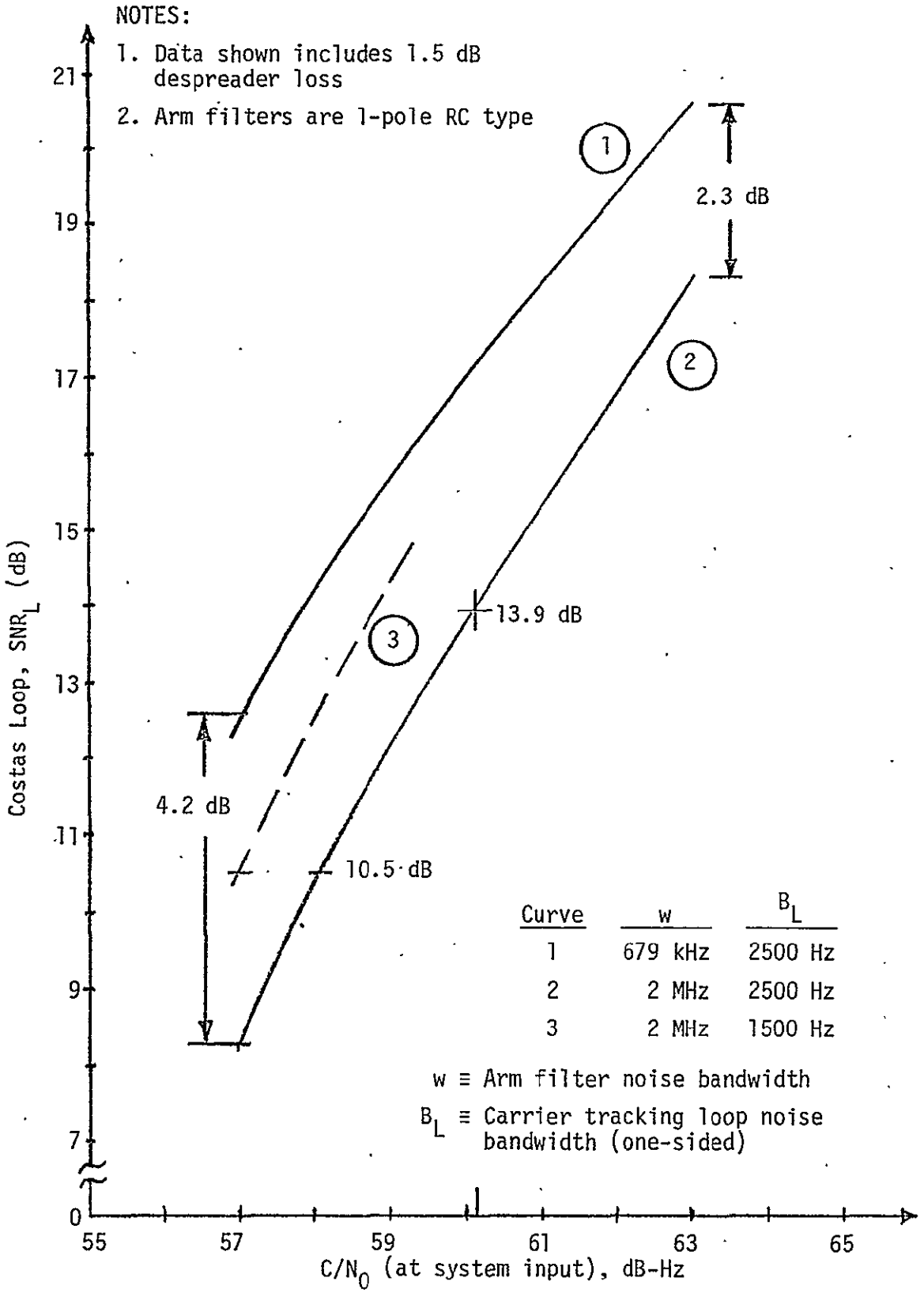

Figure 32. Carrier Tracking (Costas) Loop SNR Versus C/N$_0$

Curve 2 shows the SNR_L for the latter case. The comparison of the two curves indicates that widening the arm filter bandwidth to prevent false lock may cause 4.2 dB SNR_L degradation at 57 dB-Hz and 2.3 dB degradation at 63 dB-Hz. However, Curve 2 indicates that, at the acquisition threshold of 60.2 dB-Hz, the SNR_L is 13.9 dB, a value which is quite adequate for providing reliable carrier acquisition.

To determine the thresholding behavior of Curve 2, let us compute the SNR_L at which the mean time to unlock is 100 minutes [4]. In terms of loop parameters, this time is

$$\bar{T} = \frac{\pi}{4B_L} e^{1.5\rho} \tag{23}$$

where $\bar{T}$ = mean time to unlock

B_L = carrier loop noise bandwidth (one-sided)

ρ = loop signal-to-noise ratio (SNR_L).

Substituting the appropriate values into (23) and solving for ρ, one obtains

$$\frac{(60)(100)(4)(2500)}{\pi} = e^{1.5\rho} \tag{24}$$

$$1.91 \times 10^7 = e^{1.5\rho}$$

$$16.8 = 1.5\rho$$

or

$$\rho = 11.2 \text{ or } 10.5 \text{ dB}.$$

According to Curve 2, the SNR_L = 10.5 dB occurs at C/N_0 of about 58 dB-Hz. This C/N_0 is higher than the estimated system threshold value of 57 dB-Hz. However, the loop noise bandwidth can be narrowed after acquisition to improve threshold performance. Thus, as shown by Curve 3, narrowing the noise bandwidth after acquisition to 1500 Hz will permit the threshold criterion of 57 dB-Hz to be met with a loop designed to prevent false lock at C/N_0 of up to 80.3 dB-Hz.

Figure 33 shows the contribution of various tracking losses as a function of C/N_0. The rms angle tracking error is also shown. The data shown indicates that there is no precipitous increase in the pointing loss and code loop degradation losses. The contribution of the carrier track noise at 57 dB-Hz is also relatively small, less than 0.2 dB.

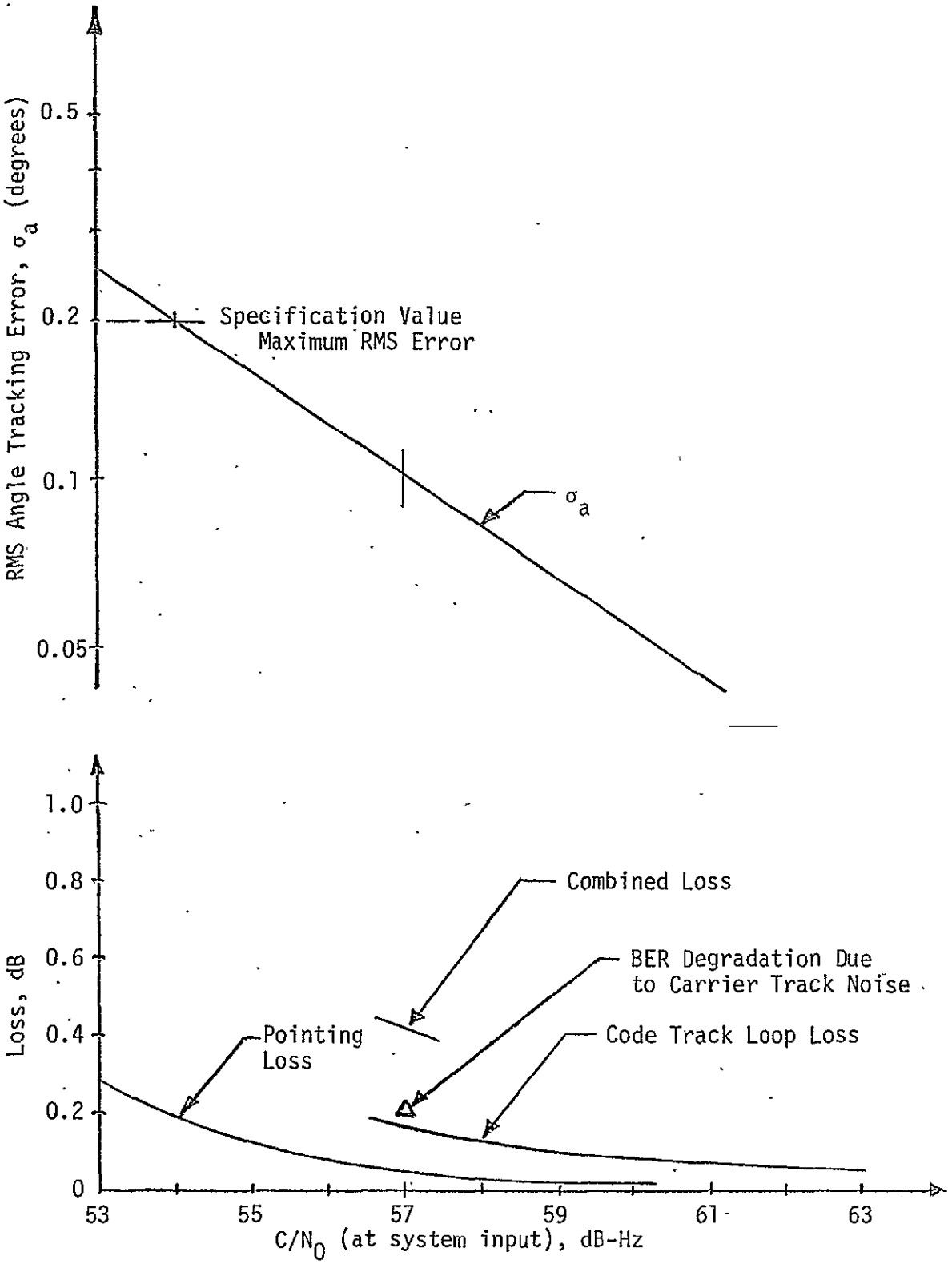

Figure 33. Tracking Function Losses and RMS Angle Tracking Error versus C/N_0 at Input of Ku-Band Receiver

The bit synchronizer threshold is expected to be in the region of about E_b/N_0 of -5 dB. For 216 kbps data rate, this corresponds to

$$C/N_0 \text{ dB-Hz} = 53.3 \text{ dB-Hz} - 5 \text{ dB}$$
$$= 48.3 \text{ dB-Hz}. \quad (25)$$

It appears, therefore, that the bit synchronizer threshold is not the limitation on any of the other system subunits.

The maximum specified rms value of angle tracking error is at about 54 dB-Hz. This is 3 dB below the 57 dB-Hz at which the phase lock loop SNR_L drops to 10.5 dB. Thus, one may conclude that the previously discussed mean time to unlock (the Costas loop) criterion may be the one that sets the overall system threshold at about 57 dB-Hz.

7.0 SIGNAL DISTORTION CONSIDERATIONS

7.1 Sources of Signal Distortion

The sources of signal distortion may involve both the passive circuits, such as filters, and active devices, such as logic gates and other digital devices. Filter losses are generally due to bandpass characteristics, such as insufficient bandwidth, excessive ripple, and phase nonlinearities. Thus, at least in principle, they can be controlled.

The distortion due to active devices generally involves the basic characteristic of the devices and is therefore more difficult to control. In the following subsections, we consider briefly the possible effects of filtering distortion, but special consideration is given to the estimate of the bit error rate degradation due to NRZ data symbol asymmetry in the 100 Msps return link channel.

7.2 Receiver Filtering and Mistuning Effects

The filtering distortion in the receiver is not likely to be severe because of the relatively low 216 kbps data rate. The effect of mistuning, however, has to be considered. Figure 34 shows such an effect. The data shown there is based on the analysis by Jones [11]. The effect may take place in the post-correlation IF filer. The mistuning shown is due to residual carrier uncertainty of ±150 kHz. The loss shown for this mistuning is about 0.3 dB and is for B_{IF} of 1.2 MHz.

7.3 Transmitter Filter Distortion

The transmitter signal filtering may introduce some distortion into the return link signal. The filter under consideration is the 300 MHz transmitter output filter, which actually can be a set of cascaded diplexer filters. Using the data given by Jones, we estimate the loss at 0.75 dB for the worst case of 100 Msps rate. Jones' data, however, is for a Chebychev filter with 0.1 dB ripple and BER of 10^{-6}. Therefore, we expect that, for our case, i.e., passband ripple of 0.01 dB and BER of 10^{-5}, the loss will be significantly smaller than the projected 0.75 dB value.

7.4 Bit Error Rate Degradation of the Return Link Channel Due to NRZ Data Symbol Asymmetry

The high data rate link from the Shuttle Orbiter through the TDRSS to the ground takes NRZ symbols at 50 Mbps and convolutionally encodes them

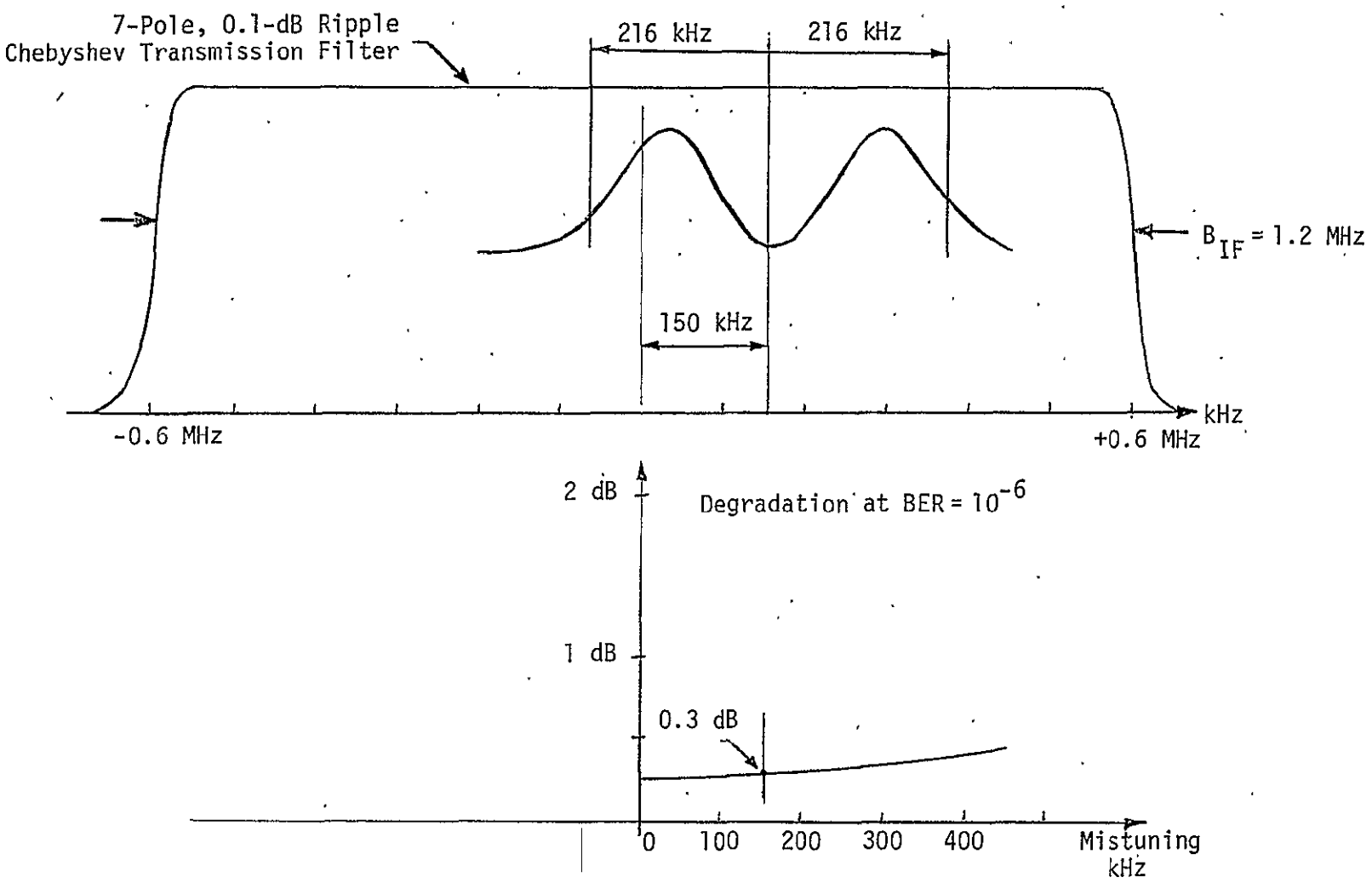

Figure 34. Effect of Forward Link Signal Mistuning

with a rate 1/2, constraint length 7, convolutional code. The bit error rate performance of the convolutional decoder depends, among other things, on the symmetry of the modulation. Any asymmetry in the NRZ symbols entering the symbol synchronizer causes a misalignment in the symbol synchronization clock which degrades the integrate-and-dump output and any soft or hard decisions derived from it for input to the decoder. For a specified degree of asymmetry (in terms of a fraction of a symbol interval), the bit error rate degradation is dependent on the transition probability of the data. Clearly, if the data transmitted was either all ones or all minus ones, then misalignment of the bit sync clock would have no degrading effect on the integrate-and-dump output since, for each symbol, this circuit would integrate up to its maximum value before being dumped. On the other hand, when the data is an alternating sequence, then the worst case degradation results since the transition which occurs at the end of each symbol in combination with the symbol sync clock misalignment prevents the integrate-and-dump output from reaching its maximum value.

To quantitatively determine the degrading effect of NRZ symbol asymmetry on error rate performance, consider first the alternating NRZ sequence illustrated in Figure 35(a), where the +1 symbols are elongated by $\Delta T/2$ (relative to their nominal value of T_{sec}) and the -1 symbols are shortened by the same amount. Thus, ΔT represents the relative asymmetry between the +1 and -1 symbols. In the absence of noise, the timing instants for the in-phase integrate-and-dump (i.e., the epoch of the symbol sync clock) are determined as follows. The mid-phase integrate-and-dump in the symbol synchronizer integrates across the transitions in the data symbol stream and determines the magnitude of the symbol sync error signal. In the steady state, this error signal must have zero value on the average. Letting ΔT denote the misalignment of the symbol sync clock, then from Figure 35(b), we see that, when integrating across a <u>negative</u> data transition, the output of the mid-phase integrate-and-dump is given by

$$V_{-} = (\frac{1}{2} + \frac{\Delta}{2} - \varepsilon)T - (\frac{1}{2} - \frac{\Delta}{2} + \varepsilon)T \ . \qquad (26)$$

Equating (26) to zero gives $\varepsilon \triangleq \varepsilon_{-} = \Delta/2$. Also from Figure 35(b), we observe that the output of the mid-phase integrate-and-dump when integrating across a <u>positive</u> data transition is given by

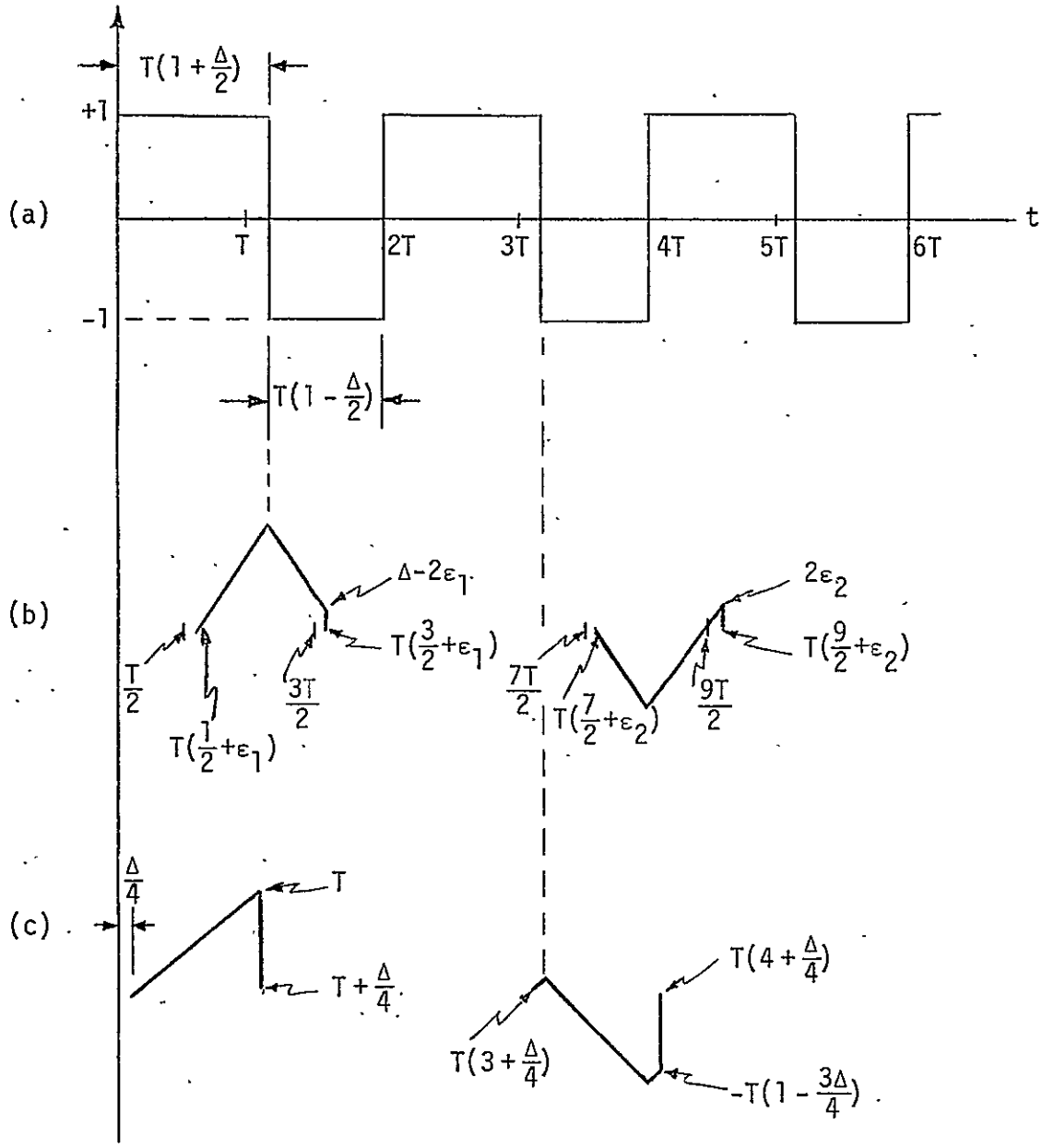

Figure 35. Symbol Sync Waveforms: (a) Input Alternating Data Sequence; (b) Mid-Phase Integrate-and-Dump Output; (c) In-Phase Integrate-and-Dump Output

$$V_+ = -\left(\frac{1}{2} - \varepsilon\right) + \left(\frac{1}{2} + \varepsilon\right) . \tag{27}$$

Equating (27) to zero gives $\varepsilon \triangleq \varepsilon_2 = 0$. Thus, since the symbol sync loop bandwidth is much narrower than the data rate, the symbol sync clock misalignment $\bar{\varepsilon}$ is determined by the average of ε_1 and ε_2 or

$$\bar{\varepsilon} = \frac{\Delta}{4} . \tag{28}$$

Assuming then a clock misalignment as in (28), Figure 35(c) illustrates the in-phase integrate-and-dump output for the two types of data transition (negative and positive). For the negative data transition, we notice that the in-phase integrate-and-dump output reaches its maximum value and thus no degradation results. For the positive data transition, this same output is degraded by the factor $(1 - 3\Delta/4)$. Thus, if E_s denotes the symbol energy and N_0 the channel noise spectral density, then the average symbol error probability associated with hard decisions made on the in-phase integrate-and-dump outputs is given by

$$P_E^A = \frac{1}{4}\,\mathrm{erfc}\,(\sqrt{E_s/N_0}) + \frac{1}{4}\,\mathrm{erfc}\,\left[\sqrt{E_s/N_0}\,\left(1 - \frac{3\Delta}{4}\right)\right] \tag{29}$$

where

$$\mathrm{erfc}\,x \triangleq \frac{2}{\sqrt{\pi}} \int_x^\infty e^{-t^2}\,dt \tag{30}$$

and the "A" superscript on P_E refers to the result for an <u>alternating</u> data symbol sequence.

Since we have already mentioned that there is no degradation when there are no transitions in the data, then for an arbitrary transition density p_t, the probability of error would be given by

$$P_E = p_t P_E^A + (1 - p_t) P_E^0 \tag{31}$$

where

$$P_E^0 \triangleq \frac{1}{2}\,\mathrm{erfc}\,(\sqrt{E_s/N_0}) \tag{32}$$

is the symbol error probability performance in the absence of any degradation and the "0" superscript denotes the absence of data transitions. Finally, then, for random data wherein $p_t = 0.5$, we have from (31) that

$$P_E^R = \frac{1}{2}P_E^A + \frac{1}{2}P_E^0 \qquad (33)$$

or, substituting (29) and (32) in (33),

$$P_E^R = \frac{3}{8}\,\mathrm{erfc}\,(\sqrt{E_s/N_0}) + \frac{1}{8}\,\mathrm{erfc}\,[\sqrt{E_s/N_0}\,(1 - \tfrac{3\Delta}{4})] \,. \qquad (34)$$

In (33) and (34), the "R" superscript refers to the fact that the result is for random data.

Tables 8 and 9 contain the symbol energy-to-noise ratio degradations (in dB) due to asymmetry for values of $\Delta = 0.03$, 0.07, and 0.10, and E_s/N_0 = 0, 0.75, and 1.5 dB. The values of E_s/N_0 selected correspond to bit energy-to-noise ratios $E_b/N_0 = 3$, 3.75, and 4.5 which, respectively, correspond to decoder bit error probabilities $P_b = 10^{-3}$, 10^{-4}, and 10^{-5}. The degradations are obtained from (29) and (34) by computing the additional E_s/N_0 required due to asymmetry (Δ) to produce the same value of symbol error probability when $\Delta = 0$, i.e., P_E^0 of (32).

Table 8. Alternating Data

E_s/N_0 (dB)	P_E^0	Degradation (dB)		
		$\Delta = 0.03$	$\Delta = 0.07$	$\Delta = 0.1$
0	0.07865	0.1	0.24	0.35
0.75	0.06157	0.1	0.24	0.35
1.5	0.0464	0.1	0.24	0.35

Table 9. Random Data

E_s/N_0 (dB)	P_E^0	Degradation (dB)		
		$\Delta = 0.03$	$\Delta = 0.07$	$\Delta = 0.1$
0	0.07865	0.05	0.12	0.175
0.75	0.06157	0.05	0.12	0.175
1.5	0.0464	0.05	0.12	0.175

8.0 CONCLUSIONS

A number of advanced analytical and design tasks have been presented in this report. Based on the results of these tasks, recommendations have been made with respect to the optimization of the Ku-band communication equipment for the Space Shuttle. The results also indicate that a communication system incorporating the recommended features will meet the specified performance requirements with a minimum amount of additional complexity. Of particular importance are the Costas loop parameters which provide false lock immunity for the Ku-band receiver. The technique of employing a sinusoidal subcarrier waveform, rather than square-wave, plays a major role in optimizing the performance of the phase-multiplexed three-channel return link.

REFERENCES

1. C. R. Cahn. "Improving Frequency Acquisition of a Costas Loop," accepted for publication in IEEE Transactions on Communications.

2. R. A. Kallas. "Shuttle Ku-Band PM Mode 1 Scaled Bit Rate Tests," NASA/JSC Report EE7-76-202, September 1976.

3. "Procurement Specification MC409-0025, Ku-Band Integrated Radar and Communications Equipment," Vol. II, Space Division/Rockwell International, March 15, 1976.

4. S. Udalov. "Acquisition and Tracking Threshold Estimates for the Forward Link of the Shuttle Ku-Band Communications Equipment," Axiomatix Report No. R7703-1 (under NASA Contract NAS 9-13467), March 22, 1977.

5. G. A. DeCouvreur. "Effects of Random Synchronization Errors in PN and PSK Systems," IEEE Transactions, AES, January 1970, pp. 98-100.

6. "Proposal for Ku-Band Integrated Radar and Communication Equipment for the Space Shuttle Orbiter Vehicle," Vol. II, Hughes Aircraft Company, Ref. No. D7768/SCG60176P, May 1976.

7. S. Udalov. "RF Spectra and Filtering Considerations for an Integrated Ku-Band Shuttle Orbiter Radar/Communication System," Axiomatix Report No. R7509-5 (under NASA Contract NAS 9-14614), September 29, 1975.

8. S. Udalov. "Signal Detection and Angular Search Procedure for Shuttle Ku-Band Communication System," Axiomatix Report No. R7410-2 (under NASA Contract NAS 9-13467), October 2, 1974.

9. "Study to Investigate and Evaluate Means of Optimizing the Radar Function for the Space Shuttle," Final Report, Axiomatix Report No. R7607-4 (under NASA Contract NAS 9-14614, Exhibit B), July 31, 1976.

10. "Integrated Source and Channel Encoded Digital Communication System Design Study," Final Report, Axiomatix Report No. R7607-3 (under NASA Contract NAS 9-13467), July 31, 1976.

11. J. J. Jones. "Filter Distortion and Intersymbol Interference Effects on PSK Signals," IEEE Transactions on Communication Technology, Vol. COM-19, No. 2, April 1971, pp. 120-132.

APPENDIX A

FALSE LOCK PERFORMANCE OF COSTAS RECEIVERS

APPENDIX A

FALSE LOCK PERFORMANCE OF COSTAS RECEIVERS

by Marvin K. Simon

In this appendix, we first demonstrate that a Costas loop can exhibit a false lock condition in the sense that the loop can lock up on a data sideband. In particular, for the case of random data, the loop can theoretically lock at a frequency which is any integer multiple of half the data symbol rate. An expression for the dc output of the lock detector is then derived in terms of the Fourier transform of the symbol pulse shape, the squared magnitude of the lowpass arm filter transfer function and the loop phase error. This expression is then evaluated at the true lock and false lock conditions and numerical results are given for the case of Manchester coded data and a single pole (RC) arm filter.

Consider the Costas loop and associated lock detector illustrated in Figure A-1. The input signal $s[t, \theta(t)]$ is a bi-phase modulated carrier of the form

$$s[t,\theta(t)] = \sqrt{2S}\, m(t) \sin [\omega_0 t + \theta(t)] \tag{1}$$

where S is the average signal power, m(t) is a binary modulation (a ± 1 digital waveform), ω_0 is the radian carrier frequency, and $\theta(t) \triangleq \theta_0 + \Omega_0 t$ is the received carrier phase. The total received signal x(t) is then

$$x(t) = s[t, \theta(t)] + n_i(t) \tag{2}$$

where $n_i(t)$ is the additive channel noise which can be expressed in the form of a narrowband process about the actual frequency of the observed data, viz.,

$$n_i(t) = \sqrt{2} \left\{ N_c(t) \cos [\omega_0 t + \theta(t)] - N_s(t) \sin [\omega_0 t + \theta(t)] \right\} \tag{3}$$

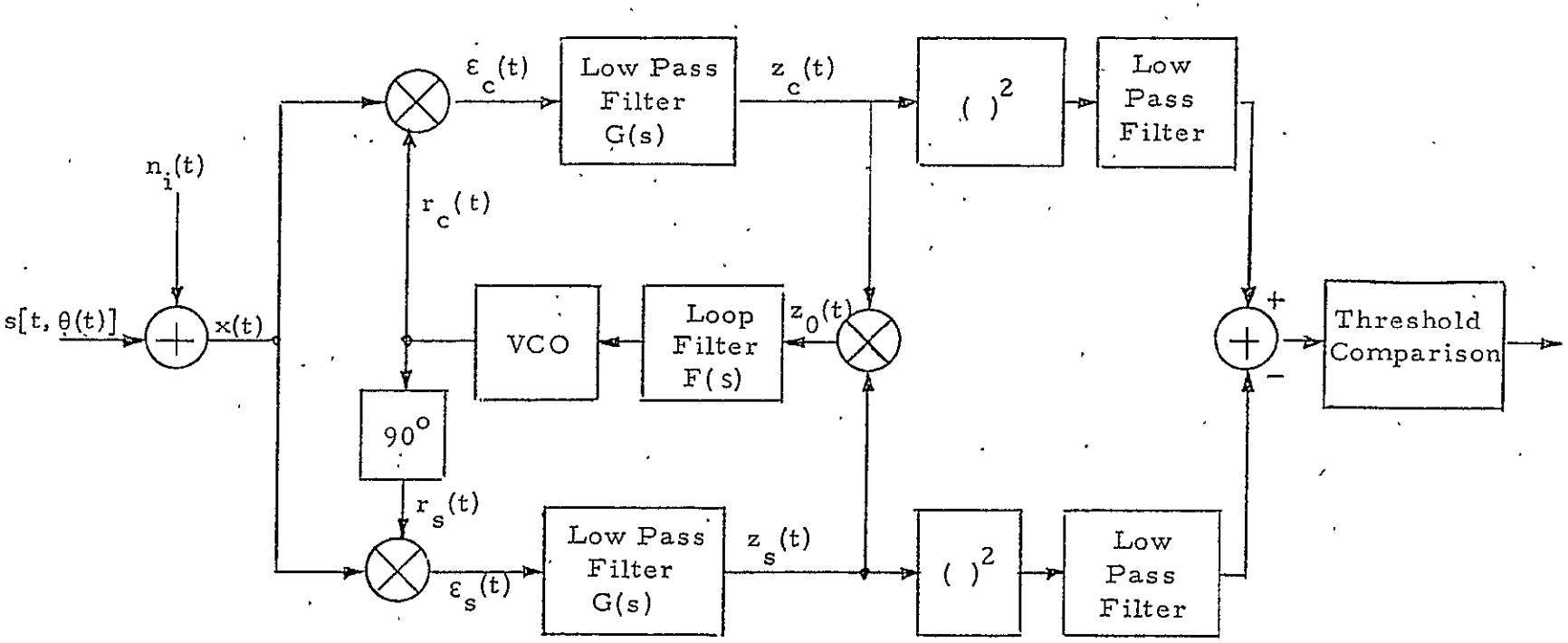

Figure A-1. Costas Loop and Associated Lock Detector

where $N_c(t)$ and $N_s(t)$ are approximately statistically independent, stationary, white Gaussian noise processes with single-sided noise spectral density N_0 w/Hz and single-sided bandwidth $B_H < \omega_0/2$.

For the true lock case; the in-phase and quadrature reference signals $r_s(t)$ and $r_c(t)$, respectively, would be given by

$$r_s(t) = \sqrt{2}\, K_1 \sin[\omega_0 t + \hat{\theta}(t)]$$

$$r_c(t) = \sqrt{2}\, K_1 \cos[\omega_0 t + \hat{\theta}(t)] \tag{4}$$

where $\hat{\theta}(t)$ is the VCO's estimate of $\theta(t)$ and K_1^2 is the reference signal power. In the false lock mode, one would have

$$r_s(t) = \sqrt{2}\, K_1 \sin[(\omega_0 - \omega_f)t + \hat{\theta}(t)]$$

$$r_c(t) = \sqrt{2}\, K_1 \cos[(\omega_0 - \omega_f)t + \hat{\theta}(t)] \tag{5}$$

where ω_f is the false lock radian frequency as yet to be determined.

Denoting the in-phase and quadrature phase detector (multiplier) gains by K_m, then using (3) and (5), the output $\epsilon_c(t)$ of the quadrature phase detector is (ignoring second-harmonic terms)

$$\begin{aligned}\epsilon_c(t) &= K_m\, x(t)\, \sqrt{2}\, K_1 \cos[(\omega_0 - \omega_f)t + \hat{\theta}(t)] \\ &= K_1 K_m [\sqrt{S}\, m(t) - N_s(t)] \sin[\omega_f t + \phi(t)] \\ &\quad + K_1 K_m\, N_c(t) \cos[\omega_f t + \phi(t)]\end{aligned} \tag{6}$$

while the in-phase arm phase detector output is

$$\begin{aligned}\epsilon_s(t) &= K_m\, x(t)\, \sqrt{2}\, K_1 \sin[(\omega_0 - \omega_f)t + \hat{\theta}(t)] \\ &= K_1 K_m [\sqrt{S}\, m(t) - N_s(t)] \cos[\omega_f t + \phi(t)] \\ &\quad - K_1 K_m\, N_c(t) \sin[\omega_f t + \phi(t)]\end{aligned} \tag{7}$$

where $\phi(t) \triangleq \theta(t) - \hat{\theta}(t)$ is the loop phase error. After lowpass filtering with the in-phase and quadrature phase arm filters, these same signals become, respectively,*

$$z_c(t) = K_1 K_m \Big\{ \sqrt{S}\, G(p) \Big[m(t) \sin [\omega_f t + \phi(t)] \Big] - G(p) \Big[N_s(t) \sin [\omega_f t + \phi(t)] \Big] \Big\}$$

$$\longmapsto \hat{m}_s(t; \omega_f, \phi) \longrightarrow \qquad \longmapsto \hat{N}_{ss}(t; \omega_f, \phi) \longrightarrow$$

$$+ K_1 K_m \Big\{ G(p) \Big[N_c(t) \cos [\omega_f t + \phi(t)] \Big] \Big\}$$

$$\longmapsto \hat{N}_{cc}(t; \omega_f, \phi) \longrightarrow$$

$$z_s(t) = K_1 K_m \Big\{ \sqrt{S}\, G(p) \Big[m(t) \cos [\omega_f t + \phi(t)] \Big] - G(p) \Big[N_s(t) \cos [\omega_f t + \varphi(t)] \Big] \Big\}$$

$$\longmapsto \hat{m}_c(t; \omega_f, \phi) \longrightarrow \qquad \longmapsto \hat{N}_{sc}(t; \omega_f, \phi) \longrightarrow$$

$$- K_1 K_m \Big\{ G(p) \Big[N_c(t) \sin [\omega_f t + \phi(t)] \Big] \Big\} \tag{8}$$

$$\longmapsto \hat{N}_{cs}(t; \omega_f, \phi) \longrightarrow$$

Here, the signals $\hat{m}_s(t; \omega_f, \varphi)$ and $\hat{m}_c(t; \omega_f, \phi)$ are the quadrature and in-phase signals emerging from passage of the data modulated false lock sinusoids, $m(t) \sin [\omega_f + \phi(t)]$ and $m(t) \cos [\omega_f t + \phi(t)]$, respectively, through the lowpass arm filters $G(s)$, and likewise, $\hat{N}_{ss}(t; \omega_f, \phi)$, $\hat{N}_{cc}(t; \omega_f, \phi)$, $\hat{N}_{sc}(t; \omega_f, \phi)$, and $\hat{N}_{cs}(t; \omega_f, \phi)$ are the equivalently filtered versions of the noise components.

Squaring $z_c(t)$ and $z_s(t)$ and differencing these quantities produces a process whose statistical mean (over the data sequence) and time average gives the dc voltage at the lock detector output. From (8), the normalized signal component of this dc voltage is**

---

*In what follows, we shall write differential equations in compact form by introducing the Heaviside operator $p \triangleq d/dt$.

**For convenience, we drop in our notation herein, the dependence of ϕ on time.

$$V_{dc} = \lim_{T_0 \to \infty} \frac{1}{T_0} \int_{-T_0/2}^{T_0/2} \left[\overline{\hat{m}_c^2(t; \omega_f, \phi)} - \overline{\hat{m}_s^2(t; \omega_f, \phi)} \right] dt \tag{9}$$

where the overbar denotes statistical mean. It now remains to characterize V_{dc} in terms of the statistical characterization of the modulation m(t) and the filter transfer function characteristic $G(j\omega)$.

The digital modulation m(t) may be represented as

$$m(t) = \sum_{n=-\infty}^{\infty} a_n \, p(t - nT) \tag{10}$$

where $a_n = \pm 1$ is the data symbol sequence and p(t) is the symbol pulse shape, e.g., for Manchester coding,

$$p(t) = \begin{cases} -1 ; & -\frac{T}{2} \le t \le 0 \\ 1 ; & 0 \le t \le \frac{T}{2} \end{cases} \tag{11}$$

Substituting (10) into the definitions of $\hat{m}_c(t; \omega_f, \phi)$ and $\hat{m}_s(t; \omega_f, \phi)$ given in (8) results, after considerable manipulation, in

$$\begin{aligned} \hat{m}_s(t; \omega_f, \phi) &\triangleq G(p)[m(t) \sin(\omega_f t + \phi)] \\ &= \sum_{n=-\infty}^{\infty} a_n \mathcal{F}^{-1} \left\{ G(j\omega) \mathcal{F} [p(t - nT) \sin(\omega_f t + \phi)] \right\} \\ &= \sum_{n=-\infty}^{\infty} a_n \hat{p}_1(t-nT) \frac{e^{j(\omega_f t + \phi)}}{2j} \\ &\quad - \sum_{n=-\infty}^{\infty} a_n \hat{p}_2(t-nT) \frac{e^{-j(\omega_f t + \phi)}}{2j} \end{aligned} \tag{12}$$

where $\mathcal{F}$ denotes Fourier transform with $\mathcal{F}^{-1}$ its inverse and

$$\hat{p}_1(t) = \int_{-\infty}^{\infty} G[j(\omega + \omega_f)]\, P(j\omega)\, e^{j\omega t}\, \frac{d\omega}{2\pi}$$

$$\hat{p}_2(t) = \int_{-\infty}^{\infty} G[j(\omega - \omega_f)]\, P(j\omega)\, e^{j\omega t}\, \frac{d\omega}{2\pi} \qquad (13)$$

Similarly,

$$\hat{m}_c(t;\omega_f,\phi) = G(p)[m(t)\cos(\omega_f t + \phi)]$$

$$= \sum_{n=-\infty}^{\infty} a_n \hat{p}_1(t-nT)\, \frac{e^{j(\omega_f t+\phi)}}{2}$$

$$+ \sum_{n=-\infty}^{\infty} a_n \hat{p}_2(t-nT)\, \frac{e^{-j(\omega_f t+\phi)}}{2} \qquad (14)$$

Squaring (12) and (14) and taking the difference of their statistical means gives

$$\overline{m_c^2(t;\omega_f,\phi)} - \overline{m_s^2(t;\omega_f,\phi)} = \frac{e^{j(2\omega_f t+2\phi)}}{2} \sum_{n=-\infty}^{\infty}\sum_{m=-\infty}^{\infty} \overline{a_n a_m}\, \hat{p}_1(t-nT)\, \hat{p}_1(t-mT)$$

$$+ \frac{e^{-j(2\omega_f t+2\phi)}}{2} \sum_{n=-\infty}^{\infty}\sum_{m=-\infty}^{\infty} \overline{a_n a_m}\, \hat{p}_2(t-nT)\, \hat{p}_2(t-mT) \qquad (15)$$

Finally, taking the time average, we get

$$V_{dc} = \frac{1}{2} \sum_{n=-\infty}^{\infty}\sum_{m=-\infty}^{\infty} \overline{a_n a_m} \left\{ \lim_{T_0\to\infty} \frac{1}{T_0} \int_{-T_0/2}^{T_0/2} e^{2j(\omega_f t+\phi)}\, \hat{p}_1(t-nT)\, \hat{p}_1(t-mT)\, dt \right.$$

$$\left. + \lim_{T_0\to\infty} \frac{1}{T_0} \int_{-T_0/2}^{T_0/2} e^{-2j(\omega_f t+\phi)}\, \hat{p}_2(t-nT)\, \hat{p}_2(t-mT)\, dt \right\} \qquad (16)$$

C.Z

where

$$\lim_{T_0\to\infty} \frac{1}{T_0} \int_{-T_0/2}^{T_0/2} e^{2j(\omega_f t+\varphi)} \hat{p}_1(t-nT)\,\hat{p}_1(t-mT)\,dt$$

$$= e^{j2\phi} \lim_{T_0\to\infty} \int_{-\infty}^{\infty}\int_{-\infty}^{\infty} G[j(\omega+\omega_f)]\,P(j\omega)\,G[j(-\omega'+\omega_f)]$$

$$\times P(-j\omega')\,\frac{\sin[(\omega-\omega'+2\omega_f)(T_0/2)]}{(\omega-\omega'+2\omega_f)(T_0/2)}\,e^{-j(\omega n-\omega' m)T}\,\frac{d\omega}{2\pi}\,\frac{d\omega'}{2\pi} \tag{17}$$

and

$$\lim_{T_0\to\infty} \frac{1}{T_0} \int_{-T_0/2}^{T_0/2} e^{-2j(\omega_f t+\phi)} \hat{p}_2(t-nT)\,\hat{p}_2(t-mT)\,dt$$

$$= e^{-j2\phi} \lim_{T_0\to\infty} \int_{-\infty}^{\infty}\int_{-\infty}^{\infty} G[j(\omega-\omega_f)]\,P(j\omega)\,G[j(-\omega'-\omega_f)]$$

$$\times P(-j\omega')\,\frac{\sin[(\omega-\omega'-2\omega_f)(T_0/2)]}{(\omega-\omega'-2\omega_f)(T_0/2)}\,e^{-j(\omega n-\omega' m)T}\,\frac{d\omega}{2\pi}\,\frac{d\omega'}{2\pi} \tag{18}$$

In order to simplify (16) any further, we must consider a specific statistical characterization of the data sequence $\{a_n\}$. For the case of random data, i.e.,

$$\overline{a_n a_m} = \delta_{mn} = \begin{cases} 1\,;\ m=n \\ 0\,;\ m\neq n \end{cases} \tag{19}$$

the double sum of (16) reduces to a single sum. Recognizing further that

$$\sum_{n=-\infty}^{\infty} e^{-j(\omega-\omega')nT} = \frac{2\pi}{T} \sum_{k=-\infty}^{\infty} \delta\left(\omega-\omega'-\frac{2\pi k}{T}\right) \tag{20}$$

then,

$$V_{dc} = \lim_{T_0 \to \infty} \frac{1}{2T} \left\{ e^{j2\varphi} \sum_{k=-\infty}^{\infty} \int_{-\infty}^{\infty} G[j(\omega' + \omega_f + \frac{2\pi k}{T})]\, P[j(\omega' + \frac{2\pi k}{T})] \right.$$

$$\times G[j(-\omega' + \omega_f)]\, P(-j\omega') \frac{\sin[(2\pi \frac{k}{T} + 2\omega_f)(T_0/2)]}{(2\pi \frac{k}{T} + 2\omega_f)(T_0/2)} \frac{d\omega'}{2\pi}$$

$$+ e^{-j2\phi} \sum_{k=-\infty}^{\infty} \int_{-\infty}^{\infty} G[j(\omega' - \omega_f + \frac{2\pi k}{T})]\, P[j(\omega' + \frac{2\pi k}{T})]$$

$$\left. \times G[j(-\omega' - \omega_f)]\, P(-j\omega') \frac{\sin[(2\pi \frac{k}{T} - 2\omega_f)(T_0/2)]}{(2\pi \frac{k}{T} - 2\omega_f)(T_0/2)} \frac{d\omega'}{2\pi} \right\} \qquad (21)$$

Now suppose that $2\omega_f = \frac{2\pi k_0}{T}$ where $k_0 = 0, 1, 2, \ldots$ is a particular value of k. Then, the value of V_{dc}, namely V_{k_0}, at this frequency is given by

$$V_{k_0} = \frac{1}{2T} \left[e^{j2\phi} \int_{-\infty}^{\infty} \left| G\left[j\left(\omega - \frac{\pi k_0}{T}\right)\right] \right|^2 P\left[j\left(\omega - \frac{2\pi k_0}{T}\right)\right] P(-j\omega) \frac{d\omega}{2\pi} \right.$$

$$\left. + e^{-j2\phi} \int_{-\infty}^{\infty} \left| G\left[j\left(\omega + \frac{\pi k_0}{T}\right)\right] \right|^2 P\left[j\left(\omega + \frac{2\pi k_0}{T}\right)\right] P(-j\omega) \frac{d\omega}{2\pi} \right] \qquad (22)$$

or equivalently

$$\boxed{V_{k_0} = \frac{1}{T} \operatorname{Re} \left\{ e^{j2\phi} \int_{-\infty}^{\infty} |G(j\omega)|^2 P\left[j\left(\omega - \frac{\pi k_0}{T}\right)\right] P\left[-j\left(\omega + \frac{\pi k_0}{T}\right)\right] \frac{d\omega}{2\pi} \right\}}$$

$$k_0 = 1, 2, 3, \ldots \qquad (23)$$

where $\operatorname{Re}\{\ \}$ denotes the real part of what is contained within the braces. Note that, for the case of true lock, i.e., $\omega_f = 0$, we get

$$V_0 = \cos 2\phi \left[\frac{1}{T} \int_{-\infty}^{\infty} |G(j\omega)|^2 \, |P(j\omega)|^2 \frac{d\omega}{2\pi} \right] = \cos 2\phi \int_{-\infty}^{\infty} S_m(\omega) \, |G(j\omega)|^2 \frac{d\omega}{2\pi}$$

(24)

where $S_m(\omega) = \frac{1}{T}|P(j\omega)|^2$ is the power spectral density of the modulation m(t). For any of the false lock frequencies $f_f = \omega_f/2\pi = k_0/2T$, the corresponding lock detector output (signal component) is given by (23).

A particular example will now be given to illustrate the theory just developed. Consider the case where m(t) is a Manchester coded data modulation and G(s) is a single pole RC filter for which

$$|G(j\omega)|^2 = \frac{1}{1 + (\omega/\omega_c)^2} \tag{25}$$

where $\omega_c = 2\pi f_c$ is the radian 3 dB cutoff frequency of the filter and is related to its two-sided noise bandwidth B_i by

$$\omega_c = 2B_i . \tag{26}$$

For the Manchester pulse described by (11), its Fourier transform is given by

$$P(j\omega) = jT\left[\frac{\sin^2 \frac{\omega T}{4}}{\frac{\omega T}{4}}\right] \tag{27}$$

After considerable algebraic manipulation and integral evaluations, we arrive at the following results

$$V_0 = \cos 2\phi\left\{1 - \frac{1}{2\pi f_c T}\left[3 - 4e^{-\pi f_c T} + e^{-2\pi f_c T}\right]\right\} \tag{28}$$

$$V_k = -\cos 2\phi\left\{\left[\frac{1}{1 + \left(\frac{k}{2f_c T}\right)^2}\right]\left[\frac{1 + e^{-2\pi f_c T}}{2\pi f_c T}\right]\right\} \; ; \; k = 1, 3, 5, \ldots \tag{29}$$

$$V_k = -\cos 2\phi\left\{\left[\frac{1}{1 + \left(\frac{k}{2f_c T}\right)^2}\right]\left[\frac{3 + 4e^{-\pi f_c T} + e^{-2\pi f_c T}}{2\pi f_c T}\right]\right\} \; ;$$

$$k = 2, 6, 10, \ldots \tag{30}$$

$$V_k = -\cos 2\phi \left\{ \left[\frac{1}{1 + \left(\frac{k}{2 f_c T} \right)^2} \right] \left[\frac{3 - 4e^{-\pi f_c T} + e^{-2\pi f_c T}}{2\pi f_c T} \right] \right\}$$

$$k = 4, 8, 12, \ldots \qquad (31)$$

At this point, it should be mentioned that, if one was to consider the error signal into the loop filter F(p), i.e.,

$$z_0(t) = z_c(t)\, z_s(t) \qquad (32)$$

where $z_c(t)$ and $z_s(t)$ are given in (8), then the dc value of the normalized signal component in $z_0(t)$, namely,

$$z_{dc} \triangleq \lim_{T_0 \to \infty} \frac{1}{T_0} \int_{-T_0/2}^{T_0/2} \hat{m}_s(t;\omega_f,\phi)\, \hat{m}_c(t;\omega_f,\phi)\, dt \qquad (33)$$

would be given by (28) through (31) with $\cos 2\phi$ replaced by $(\sin 2\phi)/2$. In view of this, we may reach the following conclusion. Since, for any $f_c T$, the braced quantity in V_0 of (28) is positive, then as is well known, true lock corresponds to the lock points $\phi = 0, \pm\pi, \pm 2\pi, \pm 3\pi, \ldots$. Furthermore, since the remaining braced quantities in (29) through (31) are also always positive for any $f_c T$, then in the false lock mode, we must have $\cos 2\phi = -1$ or $\phi = \pm\pi/2, \pm 3\pi/2, \pm 5\pi/2, \ldots$. Thus, the lock points for any false lock condition are interleaved midway between those for the true lock state.

Figure A-2 is a plot of V_k (in dB; $k = 0, 1, 2, 3, 4$, versus $f_c T$ for the example given above (assuming $\phi = 0$ for $k = 0$ and $\phi = \pi/2$ for $k \neq 0$). We note that, by continuing to widen the arm filter bandwidth beyond the optimum value which yields minimum squaring loss ($f_c T = 1.4$), the separation between V_0 and the false lock values continues to increase. This property is desirable from the standpoint of distinguishing false lock from true lock. However, widening the arm filter bandwidth allows more noise to pass through, thus degrading the signal-to-noise ratio at

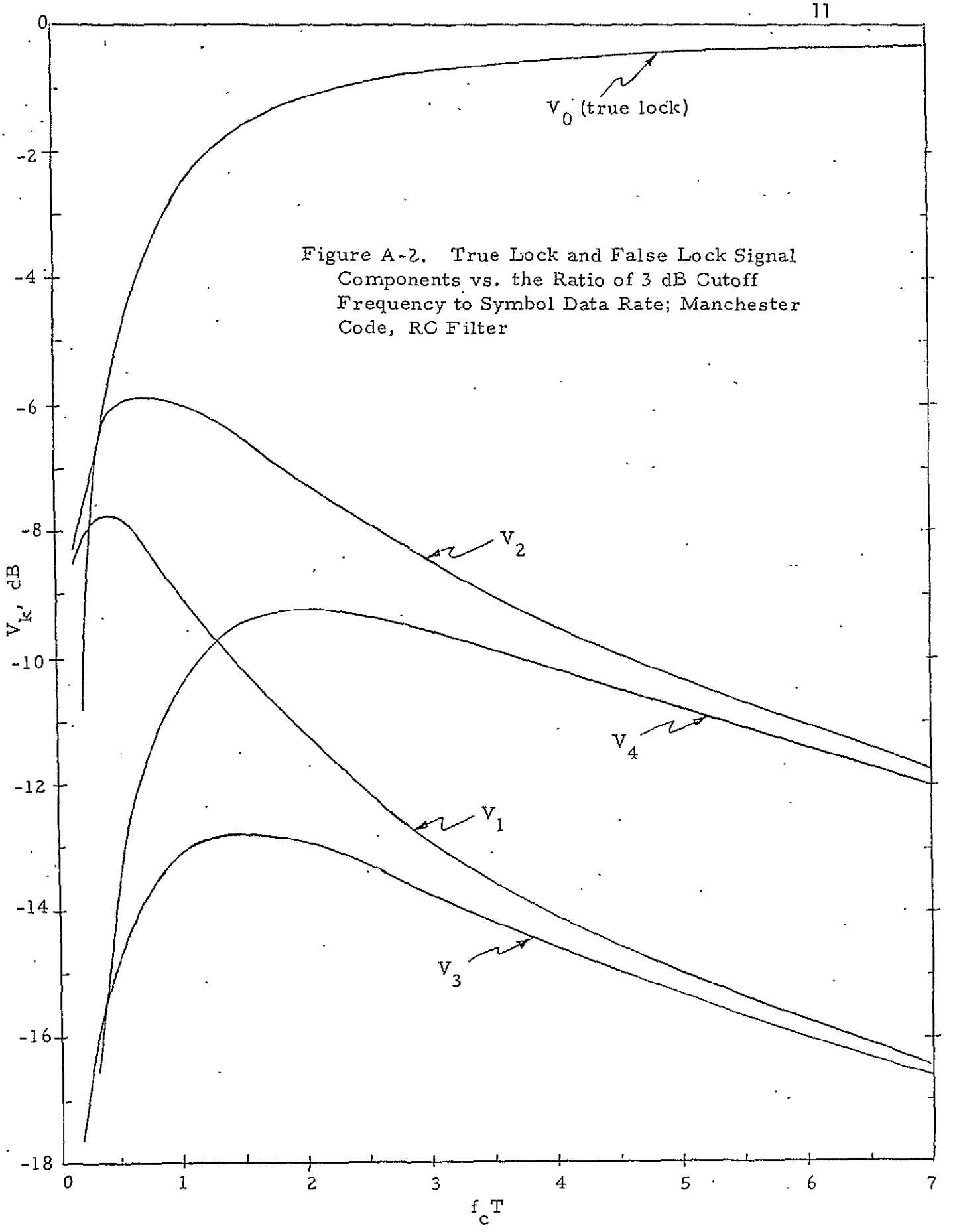

Figure A-2. True Lock and False Lock Signal Components vs. the Ratio of 3 dB Cutoff Frequency to Symbol Data Rate; Manchester Code, RC Filter

the input to the threshold detector. Thus, in conclusion, widening the arm filter bandwidth is potentially a solution to the false lock detection problem up to the point where the signal-to-noise ratio which distinguishes between true lock and out-of-lock (as opposed to false lock) becomes too low for a specified level of lock detection performance.

APPENDIX B

FALSE LOCK PERFORMANCE OF CONVENTIONAL COSTAS RECEIVERS (THE CASE OF ALTERNATING DATA SYMBOLS)

APPENDIX B

FALSE LOCK PERFORMANCE OF CONVENTIONAL COSTAS RECEIVERS (THE CASE OF ALTERNATING DATA SYMBOLS)

Marvin K. Simon

A frequency domain approach to predicting the false lock performance of conventional Costas receivers was presented in Appendix A, along with specific results (analytical and numerical) for the case of random data. We recall that equations (1) through (18) of the development were independent of the statistics of the data symbols. Thus, to avoid duplication of effort, we shall begin here from that point in the development and indicate how the ensuing results would be modified for the case of alternating data symbols.

Since the data is now deterministic, i.e., $a_n = +1$ for n odd and $a_n = -1$ for n even, then the statistical average over the data in equation (16) of Appendix A is no longer needed. Thus, combining equations (16), (17) and (18) of Appendix A gives

$$V_{dc} = \frac{1}{2} e^{j2\phi} \lim_{T_0 \to \infty} \int_{-\infty}^{\infty} \int_{-\infty}^{\infty} G[j(\omega + \omega_f)]\, P(j\omega)\, G[j(-\omega' + \omega_f)]\, P(-j\omega') \times \frac{\sin [(\omega - \omega' + 2\omega_f)\, T_0/2]}{(\omega - \omega' + 2\omega_f)\, T_0/2} \sum_{n=-\infty}^{\infty} a_n\, e^{-j\omega nT} \sum_{m=-\infty}^{\infty} a_m\, e^{j\omega' mT} \frac{d\omega}{2\pi} \frac{d\omega'}{2\pi}$$

$$+ \frac{1}{2} e^{-j2\phi} \lim_{T_0 \to \infty} \int_{-\infty}^{\infty} \int_{-\infty}^{\infty} G[j(\omega - \omega_f)]\, P(j\omega)\, G[j(-\omega' - \omega_f)]\, P(-j\omega') \times \frac{\sin [(\omega - \omega' - 2\omega_f)\, T_0/2]}{(\omega - \omega' - 2\omega_f)\, T_0/2} \sum_{n=-\infty}^{\infty} a_n\, e^{-j\omega nT} \sum_{m=-\infty}^{\infty} a_m\, e^{j\omega' mT} \frac{d\omega}{2\pi} \frac{d\omega'}{2\pi} . \quad (1)$$

For the case of alternating data, we have that

$$\sum_{n=-\infty}^{\infty} a_n\, e^{-j\omega nT} = \sum_{\substack{n=-\infty \\ n \text{ odd}}}^{\infty} e^{-j\omega nT} - \sum_{\substack{n=-\infty \\ n \text{ even}}}^{\infty} e^{-j\omega nT} . \quad (2)$$

Letting $n = 2m - 1$ in the first summation and $n = 2m$ in the second summation gives

$$\sum_{n=-\infty}^{\infty} a_n e^{-j\omega nT} = (e^{j\omega T} - 1) \sum_{m=-\infty}^{\infty} e^{-2j\omega mT}$$

$$= (e^{j\omega T} - 1) \frac{\pi}{T} \sum_{k=-\infty}^{\infty} \delta(\omega - \frac{\pi k}{T}) . \qquad (3)$$

Similarly,

$$\sum_{m=-\infty}^{\infty} a_m e^{j\omega' mT} = (e^{-j\omega' T} - 1) \frac{\pi}{T} \sum_{\ell=-\infty}^{\infty} \delta(\omega' - \frac{\pi \ell}{T}) . \qquad (4)$$

Thus, substituting (3) and (4) in (1), we get

$$V_{dc} = \lim_{T_0 \to \infty} \frac{1}{2} (\frac{1}{2T})^2 \left\{ e^{j2\phi} \sum_{k=-\infty}^{\infty} \sum_{\ell=-\infty}^{\infty} (e^{j\pi k} - 1)(e^{-j\pi \ell} - 1)\, G[j(\frac{\pi k}{T} + \omega_f)] \right.$$

$$\times P(j \frac{\pi k}{T})\, G[j(-\frac{\pi \ell}{T} + \omega_f)]\, P(-j \frac{\pi \ell}{T}) \frac{\sin [(\frac{\pi(k-\ell)}{T} + 2\omega_f)T_0/2]}{(\frac{\pi(k-\ell)}{T} + 2\omega_f)T_0/2}$$

$$+ e^{-j2\phi} \sum_{k=-\infty}^{\infty} \sum_{\ell=-\infty}^{\infty} (e^{j\pi k} - 1)(e^{-j\pi \ell} - 1)\, G[j(\frac{\pi k}{T} - \omega_f)]$$

$$\left. \times P(j \frac{\pi k}{T})\, G[j(-\frac{\pi \ell}{T} - \omega_f)]\, P(-j \frac{\pi \ell}{T}) \frac{\sin [(\frac{\pi(k-\ell)}{T} - 2\omega_f)T_0/2]}{(\frac{\pi(k-\ell)}{T} - 2\omega_f)T_0/2} \right\} . \qquad (5)$$

Letting $2\omega_f = \frac{\pi m}{T}$; $m = 0,1,2,\ldots$; and noting that

$$e^{j\pi k} - 1 = \begin{cases} 0 & k \text{ even} \\ -2 & k \text{ odd} \end{cases}$$

$$e^{-j\pi(k \pm m)} - 1 = \begin{cases} 0 & m \text{ odd, } k \text{ odd} \\ -2 & m \text{ even, } k \text{ odd} \end{cases} \qquad (6)$$

we get the following result:

$$V_{m'} \triangleq V_{dc}\Big|_{\omega_f = \frac{\pi m'}{T}} = \frac{1}{2T^2}\left\{ e^{j2\phi} \sum_{k'=-\infty}^{\infty} \left|G[j\tfrac{\pi}{T}(2k'-1+m')]\right|^2 P[j\tfrac{\pi}{T}(2k'-1)] \right.$$

$$\times P[-j\tfrac{\pi}{T}(2k'-1+2m')]$$

$$+ e^{-j2\phi} \sum_{k'=-\infty}^{\infty} \left|G[j\tfrac{\pi}{T}(2k'-1-m')]\right|^2 P[j\tfrac{\pi}{T}(2k'-1)]$$

$$\left. \times P[-j\tfrac{\pi}{T}(2k'-1-2m')] \right\} \; ; \; m' = 0,1,2,\ldots \tag{7}$$

where we have in addition made the substitutions $k = 2k' - 1$ and $m = 2m'$.

Finally, after some additional simplification and leaving off the prime superscripts on k and m for simplicity of notation, we arrive at the final results, namely,

$$\boxed{V_m = \frac{1}{T^2} \mathrm{Re}\left\{ e^{j2\phi} \sum_{k=-\infty}^{\infty} \left|G(j\tfrac{2\pi k}{T})\right|^2 P[j(\tfrac{2\pi k}{T} - \tfrac{\pi m}{T})]\, P[-j(\tfrac{2\pi k}{T} + \tfrac{\pi m}{T})] \right\} \quad \text{for } m \text{ odd}} \tag{8}$$

and

$$\boxed{V_m = \frac{1}{T^2} \mathrm{Re}\left\{ e^{j2\phi} \sum_{k=-\infty}^{\infty} \left|G[j\tfrac{\pi}{T}(2k-1)]\right|^2 P[j(\tfrac{\pi}{T}(2k-1) - \tfrac{\pi m}{T})]\, P[-j(\tfrac{\pi}{T}(2k-1) + \tfrac{\pi m}{T})] \right\} \quad \text{for } m \text{ even}} \tag{9}$$

where, again, V_m is the dc component of the lock detector output at the false lock frequency $f_f = m/2T$.

Comparing (8) and (9) with equation (23) of Appendix A, we observe a similarity in form. To demonstrate this further, equations (8) and (9) could alternately be written in the form

$$V_m = \frac{1}{T} \mathrm{Re}\left\{ e^{j2\phi} \int_{-\infty}^{\infty} \left|G(j\omega)\right|^2 P[j(\omega - \tfrac{\pi m}{T})]\, P[-j(\omega + \tfrac{\pi m}{T})] \right.$$

$$\left. \times \frac{2\pi}{T} \sum_{k=-\infty}^{\infty} \delta(\omega - \tfrac{2\pi k}{T})\, \frac{d\omega}{2\pi} \right\} \qquad \text{for } m \text{ odd} \tag{10}$$

and

$$V_m = \frac{1}{T} \mathrm{Re} \left\{ e^{j2\phi} \int_{-\infty}^{\infty} |G(j\omega)|^2 \, P[j(\omega - \tfrac{\pi m}{T})] \, P[-j(\omega + \tfrac{\pi m}{T})] \right.$$

$$\left. \times \frac{2\pi}{T} \sum_{k=-\infty}^{\infty} \delta\left(\omega - \frac{\pi}{T}(2k-1)\right) \frac{d\omega}{2\pi} \right\} \quad \text{for } m \text{ even} . \tag{11}$$

As for the case of random data, we shall now present specific results for a Manchester coded data modulation and a single pole RC filter.

Using equation (27) of Appendix A, one can show that

$$P[j(\tfrac{2\pi k}{T} - \tfrac{\pi m}{T})] \, P[-j(\tfrac{2\pi k}{T} + \tfrac{\pi m}{T})] = \frac{T^2}{\pi^2} \left[\frac{1}{k^2 - (\frac{m}{2})^2} \right] ; \; m \text{ odd} \tag{12}$$

and

$$P[j(\tfrac{\pi}{T}(2k-1) - \tfrac{\pi m}{T})] \, P[-j(\tfrac{\pi}{T}(2k-1) + \tfrac{\pi m}{T})] = \frac{T^2}{\pi^2} \left[\frac{1}{(k - \frac{1}{2})^2 - (\frac{m}{2})^2} \right] ;$$

$$m \text{ even} . \tag{13}$$

Similarly, from equation (25) of Appendix A, we have that

$$\left| G(j \tfrac{2\pi k}{T}) \right|^2 = \frac{1}{1 + (\frac{k}{f_c T})^2} . \tag{14}$$

Thus, substituting (12) and (14) in (8), and (13) and (14) in (9), we obtain, after considerable algebraic manipulation and power series evaluations, the following results:

$$V_0 = \cos 2\phi \left\{1 - \frac{1}{\pi f_c T} \tanh \pi f_c T\right\}$$

$$V_k = -\cos 2\phi \left(\frac{1}{\pi f_c T}\right) \left[\frac{1}{1 + \left(\frac{k}{2f_c T}\right)^2}\right] \coth \pi f_c T \; ; \quad k = 1,3,5,\ldots \tag{15}$$

$$V_k = -\cos 2\phi \left(\frac{1}{\pi f_c T}\right) \left[\frac{1}{1 + \left(\frac{k}{2f_c T}\right)^2}\right] \tanh \pi f_c T \quad k = 2,4,6,\ldots$$

Figure 1 is a plot of V_k (in dB); $k = 0,1,2,3,4$, versus $f_c T$ for the example given above (assuming $\phi = 0°$ for $k = 0$ and $\phi = 90°$ for $k \neq 0$). As for the random data case, we note that the separation between the true lock output V_0 and the false lock outputs V_k, $k \neq 0$, increases as the arm filter bandwidth is widened. Also in the limit as $f_c T$ approaches infinity, the false lock signal components at odd multiples of the half symbol rate are twice as strong for the alternating data case than they are for random data. On the other hand, in the same limit as above, the false lock components at even multiples of the half symbol rate are, for alternating data, only three-quarters as strong as they are for random data. These limits are trivially obtained from equation (15) of this appendix and equations (29) through (31) of Appendix A.

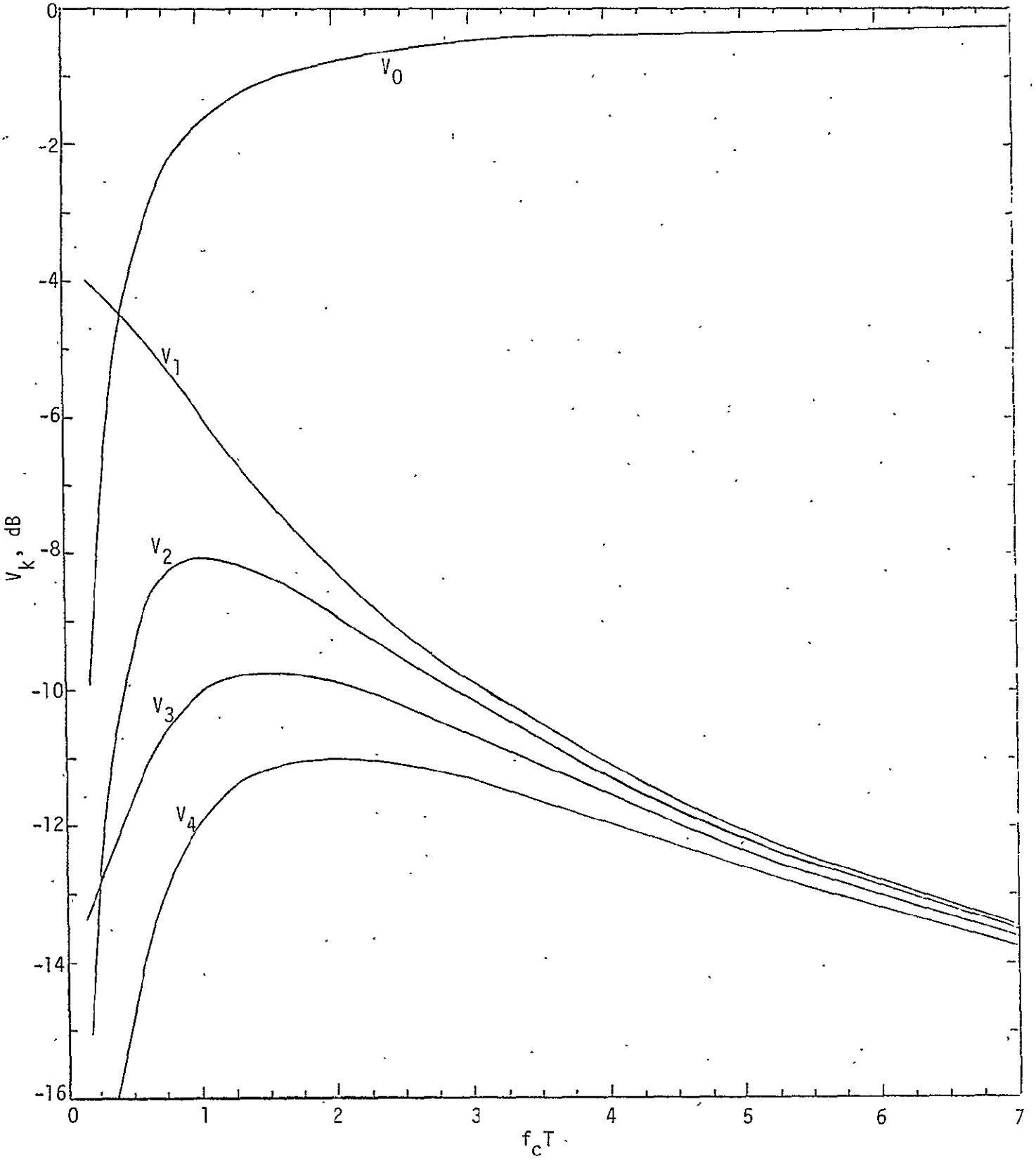

Figure 1. Alternating Data - Manchester Code, RC Filter

APPENDIX C

FALSE LOCK AND TRACKING PERFORMANCE OF A MODIFIED COSTAS LOOP (QUADRATURE ARM FILTER ABSENT)

APPENDIX C

FALSE LOCK AND TRACKING PERFORMANCE OF A MODIFIED COSTAS LOOP (QUADRATURE ARM FILTER ABSENT)

Marvin K. Simon

INTRODUCTION

In a recent paper [1], Cahn suggests that the frequency acquisition capability of a conventional Costas loop (see Figure 1) can be improved by augmenting it with an automatic frequency control (AFC) loop. Such a composite AFC/Costas loop is shown to provide a pull-in range much greater than than achieved by a conventional Costas loop which is typically on the order of the loop bandwidth. In the most general configuration, the AFC transfer function and Costas loop transfer function may be designed and adjusted independently of one another.

Quite often, such additional implementation complexity may not be justified and thus a simpler version of a composite AFC/Costas loop, which still yields improved acquisition performance with negligible degradation to phase tracking performance, is desirable. Such an implementation simplification can be achieved by merely removing the low-pass arm filter in the quadrature phase detector channel (see Figure 2). The resultant loop (called a modified Costas loop by Cahn) has a frequency restoring force approximately equivalent to that produced by half of a balanced frequency discriminator commonly used for AFC. The improved acquisition performance obtained from this simple modification gives a pull-in from initial frequency errors on the order of the in-phase arm filter bandwidth which, for optimum tracking performance design, is on the order of the data rate.

In addition to the improved acquisition performance offered by the modified Costas loop, it has the further advantage of significantly lessening

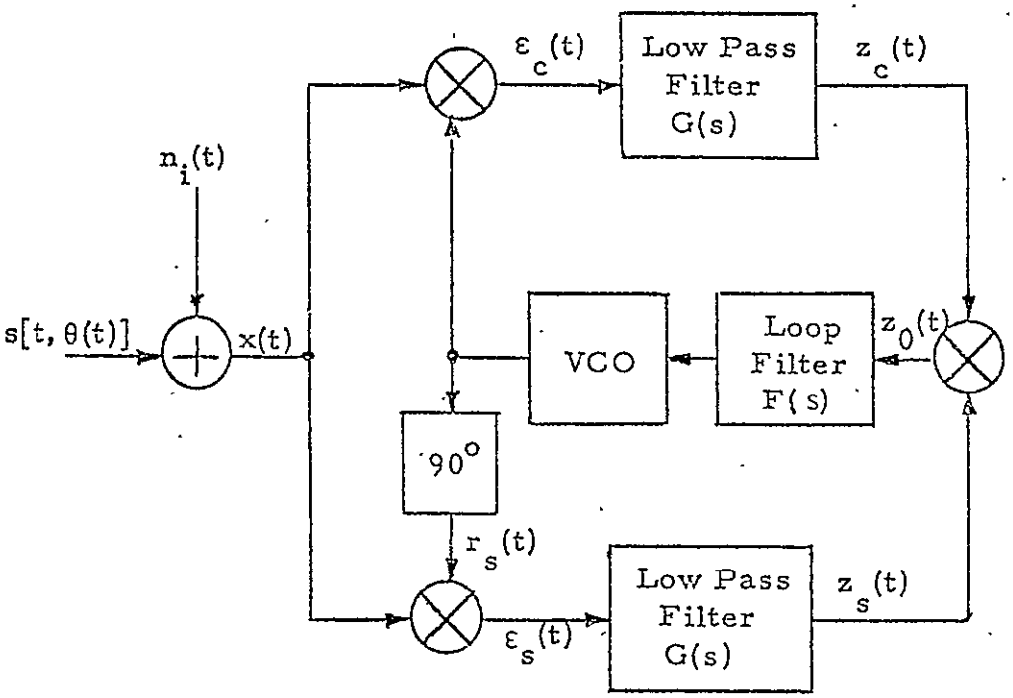

Figure 1. Costas Loop

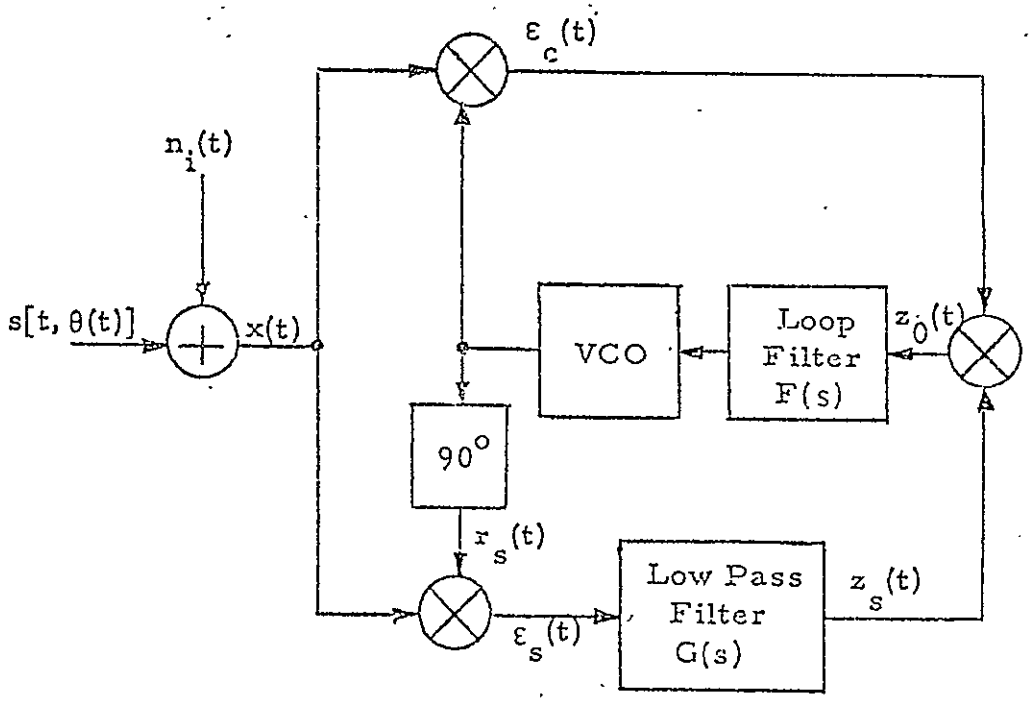

Figure 2. Modified Costas Loop

the false lock tendency of the loop. Ordinarily, a conventional Costas loop can lock to a data sideband such that the VCO frequency is offset from its nominal value by an integer multiple of half of the data rate. When this occurs, stable lock points occur at values of phase error (i.e., 90°, 270°, 540°, ...) which are midway between those values corresponding to a true lock condition. Removal of the quadrature channel arm filter produces, under false lock conditions, a dc voltage at the error control point (loop filter input) which, when added to the sinusoidal restoring force, which is normally present here, reduces the stability (in noise) of these false lock points. In the true lock condition, this additional dc voltage has zero value and thus the stability of the true phase lock points is unaffected.

These and other false lock properties of the modified Costas loop relative to the conventional Costas loop were demonstrated by Cahn [1], primarily with a computer simulation approach. The purpose of this appendix is to present an analytical verification of these false lock phenomena, along with a complete analysis of the phase tracking performance of the modified Costas loop. Once again, as in previous analyses of this type [2,3], the bandlimiting effects of the in-phase arm filter will be taken into account. Ignoring these effects leads to an inaccurate assessment of loop tracking performance and, in addition, the erroneous conclusion that the loop does not false lock.

SYSTEM MODEL

Consider the modified Costas loop illustrated in Figure 2, whose input signal $s[t,\theta(t)]$ is a bi-phase modulated carrier of the form

$$s[t,\theta(t)] = \sqrt{2S}\, m(t) \sin [\omega_0 t + \theta(t)] , \qquad (1)$$

where S is the average signal power, m(t) is a binary modulation (a ± 1 digital waveform), ω_0 is the radian carrier frequency, and $\theta(t) \triangleq \theta_0 + \Omega_0 t$ is the received carrier phase. The total received signal x(t) is then

$$x(t) = s[t, \theta(t)] + n_i(t) , \tag{2}$$

where $n_i(t)$ is the additive channel noise which can be expressed in the form of a narrowband process about the actual frequency of the observed data, viz.,

$$n_i(t) = \sqrt{2} \{N_c(t) \cos [\omega_0 t + \theta(t)] - N_s(t) \sin [\omega_0 t + \theta(t)]\} , \tag{3}$$

where $N_c(t)$ and $N_s(t)$ are approximately statistically independent, stationary, white Gaussian noise processes with single-sided noise spectral density N_0 w/Hz and single-sided bandwidth $B_H < \omega_0/2$.

For the true lock case, the in-phase and quadrature reference signals $r_s(t)$ and $r_c(t)$, respectively, would be given by

$$\begin{aligned} r_s(t) &= \sqrt{2} K_1 \sin [\omega_0 t + \hat{\theta}(t)] \\ r_c(t) &= \sqrt{2} K_1 \cos [\omega_0 t + \hat{\theta}(t)] , \end{aligned} \tag{4}$$

where $\hat{\theta}(t)$ is the VCO's estimate of $\theta(t)$, and K_1^2 is the reference signal power. In the false lock mode, one would have

$$\begin{aligned} r_s(t) &= \sqrt{2} K_1 \sin [(\omega_0 - \omega_f)t + \hat{\theta}(t)] \\ r_c(t) &= \sqrt{2} K_1 \cos [(\omega_0 - \omega_f)t + \hat{\theta}(t)] , \end{aligned} \tag{5}$$

where ω_f is the false lock radian frequency as yet to be determined.

Denoting the in-phase and quadrature phase detector (multiplier) gains by K_m, then using (3) and (5), the output $\varepsilon_c(t)$ of the quadrature phase detector is (ignoring second-harmonic terms)

$$\varepsilon_c(t) = K_m x(t) \sqrt{2}\, K_1 \cos\,[(\omega_0 - \omega_f)t + \hat{\theta}(t)]$$

$$= K_1 K_m [\sqrt{S}\, m(t) - N_s(t)] \sin\,[\omega_f t + \phi(t)]$$

$$+ K_1 K_m N_c(t) \cos\,[\omega_f t + \phi(t)]\,, \tag{6}$$

while the in-phase arm phase detector output is

$$\varepsilon_s(t) = K_m x(t) \sqrt{2}\, K_1 \sin\,[(\omega_0 - \omega_f)t + \hat{\theta}(t)]$$

$$= K_1 K_m [\sqrt{S}\, m(t) - N_s(t)] \cos\,[\omega_f t + \phi(t)]$$

$$- K_1 K_m N_c(t) \sin\,[\omega_f t + \phi(t)]\,, \tag{7}$$

where $\phi(t) \triangleq \theta(t) - \hat{\theta}(t)$ is the loop phase error. After lowpass filtering with the in-phase arm filter, equation (7) becomes*

$$z_s(t) = K_1 K_m \Big\{\sqrt{S}\, G(p)\Big[\overbrace{m(t) \cos\,[\omega_f t + \phi(t)]}^{\hat{m}_c(t;\omega_f,\phi)}\Big] - G(p)\Big[\overbrace{N_s(t) \cos\,[\omega_f t + \phi(t)]}^{\hat{N}_{sc}(t;\omega_f,\phi)}\Big]\Big\}$$

$$- K_1 K_m \Big\{G(p)\Big[\underbrace{N_c(t) \sin\,[\omega_f t + \phi(t)]}_{\hat{N}_{cs}(t;\omega_f,\phi)}\Big]\Big\}\,. \tag{8}$$

Here, the signal $\hat{m}_c(t;\omega_f,\phi)$ is the in-phase signal emerging from passage of the data modulated false lock sinusoid $m(t) \cos\,[\omega_f t + \phi(t)]$ through the lowpass arm filter $G(s)$ and, likewise, $\hat{N}_{sc}(t;\omega_f,\phi)$ and $\hat{N}_{cs}(t;\omega_f,\phi)$ are the equivalently filtered versions of the noise components.

---

*In what follows, we shall write differential equations in compact form by introducing the Heaviside operator, $p \triangleq d/dt$.

The error signal into the loop filter is then given by*

$$
\begin{aligned}
z_0(t) &= z_s(t)\, \varepsilon_c(t) \\
&= K_1^2 K_m^2 \{ S\, m(t)\, \hat{m}_c(t;\omega_f,\phi) \sin(\omega_f t + \phi) \\
&\quad - \hat{N}_{sc}(t;\omega_f,\phi)\, N_c(t) \cos(\omega_f t + \phi) \\
&\quad - \hat{N}_{cs}(t;\omega_f,\phi)\, N_c(t) \cos(\omega_f t + \phi) \\
&\quad - \hat{N}_{sc}(t;\omega_f,\phi) [\sqrt{S}\, m(t) - N_s(t)] \sin(\omega_f t + \phi) \\
&\quad - \hat{N}_{cs}(t;\omega_f,\phi) [\sqrt{S}\, m(t) - N_s(t)] \sin(\omega_f t + \phi) \\
&\quad + \sqrt{S}\, \hat{m}_c(t;\omega_f,\phi) [N_c(t) \cos(\omega_f t + \phi) - N_s(t) \sin(\omega_f t + \phi)] \}
\end{aligned}
\tag{9}
$$

ERROR CONTROL SIGNAL ANALYSIS

Using previously derived results (see equation (14) of Appendix A),

$$
\hat{m}_c(t;\omega_f,\phi) = \sum_{n=-\infty}^{\infty} a_n\, \hat{p}_1(t - nT)\, \frac{e^{j(\omega_f t + \phi)}}{2}
+ \sum_{n=-\infty}^{\infty} a_n\, \hat{p}_2(t - nT)\, \frac{e^{-j(\omega_f t + \phi)}}{2}
$$

$$
m(t) \sin(\omega_f t + \phi) = \sum_{n=-\infty}^{\infty} a_n\, p(t - nT) \left[\frac{e^{j(\omega_f t + \phi)} - e^{-j(\omega_f t + \phi)}}{2j} \right] . \tag{10}
$$

Thus, using (10), the normalized signal component of $z_0(t)$ is

*For convenience in our notation herein, we drop the dependence of ϕ on time.

$$s_0(t) \triangleq m(t)\,\hat{m}_c(t;\omega_f,\phi)\,\sin(\omega_f t+\phi)$$

$$= \sum_{n=-\infty}^{\infty}\sum_{m=-\infty}^{\infty} a_n\,a_m\,\hat{p}_1(t-nT)\,p(t-mT)\left(\frac{e^{2j(\omega_f t+\phi)}-1}{4j}\right)$$

$$+ \sum_{n=-\infty}^{\infty}\sum_{m=-\infty}^{\infty} a_n\,a_m\,\hat{p}_2(t-nT)\,p(t-mT)\left(\frac{1-e^{-2j(\omega_f t+\phi)}}{4j}\right) . \qquad (11)$$

Taking the statistical expectation over the data, and the time average gives

$$\overline{\langle s_0(t)\rangle} = \sum_{n=-\infty}^{\infty}\sum_{m=-\infty}^{\infty} \overline{a_n\,a_m}\left(\frac{e^{j2\phi}}{4j}\right) \lim_{T_0\to\infty}\frac{1}{T_0}\int_{-T_0/2}^{T_0/2} \hat{p}_1(t-nT)\,p(t-mT)\,e^{2j\omega_f t}\,dt$$

$$- \sum_{n=-\infty}^{\infty}\sum_{m=-\infty}^{\infty} \overline{a_n\,a_m}\left(\frac{1}{4j}\right) \lim_{T_0\to\infty}\frac{1}{T_0}\int_{-T_0/2}^{T_0/2} \hat{p}_1(t-nT)\,p(t-mT)\,dt$$

$$+ \sum_{n=-\infty}^{\infty}\sum_{m=-\infty}^{\infty} \overline{a_n\,a_m}\left(\frac{1}{4j}\right) \lim_{T_0\to\infty}\frac{1}{T_0}\int_{-T_0/2}^{T_0/2} \hat{p}_2(t-nT)\,p(t-mT)\,dt$$

$$- \sum_{n=-\infty}^{\infty}\sum_{m=-\infty}^{\infty} \overline{a_n\,a_m}\left(\frac{e^{-j2\phi}}{4j}\right) \lim_{T_0\to\infty}\frac{1}{T_0}\int_{-T_0/2}^{T_0/2} \hat{p}_2(t-nT)\,p(t-mT)\,e^{-2j\omega_f t}\,dt . \qquad (12)$$

Analogous to equations (17) and (18) of Appendix A, we have that

$$\lim_{T_0\to\infty}\frac{1}{T_0}\int_{-T_0/2}^{T_0/2} \hat{p}_1(t-nT)\,p(t-mT)\,e^{2j\omega_f t}\,dt =$$

$$\lim_{T_0\to\infty}\int_{-\infty}^{\infty}\int_{-\infty}^{\infty} G[j(\omega+\omega_f)]\,P(j\omega)\,P(-j\omega')\,\frac{\sin[(\omega-\omega'+2\omega_f)(T_0/2)]}{(\omega-\omega'+2\omega_f)(T_0/2)}$$

$$\times\, e^{-j(\omega n-\omega' m)T}\,\frac{d\omega}{2\pi}\,\frac{d\omega'}{2\pi}$$

and

$$\lim_{T_0\to\infty} \frac{1}{T_0} \int_{-T_0/2}^{T_0/2} \hat{p}_2(t-nT)\, p(t-mT)\, e^{-2j\omega_f t}\, dt =$$

$$\lim_{T_0\to\infty} \int_{-\infty}^{\infty}\int_{-\infty}^{\infty} G[j(\omega-\omega_f)]\, P(j\omega)\, P(-j\omega')\, \frac{\sin[(\omega-\omega'-2\omega_f)(T_0/2)]}{(\omega-\omega'-2\omega_f)(T_0/2)}$$

$$\times\, e^{-j(\omega n-\omega' m)T}\, \frac{d\omega}{2\pi}\, \frac{d\omega'}{2\pi} \quad . \tag{13}$$

For the case of random data wherein

$$\overline{a_n a_m} = \delta_{mn} = \begin{cases} 1 & m = n \\ 0 & m \neq n \end{cases} \tag{14}$$

and recognizing further that

$$\sum_{n=-\infty}^{\infty} e^{-j(\omega-\omega')nT} \doteq \frac{2\pi}{T} \sum_{k=-\infty}^{\infty} \delta\left(\omega-\omega'-\frac{2\pi k}{T}\right) , \tag{15}$$

equation (12) simplifies to

$$\overline{\langle s_0(t)\rangle} = \lim_{T_0\to\infty} \frac{1}{4jT}\left\{ e^{j2\phi} \sum_{k=-\infty}^{\infty} \int_{-\infty}^{\infty} G\left[j\left(\omega' + \omega_f + \frac{2\pi k}{T}\right)\right] P\left[j\left(\omega' + \frac{2\pi k}{T}\right)\right] \right.$$

$$\times P(-j\omega') \frac{\sin\left[\left(\frac{2\pi k}{T} + 2\omega_f\right)(T_0/2)\right]}{\left(\frac{2\pi k}{T} + 2\omega_f\right)(T_0/2)} \frac{d\omega'}{2\pi}$$

$$- e^{-j2\phi} \sum_{k=-\infty}^{\infty} \int_{-\infty}^{\infty} G\left[j\left(\omega' - \omega_f + \frac{2\pi k}{T}\right)\right] P\left[j\left(\omega' + \frac{2\pi k}{T}\right)\right]$$

$$\times P(-j\omega') \frac{\sin\left[\left(\frac{2\pi k}{T} - 2\omega_f\right)(T_0/2)\right]}{\left(\frac{2\pi k}{T} - 2\omega_f\right)(T_0/2)} \frac{d\omega'}{2\pi}$$

$$+ \sum_{k=-\infty}^{\infty} \int_{-\infty}^{\infty} G\left[j\left(\omega' - \omega_f + \frac{2\pi k}{T}\right)\right] P\left[j\left(\omega' + \frac{2\pi k}{T}\right)\right]$$

$$\times P(-j\omega') \frac{\sin\left[\frac{2\pi k}{T}(T_0/2)\right]}{\frac{2\pi k}{T}(T_0/2)} \frac{d\omega'}{2\pi}$$

$$- \sum_{k=-\infty}^{\infty} \int_{-\infty}^{\infty} G\left[j\left(\omega' + \omega_f + \frac{2\pi k}{T}\right)\right] P\left[j\left(\omega' + \frac{2\pi k}{T}\right)\right]$$

$$\left. \times P(-j\omega') \frac{\sin\left[\frac{2\pi k}{T}(T_0/2)\right]}{\frac{2\pi k}{T}(T_0/2)} \frac{d\omega'}{2\pi} \right\} \qquad (16)$$

Now suppose that $2\omega_f = (2\pi k_0)/T$, where $k_0 = 0,1,2,\ldots$ is a particular value of k. Then, the value of $\overline{\langle s_0(t)\rangle}$, namely, $\mathscr{A}_{k_0}(\phi)$, at this frequency is given by

$$\mathcal{S}_{k_0}(\phi) \triangleq \overline{\langle s_0(t)\rangle}\Big|_{\omega_f=\frac{\pi k_0}{T}} = \frac{1}{4jT}\left\{e^{j2\phi}\int_{-\infty}^{\infty} G[j(\omega'-\frac{\pi k_0}{T})]\right.$$

$$\times P[j(\omega'-\frac{2\pi k_0}{T})]P(-j\omega')\,\frac{d\omega'}{2\pi}$$

$$- e^{-j2\phi}\int_{-\infty}^{\infty} G[j(\omega'+\frac{\pi k_0}{T})$$

$$\times P[j(\omega'+\frac{2\pi k_0}{T})]\,P(-j\omega')\,\frac{d\omega'}{2\pi}$$

$$+\int_{-\infty}^{\infty} G[j(\omega'-\frac{\pi k_0}{T})]\;|P(j\omega')|^2\,\frac{d\omega'}{2\pi}$$

$$\left.-\int_{-\infty}^{\infty} G[j(\omega'+\frac{\pi k_0}{T})]\;|P(j\omega')|^2\,\frac{d\omega'}{2\pi}\right\}, \qquad (17)$$

or, equivalently,

$$\boxed{\begin{aligned}\mathcal{S}_{k_0}(\phi) &= \frac{1}{2T}\left\{\mathrm{Im}\left\{e^{j2\phi}\int_{-\infty}^{\infty} G(j\omega)\;P[j(\omega-\frac{\pi k_0}{T})]\;P[-j(\omega+\frac{\pi k_0}{T})]\,\frac{d\omega}{2\pi}\right\}\right.\\ &\qquad\left.+\;\mathrm{Im}\left\{\int_{-\infty}^{\infty} G(j\omega)\;\left|P[j(\omega+\frac{\pi k_0}{T})]\right|^2\,\frac{d\omega}{2\pi}\right\}\right\}\\ &= U_{k_0}(\phi)+W_{k_0}\;; \qquad k_0 = 0,1,2,3,\ldots\end{aligned}} \qquad (18)$$

where Im { } denotes the imaginary part of what is contained within the braces. Note that, for the case of true lock (i.e., $\omega_f = 0$), we get

$$\mathcal{S}_0(\phi) = U_0(\phi) = \frac{\sin 2\phi}{2}\left[\frac{1}{T}\int_{-\infty}^{\infty}\mathrm{Re}\;\{G(j\omega)\}\,|P(j\omega)|^2\,\frac{d\omega}{2\pi}\right]$$

or

$$\boxed{\mathcal{S}_0(\phi) = \frac{\sin 2\phi}{2}\int_{-\infty}^{\infty} S_m(\omega)\;\mathrm{Re}\;\{G(j\omega)\}\,\frac{d\omega}{2\pi}} \qquad (19)$$

where $S_m(\omega) = 1/T\ |P(j\omega)|^2$ is the power spectral density of the modulation $m(t)$ and we have also used the fact that Im $\{G(j\omega)\}$ is an odd function of frequency for any real filter. What is important about this latter fact is that $W_0 = 0$, i.e., for true lock, the error control characteristic (loop S-curve) as specified by (19) does not possess a dc component and is thus symmetric about the lock points at 0°, 180°, 360°, ... Furthermore, comparing (19) and equation (24) of Appendix A with cos 2ϕ replaced by (sin 2ϕ)/2, we observe that the effect of removing the quadrature arm filter is to replace $|G(j\omega)|^2$ by Re $\{G(j\omega)\}$. As we shall see shortly, this simple replacement follows through in the noise analysis.

Returning to equation (18), we have now verified part of a statement made in the introduction, namely, that in the false lock mode, a dc voltage, namely, W_{k_0}, exists at the error control point in addition to the sinusoidal restoring force normally present there. It now behooves us to evaluate the magnitude of this dc voltage relative to the amplitude of the sinusoidal error component to determine to what extent the false lock sensitivity of the loop has been reduced.

FALSE LOCK PERFORMANCE

As was done in Appendix A, we shall consider a specific example to illustrate the general theory, namely, the case where $m(t)$ is a Manchester coded data modulation and $G(s)$ is a single pole RC filter for which

$$G(j\omega) = \frac{1}{1 + \frac{j\omega}{\omega_c}} \tag{20}$$

where $\omega_c = 2\pi f_c$ is the radian 3 dB cutoff frequency of the filter. We note from (20) that

$$\text{Re}\{G(j\omega)\} = |G(j\omega)|^2 = \frac{1}{1 + (\frac{\omega}{\omega_c})^2} \quad . \tag{21}$$

Thus, the first term in (18), namely, $U_{k_0}(\phi)$ is identical to equations (28) through (31) of Appendix A when $\cos 2\phi$ is replaced by $(\sin 2\phi)/2$, i.e.,

$$U_0(\phi) = \frac{\sin 2\phi}{2}\left\{1 - \frac{1}{2\pi f_c T}\left[3 - 4e^{-\pi f_c T} + e^{-2\pi f_c T}\right]\right\}$$

$$U_k(\phi) = -\frac{\sin 2\phi}{2}\left\{\left[\frac{1}{1 + (\frac{k}{2f_c T})^2}\right]\left[\frac{1 + e^{-2\pi f_c T}}{2\pi f_c T}\right]\right\};\ k = 1,3,5,\ldots$$

$$U_k(\phi) = -\frac{\sin 2\phi}{2}\left\{\left[\frac{1}{1 + (\frac{k}{2f_c T})^2}\right]\left[\frac{3 + 4e^{-\pi f_c T} + e^{-2\pi f_c T}}{2\pi f_c T}\right]\right\};$$

$$k = 2,6,10,\ldots$$

$$U_k(\phi) = -\frac{\sin 2\phi}{2}\left\{\left[\frac{1}{1 + (\frac{k}{2f_c T})^2}\right]\left[\frac{3 - 4e^{-\pi f_c T} + e^{-2\pi f_c T}}{2\pi f_c T}\right]\right\};$$

$$k = 4,8,12,\ldots \tag{22}$$

Writing $U_k(\phi)$ as $\mu_k \sin 2\phi$, Figure 3 is a plot of $|\mu_k|$ (in dB), $k = 0,1,2,3,4$, versus $f_c T$ for the above example. Note this plot is identical to Figure 2 of Appendix A except for a vertical displacement of 3 dB. We now turn to an evaluation of W_k.

From (20) and (18), we get

$$W_k = -\int_{-\infty}^{\infty} \frac{(\omega/\omega_c)}{1 + (\omega/\omega_c)^2} |P[j(\omega + \frac{\pi k}{T})]|^2 \frac{d\omega}{2\pi} \quad . \tag{23}$$

For a Manchester pulse, with Fourier transform,

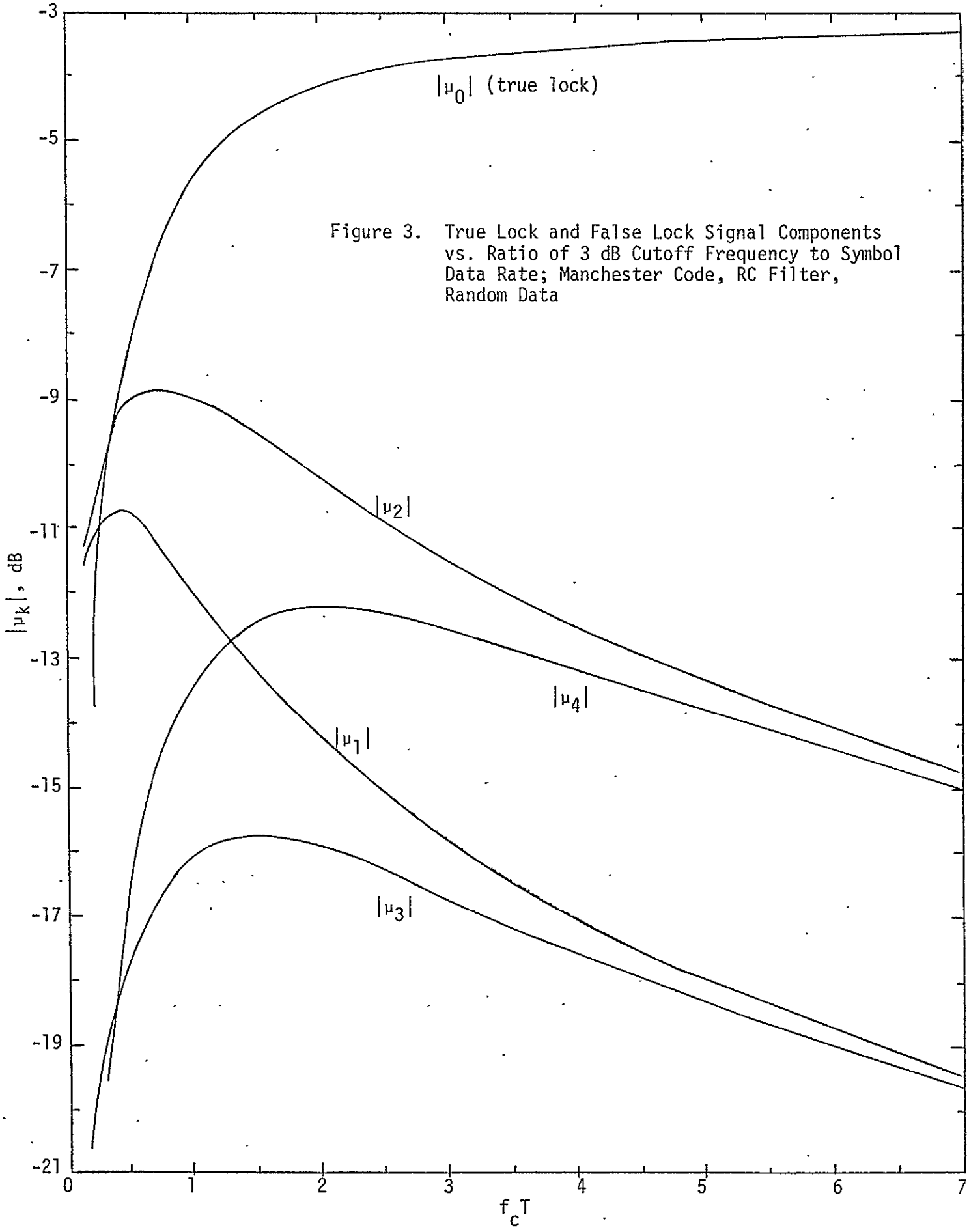

Figure 3. True Lock and False Lock Signal Components vs. Ratio of 3 dB Cutoff Frequency to Symbol Data Rate; Manchester Code, RC Filter, Random Data

$$P(j\omega) = jT\left[\frac{\sin^2\frac{\omega T}{4}}{\frac{\omega T}{4}}\right], \tag{24}$$

we have that

$$|P[j(\omega + \tfrac{\pi k}{T})]|^2 = T^2\left[\frac{\sin^4\left(\frac{\omega T + \pi k}{4}\right)}{\left(\frac{\omega T + \pi k}{4}\right)^2}\right]. \tag{25}$$

Substituting (25) and making the change of variables $x = \omega T$ gives

$$W_k = \frac{1}{4\pi}\int_{-\infty}^{\infty} \frac{\frac{x}{\omega_c T}}{1 + \left(\frac{x}{\omega_c T}\right)^2}\left[\frac{\sin^4\left(\frac{x - \pi k}{4}\right)}{\left(\frac{x - \pi k}{4}\right)^2}\right] dx . \tag{26}$$

Evaluation of W_k as given by (26) requires considerable algebraic manipulation and integral evaluations. The results are as follows:

$$W_k = \left[\frac{1}{1 + \left(\frac{k}{2f_cT}\right)^2}\right]\left\{\frac{1}{2}\left(\frac{k}{2f_cT}\right) - 3\left(\frac{k}{2f_cT}\right)\left(\frac{1}{2\pi f_cT}\right)\left[\frac{1}{1 + \left(\frac{k}{2f_cT}\right)^2}\right]\right.$$

$$+ 2\left(\frac{1}{2\pi f_cT}\right)(-1)^{(k-1)/2}\left[\frac{1 - \left(\frac{k}{2f_cT}\right)^2}{1 + \left(\frac{k}{2f_cT}\right)^2}\right] e^{-\pi f_cT}$$

$$\left. + \left(\frac{k}{2f_cT}\right)\left(\frac{1}{2\pi f_cT}\right)\left[\frac{1}{1 + \left(\frac{k}{2f_cT}\right)^2}\right] e^{-2\pi f_cT}\right\} ;$$

$$k = 1,3,5,7,\ldots$$

$$W_k = \left[\frac{\frac{k}{2f_cT}}{1 + \left(\frac{k}{2f_cT}\right)^2}\right]\left\{\frac{1}{2} - \left(\frac{1}{2\pi f_cT}\right)\left[\frac{1}{1 + \left(\frac{k}{2f_cT}\right)^2}\right]\left(3 + 4e^{-\pi f_cT} + e^{-2\pi f_cT}\right)\right\} ;$$

$$k = 2,6,10,\ldots$$

$$W_k = \left[\frac{\frac{k}{2f_cT}}{1+\left(\frac{k}{2f_cT}\right)^2}\right]\left\{\frac{1}{2} - \left(\frac{1}{2\pi f_cT}\right)\left[\frac{1}{1+\left(\frac{k}{2f_cT}\right)^2}\right]\left(3 - 4e^{-\pi f_cT} + e^{-2\pi f_cT}\right)\right\}; \quad k = 4,8,12,\ldots \tag{27}$$

Figure 4 is a plot of W_k (in dB), $k = 1,2,3,4$, as determined from (27) versus f_cT. If the value of f_cT is fixed at 1.4 (i.e., the optimum in-phase arm filter bandwidth in the sense of minimum squaring loss), then one can plot the error control characteristic of (18) using (18) together with (22) and (27). In particular, Figure 5 plots $\mathscr{S}_1(\phi) \triangleq \mu_1 \sin 2\phi + W_1$ versus ϕ for this case. This corresponds to the situation that exists at the <u>first</u> false lock frequency away from the carrier, i.e., $f_f = 1/2T$. Also plotted in Figure 5 is the same result for the conventional Costas loop with identical RC arm filter whose bandwidths are optimized as above. This result is merely $\mathscr{S}_1(\phi) = \mu_1 \sin 2\phi$. We observe from this figure that removal of the quadrature arm filter from the conventional Costas loop has theoretically <u>eliminated</u> the possibility of false lock at the frequency $f_f = 1/2T$.

TRUE LOCK NOISE AND TRACKING PERFORMANCE

Having thus far concluded that the modified Costas loop offers superior acquisition and false lock performance relative to the conventional Costas loop, what remains is to determine the penalty paid in true lock tracking performance. To do this, we begin, as in previous analyses of this type, with a statistical characterization of the noise process at the input to the loop filter. From (9), the normalized noise component of $z_0(t)$ is (assuming $\omega_f = 0$)

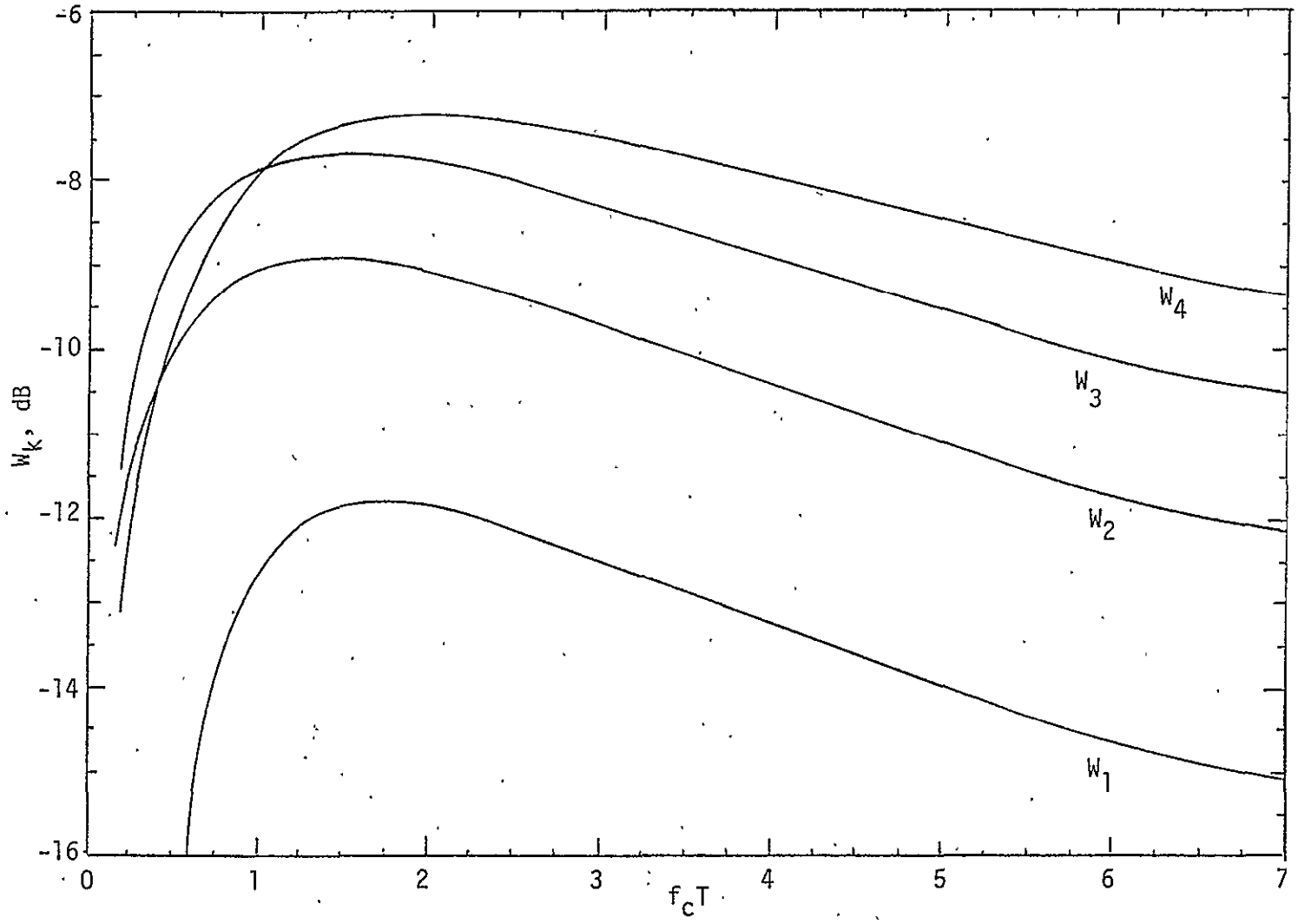

Figure 4. DC Signal Component at Error Control Point vs. Ratio of 3 dB Cutoff Frequency to Symbol Data; Manchester Code, RC Filter, Random Data

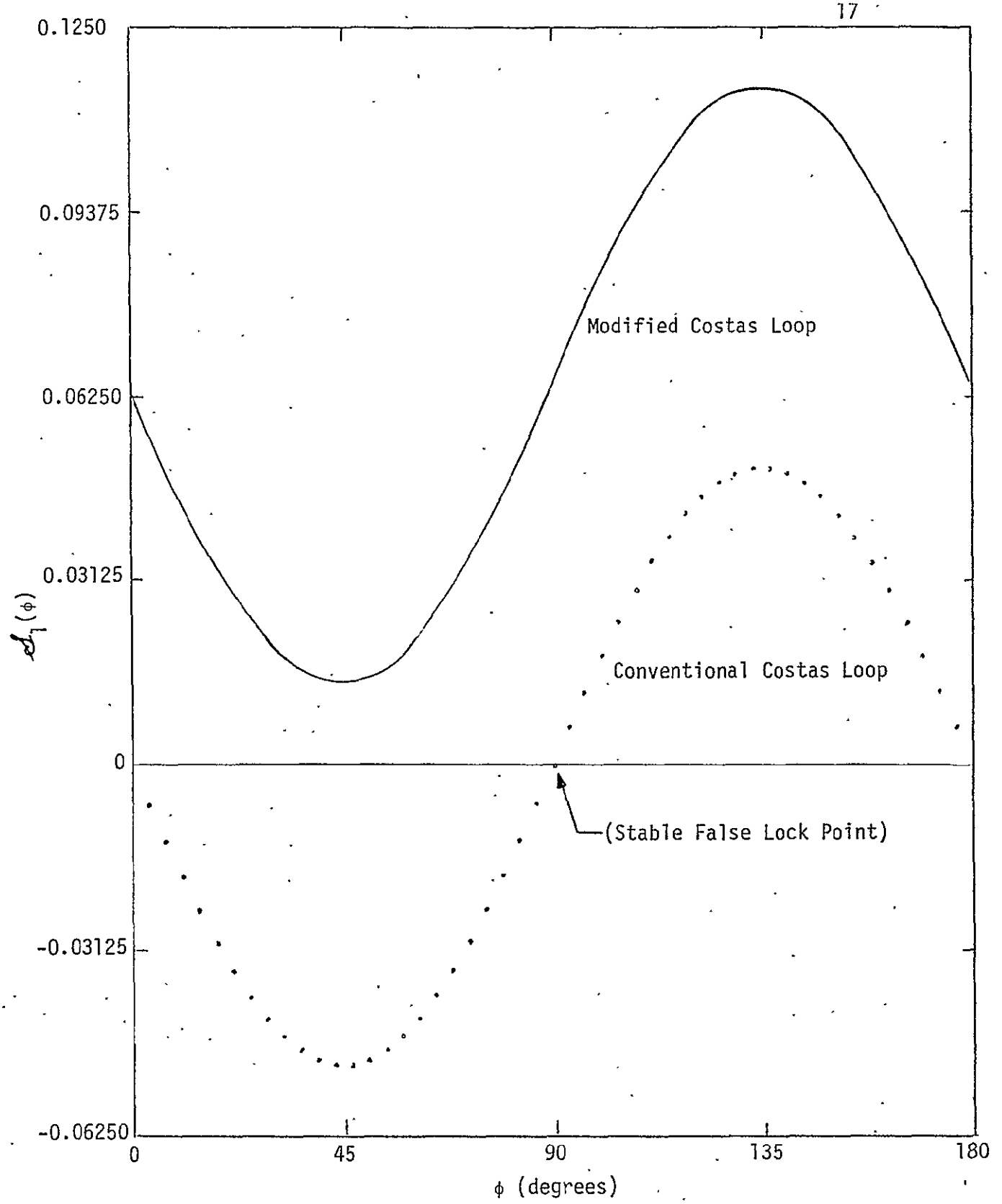

Figure 5. False Lock Error Characteristic for Modified and Conventional Costas Loops; Manchester Code, RC Filter, Random Data; $f_c T = 1.4$

$$v_2[t,2\phi] = [-N_c(t)\,\hat{N}_c(t) + N_s(t)\,\hat{N}_s(t) - \sqrt{S}\,m(t)\,\hat{N}_s(t) - \sqrt{S}\,\hat{m}(t)\,N_s(t)]\sin 2\phi$$
$$+ [\sqrt{S}\,m(t)\,\hat{N}_c(t) + \sqrt{S}\,\hat{m}(t)\,N_c(t) - \hat{N}_c(t)\,N_s(t) - N_c(t)\,\hat{N}_s(t)]\cos 2\phi$$
$$+ [\sqrt{S}\,\hat{m}(t)\,N_c(t) - \sqrt{S}\,m(t)\,\hat{N}_c(t) + N_s(t)\,\hat{N}_c(t) - \hat{N}_s(t)\,N_c(t)] \quad , \qquad (28)$$

where we have made use of the fact that, for $\omega_f = 0$,

$$\hat{N}_{sc}(t;\omega_f,\phi) = \hat{N}_s(t)\cos\phi \qquad \hat{N}_s(t) = G(p)\,N_s(t)$$
$$\hat{N}_{cs}(t;\omega_f,\phi) = \hat{N}_c(t)\sin\phi \qquad \hat{N}_c(t) = G(p)\,N_c(t)$$
$$\hat{m}_c(t;\omega_f,\phi) = \hat{m}(t)\cos\phi \qquad (29)$$

Since the bandwidth of the Costas loop is ordinarily designed to be narrow with respect to the equivalent noise bandwidth of $v_2(t,2\phi)$, we can approximate $v_2(t,2\phi)$ as a delta correlated process with equivalent single-sided noise spectral density

$$N_{sq} \triangleq 2\int_{-\infty}^{\infty} R_{v_2}(\tau)\,d\tau \quad , \qquad (30)$$

where

$$R_{v_2}(\tau) \triangleq \overline{v_2(t,2\phi)\,v_2(t+\tau,2\phi)} \quad . \qquad (31)$$

With $v_2(t,2\phi)$ as functionally defined in (28), it is relatively straightforward to show (analogous to Appendix A of Reference 4, Chapter 2) that

$$R_{v_2}(\tau) = 4R_N(\tau)R_{\hat{N}}(\tau) + 2S[R_m(\tau)R_{\hat{N}}(\tau) + R_{\hat{m}}(\tau)R_N(\tau)]$$
$$+ 2S[R_{\hat{m}}(\tau)R_N(\tau) - R_m(\tau)R_{\hat{N}}(\tau)]\cos 2\phi \quad , \qquad (32)$$

where

$$R_m(\tau) = \int_{-\infty}^{\infty} S_m(f)\,e^{j2\pi f\tau}\,df$$

$$R_{\hat{m}}(\tau) = \int_{-\infty}^{\infty} S_m(f) \, |G(j2\pi f)|^2 \, e^{j2\pi f\tau} \, df$$

$$R_N(\tau) \cong \frac{N_0}{2} \delta(\tau)$$

$$R_{\hat{N}}(\tau) = \frac{N_0}{2} \int_{-\infty}^{\infty} |G(j2\pi f)|^2 \, e^{j2\pi f\tau} \, df \tag{33}$$

Substituting (32) along with (33) into (30) gives

$$N_{sq} = 4 S N_0 \left[\left(\frac{N_0}{2S} \right) \int_{-\infty}^{\infty} |G(j2\pi f)|^2 \, df + \int_{-\infty}^{\infty} S_m(f) \, |G(j2\pi f)|^2 \, df \right] \tag{34}$$

or

$$N_{sq} = 4 S N_0 \left[\frac{N_0 B_i}{2S} + D_m \right] , \tag{35}$$

where

$$D_m \triangleq \int_{-\infty}^{\infty} S_m(f) \, |G(j2\pi f)|^2 \, df \tag{36}$$

and the two-sided noise bandwidth of $G(j\omega)$ is given by

$$B_i \triangleq \int_{-\infty}^{\infty} |G(j2\pi f)|^2 \, df . \tag{37}$$

In the linear region of operation, the mean-squared tracking jitter of a Costas loop has the well-known form (References 2 and 4)

$$\sigma_{2\phi}^2 = \frac{4}{\rho \mathcal{S}_L} \tag{38}$$

where*

ρ = equivalent loop signal-to-noise ratio in the loop bandwidth of a phase-locked loop = $2S/N_0 B_L$

$\mathcal{S}_L$ = loop squaring loss = $\dfrac{4 S N_0 D_m^2}{N_{sq}}$. (39)

*The expression for $\mathcal{S}_L$ in (39) is approximate in that the self-noise of the modulation process is ignored. This is shown in Reference 2 to yield negligible error.

and

$$D_m \triangleq \int_{-\infty}^{\infty} S_m(f)\ \mathrm{Re}\ \{G(j2\pi f)\}\ df\ . \tag{40}$$

Substituting (35) in (39) gives

$$S_L = \frac{D_m^2/D_m}{1 + \frac{1}{\rho_i D_m}}, \tag{41}$$

where $\rho_i \triangleq 2S/N_0B_i$ is the signal-to-noise ratio in the in-phase arm filter bandwidth. Alternately, in terms of the data (symbol) signal-to-noise ratio $R_d = ST/N_0$ and the ratio of two-sided arm filter bandwidth to data rate B_i/R_s ($R_s = 1/T$), equation (41) can be rewritten as

$$S_L = \frac{D_m^2/D_m}{1 + \frac{B_i/R_s}{2R_dD_m}}\ . \tag{42}$$

Comparing (36) and (40), we observe that, if $\mathrm{Re}\ \{G(j2\pi f)\} = |G(j2\pi f)|^2$ (such is the case for an RC filter), then $D_m = D_m$ and (42) simplifies to

$$S_L = \frac{D_m}{1 + \frac{B_i/R_s}{2R_dD_m}}\ . \tag{43}$$

For ρ_i small (the usual case of interest), we see by comparing (43) with equation (46) of Reference 2, and making use of (38), that

$$\frac{\sigma^2_{2\phi}\big|_{\text{modified loop}}}{\sigma^2_{2\phi}\big|_{\text{conventional loop}}} \cong \frac{1}{K_L} = 2\ . \tag{44}$$

Thus, complete removal of the quadrature RC arm filter results in approximately a 3 dB penalty in tracking performance. This is the price paid for

improved acquisition and false lock performance. As ρ_i is increased, the tracking performance difference between the two loops diminishes.

THE CASE OF ALTERNATING DATA

By analogy with the development leading to the result presented in Appendix B (in particular, equations [8] through [11]), one can readily show that, for the case of alternating data, equation (18) is replaced by

$$\mathcal{J}_{k_0}(\phi) = \frac{1}{2T^2}\left[\mathrm{Im}\left\{e^{j2\phi}\sum_{k=-\infty}^{\infty}\left|G\left(j\,\frac{2\pi k}{T}\right)\right|^2 P\left[j\left(\frac{2\pi k}{T}-\frac{\pi k_0}{T}\right)\right]P\left[-j\left(\frac{2\pi k}{T}+\frac{\pi k_0}{T}\right)\right]\right\}\right.$$
$$\left. + \mathrm{Im}\left\{\sum_{k=-\infty}^{\infty} G\left(j\,\frac{2\pi k}{T}\right)\left|P\left[j\left(\frac{2\pi k}{T}+\frac{\pi k_0}{T}\right)\right]\right|^2\right\}\right] \quad \text{for } k_0 \text{ odd} \tag{45}$$

and

$$\mathcal{J}_{k_0}(\phi) = \frac{1}{2T^2}\left[\mathrm{Im}\left\{e^{j2\phi}\sum_{k=-\infty}^{\infty}\left|G\left[j\,\frac{\pi}{T}(2k-1)\right]\right|^2 P\left[j\left(\frac{\pi}{T}(2k-1)-\frac{\pi k_0}{T}\right)\right]\right.\right.$$
$$\left.\times P\left[-j\left(\frac{\pi}{T}(2k-1)+\frac{\pi k_0}{T}\right)\right]\right\}$$
$$\left. + \mathrm{Im}\left\{\sum_{k=-\infty}^{\infty} G\left[j\,\frac{\pi}{T}(2k-1)\right]\left|P\left[j\left(\frac{\pi}{T}(2k-1)+\frac{\pi k_0}{T}\right)\right]\right|^2\right\}\right]$$
$$\text{for } k_0 \text{ even}. \tag{46}$$

Evaluating (45) and (46) for the Manchester code, RC filter case yields the following results

$$\mathcal{J}_k(\phi) = U_k(\phi) + W_k$$
$$= \left(\frac{\sin 2\phi}{2}\right)\left\{1 - \frac{1}{\pi f_c T}\tanh \pi f_c T\right\}; \qquad k = 0$$

$$\mathcal{S}_k(\phi) = U_k(\phi) + W_k$$

$$= -\left(\frac{\sin 2\phi}{2}\right)\left(\frac{1}{\pi f_c T}\right)\left[\frac{1}{1+\left(\frac{k}{2f_cT}\right)^2}\right]\coth \pi f_c T$$

$$+\frac{\left(\frac{k}{2f_cT}\right)}{1+\left(\frac{k}{2f_cT}\right)^2}\left\{\frac{1}{2}-\left(\frac{1}{\pi f_c T}\right)\left[\frac{1}{1+\left(\frac{k}{2f_cT}\right)^2}\right]\coth \pi f_c T\right\};\quad k=1,3,5,\ldots$$

$$\mathcal{S}_k(\phi) = U_k(\phi) + W_k$$

$$= -\left(\frac{\sin 2\phi}{2}\right)\left(\frac{1}{\pi f_c T}\right)\left[\frac{1}{1+\left(\frac{k}{2f_cT}\right)^2}\right]\tanh \pi f_c T$$

$$+\frac{\left(\frac{k}{2f_cT}\right)}{1+\left(\frac{k}{2f_cT}\right)^2}\left\{\frac{1}{2}-\left(\frac{1}{\pi f_c T}\right)\left[\frac{1}{1+\left(\frac{k}{2f_cT}\right)^2}\right]\tanh \pi f_c T\right\};$$

$$k=2,4,6,\ldots \qquad (47)$$

The first terms, i.e., $U_k(\phi)$, in (47) are obtained from equation (15) of Appendix B. The latter terms again represent the additional dc voltage present at the error control point in the loop, in addition to the sinusoidal restoring force. For the true lock case, i.e., $k=0$, this dc term is absent as was true for random data; whereas, for the false lock situation, its value is of an order of magnitude necessary to significantly reduce the false lock sensitivity of the loop (see, for example, Figure 6).

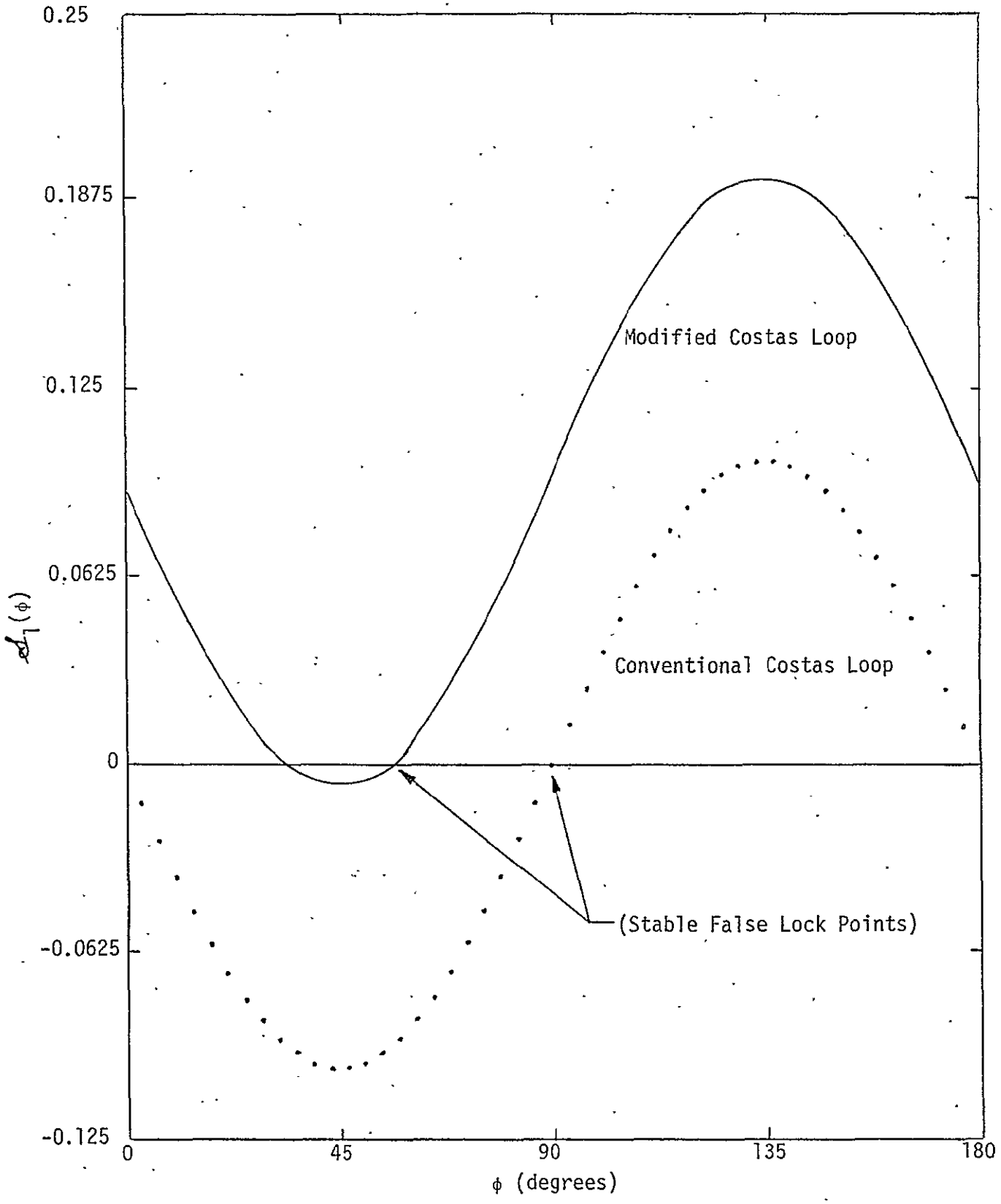

Figure 6. False Lock Error Characteristic for Modified and Conventional Costas Loops; Manchester Code, RC Filter, Alternating Data; $f_cT = 1.4$

REFERENCES

1. Cahn, C. R. "Improving Frequency Acquisition of a Costas Loop," accepted for publication in the IEEE Transactions on Communications.

2. Simon, M. K., and Lindsey, W. C. "Optimum Performance of Suppressed Carrier Receivers with Costas Loop Tracking," IEEE Transactions on Communications, Vol. COM-25, No. 2, February 1977, pp. 215-227.

3. Lindsey, W. C., and Simon, M. K. "Optimum Performance of Costas Receivers Containing Soft Bandpass Limiters," to appear in a special issue on Spread Spectrum Communications of the IEEE Transactions on Communications.

4. Lindsey, W. C., and Simon, M. K. Telecommunication Systems Engineering, Prentice-Hall, Inc., Englewood Cliffs, N.J., 1973.

APPENDIX D

FALSE LOCK AND TRACKING PERFORMANCE OF A COMPOSITE AFC/COSTAS LOOP

APPENDIX D

FALSE LOCK AND TRACKING PERFORMANCE OF A COMPOSITE AFC/COSTAS LOOP

Marvin K. Simon

INTRODUCTION

Appendixes A, B, and C studied the false lock problem in conventional Costas loops with both random and alternating data, and the false lock and tracking performance of a modified Costas loop [1] in which the quadrature arm filter is absent. In this appendix, we examine the false lock and tracking performance tradeoffs of the more general composite AFC/Costas loop configuration suggested by Cahn [1]. It is shown herein that, for single pole (RC) Butterworth arm filters which are shared in common between the AFC and Costas loop portions of the overall hybrid configuration, the tracking and false lock performances are identical to those of the modified Costas loop (Appendix C). The composite AFC/Costas loop has the advantage, however, of being a balanced configuration and, further, the degree of tradeoff between tracking performance degradation and false lock performance improvement is continuously variable depending on the relative gains of the two error signal components.

SYSTEM MODEL

Consider the composite AFC/Costas loop illustrated in Figure 1. The error signal into the loop filter has two components, one due to the conventional Costas loop denoted by $z_0(t)$ and the other produced by the AFC portion and denoted by $w_0(t)$. The behavior of $z_0(t)$ for both the true lock and false lock modes of operation is well documented in Reference 2 and Appendix C, respectively. Briefly reviewing these results, we have for true lock that

$$z_0(t) = \frac{K_1^2 K_m^2}{2} \left\{ [\sqrt{S}\hat{m}(t) - \hat{N}_s(t)]^2 - \hat{N}_c^2(t) \right\} \sin 2\phi(t)$$
$$+ K_1^2 K_m^2 \hat{N}_c(t) [\sqrt{S}\hat{m}(t) - \hat{N}_s(t)] \cos 2\phi(t) , \quad (1)$$

whereas for the false lock mode, the signal component of $z_0(t)$ is

$$z_0(t)\Big|_{\substack{\text{signal}\\\text{only}}} = K_1^2 K_m^2 S \hat{m}_s(t;\omega_f,\phi)\, \hat{m}_c(t;\omega_f,\phi) . \quad (2)$$

On the other hand, the corresponding behavior of $w_0(t)$ has been studied only in part in Appendix C. Following the approach given there, we get that, for true lock,

$$w_0(t) \triangleq z_s(t)\varepsilon_c(t) - z_c(t)\varepsilon_s(t)$$
$$= K_1^2 K_m^2 \{N_c(t) [\sqrt{S}\hat{m}(t) - \hat{N}_s(t)]$$
$$- \hat{N}_c(t) [\sqrt{S}m(t) - N_s(t)]\} . \quad (3)$$

Note the lack of dependence of $w_0(t)$ on the phase error $\phi(t)$. In the false lock mode, the signal component of $w_0(t)$ is

$$w_0(t)\Big|_{\substack{\text{signal}\\\text{only}}} = K_1^2 K_m^2 S \{m(t)\, \hat{m}_c(t;\omega_f,\phi) \sin(\omega_f t + \phi)$$
$$- m(t)\, \hat{m}_s(t;\omega_f,\phi) \cos(\omega_f t + \phi)\} . \quad (4)$$

Finally, the total error signal $u(t)$ is, from Figure 1,

$$u(t) = z_0(t) + \frac{1}{2} w_0(t) . \quad (5)$$

The factor of one-half in (5) or, equivalently, the 3 dB loss following $w_0(t)$ in Figure 1, is arbitrarily chosen here to allow a direct comparison with the results obtained for the modified Costas loop (Appendix C). The latter,

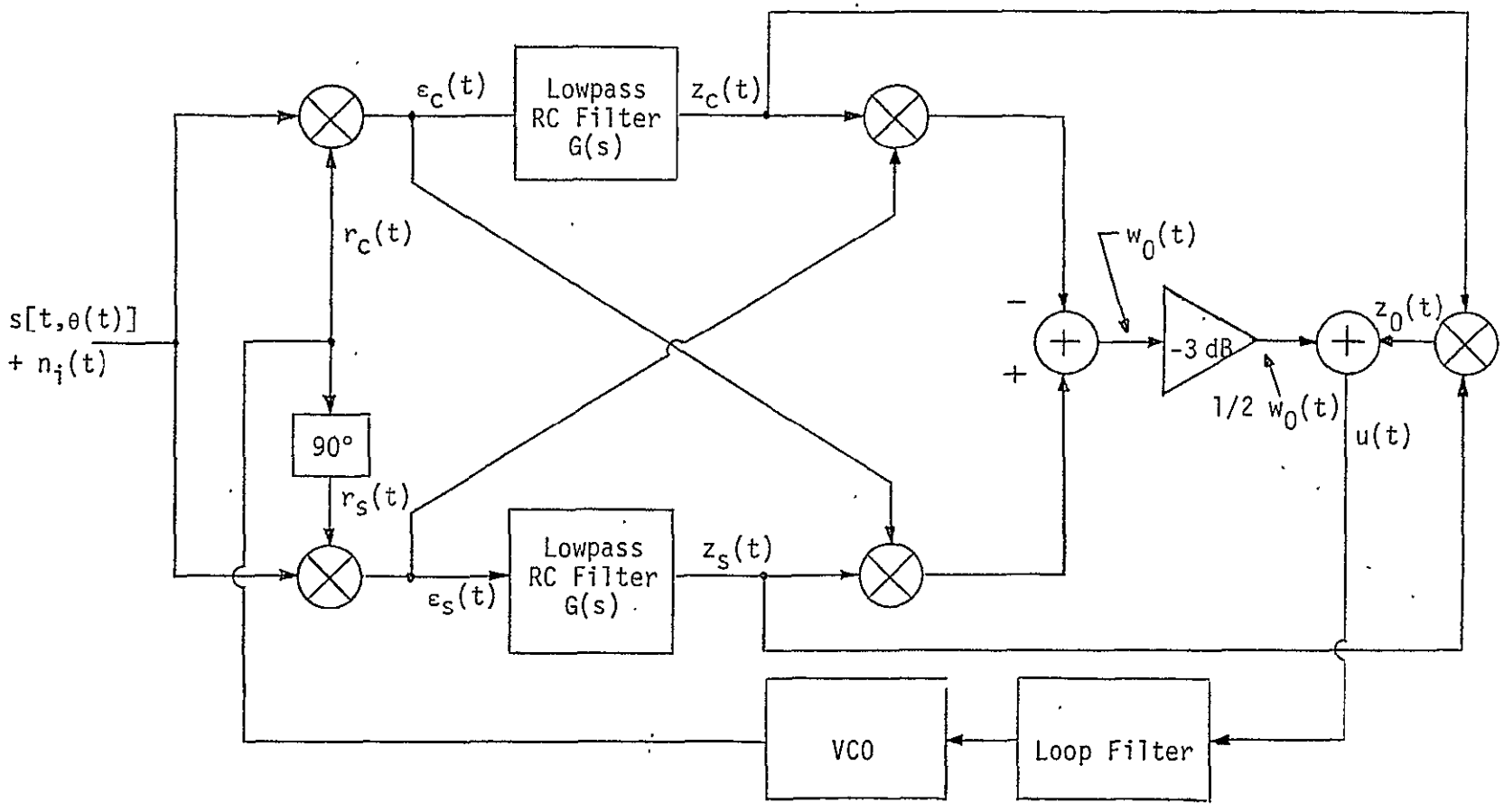

Figure 1. A Composite AFC/Costas Loop

in effect, employs one-half of the AFC portion of the composite loop of Figure 1. Substituting (1) and (3) into (5) gives

$$u(t) = \frac{K_1^2 K_m^2}{2} \{S \hat{m}^2(t) \sin 2\phi + v_2(t,2\phi)\}, \tag{6}$$

where

$$\begin{aligned} v_2(t,2\phi) = {} & [-\hat{N}_c^2(t) + \hat{N}_s^2(t) - 2\sqrt{S}\hat{m}(t)\hat{N}_s(t)] \sin 2\phi \\ & + [2\sqrt{S}\hat{m}(t)\hat{N}_c(t) - 2\hat{N}_c(t)\hat{N}_s(t)] \cos 2\phi \\ & + \sqrt{S}\hat{m}(t)N_c(t) - N_c(t)\hat{N}_s(t) \\ & - \sqrt{S}m(t)\hat{N}_c(t) + \hat{N}_c(t)N_s(t) . \end{aligned} \tag{7}$$

As before, we are interested in the autocorrelation function $R_{v_2}(\tau,2\phi)$ of $v_2(t,2\phi)$. Following an approach similar to that used in Reference 2, we obtain

$$\begin{aligned} R_{v_2}(\tau,2\phi) \triangleq {} & \overline{v_2(t,2\phi)\, v_2(t+\tau,2\phi)} \\ = {} & 4S R_{\hat{m}}(\tau) R_{\hat{N}}(\tau) + 4 R_{\hat{N}}^2(\tau) \\ & + S R_{\hat{m}}(\tau) R_N(\tau) + S R_m(\tau) R_{\hat{N}}(\tau) \\ & - S R_{m\hat{m}}(-\tau) R_{N\hat{N}}(\tau) - S R_{m\hat{m}}(\tau) R_{N\hat{N}}(-\tau) \\ & + 2 R_N(\tau) R_{\hat{N}}(\tau) - 2 R_{N\hat{N}}(\tau) R_{N\hat{N}}(-\tau) \\ & + 2 [S R_{\hat{m}}(\tau) R_{N\hat{N}}(-\tau) - S R_{m\hat{m}}(-\tau) R_{\hat{N}}(\tau) \\ & + S R_{\hat{m}}(\tau) R_{N\hat{N}}(\tau) - S R_{m\hat{m}}(\tau) R_{\hat{N}}(\tau)] \cos 2\phi , \end{aligned} \tag{8}$$

where

$$R_{\hat{m}}(\tau) = \int_{-\infty}^{\infty} S_m(f) |G(j2\pi f)|^2 e^{j2\pi f\tau} \, df$$

$$
\begin{aligned}
R_{\hat{N}}(\tau) &= \frac{N_0}{2} \int_{-\infty}^{\infty} |G(j2\pi f)|^2 \, e^{-j2\pi f\tau} \, df \\
R_{N}(\tau) &\cong \frac{N_0}{2} \, \delta(\tau) \\
R_{N\hat{N}}(\tau) &= \frac{N_0}{2} \int_{-\infty}^{\infty} G(j2\pi f) \, e^{j2\pi f\tau} \, df \\
R_{m\hat{m}}(\tau) &= \int_{-\infty}^{\infty} S_m(f) \, G(j2\pi f) \, e^{j2\pi f\tau} \, df \, . \qquad (9)
\end{aligned}
$$

The equivalent single-sided noise spectral density, N_{sq}, of the delta correlated process $v_2(t,2\phi)$ is then

$$
N_{sq} \triangleq 2 \int_{-\infty}^{\infty} R_{v_2}(\tau,2\phi) \, d\tau \, . \qquad (10)
$$

Substituting (8) into (10) and making use of (9), we obtain, after much simplification,

$$
\begin{aligned}
N_{sq} &= 8 \, S\left(\frac{N_0}{2}\right) \int_{-\infty}^{\infty} S_m(f) \, |G(j2\pi f)|^4 \, df \\
&\quad + 8\left(\frac{N_0}{2}\right)^2 \int_{-\infty}^{\infty} |G(j2\pi f)|^4 \, df \\
&\quad + 8\left(\frac{N_0}{2}\right)^2 \int_{-\infty}^{\infty} [\mathrm{Im}\,\{G(j2\pi f)\}]^2 \, df \\
&\quad + 8 \, S\left(\frac{N_0}{2}\right) \int_{-\infty}^{\infty} S_m(f) \, [\mathrm{Im}\,\{G(j2\pi f)\}]^2 \, df \, . \qquad (11)
\end{aligned}
$$

In arriving at (11), we have evaluated the following integrals:

$$
\int_{-\infty}^{\infty} R_{\hat{N}}^2(\tau) \, d\tau = \left(\frac{N_0}{2}\right)^2 \int_{-\infty}^{\infty} |G(j2\pi f)|^4 \, df
$$

$$
\int_{-\infty}^{\infty} R_{N\hat{N}}(\tau) \, R_{N\hat{N}}(-\tau) \, d\tau = \left(\frac{N_0}{2}\right)^2 \int_{-\infty}^{\infty} \left\{[\mathrm{Re}\,\{G(j2\pi f)\}]^2 - [\mathrm{Im}\,\{G(j2\pi f)\}]^2\right\} df
$$

$$\int_{-\infty}^{\infty} R_N(\tau)\, R_{\hat{N}}(\tau)\, d\tau = \left(\frac{N_0}{2}\right)^2 \int_{-\infty}^{\infty} |G(j2\pi f)|^2\, df$$

$$= \left(\frac{N_0}{2}\right)^2 \int_{-\infty}^{\infty} \left\{[\mathrm{Re}\ \{G(j2\pi f)\}]^2 + [\mathrm{Im}\ \{G(j2\pi f)\}]^2\right\} df$$

$$\int_{-\infty}^{\infty} R_{\hat{m}}(\tau)\, R_{\hat{N}}(\tau)\, d\tau = \frac{N_0}{2} \int_{-\infty}^{\infty} S_m(f)\, |G(j2\pi f)|^4\, df$$

$$\int_{-\infty}^{\infty} R_m(\tau)\, R_{\hat{N}}(\tau)\, d\tau = \frac{N_0}{2} \int_{-\infty}^{\infty} S_m(f)\, |G(j\pi f)|^2\, df$$

$$= \int_{-\infty}^{\infty} R_{\hat{m}}(\tau)\, R_N(\tau)\, d\tau$$

$$\int_{-\infty}^{\infty} R_{m\hat{m}}(\tau)\, R_{N\hat{N}}(-\tau)\, d\tau = \frac{N_0}{2} \int_{-\infty}^{\infty} S_m(f)\, G^2(j2\pi f)\, df$$

$$= \int_{-\infty}^{\infty} R_{m\hat{m}}(-\tau)\, R_{N\hat{N}}(\tau)\, d\tau$$

$$\int_{-\infty}^{\infty} R_{\hat{m}}(\tau)\, R_{N\hat{N}}(-\tau)\, d\tau = \frac{N_0}{2} \int_{-\infty}^{\infty} S_m(f)\, |G(j2\pi f)|^2\, \mathrm{Re}\ \{G(j2\pi f)\}\, df$$

$$= \int_{-\infty}^{\infty} R_{m\hat{m}}(-\tau)\, R_{\hat{N}}(\tau)\, d\tau\ . \qquad (12)$$

Employing notation similar to that used previously (see Appendix C and Reference 2), equation (11) can be rewritten as

$$N_{sq} = 4\, S\, N_0 \left[D_m(K_D + \mathcal{K}_D) + \frac{N_0 B_i}{2S}(K_L + \mathcal{K}_L)\right]\ , \qquad (13)$$

where, as before,

$$D_m \triangleq \int_{-\infty}^{\infty} S_m(f)\, |G(j2\pi f)|^2\, df$$

$$K_L = \frac{\int_{-\infty}^{\infty} |G(j2\pi f)|^4\, df}{\int_{-\infty}^{\infty} |G(j2\pi f)|^2\, df}$$

$$K_D = \frac{\int_{-\infty}^{\infty} S_m(f)\ |G(j2\pi f)|^4\ df}{\int_{-\infty}^{\infty} S_m(f)\ |G(j2\pi f)|^2\ df}$$

$$B_i = \int_{-\infty}^{\infty} |G(j2\pi f)|^2\ df \tag{14}$$

and now, in addition,

$$\mathcal{K}_D = \frac{\int_{-\infty}^{\infty} S_m(f)\ [\mathrm{Im}\ \{G(j2\pi f)\}]^2\ df}{\int_{-\infty}^{\infty} S_m(f)\ |G(j2\pi f)|^2\ df}$$

$$\mathcal{K}_L = \frac{\int_{-\infty}^{\infty} [\mathrm{Im}\ \{G(j2\pi f)\}]^2\ df}{\int_{-\infty}^{\infty} |G(j2\pi f)|^2\ df} \tag{15}$$

Since, from (3), $w_0(t)$ has no signal component for purposes of tracking, then the composite error signal u(t) of (6) has an identical signal component to that of a conventional Costas loop. Thus, analogous to equation (31) of Reference 2, we have that the "squaring loss" of the composite AFC/Costas loop is given by

$$\mathscr{L}_L = \frac{4\,S\,N_0\,D_m^2}{N_{sq}} \tag{16}$$

Substituting (13) and (14) into (16), we get the final result, namely,

$$\boxed{\mathscr{L}_L = \frac{D_m}{(K_D + \mathcal{K}_D) + \dfrac{K_L + \mathcal{K}_L}{D_m\,\rho_i}}} \tag{17}$$

where $\rho_i \triangleq 2S/N_0B_i$ is the signal-to-noise ratio in the arm filter bandwidth.

For ρ_i small (the usual case of interest), we see by comparing (17) with equation (36) of Reference 2, and recognizing that for either case,

$$\sigma_{2\phi}^2 = \frac{4}{\rho \mathcal{K}_L} ; \qquad \rho = \frac{S}{N_0 B_L} \tag{18}$$

where B_L is the single-sided loop bandwidth, that

$$\frac{\sigma_{2\phi}^2\big|_{\text{composite loop}}}{\sigma_{2\phi}^2\big|_{\text{conventional loop}}} \cong \frac{K_L + \mathcal{K}_L}{K_L} . \tag{19}$$

It remains now to evaluate $\mathcal{K}_L$ for the case of an RC arm filter and to compare its value to that of K_L for the same filter, namely, $K_L = 1/2$. Since, for an RC filter,

$$G(j2\pi f) = \frac{1}{1 + j\, f/f_c} , \tag{20}$$

then

$$[\text{Im}\ \{G(j2\pi f)\}]^2 = \frac{(f/f_c)^2}{[1 + (f/f_c)^2]^2} = (f/f_c)^2\ |G(j2\pi f)|^4 \tag{21}$$

and

$$|G(j2\pi f)|^2 = \frac{1}{1 + (f/f_c)^2} . \tag{22}$$

Substituting (21) and (22) into (15) and carrying out the integrations yields

$$\mathcal{K}_L = 1/2 . \tag{23}$$

Hence, we see from (19) that, for an RC arm filter,

$$\frac{\sigma_{2\phi}^2\big|_{\text{composite loop}}}{\sigma_{2\phi}^2\big|_{\text{conventional loop}}} \cong 2 , \tag{24}$$

which is the identical result obtained for the modified loop (Appendix C).

FALSE LOCK PERFORMANCE OF COMPOSITE AFC/COSTAS LOOP

From Equations (2), (4) and (5), the normalized signal component of u(t) is

$$s_0(t) = \hat{m}_s(t;\omega_f,\phi)\,\hat{m}_c(t;\omega_f,\phi) + \frac{1}{2}\left[m(t)\,\hat{m}_c(t;\omega_f,\phi)\sin(\omega_f t+\phi) - m(t)\,\hat{m}_s(t;\omega_f,\phi)\cos(\omega_f t+\phi)\right] \quad (25)$$

The first term of (25) comes from the conventional Costas loop, while the latter bracketed term is contributed by the AFC component. As before, we are interested in

$$\langle\overline{s_0(t)}\rangle = \langle\overline{\hat{m}_s(t;\omega_f,\phi)\,\hat{m}_c(t;\omega_f,\phi)}\rangle + \frac{1}{2}\langle\overline{m(t)\,\hat{m}_c(t;\omega_f,\phi)\sin(\omega_f t+\phi)}\rangle - \frac{1}{2}\langle\overline{m(t)\,\hat{m}_s(t;\omega_f,\phi)\cos(\omega_f t+\phi)}\rangle \quad (26)$$

From Appendix A, equation (30), and the ensuing remarks, we immediately have that

$$\langle\overline{m_s(t;\omega_f,\phi)\,m_c(t;\omega_f,\phi)}\rangle\Big|_{\omega_f=\frac{k\pi}{T}} = \frac{1}{2T}\,\mathrm{Im}\left\{e^{j2\phi}\int_{-\infty}^{\infty}|G(j\omega)|^2 \times P\left[j\left(\omega-\frac{\pi k}{T}\right)\right]P\left[-j\left(\omega+\frac{\pi k}{T}\right)\right]\frac{d\omega}{2\pi}\right\}. \quad (27)$$

The second term in (26) is identical to equation (11) of Appendix C (except for the factor of one-half) and is thus evaluated as (see equation (18) of Appendix C):

$$\frac{1}{2}\left\langle \overline{m(t)\; m_c(t;\omega_f,\phi)\sin(\omega_f t+\phi)} \right\rangle\Bigg|_{\omega_f=\frac{k\pi}{T}} =$$

$$\frac{1}{4T}\left[\mathrm{Im}\left\{e^{j2\phi}\int_{-\infty}^{\infty} G(j\omega)\; P\left[j(\omega-\frac{\pi k}{T})\right]\; P\left[-j(\omega+\frac{\pi k}{T})\right]\frac{d\omega}{2\pi}\right\}\right.$$

$$\left. +\;\mathrm{Im}\left\{\int_{-\infty}^{\infty} G(j\omega)\;\left|P\left[j(\omega+\frac{\pi k}{T})\right]\right|^2\frac{d\omega}{2\pi}\right\}\right]. \tag{28}$$

Similarly,

$$\frac{1}{2}\left\langle \overline{m(t)\; m_s(t;\omega_f,\phi)\cos(\omega_f t+\phi)} \right\rangle\Bigg|_{\omega_f=\frac{\pi k}{T}} =$$

$$\frac{1}{4T}\left[\mathrm{Im}\left\{e^{j2\phi}\int_{-\infty}^{\infty} G(j\omega)\; P\left[j(\omega-\frac{\pi k}{T})\right]\; P\left[-j(\omega+\frac{\pi k}{T})\right]\frac{d\omega}{2\pi}\right\}\right.$$

$$\left. -\;\mathrm{Im}\left\{\int_{-\infty}^{\infty} G(j\omega)\;\left|P\left[j(\omega+\frac{\pi k}{T})\right]\right|^2\frac{d\omega}{2\pi}\right\}\right]. \tag{29}$$

Substituting (27), (28) and (29) into (26) gives the final result, namely,

$$\mathscr{A}_k(\phi) \;\triangleq\; \left\langle \overline{s_0(t)} \right\rangle\Bigg|_{\omega_f=\frac{\pi k}{T}} =$$

$$\frac{1}{2T}\left[\mathrm{Im}\left\{e^{j2\phi}\int_{-\infty}^{\infty} |G(j\omega)|^2\; P\left[j(\omega-\frac{\pi k}{T})\right]\; P\left[-j(\omega+\frac{\pi k}{T})\right]\frac{d\omega}{2\pi}\right\}\right.$$

$$\left. +\;\mathrm{Im}\left\{\int_{-\infty}^{\infty} G(j\omega)\;\left|P\left[j(\omega+\frac{\pi k}{T})\right]\right|^2\frac{d\omega}{2\pi}\right\}\right]. \tag{30}$$

Comparing (30) with equation (18) of Appendix C, we observe that the modified and composite loops offer identical improvement in false lock performance.

REFERENCES

1. Cahn, C. R. "Improved Frequency Acquisition of a Costas Loop," accepted for publication in the IEEE Transactions on Communications.

2. Simon, M. K., and Lindsey, W. C. "Optimum Performance of Suppressed Carrier Receivers with Costas Loop Tracking," IEEE Transactions on Communications, Vol. COM-25, No. 2, February 1977, pp. 215-227.

APPENDIX E

ACQUISITION AND TRACKING PERFORMANCE OF A COMPOSITE AFC/COSTAS LOOP

APPENDIX E

ACQUISITION AND TRACKING PERFORMANCE OF A COMPOSITE AFC/COSTAS LOOP

by

Marvin K. Simon

INTRODUCTION

In Appendix D, we examined the improvement in protection against false lock obtained by superimposing an AFC network on a conventional Costas loop. In addition, the corresponding penalty in tracking performance was assessed. Since a common loop filter was assumed in these analyses for the purpose of comparing the results with those obtained for the modified Costas loop (Appendix C), we lacked the complete flexibility necessary to trade off acquisition and tracking performance.

In this appendix, we propose a composite AFC/Costas loop with independent AFC and Costas loops in the sense that each has its own loop filter. By varying the ratio of the two loop bandwidths, one now has an additional degree of freedom available for performing acquisition and tracking tradeoffs. We begin our analyses of this more general loop with a characterization of the AFC discriminator (output signal amplitude versus input frequency) characteristic. In particular, we determine the range of linear operation and the equivalent discriminator gain (in the presence of a random data input) in this linear region. Following this, we derive an upper bound on acquisition time as a function of frequency offset over the acquisition range of the composite loop. Finally, the tracking behavior is analyzed by generalizing the results given in Appendix D for mean-square tracking jitter and squaring loss.

AFC DISCRIMINATOR CHARACTERISTICS

Consider the composite AFC/Costas loop illustrated in Figure 1, where the AFC discriminator is contained within the dashed lines. Note that the 3 dB attenuator following $w_0(t)$ in Figure 1 of Appendix D has been omitted here, since our purpose is no longer a comparison with the modified Costas loop of Appendix C.

When the composite loop is out of lock, a radian frequency error $\Delta\omega(t)$ exists in the phase detector output signals $\varepsilon_c(t)$ and $\varepsilon_s(t)$. Since, typically, the AFC loop bandwidth is small relative to the noise bandwidth

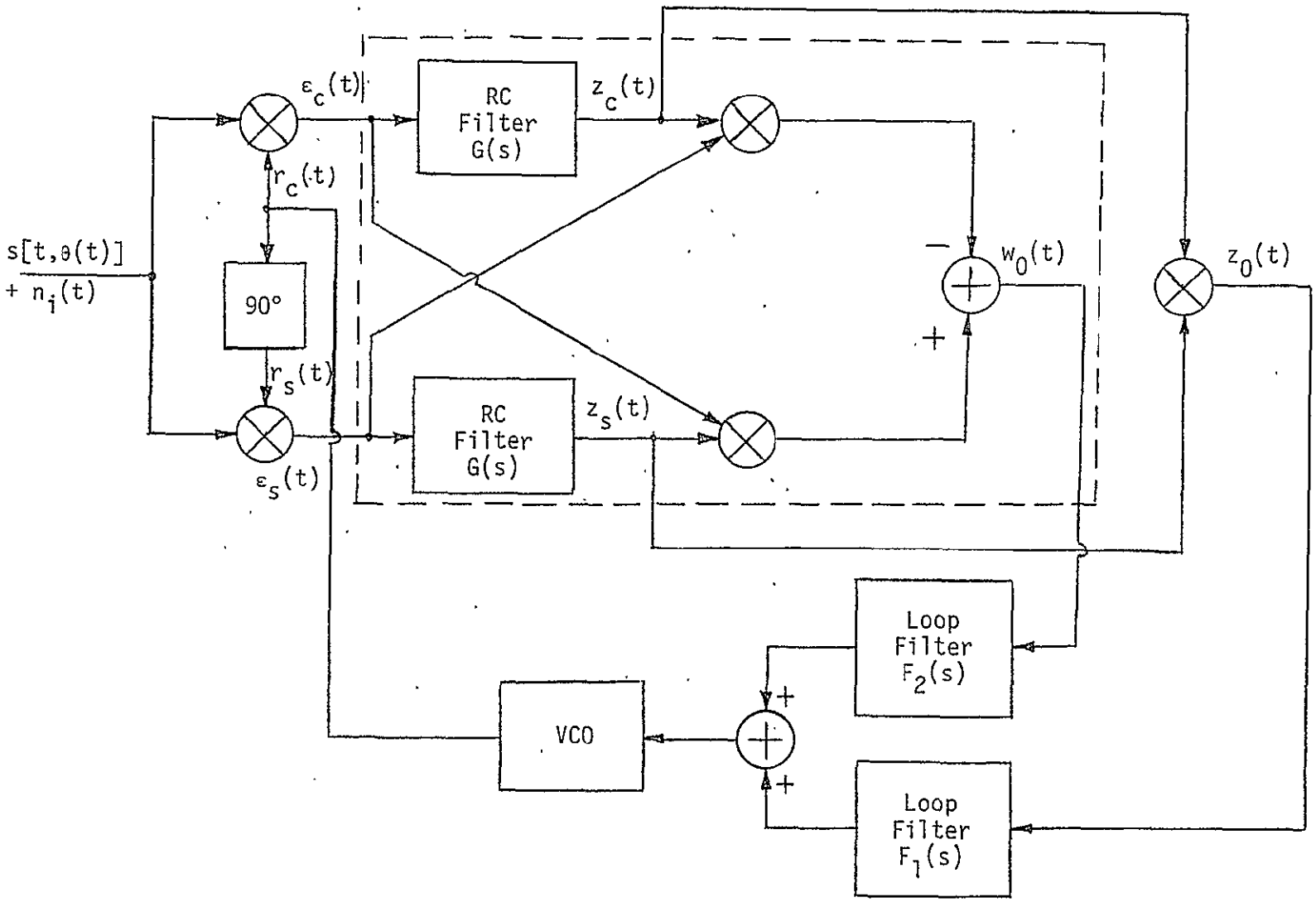

Figure 1. A Composite AFC/Costas Loop

of the RC arm filters, then the average AFC output signal $\langle \overline{w_0(t)} \rangle$ can be computed, assuming $\Delta\omega(t)$ fixed equal to $\Delta\omega$. In particular, equation (4) of Appendix D applies with ω_f replaced by $\Delta\omega$, i.e.,

$$w_0(t) = K_1^2 K_m^2 S \{m(t)\, \hat{m}_c(t;\Delta\omega,\phi) \sin(\Delta\omega t + \phi) - m(t)\, \hat{m}_s(t;\Delta\omega,\phi) \cos(\Delta\omega t + \phi)\}, \quad (1)$$

where

$$\hat{m}_s(t;\Delta\omega,\phi) \triangleq G(p)\, \varepsilon_s(t) = G(p)\{m(t) \sin[\Delta\omega t + \phi]\}$$

$$\hat{m}_c(t;\Delta\omega,\phi) \triangleq G(p)\, \varepsilon_c(t) = G(p)\{m(t) \cos[\Delta\omega t + \phi]\}. \quad (2)$$

Substituting (10), (12), and (14) of Appendix A into (1) and (2) above gives

$$w_0(t) = K_1^2 K_m^2 S \left\{ \frac{1}{2j} \sum_{n=-\infty}^{\infty} \sum_{m=-\infty}^{\infty} a_n a_m \hat{p}_2(t - nT)\, p(t - mT) - \frac{1}{2j} \sum_{n=-\infty}^{\infty} \sum_{m=-\infty}^{\infty} a_n a_m \hat{p}_1(t - nT)\, p(t - mT) \right\}, \quad (3)$$

where $\hat{p}_1(t)$ and $\hat{p}_2(t)$ are defined in (13) of Appendix A with ω_f replaced by $\Delta\omega$. Taking both the statistical and time averages of (3) and recalling that, for random data,

$$\overline{a_n a_m} = \delta_{mn} = \begin{cases} 1; & m = n \\ 0; & m \neq n \end{cases}, \quad (4)$$

we get

$$\frac{\langle \overline{w_0(t)} \rangle}{K_1^2 K_m^2 S} = \frac{1}{2j} \lim_{T_0 \to \infty} \frac{1}{T_0} \int_{-T_0/2}^{T_0/2} \sum_{n=-\infty}^{\infty} p(t - nT)[\hat{p}_2(t - nT) - \hat{p}_1(t - nT)]\, dt \quad (5a)$$

and

$$\frac{\overline{\langle w_0(t)\rangle}}{K_1^2 K_m^2 S} = \frac{1}{2j} \lim_{T_0 \to \infty} \sum_{n=-\infty}^{\infty} \int_{-\infty}^{\infty} \int_{-\infty}^{\infty} G[j(\omega - \Delta\omega)]\, P(j\omega)\, P(-j\omega')$$

$$\times \frac{\sin [(\omega - \omega')\, T_0/2]}{(\omega - \omega')\, T_0/2} e^{-j(\omega-\omega')nT} \frac{d\omega}{2\pi} \frac{d\omega'}{2\pi}$$

$$- \frac{1}{2j} \lim_{T_0 \to \infty} \sum_{n=-\infty}^{\infty} \int_{-\infty}^{\infty} \int_{-\infty}^{\infty} G[j(\omega + \Delta\omega)]\, P(j\omega)\, P(-j\omega')$$

$$\times \frac{\sin [(\omega - \omega')\, T_0/2]}{(\omega - \omega')\, T_0/2} e^{-j(\omega-\omega')nT} \frac{d\omega}{2\pi} \frac{d\omega'}{2\pi} . \qquad (5b)$$

Recognizing, as in Appendix A, that

$$\sum_{n=-\infty}^{\infty} e^{-j(\omega-\omega')nT} = \frac{2\pi}{T} \sum_{k=-\infty}^{\infty} \delta\left(\omega - \omega' - \frac{2\pi k}{T}\right) , \qquad (6)$$

then (5) simplifies to

$$\frac{\overline{\langle w_0(t)\rangle}}{K_1^2 K_m^2 S} = \frac{1}{2jT} \lim_{T_0 \to \infty} \sum_{k=-\infty}^{\infty} \int_{-\infty}^{\infty} G[j(\omega - \Delta\omega)]\, P(j\omega)\, P\left[-j\left(\omega - \frac{2\pi k}{T}\right)\right]$$

$$\times \frac{\sin \left[\frac{2\pi k}{T}\left(\frac{T_0}{2}\right)\right]}{\frac{2\pi k}{T}\left(\frac{T_0}{2}\right)} \frac{d\omega}{2\pi}$$

$$- \frac{1}{2jT} \lim_{T_0 \to \infty} \sum_{k=-\infty}^{\infty} \int_{-\infty}^{\infty} G[j(\omega + \Delta\omega)]\, P(j\omega)\, P\left[-j\left(\omega - \frac{2\pi k}{T}\right)\right]$$

$$\times \frac{\sin \left[\frac{2\pi k}{T}\left(\frac{T_0}{2}\right)\right]}{\frac{2\pi k}{T}\left(\frac{T_0}{2}\right)} \frac{d\omega}{2\pi} . \qquad (7)$$

Since the only term in (7) which yields a nonzero contribution is that corresponding to k=0, then (7) reduces to

$$\frac{\overline{\langle w_0(t)\rangle}}{K_1^2 K_m^2 S} = \frac{1}{2j}\int_{-\infty}^{\infty} S_m(\omega)\left\{G[j(\omega-\Delta\omega)] - G[j(\omega+\Delta\omega)]\right\}\frac{d\omega}{2\pi}$$

$$= \int_{-\infty}^{\infty} S_m(\omega)\ \mathrm{Im}\left\{G[j(\omega-\Delta\omega)]\right\}\frac{d\omega}{2\pi}\ , \tag{8}$$

or, finally,

$$f(\Delta\omega) \triangleq \frac{\overline{\langle w_0(t)\rangle}}{K_1^2 K_m^2 S} = \int_{-\infty}^{\infty} S_m(\omega+\Delta\omega)\ \mathrm{Im}\left\{G(j\omega)\right\}\frac{d\omega}{2\pi}\ , \tag{9}$$

where

$$S_m(\omega) \triangleq \frac{1}{T}|P(j\omega)|^2 \tag{10}$$

is the power spectrum of the modulation m(t) and Im{G(jω)} denotes the imaginary part of the arm filter transfer function. Since G(s) is an RC filter with transfer function

$$G(j\omega) = \frac{1}{1 + j(\omega/\omega_c)} = \frac{-j(\omega/\omega_c)}{1 + (\omega/\omega_c)^2}\ ;\ \omega_c = \frac{1}{RC}\ , \tag{11}$$

then

$$\mathrm{Im}\left\{G(j\omega)\right\} = -\frac{\omega/\omega_c}{1 + (\omega/\omega_c)^2}\ . \tag{12}$$

Furthermore, for Manchester coded data,

$$S_m(\omega) = T\,\frac{\sin^4\frac{\omega T}{4}}{\left(\frac{\omega T}{4}\right)^2}\ . \tag{13}$$

Substituting (12) and (13) in (9) and letting $\Delta x = \Delta\omega T$, we obtain, after considerable algebraic manipulation and integral evaluation, the desired discriminator characteristic, viz.,

$$f(\Delta x) = \frac{1}{(\omega_c T)\left[1 + \left(\frac{\Delta x}{\omega_c T}\right)^2\right]} \left\{ \frac{\Delta x}{\omega_c T}(\omega_c T - 3) - \left[\frac{\Delta x}{\omega_c T}\cos \Delta x + \sin \Delta x\right] e^{-\omega_c T} \right.$$

$$\left. + 4\left[\frac{\Delta x}{\omega_c T}\cos \frac{\Delta x}{2} + \sin \frac{\Delta x}{2}\right] e^{-(\omega_c T)/2} \right\}$$

$$+ \frac{\frac{\Delta x}{\omega_c T}}{(\omega_c T)\left[1 + \left(\frac{\Delta x}{\omega_c T}\right)^2\right]^2} \left\{ \left[\left[\left(\frac{\Delta x}{\omega_c T}\right)^2 - 1\right]\cos \Delta x + 2\left(\frac{\Delta x}{\omega_c T}\right)\sin \Delta x\right] e^{-\omega_c T} \right.$$

$$- 4\left[\left[\left(\frac{\Delta x}{\omega_c T}\right)^2 - 1\right]\cos \frac{\Delta x}{2} + 2\left(\frac{\Delta x}{\omega_c T}\right)\sin \frac{\Delta x}{2}\right] e^{-(\omega_c T)/2}$$

$$\left. + 3\left[\left(\frac{\Delta x}{\omega_c T}\right)^2 - 1\right] \right\} . \qquad (14)$$

Figure 2 illustrates $f(\Delta x)$ versus $\Delta x/\omega_c T = \Delta\omega/\omega_c$ for $\omega_c T = 2.8\pi$ (the optimum ratio of arm filter 3 dB frequency to data rate for small values of ST/N_0; see [1]) and $\omega_c T = 5.6\pi$, respectively. The <u>equivalent linear gain</u>, $K_{\dot\varphi}$, of these discriminator characteristics is indicated on Figure 2 by dotted lines and is found analytically as follows. Assuming $\Delta x/\omega_c T$ to be small, then from (14),

$$f(\Delta x) \cong \frac{1}{\omega_c T}\left\{ \frac{\Delta x}{\omega_c T}(\omega_c T - 3) - \frac{\Delta x}{\omega_c T}(1 + \omega_c T) e^{-\omega_c T} + 4\frac{\Delta x}{\omega_c T}\left(1 + \frac{\omega_c T}{2}\right) e^{-(\omega_c T)/2} \right\}$$

$$- \frac{1}{\omega_c T}\left(\frac{\Delta x}{\omega_c T}\right)\left\{ e^{-\omega_c T} - 4e^{-(\omega_c T)/2} + 3 \right\} , \qquad (15)$$

or

$$f(\Delta x) \cong \frac{\Delta x}{\omega_c T}\left\{ 1 - 2\left[\frac{3 - 4\left(1 + \frac{\omega_c T}{4}\right) e^{-(\omega_c T)/2} + \left(1 + \frac{\omega_c T}{2}\right) e^{-\omega_c T}}{\omega_c T}\right] \right\}$$

$$\triangleq K_{\dot\varphi}\frac{\Delta x}{\omega_c T} = K_{\dot\varphi}\frac{\Delta\omega}{\omega_c} . \qquad (16)$$

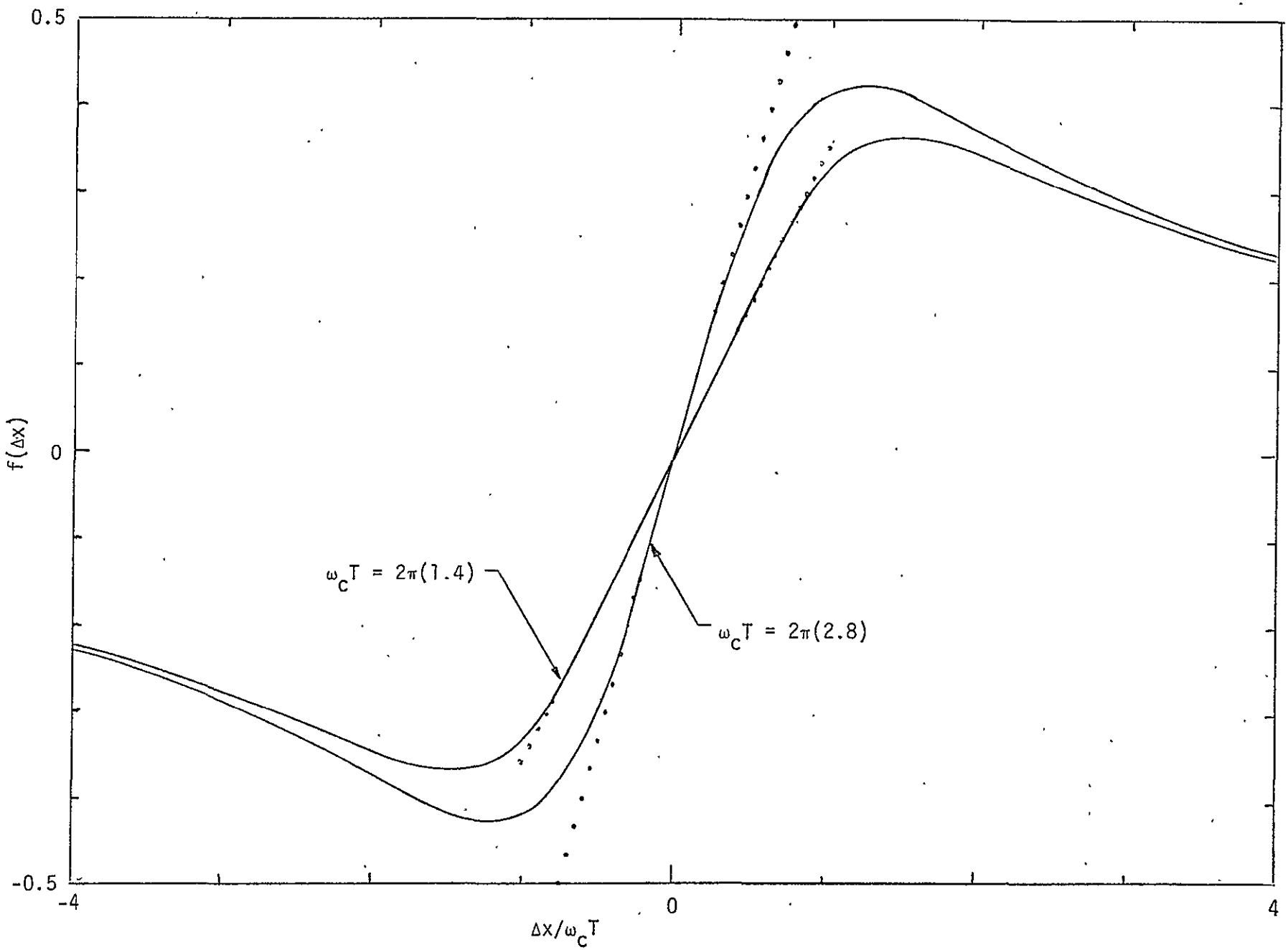

Figure 2. AFC Discriminator Characteristics

Thus,

$$K_{\dot{\varphi}} = 1 - 2\left[\frac{3 - 4\left(1 + \frac{\omega_c T}{4}\right) e^{-(\omega_c T)/2} + \left(1 + \frac{\omega_c T}{2}\right) e^{-\omega_c T}}{\omega_c T}\right] . \quad (17)$$

Figure 3 is a plot of $K_{\dot{\varphi}}$ versus $f_c T = \omega_c T/2\pi$.

AFC LOOP RESPONSE - LINEAR MODEL

We observe from Figure 2 that, for a given value of $\omega_c T$, the discriminator characteristic is linear over a certain range of frequency offset and, in particular, is described by (16) in this region. Moreover, since (14) and hence (16) were derived under the assumption of a constant frequency offset, i.e., $\omega(t) - \hat{\omega}(t) = \Delta\omega$, then from Figure 1, the closed loop AFC response is described by

$$\hat{\omega}(t) = K_V F_2(p) K_1^2 K_m^2 S K_{\dot{\varphi}} \left(\omega(t) - \hat{\omega}(t)\right) \Big/ \omega_c \quad (18)$$

or, in LaPlace Transform notation,

$$\frac{\hat{\omega}(s)}{\omega(s)} = \frac{S K K_{\dot{\varphi}} F_2(s)/\omega_c}{1 + S K K_{\dot{\varphi}} F_2(s)/\omega_c} , \quad (19)$$

where K_V is the VCO gain in rad/sec/v and $K \triangleq K_V K_1^2 K_m^2$.* Assuming that $F_2(s)$ is an imperfect integrating filter, i.e.,

$$F_2(s) = \frac{1 + s\tau_{22}}{1 + s\tau_{12}} , \quad (20)$$

then

$$\frac{\hat{\omega}(s)}{\omega(s)} = \frac{S K K_{\dot{\varphi}} (1 + s\tau_{22})/\omega_c}{1 + S K K_{\dot{\varphi}}/\omega_c + s\left(\tau_{12} + S K K_{\dot{\varphi}} \tau_{22}/\omega_c\right)} , \quad (21)$$

which implies a <u>first-order loop</u> response with radian cutoff frequency

$$\omega_{nF} = \frac{1 + S K K_{\dot{\varphi}}/\omega_c}{\tau_{12} + S K K_{\dot{\varphi}} \tau_{22}/\omega_c} . \quad (22)$$

---

*$K_{\dot{\varphi}}$ is not included in the definition of K since it is actually a function of $\omega_c T$ rather than a constant.

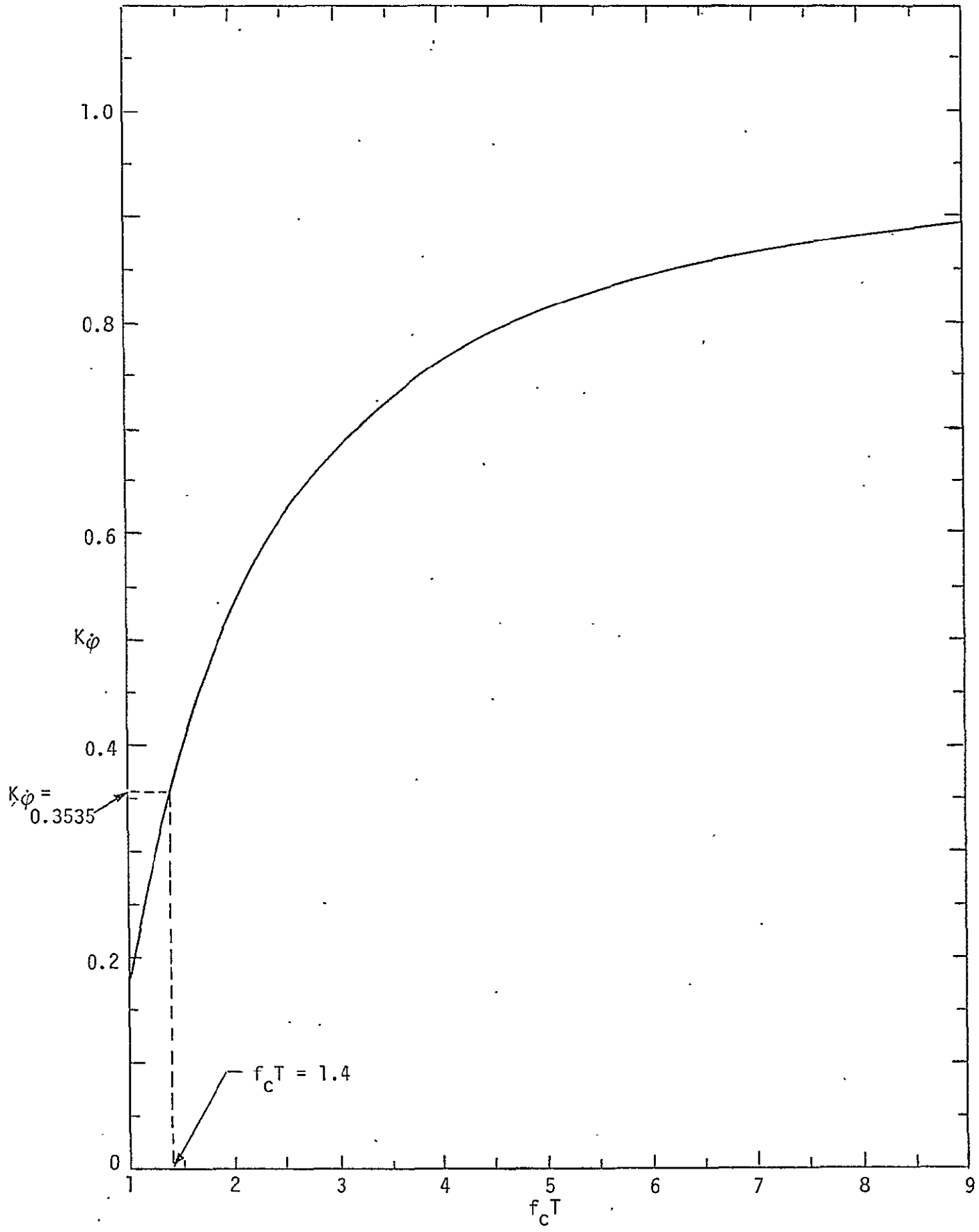

Figure 3. Discriminator Linear Gain vs. Ratio of Arm Filter 3 dB Cutoff Frequency to Data Rate

If a conventional Costas loop were to employ $F_2(s)$ of (20) as its loop filter, then the loop response would be second-order and characterized by the following parameters:

$$r_2 \triangleq SKD_m\tau_{22}F_{02}\ ; \qquad F_{02} \triangleq \frac{\tau_{22}}{\tau_{12}}$$

$$\omega_{n2} = \frac{\sqrt{r_2}}{\tau_{22}} \tag{23}$$

In (23), ω_{n2} is the natural frequency of the loop, and for small F_{02} (the usual case in design),

$$r_2 \cong 4\zeta_2^2\ , \tag{24}$$

where ζ_2 is the loop's damping factor. Also in (23),

$$D_m \triangleq \int_{-\infty}^{\infty} S_m(\omega)\,|G(j\omega)|^2\,\frac{d\omega}{2\pi} \tag{25}$$

is the data modulation distortion factor (equivalent power reduction due to arm filters).* Using these definitions in (21), we obtain, after considerable algebraic manipulation:

$$\frac{\hat{\omega}(s)}{\omega(s)} = \left(\frac{K_{\dot\varphi}}{D_m\omega_c}\right)\frac{\omega_{n2}^2 + s\sqrt{r_2}\,\omega_{n2}}{\frac{\omega_{n2}}{\sqrt{r_2}}\left(F_{02} + \frac{K_{\dot\varphi}}{D_m\omega_c}\sqrt{r_2}\,\omega_{n2}\right) + s\left(1 + \frac{K_{\dot\varphi}}{D_m\omega_c}\sqrt{r_2}\,\omega_{n2}\right)} \tag{26}$$

$$\omega_{nF} = \frac{\omega_{n2}}{\sqrt{r_2}}\left[\frac{F_{02} + \frac{K_{\dot\varphi}}{D_m\omega_c}\sqrt{r_2}\,\omega_{n2}}{1 + \frac{K_{\dot\varphi}}{D_m\omega_c}\sqrt{r_2}\,\omega_{n2}}\right]. \tag{27}$$

The function $K_{\dot\varphi}/(D_m\omega_c)$ which appears in many places in (26) and (27) can be evaluated as follows. For an RC arm filter and Manchester coded data, one can show from (25) that

*The parameter D_m, like $K_{\dot\varphi}$, is a function of $\omega_c T$.

$$D_m = 1 - \frac{1}{\omega_c T}\left[3 - 4\exp\left(-\frac{\omega_c T}{2}\right) + \exp\left(-\omega_c T\right)\right] . \tag{28}$$

Thus, from (17) and (28), we have that

$$\frac{K_{\dot{\varphi}}}{D_m \omega_c} = \left(\frac{K_{\dot{\varphi}}}{D_m \omega_c T}\right) T \triangleq K_c T , \tag{29}$$

with

$$K_c = \left(\frac{1}{\omega_c T}\right) \frac{1 - 2\left[\dfrac{3 - 4\left(1 + \dfrac{\omega_c T}{4}\right) e^{-(\omega_c T)/2} + \left(1 + \dfrac{\omega_c T}{2}\right) e^{-\omega_c T}}{\omega_c T}\right]}{1 - \left[\dfrac{3 - 4e^{-(\omega_c T)/2} + e^{-\omega_c T}}{\omega_c T}\right]} . \tag{30}$$

For example, at the optimum design ratio of arm filter cutoff frequency to data rate, viz., $\omega_c T = 2.8\pi$, we have that $K_c = 0.0605$.

AFC LOOP RESPONSE TO AN INPUT FREQUENCY STEP

Using (29), we can write (26) in the form

$$\frac{\hat{\omega}(s)}{\omega(s)} = K_c T\left[\frac{A + Bs}{C + Ds}\right] = K_c T\left[\frac{A - \dfrac{BC}{D}}{C + Ds} + \frac{B}{D}\right] , \tag{31}$$

where

$$A = \omega_{n2}^2 ; \qquad B = \sqrt{r_2}\,\omega_{n2} ;$$

$$C = \frac{\omega_{n2}}{\sqrt{r_2}}\left(F_{02} + K_c T\sqrt{r_2}\,\omega_{n2}\right) ; \quad D = 1 + K_c T\sqrt{r_2}\,\omega_{n2} . \tag{32}$$

If $\omega(t)$ is now a frequency step $\Lambda_0 u(t)$, i.e., $\omega(s) = \Lambda_0/s$, then

$$\hat{\omega}(s) = K_c T\left[\frac{\Lambda_0}{s}\left(\frac{A - \dfrac{BC}{D}}{C + Ds}\right) + \frac{\Lambda_0 \dfrac{B}{D}}{s}\right]$$

$$= K_c T \frac{A}{C}\Lambda_0\left[\frac{1}{s} - \frac{1 - \dfrac{B/D}{A/C}}{s + C/D}\right] . \tag{33}$$

From (32),

$$1 - \frac{B/D}{A/C} = \frac{1 - F_{02}}{1 + K_c T\sqrt{r_2}\,\omega_{n2}} \cong \frac{1}{1 + K_c T\sqrt{r_2}\,\omega_{n2}} = \frac{1}{D}\,, \tag{34}$$

since $F_{02} << 1$. To simplify (33) any further, we must express $K_c T\sqrt{r_2}\,\omega_{n2}$ in the denominator of (34) in terms of the parameters of the conventional Costas loop portion of the overall composite loop. Assuming for $F_1(s)$ an imperfect integration filter of the form

$$F_1(s) = \frac{1 + s\tau_{21}}{1 + s\tau_{11}}\,, \tag{35}$$

then the Costas loop is second-order with parameters [analogous to (23)]

$$\begin{aligned} r_1 &\triangleq S K D_m \tau_{21} F_{01}\,; \qquad F_{01} \triangleq \frac{\tau_{21}}{\tau_{11}} \\ \omega_{n1} &= \frac{\sqrt{r_1}}{\tau_{21}}\,; \qquad B_{L1} \cong \frac{r_1 + 1}{4\tau_{21}} \end{aligned} \tag{36}$$

where, in addition, B_{L1} is the single-sided bandwidth of the Costas loop portion alone. Thus, from (23) and (36), we have that

$$\begin{aligned} K_c T\sqrt{r_2}\,\omega_{n2} &= K_c T S K D_m F_{02} \\ &= K_c T \frac{r_1}{\tau_{21}}\left(\frac{F_{02}}{F_{01}}\right) = K_c\left(\frac{4 r_1}{r_1 + 1}\right)\left(\frac{F_{02}}{F_{01}}\right) B_{L1} T\,. \end{aligned} \tag{37}$$

Since a conventional Costas loop is typically designed for critical damping ($r_1 = 2$) and $B_{L1}T << 1$, then if we arbitrarily choose $F_{02} \leq F_{01}$, we have that

$$K_c T\sqrt{r_2}\,\omega_{n2} = (0.0605)\left(\frac{8}{3}\right)\left(\frac{F_{02}}{F_{01}}\right) B_{L1} T = 0.161\left(\frac{F_{02}}{F_{01}}\right) B_{L1} T << 1 \tag{38}$$

or equivalently, from (32) and (34),

$$D \cong 1\,; \qquad 1 - \frac{B/D}{A/C} \cong 1\,. \tag{39}$$

Thus, (31) simplifies to

$$\frac{\hat{\omega}(s)}{\omega(s)} = K_c T\left(\frac{A}{s + C}\right) = K_c T\left(\frac{\omega_{n2}^2}{s + \omega_{nF}}\right) \tag{40}$$

and accordingly, (33) becomes

$$\hat{\omega}(s) = K_c T \frac{A}{C} \Lambda_0 \left[\frac{1}{s} - \frac{1}{s+C}\right] \tag{41}$$

$$= \frac{\Lambda_0}{1 + \dfrac{F_{02}}{K_c T \sqrt{r_2}\, \omega_{n2}}} \left[\frac{1}{s} - \frac{1}{s + \omega_{nF}}\right]$$

$$\doteq \frac{\Lambda_0}{1 + \dfrac{6.2\, F_{01}}{B_{L1} T}} \left[\frac{1}{s} - \frac{1}{s + \omega_{nF}}\right] . \tag{42}$$

The equivalent time domain response is then

$$\hat{\omega}(t) = \frac{\Lambda_0}{1 + \xi} \left[1 - e^{-\omega_{nF} t}\right] u(t) , \tag{43}$$

where we have defined

$$\xi = \frac{6.2\, F_{01}}{B_{L1} T} . \tag{44}$$

The corresponding frequency error response, $\dot{\varphi}(t) = \omega(t) - \hat{\omega}(t)$, is given by

$$\dot{\varphi}(t) = \Lambda_0 \left(\frac{\xi}{1 + \xi}\right) u(t) + \frac{\Lambda_0}{1 + \xi} e^{-\omega_{nF} t}\, u(t) . \tag{45}$$

Furthermore, since from (40), the AFC acts like a first-order loop, its two-sided noise bandwidth W_{LF} is related to ω_{nF} by

$$W_{LF} = \frac{\dfrac{1}{2\pi j} \int_{-j\infty}^{j\infty} \left(\dfrac{\hat{\omega}(s)}{\omega(s)}\right)\left(\dfrac{\hat{\omega}(-s)}{\omega(-s)}\right) ds}{\left|\dfrac{\hat{\omega}(0)}{\omega(0)}\right|^2} ; \tag{46a}$$

or

$$W_{LF} = \frac{1}{2\pi j}\int_{-j\infty}^{j\infty}\left(\frac{\omega_{nF}}{s+\omega_{nF}}\right)\left(\frac{\omega_{nF}}{-s+\omega_{nF}}\right)ds = \frac{\omega_{nF}}{2}. \tag{46b}$$

Alternately, the single-sided noise bandwidth $B_{LF} \triangleq W_{LF}/2$ is related to ω_{nF} by

$$B_{LF} = \frac{\omega_{nF}}{4}. \tag{47}$$

Substituting (47) into (45), we obtain the desired radian frequency error response:

$$\dot{\varphi}(t) = A_0\left(\frac{\xi}{1+\xi}\right)u(t) + \frac{A_0}{1+\xi}e^{-4B_{LF}t}\,u(t). \tag{48}$$

ACQUISITION BEHAVIOR OF THE COMPOSITE AFC/COSTAS LOOP IN THE ABSENCE OF NOISE

It is well known that an imperfect second-order phase-locked loop is characterized by a finite acquisition range (often called capture or pull-in range) which represents the largest frequency difference between the frequency of the received carrier and that of the VCO for which phase-lock will occur. Typically for high-gain loops, this acquisition range (relative to the loop-bandwidth) is solely a function of the loop damping and the ratio of the time constants of the imperfect loop filter. In view of the similarity between the differential equations of operation of the conventional Costas loop and the phase-locked loop, one might expect the two to have similar acquisition behavior. Since, in effect, a Costas loop reconstructs and tracks a phantom carrier at twice the input frequency, the above statement is indeed true, at least for frequency errors on the order of the loop bandwidth. The similarity to a phase-locked loop, however, tends to break down as the frequency error becomes large, due to the tendency of the Costas loop to false lock to a sideband of the data modulation. Such a false lock phenomenon does not occur in a phase-locked loop, since it tracks an unmodulated carrier. This false lock tendency of the Costas loop often prohibits acquisition by sweeping the VCO frequency over the range of frequency uncertainty, particularly if the false lock frequencies, which occur at integer multiples of half the data rate, fall within the uncertainty region.

The addition of an AFC network to a conventional Costas loop, as we have already observed (see Appendix D), considerably improves the false lock problem and, as we shall also demonstrate shortly, increases the acquisition range to a value on the order of the arm filter bandwidth.

To begin our analysis of the acquisition behavior of the composite AFC/Costas loop, we present (by analogy with the phase-locked loop) the results for acquisition range and frequency acquisition time* for the Costas loop portion alone.

For a phase-locked loop with frequency error Δf, the loop will lock if [2]:

$$|\Delta f| \leq \frac{B_L}{\pi}\left(\frac{2r}{r+1}\right)\sqrt{\frac{2}{F_0} - 1} \tag{49}$$

and the corresponding time to achieve the frequency lock is [2]:

$$T_f = \left(\frac{r+1}{4B_L}\right)\frac{\left[\frac{\pi}{2}\left(\frac{r+1}{r}\right)\left(\frac{\Delta f}{B_L}\right)\right]^2 - \frac{1}{2}\ln\left[\pi\left(\frac{r+1}{r}\right)\left(\frac{\Delta f}{B_L}\right)\right]}{1 - \frac{F_0}{2-F_0}\left[\frac{\pi}{2}\left(\frac{r+1}{r}\right)\left(\frac{\Delta f}{B_L}\right)\right]^2}. \tag{50}$$

Since, as we have seen many times ([1], for example), the differential equation of operation of the Costas loop is identical in form to that of the phase-locked loop except that ϕ is replaced by 2ϕ and Δf by $2\Delta f$, then (49) and (50) apply for the Costas loop if Δf is replaced by $2\Delta f$. In particular, for the Costas loop portion of the composite loop of Figure 1, we have that frequency lock is achieved if

$$|\Delta f| < \frac{B_{L1}}{\pi}\left(\frac{r_1}{r_1+1}\right)\sqrt{\frac{2}{F_{01}} - 1} \tag{51}$$

and the time to reach this condition is

*We shall ignore the phase stabilization time (the additional time to reach phase lock once frequency lock has been established) since this time has only a small effect on acquisition time for appreciable initial frequency errors.

$$T_f = \left(\frac{r_1+1}{4B_{L1}}\right)\frac{\left[\frac{\pi}{2}\left(\frac{r_1+1}{r_1}\right)\left(\frac{2\Delta f}{B_{L1}}\right)\right]^2 - \frac{1}{2}\ln\left[\pi\left(\frac{r_1+1}{r_1}\right)\left(\frac{2\Delta f}{B_{L1}}\right)\right]}{1 - \frac{F_{01}}{2-F_{01}}\left[\frac{\pi}{2}\left(\frac{r_1+1}{r_1}\right)\left(\frac{2\Delta f}{B_{L1}}\right)\right]^2}, \quad (52)$$

where B_{L1}, r_1, and F_{01} are the loop parameters defined in (36).

Since the AFC increases the acquisition range by producing a restoring force proportional to the frequency error [see (14) or its linear equivalent (16)], it is essential that the value of initial frequency error be such that the AFC can reduce this error to a value within the pull-in range of the Costas loop. Since, from (48), the initial radian frequency error can, in the limit as t approaches infinity, be reduced no further than $\Lambda_0\xi/(1+\xi)$, then for acquisition of the composite loop, we require that

$$\frac{\Lambda_0\,\xi}{1+\xi} < 2\pi\left[\frac{B_{L1}}{\pi}\left(\frac{r_1}{r_1+1}\right)\sqrt{\frac{2}{F_{01}}-1}\right]. \quad (53)$$

Letting $r_1 = 2$ and using the corresponding definition of ξ given in (44), we arrive at the inequality

$$\frac{6.2\left(\frac{F_{01}}{B_{L1}T}\right)}{1+6.2\left(\frac{F_{01}}{B_{L1}T}\right)} < \frac{1}{6.6\left(\frac{F_{01}}{B_{L1}T}\right)}\sqrt{2F_{01}-F_{01}^2}. \quad (54)$$

For example, for $F_{01} = 0.001$, we find that

$$\frac{F_{01}}{B_{L1}T} < 0.0365 \quad (55)$$

or equivalently,

$$B_{L1}T > 0.0274. \quad (56)$$

Since, from Figure 2, the AFC discriminator characteristic is approximately linear over the frequency range $\Delta\omega < \omega_c$ (for $\omega_c T = 2.8\pi$) with slope K_ϕ, then the maximum acquisition range of the composite loop is approximately

$$\frac{|\Delta f|}{B_{L1}} < \left(\frac{\omega_c T}{2\pi}\right)\frac{1}{B_{L1}T} = \frac{1.4}{B_{L1}T} \tag{57}$$

or, in view of (56), we have that, for $r_1 = 2$ and $F_{01} = 0.001$,

$$\left(\frac{|\Delta f|}{B_{L1}}\right)_{max} < 51.1 \ . \tag{58}$$

The corresponding maximum acquisition range for the Costas loop alone and the same loop parameters is obtained from (51) and is given by

$$\left(\frac{|\Delta f|}{B_{L1}}\right)_{max} = 9.488 \ . \tag{59}$$

Thus, a modest improvement in acquisition range is possible through the addition of the AFC. More important, however, this increased acquisition range is accompanied by a considerably reduced acquisition time, as we shall now demonstrate.

When the frequency error is large, the behavior of the composite loop is controlled primarily by the AFC loop. Thus, the time t_1 to reduce the frequency error from its initial value $\Delta f_0 \triangleq \Lambda_0/2\pi$ to another value, say Δf_1, can be determined from (48), viz.,

$$2\pi\Delta f_1 = 2\pi\Delta f_0\left(\frac{\xi}{1+\xi}\right) + \frac{2\pi\Delta f_0}{1+\xi}e^{-4B_{LF}t_1} \tag{60}$$

or

$$t_1 = -\frac{1}{4B_{LF}} \ln\left\{\left[\frac{\Delta f_1}{\Delta f_0} - \frac{\xi}{1+\xi}\right](1+\xi)\right\} \ . \tag{61}$$

When Δf_1 becomes within the pull-in range of the Costas loop, then the time t_2 to complete the frequency acquisition process is determined by the combined action of the AFC and Costas loops. This time will, in general, be less than that computed for the Costas loop alone attempting to achieve frequency lock from an initial frequency error of Δf_1. The latter is computed from (52) with Δf replaced by Δf_1. Since an expression for t_2 is difficult to obtain, we shall upper bound t_2 by the value t_2' computed for the Costas loop acting alone as discussed above. Thus, we propose to upper bound the acquisition time T_{ACQ} of the composite loop

by the sum of t_1 as determined by (61) and t_2' as determined by (52) with Δf_1 replacing Δf. Since Δf_1 is thus far arbitrary, we shall choose its value so as to minimize $T'_{ACQ} = t_1 + t_2'$. Furthermore, if Δf_1 is considerably less than the pull-in range of the Costas loop, then the acquisition time formula of (52) simplifies to

$$t_2' \doteq \frac{r_1+1}{4B_{L1}}\left\{\left[\frac{\pi}{2}\left(\frac{r_1+1}{r_1}\right)\left(\frac{2\Delta f_1}{B_{L1}}\right)\right]^2 - \frac{1}{2}\ln\left[\pi\left(\frac{r_1+1}{r_1}\right)\left(\frac{2\Delta f_1}{B_{L1}}\right)\right]\right\} . \quad (62)$$

We shall make this assumption in what follows and check its region of validity later on. Since we wish to choose Δf_1 so as to minimize $T_{ACQ} = t_1 + t_2'$, we can differentiate T_{ACQ} with respect to Δf_1 and equate the resulting expression to zero. Letting

$$C = \frac{\pi}{2}\left(\frac{r_1+1}{r_1}\right)\frac{1}{B_{L1}} \quad (63)$$

and

$$x = 2\Delta f_1 ,$$

we have from (61) and (62) that

$$T'_{ACQ} = -\frac{1}{4B_{LF}}\ln\left\{\frac{(1+\xi)x}{2\Delta f_0} - \xi\right\} + \left(\frac{r_1+1}{4B_{L1}}\right)\left\{C^2x^2 - \frac{1}{2}\ln 2Cx\right\} . \quad (64)$$

Thus,

$$\frac{\partial T'_{ACQ}}{\partial x} = -\frac{1}{4B_{LF}\left\{x - \frac{2\Delta f_0 \xi}{1+\xi}\right\}} + \frac{(r_1+1)}{4B_{L1}}\left[2C^2x - \frac{1}{2x}\right] = 0 , \quad (65)$$

or, after simplification,

$$x^3 - \frac{2\Delta f_0 \xi}{1+\xi}x^2 - \left[\frac{1}{4C^2} + \frac{1}{2C^2(r_1+1)\frac{B_{LF}}{B_{L1}}}\right]x + \frac{\Delta f_0 \xi}{2C^2(1+\xi)} = 0 . \quad (66)$$

A cubic equation of the form $x^3 + px^2 + qx + r = 0$ may be reduced to

$$y^3 + ax + b = 0 \quad (67)$$

by substituting for x the value of $y - p/3$. Here,

$$a = q - \frac{p^2}{3}$$

$$b = \frac{1}{27}(2p^3 - 9pq + 27r) . \tag{68}$$

The case of interest here is where

$$\frac{b^2}{4} + \frac{a^3}{27} < 0 , \tag{69}$$

for which there will be three real and unequal roots. These solutions for y are obtained as follows. Compute the value of the angle θ in the expression

$$\cos\theta = \frac{b/2}{\sqrt{-\frac{a^3}{27}}} . \tag{70}$$

Then the three solutions y_1, y_2, and y_3 are

$$\begin{aligned} y_1 &= 2\sqrt{-\frac{a}{3}}\cos\frac{\theta}{3} \\ y_2 &= 2\sqrt{-\frac{a}{3}}\cos\left(\frac{\theta}{3} + \frac{2\pi}{3}\right) \\ y_3 &= 2\sqrt{-\frac{a}{3}}\cos\left(\frac{\theta}{3} + \frac{4\pi}{3}\right) \end{aligned} \tag{71}$$

or, equivalently, the three solutions for x are

$$\begin{aligned} x_1 &= 2\sqrt{-\frac{a}{3}}\cos\frac{\theta}{3} - \frac{p}{3} \\ x_2 &= 2\sqrt{-\frac{a}{3}}\cos\left(\frac{\theta}{3} + \frac{2\pi}{3}\right) - \frac{p}{3} \\ x_3 &= 2\sqrt{-\frac{a}{3}}\cos\left(\frac{\theta}{3} + \frac{4\pi}{3}\right) - \frac{p}{3} . \end{aligned} \tag{72}$$

Comparing (66) and (67) and normalizing x by $2\Delta f_0$, we find that, corresponding to (72), we have the three solutions

$$\frac{x_1}{2\Delta f_0} = 2\sqrt{-\frac{a'}{3}}\cos\frac{\theta'}{3} + \frac{\xi}{3(1+\xi)}$$

$$\frac{x_2}{2\Delta f_0} = 2\sqrt{-\frac{a'}{3}}\cos\left(\frac{\theta'}{3} + \frac{2\pi}{3}\right) + \frac{\xi}{3(1+\xi)}$$

$$\frac{x_3}{2\Delta f_0} = 2\sqrt{-\frac{a'}{3}}\cos\left(\frac{\theta'}{3} + \frac{4\pi}{3}\right) + \frac{\xi}{3(1+\xi)}, \tag{73}$$

where

$$\theta' = \cos^{-1}\left\{-\frac{b'}{\sqrt{-\frac{a'^3}{27}}}\right\} \tag{74}$$

and

$$a' \triangleq \frac{a}{(2\Delta f_0)^2} = -\left\{\frac{\left(\frac{r_1}{r_1+1}\right)^2}{2\pi^2\left(\frac{\Delta f_0}{B_{L1}}\right)^2}\left[\frac{1 + \frac{(r_1+1)}{2}\frac{B_{LF}}{B_{L1}}}{(r_1+1)\frac{B_{LF}}{B_{L1}}}\right] + \frac{1}{3}\left(\frac{\xi}{1+\xi}\right)^2\right\}$$

$$b' \triangleq \frac{b}{(2\Delta f_0)^3} = -\frac{2}{27}\left(\frac{\xi}{1+\xi}\right)\left\{\left(\frac{\xi}{1+\xi}\right)^2 + \frac{9\left(\frac{r_1}{r_1+1}\right)^2}{4\pi^2\left(\frac{\Delta f_0}{B_{L1}}\right)^2}\left[\frac{1 - (r_1+1)\frac{B_{LF}}{B_{L1}}}{(r_1+1)\frac{B_{LF}}{B_{L1}}}\right]\right\}. \tag{75}$$

Letting $r_1 = 2$ and substituting the relation for ξ found in (44), we get

$$a' = -\left\{\frac{4/9}{2\pi^2\left(\frac{\Delta f_0}{B_{L1}}\right)^2}\left[\frac{1 + 1.5\left(\frac{B_{LF}}{B_{L1}}\right)}{3\left(\frac{B_{LF}}{B_{L1}}\right)}\right] + \frac{1}{3}\left(\frac{6.2\,\frac{F_{01}}{B_{L1}T}}{1 + 6.2\,\frac{F_{01}}{B_{L1}T}}\right)^2\right\}$$

$$b' = -\frac{2}{27}\left(\frac{6.2\,\frac{F_{01}}{B_{L1}T}}{1 + 6.2\,\frac{F_{01}}{B_{L1}T}}\right)\left\{\left(\frac{6.2\,\frac{F_{01}}{B_{L1}T}}{1 + 6.2\,\frac{F_{01}}{B_{L1}T}}\right)^2 + \frac{1}{\pi^2\left(\frac{\Delta f_0}{B_{L1}}\right)^2}\left[\frac{1 - 3\left(\frac{B_{LF}}{B_{L1}}\right)}{3\left(\frac{B_{LF}}{B_{L1}}\right)}\right]\right\}. \tag{76}$$

Although it appears from (73) that three solutions exist, in reality only the first, namely $x_1/2\Delta f_0$ results in

$$(1 + \xi)\frac{x_1}{2\Delta f_0} - \xi > 0 . \tag{77}$$

The inequality of (77) is necessary to insure a real solution for T_{ACQ}, since we observe that the above expression is the argument of the natural logarithm in the first term of (64). Finally, then, solving the first equation in (73) using (74) and (76), we can compute our desired upper bound on T_{ACQ} from [see (64)]

$$B_{L1}T'_{ACQ} = -\frac{1}{4}\left(\frac{B_{L1}}{B_{LF}}\right)\ln\left[\left(1 + 6.2\frac{F_{01}}{B_{L1}T}\right)\left(\frac{x_1}{2\Delta f_0}\right) - 6.2\frac{F_{01}}{B_{L1}T}\right]$$

$$+ 0.75\left\{\frac{9\pi^2}{4}\left(\frac{x_1}{2\Delta f_0}\right)^2\left(\frac{\Delta f_0}{B_{L1}}\right)^2 - \frac{1}{2}\ln\left[3\pi\left(\frac{x}{2\Delta f_0}\right)\left(\frac{\Delta f_0}{B_{L1}}\right)\right]\right\} . \tag{78}$$

Figures 4 and 5 illustrate $B_{L1}T'_{ACQ}$ as computed from (78) versus $\Delta f_0/B_{L1}$ for $F_{01} = 0.001$, $r_1 = 2$, and $B_{L1}T = 0.1$ and $B_{L1}T = 0.05$, respectively. The parameter of variation in both of these curves is the ratio of AFC loop bandwidth B_{LF} to Costas loop bandwidth B_{L1}. Also included on these curves is the acquisition time performance of a conventional Costas loop as computed from (52). The asymptote indicated by dashed lines is the pull-in range determined from (51) at which point the denominator of (52) vanishes and the acquisition time becomes infinite.

One final point before leaving the discussion of acquisition performance regards verification of the assumption made just prior to (62), allowing use of this simplified acquisition time formula rather than (52) in deriving the bound on acquisition time. The assumption made was that the solution found for the value of Δf_1 which minimized T'_{ACQ} would satisfy

$$\Delta f_1 << \frac{B_{L1}}{\pi}\left(\frac{r_1}{r_1 + 1}\right)\sqrt{\frac{2}{F_{01}} - 1} \tag{79}$$

or, equivalently,

$$\left(\frac{x_1}{2\Delta f_0}\right)\left(\frac{\Delta f_0}{B_{L1}}\right) << \frac{1}{\pi}\left(\frac{r_1}{r_1 + 1}\right)\sqrt{\frac{2}{F_{01}} - 1} . \tag{80}$$

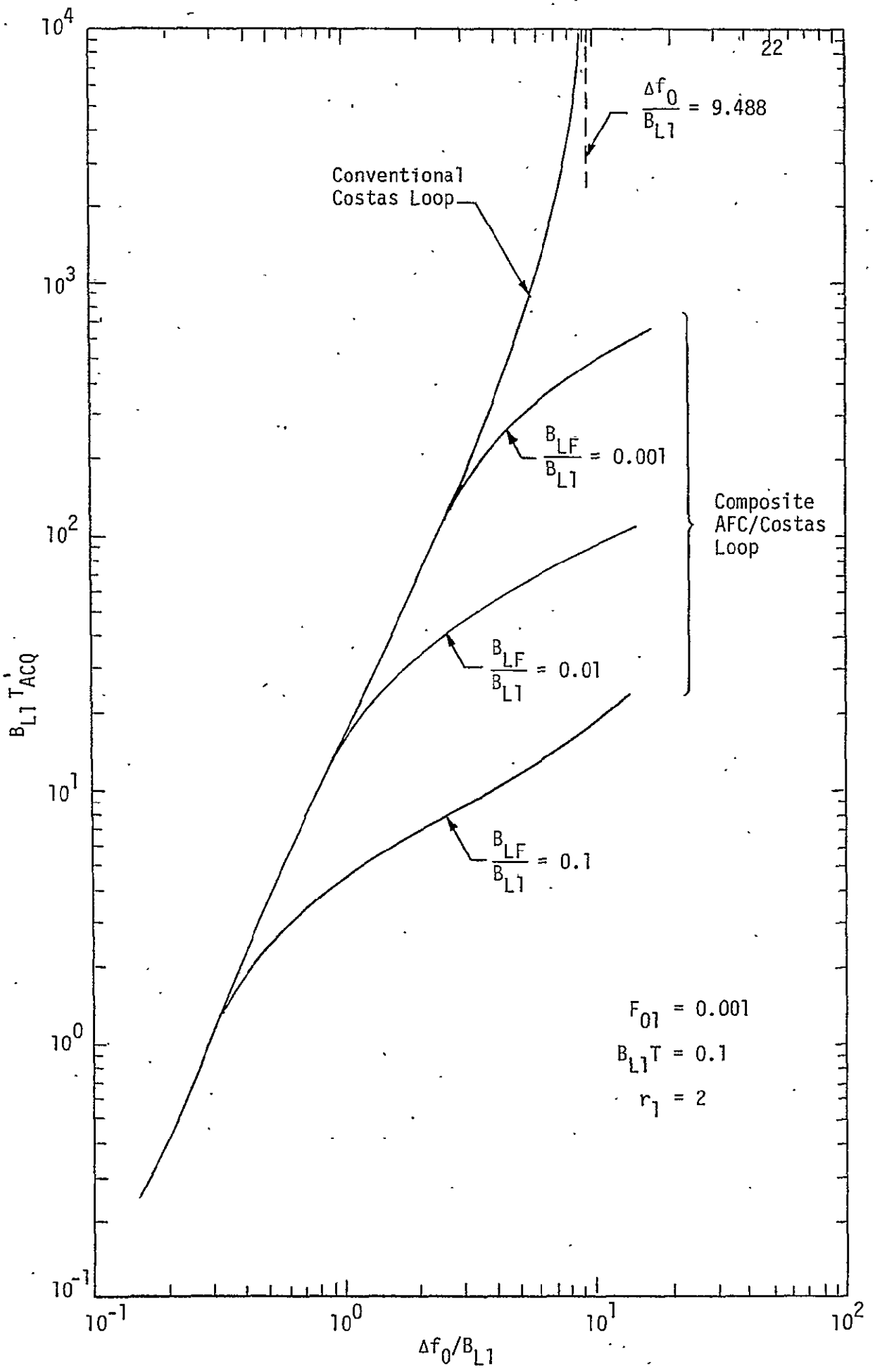

Figure 4. Acquisition Behavior of Composite AFC/Costas Loop

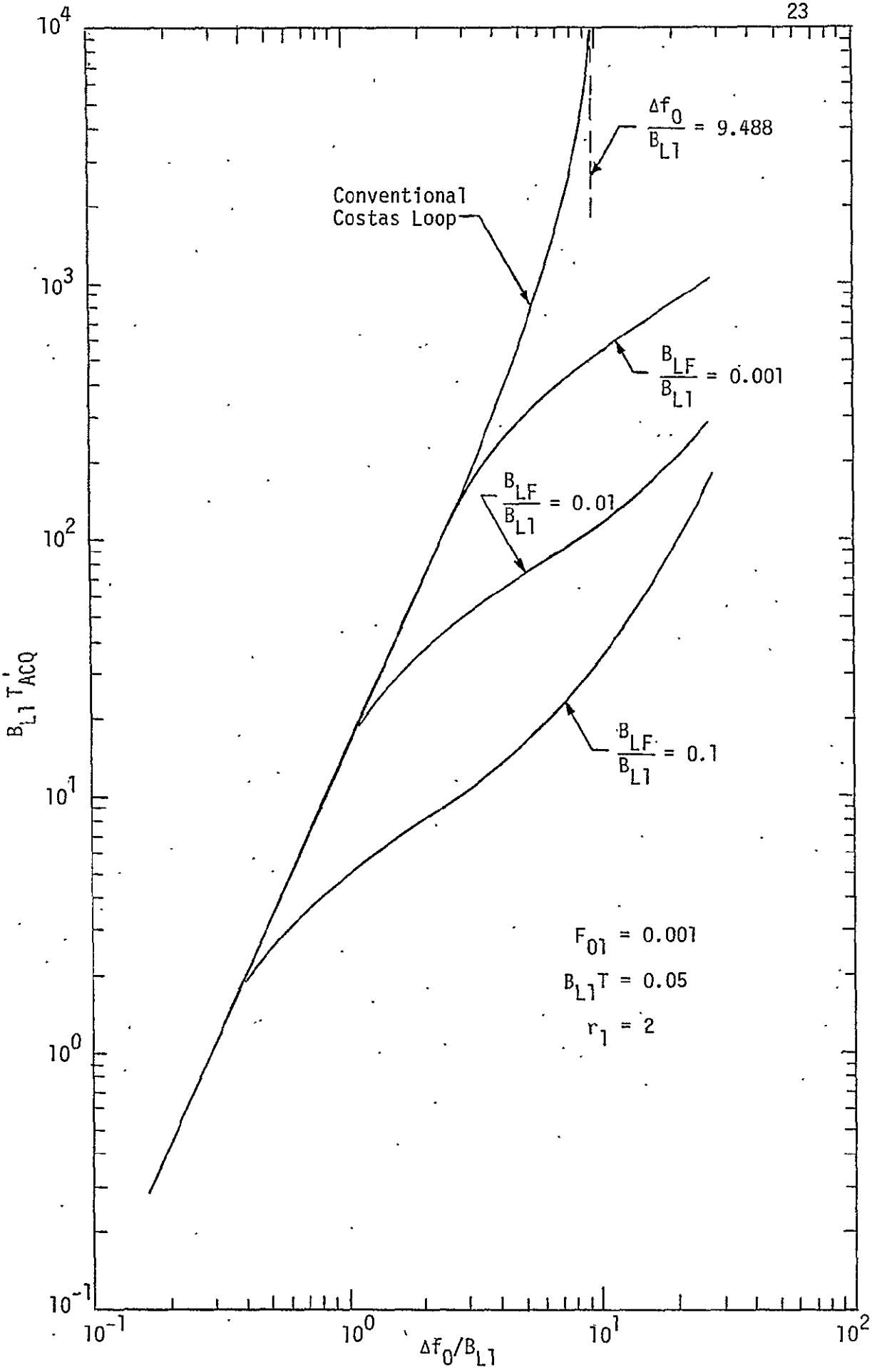

Figure 5. Acquisition Behavior of Composite AFC/Costas Loop

Using $x_1/(2\Delta f_0)$ as determined from (73), Figure 6 plots the left-hand side of (80) versus $\Delta f_0/B_{L1}$ for $r_1 = 2$ and $F_{01} = 0.001$. For these parameter values, the righthand side of (80) equals 9.488. Since the denominator of (52) is computed as one minus the square of the ratio of the lefthand to righthand side of (80), we observe from Figure 6 that this correction factor is well within our approximation over most values of frequency offset within the acquisition range.

TRACKING PERFORMANCE OF COMPOSITE AFC/COSTAS LOOP

In Appendix D, we considered the tracking performance of a composite AFC/Costas whose AFC and Costas loops shared a common loop filter. When separate loop filters are employed, as in Figure 1, the analysis is somewhat more complex due to the fact that the equivalent additive Costas loop noise and AFC error signal (which acts like additive noise when the loop is locked) are processed by different closed loop transfer functions insofar as evaluating phase tracking jitter. To see this, we begin by relating the VCO output phase to its two input signal components, i.e.,

$$\hat{\theta}(t) = \frac{K_V}{p}\left[F_1(p)\, z_0(t) + F_2(p)\, w_0(t)\right], \tag{81}$$

where $z_0(t)$ and $w_0(t)$ are given by equations (1) and (3) of Appendix D, namely,

$$z_0(t) = \frac{K_1^2 K_m^2}{2}\left\{\left[\sqrt{S}\,\hat{m}(t) - \hat{N}_s(t)\right]^2 - \hat{N}_c^2(t)\right\}\sin 2\phi(t) + K_1^2 K_m^2\, \hat{N}_c(t)\left[\sqrt{S}\,\hat{m}(t) - \hat{N}_s(t)\right]\cos 2\phi(t) \tag{82}$$

and

$$w_0(t) = K_1^2 K_m^2\left\{N_c(t)\left[\sqrt{S}\,\hat{m}(t) - \hat{N}_s(t)\right] - \hat{N}_c(t)\left[\sqrt{S}\,m(t) - N_s(t)\right]\right\}. \tag{83}$$

Alternately, separating $z_0(t)$ into its signal and noise components, we can rewrite (81) as

$$\hat{\theta}(t) = \frac{K_V K_1^2 K_m^2}{p}\left\{F_1(p)\left[S\hat{m}^2(t)\,\frac{\sin 2\phi}{2} + \frac{1}{2}\, v_2(t,2\phi)\right] + F_2(p)\,\frac{1}{2}\, w(t)\right\}, \tag{84}$$

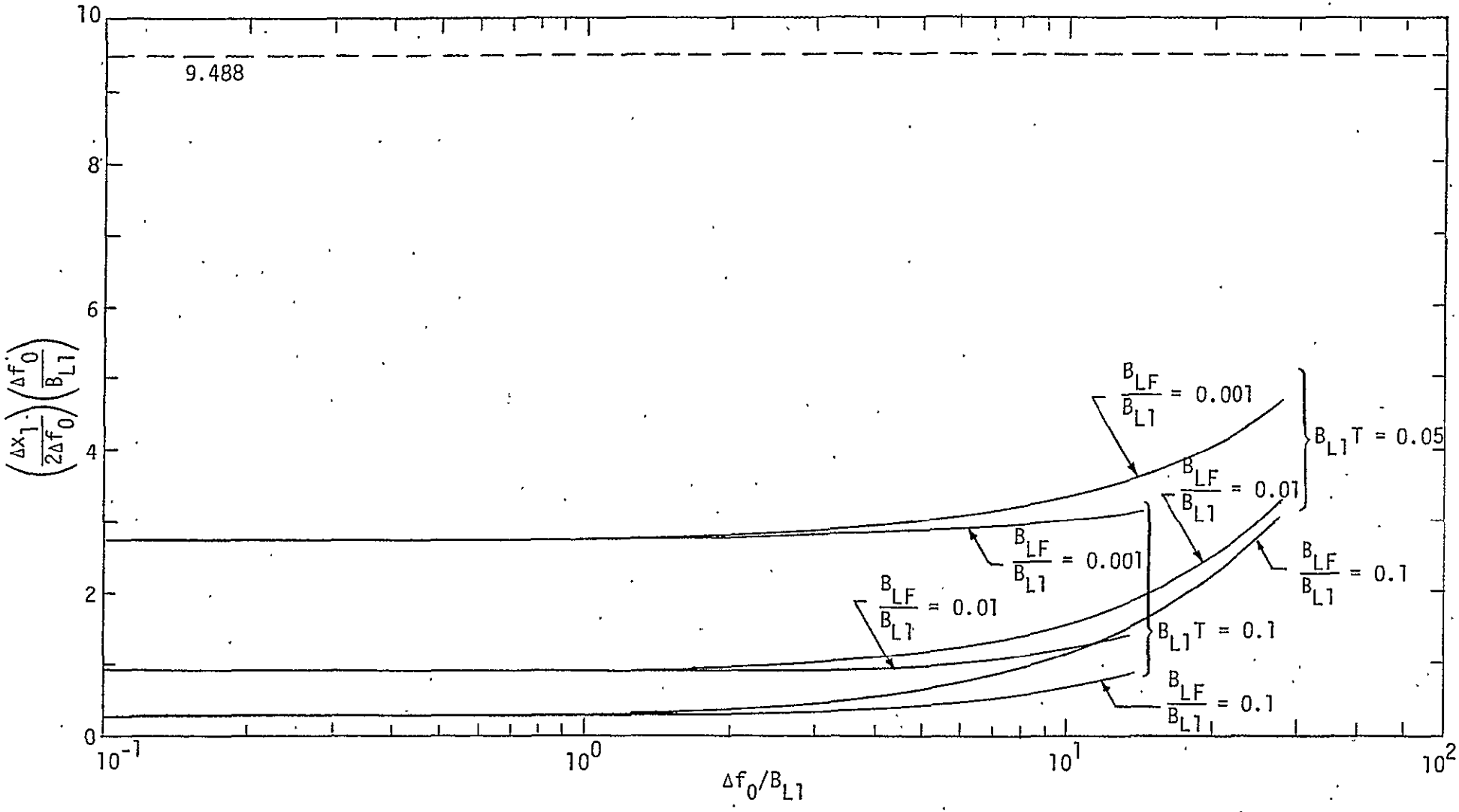

Figure 6. Check on Validity of Using Simplified Formula for Calculation of Costas Loop Acquisition Time

where

$$v_2(t,2\phi) \triangleq [-\hat{N}_c^2(t) + \hat{N}_s^2(t) - 2\sqrt{S}\,\hat{m}(t)\hat{N}_s(t)]\sin 2\phi + [2\sqrt{S}\,\hat{m}(t)\hat{N}_c(t) - 2\hat{N}_c(t)\hat{N}_s(t)]\cos 2\phi \quad (85)$$

and

$$w(t) \triangleq 2w_0(t) = 2\sqrt{S}\,\hat{m}(t)N_c(t) - 2N_c(t)\hat{N}_s(t) - 2\sqrt{S}\,m(t)\hat{N}_c(t) - 2\hat{N}_c(t)N_s(t) \quad . \quad (86)$$

Then, letting $K \triangleq K_V K_1^2 K_m^2$, replacing $\hat{m}^2(t)$ by $D_m \triangleq \langle\overline{m^2(t)}\rangle$, and ignoring as has been done previously (see [1]), the self-noise of the modulation, we get

$$2\dot{\hat{\theta}}(t) = \frac{K}{p}\{F_1(p)[S D_m \sin 2\phi(t) + v_2(t,2\phi)] + F_2(p)\,w(t)\} \quad . \quad (87)$$

Finally, letting $\phi_2(t) \triangleq 2\phi(t) = 2[\theta(t) - \hat{\theta}(t)] \triangleq \theta_2(t) - \hat{\theta}_2(t)$ and taking the linearized case, i.e., $\sin 2\phi(t) \cong 2\phi(t)$, gives the desired differential equation of loop operation, viz.,

$$\phi_2(t) = \theta_2(t) - \frac{K}{p}F_1(p)\,S D_m\,\phi_2(t) + \frac{K}{p}F_1(p)\,v_2(t,\phi_2) + \frac{K}{p}F_2(p)\,w(t) \quad (88)$$

or

$$\phi_2(t) = \frac{p}{p + S D_m K F_1(p)}\,\theta_2(t) + \frac{S D_m K F_1(p)}{p + S D_m K F_1(p)}\,\frac{v_2(t,\phi_2)}{S D_m} + \frac{S D_m K F_2(p)}{p + S D_m K F_1(p)}\,\frac{w(t)}{S D_m} \quad . \quad (89)$$

Defining, as is done for conventional Costas loops, the closed loop transfer function,

$$H_1(p) = \frac{S D_m K F_1(p)}{p + S D_m K F_1(p)} \quad , \quad (90)$$

equation (89) simplifies to

$$\phi_2(t) = [1 - H_1(p)]\,\theta_2(t) + H_1(p)\frac{v_2(t,\phi_2)}{S D_m} + \left[H_1(p)\,\frac{F_2(p)}{F_1(p)}\right]\frac{w(t)}{S D_m}$$

$$= [1 - H(p)]\,\theta_2(t) + N_e(t)\,, \tag{91}$$

where $N_e(t)$ is the total equivalent noise and, as predicted, is composed of the sum of the additive Costas loop noise $v_2(t,2\phi)$ and AFC error signal $w(t)$, each processed by different closed loop transfer functions. To evaluate the tracking performance of the composite loop, we must find the spectral density of $N_e(t)$.

From the definition of $N_e(t)$ given in (91), we see by inspection that its power spectral density $S_{N_e}(\omega)$ is given by

$$S_{N_e}(\omega) = \frac{1}{(S D_m)^2}\left|H_1(j\omega)\right|^2 S_{v_2}(\omega) + \frac{1}{(S D_m)^2}\left|H_1(j\omega)\right|^2 \left|\frac{F_2(j\omega)}{F_1(j\omega)}\right|^2 S_w(\omega)$$

$$+ \left(\frac{1}{S D_m}\right)^2 \left|H_1(j\omega)\right|^2 \frac{F_2(j\omega)}{F_1(j\omega)}\, S_{v_2 w}(\omega) + \left(\frac{1}{S D_m}\right)^2 \left|H_1(j\omega)\right|^2 \frac{F_2^*(j\omega)}{F_1^*(j\omega)}\, S_{w v_2}(\omega) \tag{92}$$

where the asterisk denotes complex conjugate, $S_{v_2}(\omega)$ and $S_w(\omega)$ are the power spectral densities of $v_2(t,\phi_2)$ and $w(t)$, respectively, and $S_{v_2 w}(\omega)$ and $S_{w v_2}(\omega)$ are the corresponding cross-spectral densities. Since the bandwidth of the Costas loop is ordinarily designed to be narrow with respect to the equivalent noise bandwidth of $v_2(t,\phi_2)$ and likewise for the AFC loop with respect to $w(t)$, we can approximate $v_2(t,\phi_2)$ and $w(t)$ as delta-correlated processes with power spectral densities $S_{v_2}(0)$ and $S_w(0)$, and cross-spectral densities $S_{v_2 w}(0)$ and $S_{w v_2}(0)$. From [1],

$$S_{v_2}(0) = 4S\left(\frac{N_0}{2}\right)\int_{-\infty}^{\infty} S_m(\omega)\,|G(j\omega)|^4\,\frac{d\omega}{2\pi} + 4\left(\frac{N_0}{2}\right)^2\int_{-\infty}^{\infty}|G(j\omega)|^4\,\frac{d\omega}{2\pi}\,. \tag{93}$$

Similarly, from the definition of $w(t)$ in (86) and the results of Appendix D, we find after some algebraic manipulation that

$$S_w(0) = 16 S \left(\frac{N_0}{2}\right) \int_{-\infty}^{\infty} S_m(\omega) \left[\text{Im } \{G(j\omega)\}\right]^2 \frac{d\omega}{2\pi}$$

$$+ 16 \left(\frac{N_0}{2}\right)^2 \int_{-\infty}^{\infty} \left[\text{Im } \{G(j\omega)\}\right]^2 \frac{d\omega}{2\pi}$$

$$S_{v_2 w}(0) = S_{w v_2}(0) = 0 . \tag{94}$$

Thus, substituting (93) and (94) into (92), and using similar definitions to those in Appendix D and [1], we get

$$S_{N_e}(\omega) = \frac{1}{(S D_m)^2} |H_1(j\omega)|^2 \left[2 S N_0 D_m K_D + N_0^2 B_i K_L\right]$$

$$+ \frac{1}{(S D_m)^2} |H_1(j\omega)|^2 \left|\frac{F_2(j\omega)}{F_1(j\omega)}\right|^2 \left[2 S N_0 D_m K_D + N_0^2 B_i K_L\right] , \tag{95}$$

where

$$K_D = \frac{\int_{-\infty}^{\infty} S_m(\omega) |G(j\omega)|^4 \frac{d\omega}{2\pi}}{\int_{-\infty}^{\infty} S_m(\omega) |G(j\omega)|^2 \frac{d\omega}{2\pi}} ; \quad K_D = \frac{\int_{-\infty}^{\infty} S_m(\omega) \left[\text{Im } \{G(j\omega)\}\right]^2 \frac{d\omega}{2\pi}}{\int_{-\infty}^{\infty} S_m(\omega) |G(j\omega)|^2 \frac{d\omega}{2\pi}}$$

$$K_L = \frac{\int_{-\infty}^{\infty} |G(j\omega)|^4 \frac{d\omega}{2\pi}}{\int_{-\infty}^{\infty} |G(j\omega)|^2 \frac{d\omega}{2\pi}} ; \quad K_L = \frac{\int_{-\infty}^{\infty} \left[\text{Im } \{G(j\omega)\}\right]^2 \frac{d\omega}{2\pi}}{\int_{-\infty}^{\infty} |G(j\omega)|^2 \frac{d\omega}{2\pi}}$$

$$D_m = \int_{-\infty}^{\infty} S_m(\omega) |G(j\omega)|^2 \frac{d\omega}{2\pi} ; \quad B_i = \int_{-\infty}^{\infty} |G(j\omega)|^2 \frac{d\omega}{2\pi} . \tag{96}$$

The total equivalent noise power, $\sigma_{N_e}^2$, can now be obtained by integrating (95) between minus infinity and infinity, viz.,

$$\sigma_{N_e}^2 \triangleq \int_{-\infty}^{\infty} S_{N_e}(\omega) \frac{d\omega}{2\pi} = \frac{1}{(S D_m)^2} \left[2 S N_0 D_m K_D + N_0^2 B_i K_L\right] \int_{-\infty}^{\infty} |H_1(j\omega)|^2 \frac{d\omega}{2\pi}$$

$$+ \frac{4}{(S D_m)^2} \left[2 S N_0 D_m K_D + N_0^2 B_i K_L\right] \int_{-\infty}^{\infty} |H_1(j\omega)|^2 \left|\frac{F_2(j\omega)}{F_1(j\omega)}\right|^2 \frac{d\omega}{2\pi} . \tag{97}$$

The first integral in (97) is the well-known relation for loop bandwidth of a second-order Costas loop, i.e.,

$$\int_{-\infty}^{\infty} |H_1(j\omega)|^2 \frac{d\omega}{2\pi} = 2B_{L1} \triangleq \frac{r_1 + 1}{2\tau_{21}} . \tag{98}$$

The second integral in (97) is evaluated as follows. Define

$$I_3 \triangleq \int_{-\infty}^{\infty} |H_1(j\omega)|^2 \left|\frac{F_2(j\omega)}{F_1(j\omega)}\right|^2 \frac{d\omega}{2\pi}$$

$$= \frac{1}{2\pi j} \int_{-\infty}^{\infty} A_3(s)\, A_3(-s)\, ds , \tag{99}$$

where

$$A_3(s) \triangleq H_1(s) \frac{F_2(s)}{F_1(s)}$$

$$= \frac{S D_m K + s[S D_m K(\tau_{22} + \tau_{11})] + s^2 S D_m K \tau_{11} \tau_{22}}{S D_m K + s[S D_m K(\tau_{21} + \tau_{12}) + 1] + s^2[\tau_{11} + \tau_{12}(S D_m K \tau_{21} + 1)] + s^3 \tau_{12}\tau_{11}}$$

$$= \frac{c_0 + c_1 s + c_2 s^2}{d_0 + d_1 s + d_2 s^2 + d_3 s^3} . \tag{100}$$

Integrals of the type given in (99) have been previously tabulated (see, for example, Ref. 2, p. 135, Table 4-1). When the denominator of $A_n(s)$ is a third-order polynomial, i.e., $n = 3$, then the result is

$$I_3 = \frac{c_2^2 d_0 d_1 + (c_1^2 - 2 c_0 c_2) d_0 d_3 + c_0^2 d_2 d_3}{2 d_0 d_3 (d_1 d_2 - d_0 d_3)} . \tag{101}$$

Substituting (100) into (101), one obtains after considerable simplification

$$I_3 \triangleq 2B_{L12} = \left(\frac{F_{02}}{F_{01}}\right)^2 \frac{r_1 + \left(\frac{\tau_{21}}{\tau_{22}}\right)^2}{2\tau_{21}} , \tag{102}$$

where we have made only the assumption that $F_{01}, F_{02} \ll 1$. Further relating B_{L12} to the bandwidth B_{L1} of the Costas loop alone by

$$B_{L12} = \gamma_B B_{L1} , \tag{103}$$

one can show, using (23), (27), (29), (36), (47), and (102), that

$$\gamma_B = \frac{r_2\left(\frac{B_{LF}}{B_{L1}}\right)}{\left(\frac{r_1}{r_1+1}\right)^2\left[K_c B_{L1} T + \frac{F_{01}(r_1+1)}{4 r_1}\right]}\left\{\left(\frac{r_1}{r_1+1}\right) + \frac{\left(\frac{r_1+1}{4 r_2}\right)\left(\frac{B_{LF}}{B_{L1}}\right)}{K_c B_{L1} T + \frac{F_{01}(r_1+1)}{4 r_1}}\right\}$$

$$\cong \frac{\frac{(r_1+1)}{4}\left(\frac{B_{LF}}{B_{L1}}\right)^2}{\left(\frac{r_1}{r_1+1}\right)^2\left\{K_c B_{L1} T\left[1 + \frac{F_{01}(r_1+1)}{4 r_1 K_c B_{L1} T}\right]\right\}^2} . \tag{104}$$

For $r_1 = 2$ and $\omega_c T = 2.8\pi$, we recall that $K_c = 0.0605$. Thus, for these parameters, (104) reduces to

$$\gamma_B = \frac{12\left(\frac{B_{LF}}{B_{L1}}\right)^2}{\left[\frac{B_{L1} T}{6.2}(1+\xi)\right]^2} \tag{105}$$

where ξ is defined in (44). Figure 7 illustrates the bandwidth ratio γ_B as computed from (105) versus B_{LF}/B_{L1} for $F_{01} = 0.001$ and $B_{L1} T = 0.05, 0.1$.

Finally, combining (97), (98), (102), and (103), the total equivalent noise power, which is identical to the mean-square phase tracking jitter $\sigma_{\phi_2}^2$, is given by

$$\sigma_{\phi_2}^2 = \frac{4}{\rho S_{L_1}} + \frac{4}{\rho S_{L_2}}$$

$$= \sigma_1^2 + \sigma_2^2 , \tag{106}$$

where

$$\rho = \frac{S}{N_0 B_{L1}}$$

is the signal-to-noise ratio of an equivalent linear loop, e.g., a phase-locked loop, having a bandwidth equal to that of the Costas loop, S_{L_1} is

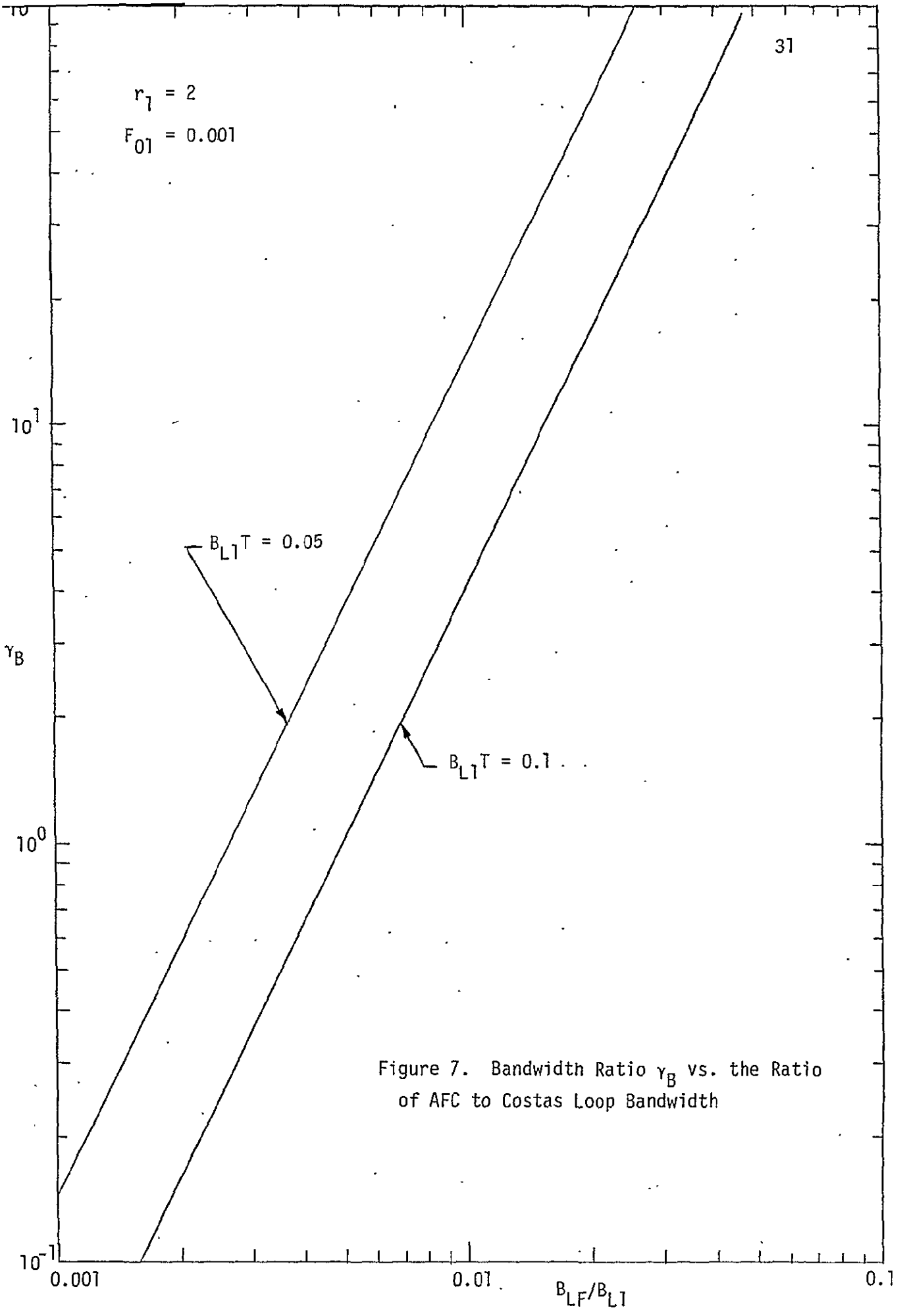

Figure 7. Bandwidth Ratio γ_B vs. the Ratio of AFC to Costas Loop Bandwidth

the familiar squaring loss of the Costas loop, namely,

$$S_{L_1} = \frac{D_m}{K_D + \frac{K_L}{\rho_i D_m}} \tag{107}$$

and S_{L_2} is the squaring loss of the AFC loop which is defined by

$$S_{L_2} = \frac{D_m}{4\gamma_B \left[K_D + \frac{K_L}{\rho_i D_m}\right]} . \tag{108}$$

In (107) and (108), $\rho_i \triangleq 2S/N_0B_i$ is the signal-to-noise ratio in the arm filter bandwidth. For a single-pole RC arm filter as in Figure 1, we have already shown in Appendix D that

$$K_L = K_L = \frac{1}{2} . \tag{109}$$

Furthermore, for Manchester coded data, K_D and K_D defined in (96) can be evaluated as

$$K_D = \frac{1 - \frac{9 - 4\left(3 + \frac{\omega_c T}{2}\right) e^{-\omega_c T/2} + (3 + \omega_c T) e^{-\omega_c T}}{2\omega_c T}}{1 - \frac{3 - 4e^{-\omega_c T/2} + e^{-\omega_c T}}{\omega_c T}} \tag{110}$$

and

$$K_D = \frac{\frac{2}{\omega_c T}\left[\frac{3}{4} - \left(1 + \frac{\omega_c T}{2}\right) e^{-\omega_c T/2} + \frac{(1 + \omega_c T)}{4} e^{-\omega_c T}\right]}{1 - \frac{3 - 4e^{-\omega_c T/2} + e^{-\omega_c T}}{\omega_c T}} . \tag{111}$$

Figure 8 illustrates K_D and K_D as defined in (110) and (111) versus $f_c T = \omega_c T/2\pi$. At $\omega_c T = 2.8\pi$, (110) and (111) are evaluated as $K_D = 0.766$ and $K_D = 0.234$. Also, from (28), $D_m = 0.6645$. Thus, the component of phase tracking jitter due to the Costas loop is given by

$$\sigma_1^2 = \frac{4N_0B_{L1}}{S}\left[\frac{0.766 + \frac{0.7524}{\rho_i}}{0.6645}\right] . \tag{112}$$

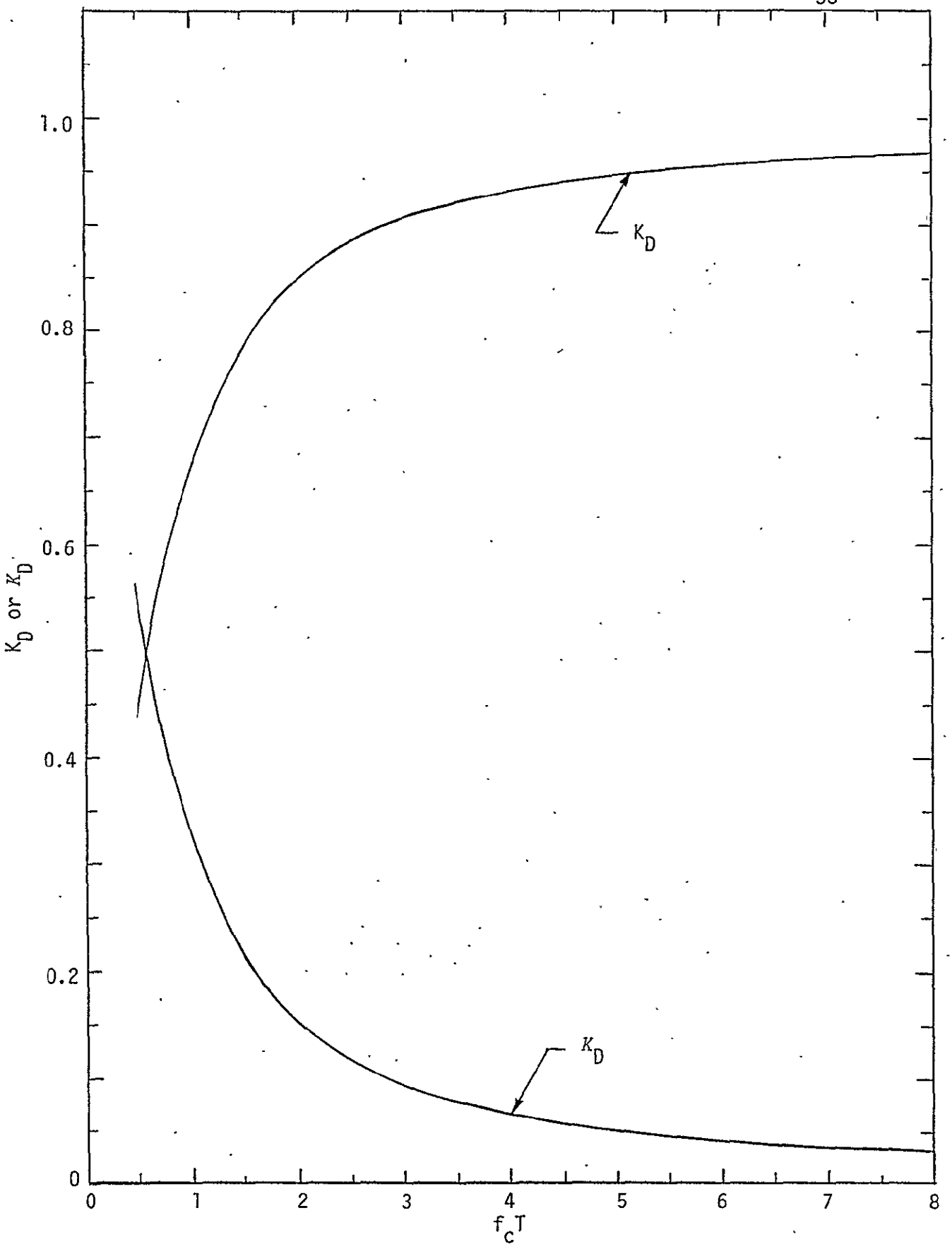

Figure 8. K_D and $\mathcal{K}_D$ vs. f_cT for RC Arm Filter and Manchester Coded Data

Since for a single-pole RC filter, $B_i = \omega_c/2$, we can express ρ_i as

$$\rho_i \triangleq \frac{S}{N_0 B_i} = \frac{S}{N_0 B_{L1}} (B_{L1} T) \frac{1}{B_i T}$$

$$= \frac{S}{N_0 B_{L1}} (B_{L1} T) \frac{2}{\omega_c T} = \frac{S}{N_0 B_{L1}} \left(\frac{B_{L1} T}{1.4\pi}\right). \quad (113)$$

Thus, (112) can be rewritten as

$$\sigma_1^2 = \frac{4 N_0 B_{L1}}{S} \left[1.153 + 4.98 \left(\frac{N_0 B_{L1}}{S}\right)\left(\frac{1}{B_{L1} T}\right)\right]. \quad (114)$$

Similarly, the AFC loop component of phase tracking jitter is given by

$$\sigma_2^2 = \frac{4 N_0 B_{L1}}{S} \left[0.352 + 4.98 \left(\frac{N_0 B_{L1}}{S}\right)\left(\frac{1}{B_{L1} T}\right)\right] \left\{ \frac{48 \left(\frac{B_{LF}}{B_{L1}}\right)^2}{\left[\frac{B_{L1} T}{6.2}\left(1 + \frac{6.2 F_{01}}{B_{L1} T}\right)\right]^2} \right\} \quad (115)$$

Figures 9 and 10 illustrate the component mean-square phase tracking jitters σ_1^2, σ_2^2 as computed from (114) and (115) versus $S/N_0 B_{L1}$ in dB for $F_{01} = 0.001$ and $B_{L1} T = 0.1, 0.05$, respectively. The parameter in both of the figures is the ratio of AFC to Costas loop bandwidth. Comparing Figures 9 and 10 with Figures 4 and 5, one immediately observes the tradeoff between acquisition and tracking performance of the composite loop as the above-mentioned bandwidth ratio is varied.

REFERENCES

1. Simon, M. K., and Lindsey, W. C. "Optimum Performance of Suppressed Carrier Receivers with Costas Loop Tracking," IEEE Transactions on Communications, Vol. COM-25, No. 2, February 1977, pp. 215-227.

2. Lindsey, W. C. Synchronization Systems in Communication and Control, Prentice-Hall, Inc., Englewood Cliffs, N.J., 1972.

Figure 9. Tracking Jitter Performance Components for Composite AFC/Costas Loop

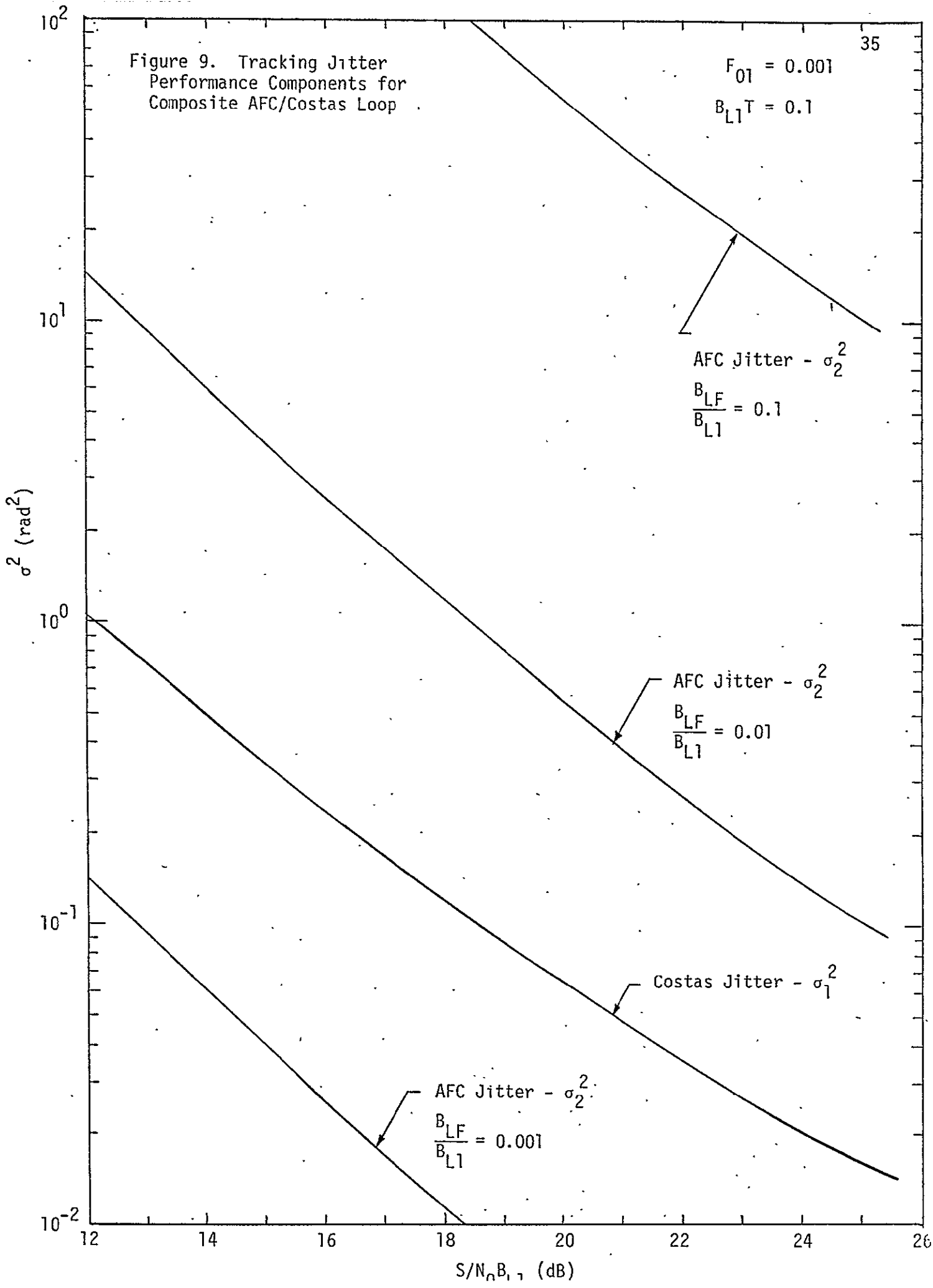

Figure 10. Tracking Jitter Performance Components for Composite AFC/Costas Loop

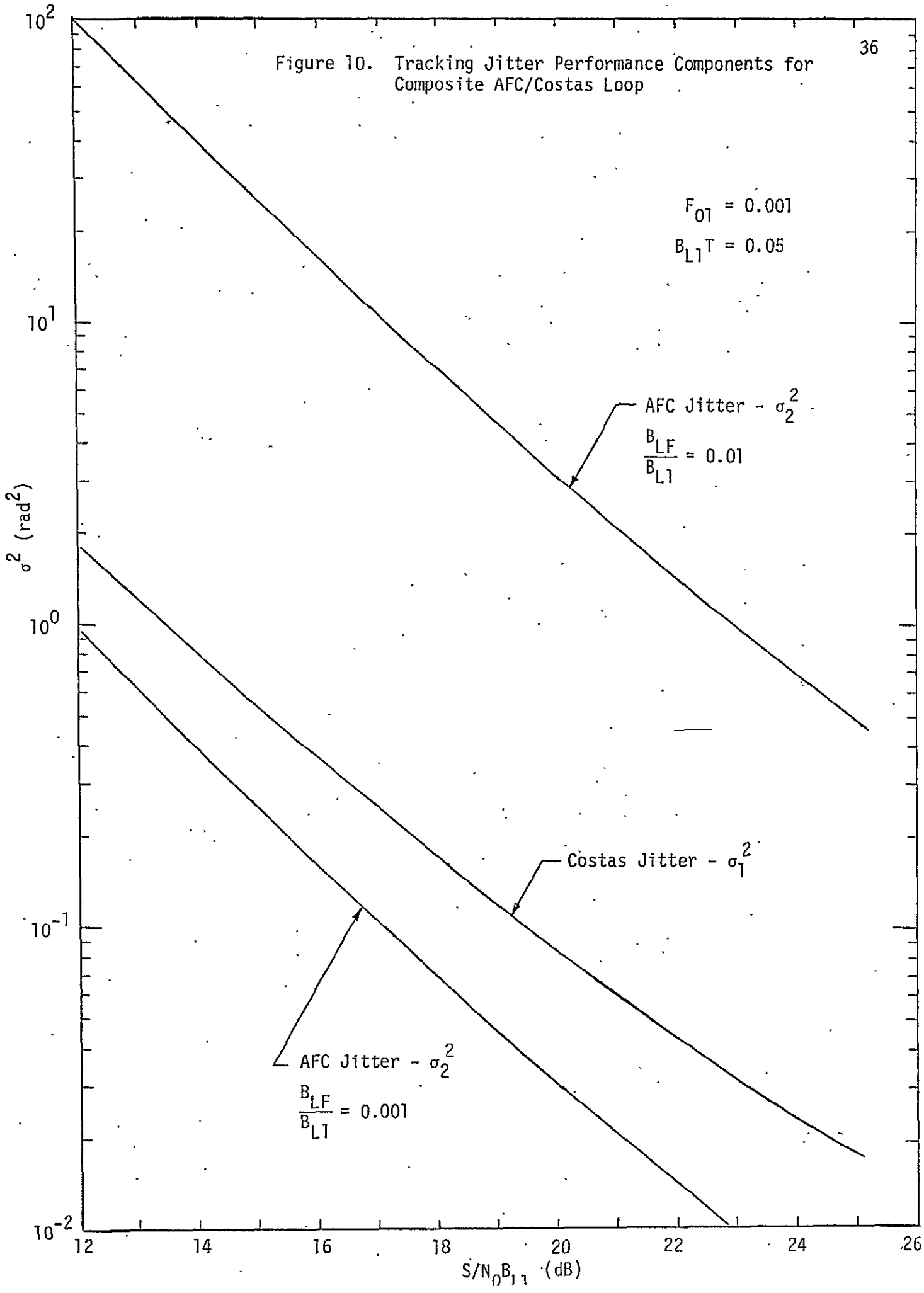

APPENDIX F

THE PERFORMANCE OF A LOCK DETECTOR FOR COSTAS-TYPE RECEIVERS

APPENDIX F

THE PERFORMANCE OF A LOCK DETECTOR FOR COSTAS-TYPE RECEIVERS

by

Marvin K. Simon

INTRODUCTION

An important consideration in the design of Costas-type receivers is the role played by the lock detector associated with the Costas loop. In particular, the primary purpose of the lock detector is to identify the locked state during the carrier acquisition process. Furthermore, since carrier acquisition in the presence of large frequency uncertainties caused by doppler shift and oscillator instabilities is commonly achieved by sweeping the carrier VCO (either discretely or continuously) in frequency, a secondary function of the lock detector is to kill this sweep once carrier lock has been detected. By doing this, the Costas loop is not required to track its own sweep, and thus the steady-state tracking performance is not degraded by the loop stress which would accompany the sweep waveform. Also, killing the sweep serves to minimize the acquisition time.

Lock detection in a Costas loop is most readily achieved by nonlinear processing the signals out of the in-phase and quadrature phase channels, differencing the results, and comparing to a preset threshold. The nonlinear processing is customarily accomplished using balanced square-law devices, although an absolute-value type of nonlinearity, e.g., full-wave rectifiers, has advantage when such effects as AGC gain variations, phase detector dc offsets, and arm gain imbalance are other than small. The threshold is fixed by the false alarm probability, i.e., the probability of deciding that the loop has achieved a locked state given that it is in reality out of lock.

When the loop is far out of lock, a double frequency beat note appears at the input to the integrate-and-dump. For a stepped sweep acquisition, the beat note will remain constant in frequency over the duration in time of a single step. As the sweep continues and the loop approaches a locked condition (either true or false lock), a point is reached where the beat note becomes within the pull-in range of the loop

at which time the beat note disappears and a sync pulse whose amplitude is proportional to the steady-state tracking loop jitter appears at the input of the integrate-and-dump. As soon as the sync pulse is sensed by the lock detector, an action is taken to kill the sweep; however, until such time the sweep continues to step along and, depending on the sweep rate, the loop may break lock and resume beating. Since, as we shall see, for a fixed data rate, signal power to noise spectral density ratio, and specified probabilities of false alarm and false detection, the integration time of the integrate-and-dump is determined, the sweep rate is also set by these same quantities.

LOCK DETECTOR MODEL

Figure 1 illustrates a conventional Costas loop and its associated lock detector. The approach taken in Appendix A to characterize the false lock behavior of the loop can also be used here to good advantage in deriving the performance of the lock detector. In particular, starting with equation (8) of the above reference for $z_c(t)$ and $z_s(t)$, we get after square-law detection and differencing the result:*

$$\begin{aligned} z_d(t) \triangleq z_s^2(t) - z_c^2(t) = {} & K_1^2 K_m^2 S\,[\hat{m}_c^2(t;\omega_b,\phi) - \hat{m}_s^2(t;\omega_b,\phi)] \\ & + K_1^2 K_m^2\,[\hat{N}_{sc}^2(t;\omega_b,\phi) + \hat{N}_{cs}^2(t;\omega_b,\phi) \\ & \quad - \hat{N}_{ss}^2(t;\omega_b,\phi) - \hat{N}_{cc}^2(t;\omega_b,\phi) \\ & \quad + 2\,\hat{N}_{sc}(t;\omega_b,\phi)\,\hat{N}_{cs}(t;\omega_b,\phi) \\ & \quad - 2\,\hat{N}_{ss}(t;\omega_b,\phi)\,\hat{N}_{cc}(t;\omega_b,\phi)] \\ & - 2K_1^2K_m^2\sqrt{S}\,\{\hat{m}_c(t;\omega_b,\phi)[\hat{N}_{sc}(t;\omega_b,\phi) + \hat{N}_{cs}(t;\omega_b,\phi)] \\ & \quad - \hat{m}_s(t;\omega_b,\phi)[\hat{N}_{ss}(t;\omega_b,\phi) - \hat{N}_{cc}(t;\omega_b,\phi)]\} \end{aligned} \tag{1a}$$

*Note that we are using ω_b instead of ω_f as was done in Appendix A, since here we are concerned with the beat note frequency rather than the false lock frequency. Also, the overbar in (1) denotes statistical expectation with respect to the data sequence.

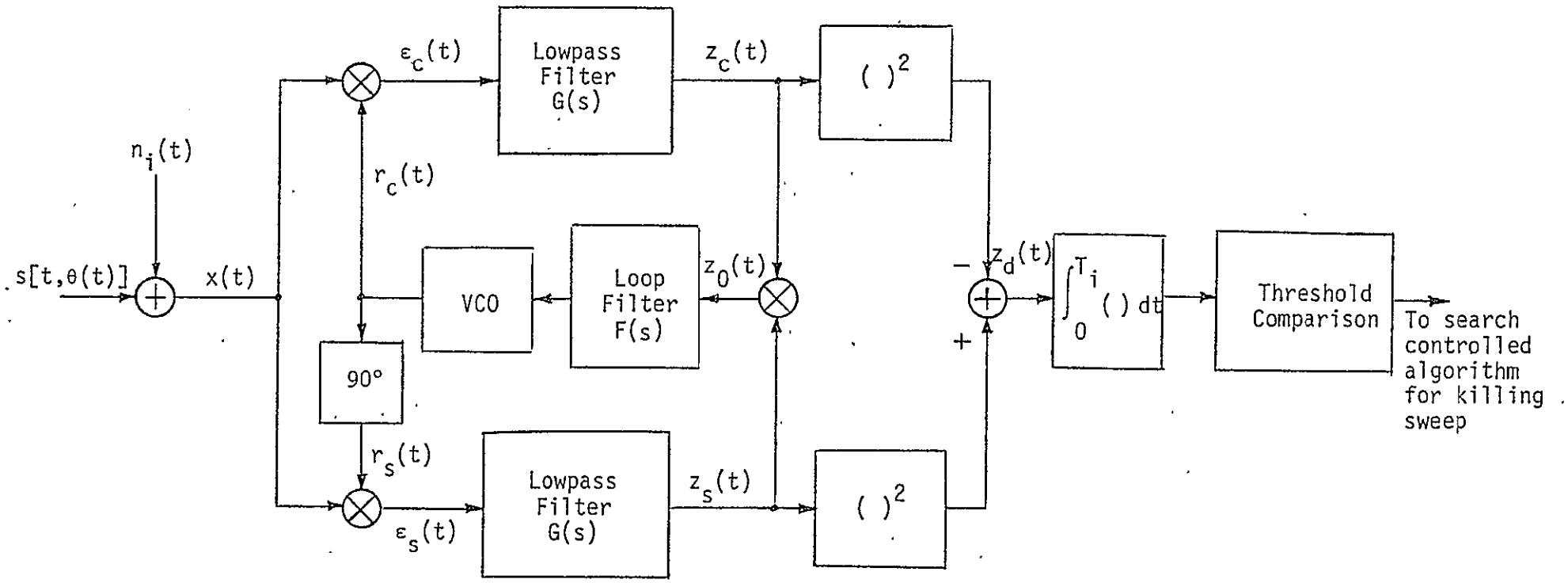

Figure 1. Costas Loop and Associated Lock Detector

$$z_d(t) \triangleq z_s^2(t) - z_c^2(t) = K_1^2 K_m^2 S\,\overline{\hat{m}_c^2(t;\omega_b,\phi) - \hat{m}_s^2(t;\omega_b,\phi)} + K_1^2 K_m^2 S\, n_\Delta(t;\omega_b,\phi) + K_1^2 K_m^2 u_2(t;\omega_b,\phi) , \quad (1b)$$

where the self-noise process $n_\Delta(t;\omega_b,\phi)$ is defined by

$$n_\Delta(t;\omega_b,\phi) \triangleq \hat{m}_c^2(t;\omega_b,\phi) - \hat{m}_s^2(t;\omega_b,\phi) - \overline{[\hat{m}_c^2(t;\omega_b,\phi) - \hat{m}_s^2(t;\omega_b,\phi)]} \quad (2)$$

and $u_2(t;\omega_b,\phi)$ is the total of the signal x noise and noise x noise terms. When the loop is out of lock, the parameter ω_b denotes the beat note radian frequency, i.e., the difference between the frequency of the Costas loop input signal and that of the swept VCO, and ϕ is the loop phase error which may be assumed to be uniformly distributed between $-\pi$ and π. When the loop is in lock, then $\omega_b = 0$ for true lock or $\omega_b = \omega_f = \pi k/T$ for the kth false lock frequency, and ϕ is the tracking phase error of the loop (see [1] for the statistical characterization of ϕ).

The mean (signal) term in (1) can be derived starting with (15) of Appendix A and the assumption of random data with the result:

$$\overline{\hat{m}_c^2(t;\omega_b,\phi) - \hat{m}_s^2(t;\omega_b,\phi)} = \sum_{k=-\infty}^{\infty} C_k \cos\left[2\left(\omega_b + \frac{\pi k}{T}\right)t + 2\phi\right] - S_k \sin\left[2\left(\omega_b + \frac{\pi k}{T}\right)t + 2\phi\right] \quad (3)$$

where

$$C_k \triangleq \frac{1}{T}\,\mathrm{Re}\left\{\int_{-\infty}^{\infty} G\left[j\left(-\omega + \frac{2\pi k}{T} + \omega_b\right)\right] G[j(\omega+\omega_b)]\, P\left[j\left(-\omega + \frac{2\pi k}{T}\right)\right] P(j\omega)\frac{d\omega}{2\pi}\right\}$$

$$S_k \triangleq \frac{1}{T}\,\mathrm{Im}\left\{\int_{-\infty}^{\infty} G\left[j\left(-\omega + \frac{2\pi k}{T} + \omega_b\right)\right] G[j(\omega+\omega_b)]\, P\left[j\left(-\omega + \frac{2\pi k}{T}\right)\right] P(j\omega)\frac{d\omega}{2\pi}\right\} . \quad (4)$$

The self-noise term in (1) has only a continuous power spectrum. Analogous with (17) of [1], the value of this spectrum at the origin is given by

$$S_{\Delta_c}(0) = 4T \cdot \sum_{\ell=1}^{\infty} R_{\hat{m}}^2(\ell T;\omega_b) \tag{5}$$

where

$$R_{\hat{m}}(\tau;\omega_b) \triangleq \frac{1}{T}\int_{-\infty}^{\infty} |G(j\omega)|^2 \cdot P[j(\omega-\omega_b)]\, P[-j(\omega+\omega_b)]\, e^{j\omega\tau}\,\frac{d\omega}{2\pi} \tag{6}$$

or, equivalently,

$$S_{\Delta_c}(0) = \frac{4}{T^2}\cdot\sum_{\ell=1}^{\infty}\int_{-\infty}^{\infty} |G(j\omega)|^2\, P[j(\omega-\omega_b)]\, P[-j(\omega+\omega_b)] \times \left|G\left[j\left(\frac{2\pi\ell}{T}-\omega\right)\right]\right|^2 P\left[j\left(\frac{2\pi\ell}{T}-\omega-\omega_b\right)\right] P\left[-j\left(\frac{2\pi\ell}{T}-\omega-\omega_b\right)\right]\frac{d\omega}{2\pi}\,. \tag{7}$$

Finally, we must characterize the additive noise $u_2(t;\omega_b,\phi)$ in (1). When the loop is in a true lock condition, i.e., $\omega_b = 0$, then

$$\begin{aligned} u_2(t;0,\phi) &= [-\hat{N}_c^2(t) + \hat{N}_s^2(t) - 2\sqrt{S}\,\hat{m}(t)\,\hat{N}_s(t)]\cos 2\phi(t) \\ &\quad - [2\sqrt{S}\,\hat{m}(t)\,\hat{N}_c(t) - 2\,\hat{N}_c(t)\,\hat{N}_s(t)]\sin 2\phi(t) \\ &\triangleq u_2(t,2\phi)\,, \end{aligned} \tag{8}$$

which is identical to the total signal x noise and noise x noise at the error control point $z_0(t)$ in the loop (see [1]). Thus, $u(t,2\phi)$ can be characterized as a delta-correlated process with equivalent spectral density

$$N_{sq} \triangleq 2\int_{-\infty}^{\infty} R_{u_2}(\tau)\, d\tau\,, \tag{9}$$

where

$$R_{u_2}(\tau) \triangleq \overline{u_2(t,2\phi)\, u_2(t+\tau,2\phi)}\,. \tag{10}$$

Since, when the loop is approaching true lock, the beat note frequency ω_b is quite small with respect to the data rate, the additive noise $u_2(t;\omega_b,\phi)$ is approximately characterized by (8) with $\phi(t)$ replaced by $\phi(t) + \omega_b t$. Thus, the equivalent spectral density of the out-of-lock total signal x noise and noise x noise is also given by (9).

Passing $z_d(t)$ through an integrate-and-dump of duration T_i results in an output random variable x which, for large T_i/T, is approximately Gaussian distributed with mean μ_x given by

$$\mu_x = K_1^2 K_m^2 S \left\{ \sum_{k=-\infty}^{\infty} C_k \overline{\int_0^{T_i} \cos \left[2\left(\omega_b + \frac{\pi k}{T}\right)t + 2\phi \right] dt} - \sum_{k=-\infty}^{\infty} S_k \overline{\int_0^{T_i} \sin \left[2\left(\omega_b + \frac{\pi k}{T}\right)t + 2\phi \right] dt} \right\} \qquad (11)$$

where the overbar now denotes statistical mean with respect to the probability density function (p.d.f.) of ϕ. When the loop is out of lock, and $p(\phi)$ is a uniform distribution on $(-\pi,\pi)$ as previously assumed, then

$$\mu_x\Big|_{O.L.} = 0 . \qquad (12)$$

When the loop is in lock, i.e., $\omega_b = 0$, then

$$\mu_x\Big|_{I.L.} = K_1^2 K_m^2 S T_i \left[C_0\Big|_{\omega_b=0} \overline{\cos 2\phi} - S_0\Big|_{\omega_b=0} \overline{\sin 2\phi} \right] . \qquad (13)$$

Substituting $\omega_b = 0$ and $k = 0$ in (4) gives

$$C_0\Big|_{\omega_b=0} = \frac{1}{T} \int_{-\infty}^{\infty} |G(j\omega)|^2 |P(j\omega)|^2 \frac{d\omega}{2\pi} = \int_{-\infty}^{\infty} S_m(\omega) |G(j\omega)|^2 \frac{d\omega}{2\pi} \triangleq D_m$$

$$S_0\Big|_{\omega_b=0} = 0 , \qquad (14)$$

where $S_m(f)$ is the power spectrum of the data modulation m(t). Thus, using (14), the mean μ_x of (13) simplifies to

$$\mu_x\Big|_{I.L.} = K_1^2 K_m^2 S T_i D_m \overline{\cos 2\phi} . \qquad (15)$$

The total noise out of the integrate-and-dump consists of three components: one due to the total signal x noise and noise x noise terms, a second due to the self-noise of the modulation, and a third which, when the loop is out of lock, is referred to as "beat note noise" and, when the loop is in lock, is proportional to the loop tracking jitter. The

variance of the first two noise components in x is then

$$\sigma_{x_1}^2 + \sigma_{x_2}^2 = K_1^4 K_m^4 \left[\frac{N_{sq} + 2S^2 S_{\Delta_c}(0)\ \overline{\cos^2 2\phi}}{2}\right] T_i \ . \qquad (16)$$

The beat note noise is caused by the lack of coherence between the beat note and the integrate-and-dump timing instants. In particular,

$$E\left\{x_3^2\right\} = K_1^4 K_m^4 S^2 T_i^2 \left\{\sum_{k=-\infty}^{\infty} C_k \frac{1}{T_i}\int_0^{T_i} \cos\left[2\left(\omega_b + \frac{\pi k}{T}\right)t + 2\phi\right] dt\right.$$

$$\left. - \sum_{k=-\infty}^{\infty} S_k \frac{1}{T_i}\int_0^{T_i} \sin\left[2\left(\omega_b + \frac{\pi k}{T}\right)t + 2\phi\right] dt\right\}^2 \qquad (17)$$

which, for $T_i/T \gg 1$, simplifies to

$$E\left\{x_3^2\right\} = K_1^4 K_m^4 S^2 T_i^2 \left\{C_0\left[\frac{\sin\left[2\omega_b T_i + 2\phi\right]}{2\ \omega_b T_i} - \frac{\sin 2\phi}{2\ \omega_b T_i}\right]\right.$$

$$\left. + S_0\left[\frac{\cos\left[2\omega_b T_i + 2\phi\right]}{2\ \omega_b T_i} - \frac{\cos 2\phi}{2\ \omega_b T_i}\right]\right\}^2 . \qquad (18)$$

For ϕ uniformly distributed and $\mu_x = 0$, (18) becomes

$$\sigma_{x_3}^2\Big|_{O.L.} = K_1^4 K_m^4 S^2 T_i^2 \left\{\frac{C_0^2}{(2\omega_b T_i)^2}\left[1 - \cos 2\omega_b T_i\right] + \frac{S_0^2}{(2\omega_b T_i)^2}\left[1 - \cos 2\omega_b T_i\right]\right\} \qquad (19)$$

or

$$\sigma_{x_3}^2\Big|_{O.L.} = \frac{K_1^4 K_m^4 S^2 T_i^2 (C_0^2 + S_0^2)}{2}\left(\frac{\sin \omega_b T_i}{\omega_b T_i}\right)^2 . \qquad (20)$$

Letting $k = 0$ in (4) and recalling that $S_m(\omega) = |P(j\omega)|^2/T$, we get

$$C_0^2 + S_0^2 = \left|\int_{-\infty}^{\infty} S_m(\omega)\ G[j(-\omega + \omega_b)]\ G[j(\omega + \omega_b)]\ \frac{d\omega}{2\pi}\right|^2 . \qquad (21)$$

In general, the beat note noise is a function of the beat note frequency. However, as the loop approaches true lock and the beat note frequency becomes small with respect to the data rate 1/T, then

$$C_0^2 + S_0^2 \longrightarrow D_m^2 \tag{22}$$

and

$$\sigma_{x_3}^2\Big|_{O.L.} \longrightarrow \frac{K_1^4 K_m^4 S^2 T_i^2 D_m^2}{2} \left(\frac{\sin \omega_b T_i}{\omega_b T_i}\right)^2 . \tag{23}$$

When the loop is in lock, $\sigma_{x_3}^2$ is given by (17) with $\omega_b = 0$ minus μ_x of (15) squared, or

$$\sigma_{x_3}^2\Big|_{I.L.} = K_1^4 K_m^4 S^2 T_i^2 D_m^2 \, \sigma_{\cos 2\phi}^2 , \tag{24}$$

where

$$\sigma_{\cos 2\phi}^2 \triangleq \overline{\cos^2 2\phi} - (\overline{\cos 2\phi})^2 . \tag{25}$$

Finally, the total variance of x is given by the sum of (16) and (23) or (24), i.e.,

$$\sigma_x^2 = \sigma_{x_1}^2 + \sigma_{x_2}^2 + \sigma_{x_3}^2 . \tag{26}$$

Thus, for the out-of-lock case,

$$\mu_x\Big|_{O.L.} = 0$$

$$\sigma_x^2\Big|_{O.L.} = K_1^4 K_m^4 T_i \left[\frac{N_{sq} + S^2 S_{\Delta_c}(0) + S^2 T_i D_m^2 \left(\frac{\sin \omega_b T_i}{\omega_b T_i}\right)^2}{2}\right] . \tag{27}$$

For the true lock case, we shall assume that the loop signal-to-noise ratio is sufficiently high that

$$\overline{\cos 2\phi} \cong 1$$

$$\sigma^2_{\cos 2\phi} \cong 0 . \tag{28}$$

Thus, from (15), (16) and (24),

$$\mu_x\Big|_{I.L.} = K_1^2 K_m^2 S T_i D_m$$

$$\sigma_x^2\Big|_{I.L.} = K_1^4 K_m^4 T_i \left[\frac{\bar{N}_{sq} + 2S^2 S_{\Delta_c}(0)}{2}\right] . \tag{29}$$

FALSE ALARM PROBABILITY

The false alarm probability α is defined as the probability of deciding that the loop is in lock given that it is out of lock. For a test against a threshold T_h, we get

$$\alpha = \text{Prob}\{x > T_h\} = \frac{1}{\sqrt{2\pi\sigma_x^2\big|_{0.L.}}} \int_{T_h}^{\infty} \exp\left(\frac{-x^2}{2\sigma_x^2\big|_{0.L.}}\right) dx \tag{30}$$

or

$$\alpha = \frac{1}{2} \operatorname{erfc} T_h' \tag{31}$$

where

$$T_h' \triangleq \frac{T_h}{\sqrt{2}\,\sigma_x\big|_{0.L.}}$$

$$\operatorname{erfc} x \triangleq \frac{2}{\sqrt{\pi}} \int_x^{\infty} \exp(-t^2)\, dt \tag{32}$$

and $\sigma_x^2\big|_{0.L.}$ is defined by (27). Since $\sigma_x^2\big|_{0.L.}$ is a function of the beat note frequency, a question arises as to the value of ω_b at which to set T_h' for a given α. If the threshold is set based upon the standard deviation of x when the loop is far out of lock, i.e., $\sigma_{x_3} = 0$ and $\sigma_x\big|_{0.L.} = \sqrt{\sigma_{x_1}^2 + \sigma_{x_2}^2}$ [see (16) and (20)], then as the loop approaches lock, $\sigma_x\big|_{0.L.}$ increases and the lock detector is likely to kill the sweep before lock is actually achieved. In practice, a more reasonable compromise would

be to set the threshold based upon a value of σ_{x_3} computed from (20) which corresponds to a beat note ω_b on the order of the radian pull-in frequency of the loop.

FALSE DETECTION PROBABILITY

The false detection probability β is defined as the probability of deciding that the loop is out of lock when in fact it is in lock. For the same threshold as above, β is given by

$$\beta = \text{Prob}\{x > T_h\}$$

$$= \frac{1}{2}\,\text{erfc}\left[-\left(T_h' \frac{\sigma_{x|O.L.}}{\sigma_{x|I.L.}} - \frac{\mu_{x|I.L.}}{\sqrt{2}\,\sigma_{x|I.L.}}\right)\right]. \tag{33}$$

Combining (31) and (33) gives

$$\text{erfc}^{-1}\,2\beta + \frac{\sigma_{x|O.L.}}{\sigma_{x|I.L.}}\,\text{erfc}^{-1}\,2\alpha = \frac{\mu_{x|I.L.}}{\sqrt{2}\,\sigma_{x|I.L.}} \tag{34}$$

where erfc^{-1} is the inverse complementary error function.

TRUE LOCK PERFORMANCE IN TERMS OF SYSTEM PARAMETERS

Previous analyses of this type have demonstrated that the effect of the modulation self-noise is negligible (see [1]). Thus, in what follows, we shall ignore $S_{\Delta_c}(0)$ in equations (27) and (29).

The equivalent squared noise has also been previously evaluated when studying the tracking performance of the Costas loop with the result (see equation (32) of [1]):

$$N_{sq} = 4\,S\,N_0\left[D_m K_D + \frac{N_0 B_i}{2S} K_L\right] \tag{35}$$

where K_L is a constant dependent only on the filter type and is defined by

$$K_L = \frac{\int_{-\infty}^{\infty} |G(j\omega)|^4 \frac{d\omega}{2\pi}}{\int_{-\infty}^{\infty} |G(j\omega)|^2 \frac{d\omega}{2\pi}}, \tag{36}$$

K_D is a constant dependent on both the baseband data power spectrum and the filter type, i.e.,

$$K_D = \frac{\int_{-\infty}^{\infty} S_m(\omega)|G(j\omega)|^4 \frac{d\omega}{2\pi}}{\int_{-\infty}^{\infty} S_m(\omega)|G(j\omega)|^2 \frac{d\omega}{2\pi}} , \tag{37}$$

and B_i denotes the two-sided noise bandwidth of the arm filter $G(j\omega)$, i.e.,

$$B_i = \int_{-\infty}^{\infty} |G(j\omega)|^2 \frac{d\omega}{2\pi} . \tag{38}$$

Alternately, in terms of the "squaring loss" S_L, previously defined as

$$S_L \triangleq \frac{D_m}{K_D + K_L\left(\frac{N_0 B_i}{2S D_m}\right)} , \tag{39}$$

we have

$$N_{sq} = \frac{4S N_0 D_m^2}{S_L} . \tag{40}$$

Substituting (40) in (27) and (29) gives

$$\frac{\sigma_x|_{O.L.}}{\sigma_x|_{I.L.}} = \sqrt{\frac{N_{sq} + S^2 T_i D_m^2 \left(\frac{\sin \omega_b T_i}{\omega_b T_i}\right)^2}{N_{sq}}} = \sqrt{1 + \left(\frac{S T_i}{N_0}\right)\frac{S_L}{4}\left(\frac{\sin \omega_b T_i}{\omega_b T_i}\right)^2}$$

$$= \sqrt{1 + \left(\frac{T_i}{T}\right)\frac{R_d S_L}{4}\left(\frac{\sin \omega_b T_i}{\omega_b T_i}\right)^2} , \tag{41}$$

where $R_d \triangleq ST/N_0$ is the data signal-to-noise ratio. Also, from the above substitutions,

$$\frac{\mu_x|_{I.L.}}{\sqrt{2}\,\sigma_x|_{I.L.}} = \sqrt{\left(\frac{T_i}{T}\right)\frac{R_d S_L}{4}} . \tag{42}$$

Finally, substituting (41) and (42) into (34) gives the desired result (for $\omega_b/2\pi << 1/T$):

$$\text{erfc}^{-1}\, 2\beta + \sqrt{1 + \left(\frac{T_i}{T}\right)\frac{R_d S_L}{4}\left(\frac{\sin \omega_b T_i}{\omega_b T_i}\right)^2}\ \text{erfc}^{-1}\, 2\alpha = \sqrt{\left(\frac{T_i}{T}\right)\frac{R_d S_L}{4}} \quad . \tag{43}$$

Recall that T_i/T is the number of symbol intervals in the integration time of the integrate-and-dump. For an RC (single-pole Butterworth) arm filter with optimally designed bandwidth, and a Manchester coded data, Figure 2 plots β versus R_d in dB for fixed α and T_i/T varying between 50 and 500. The value of $f_b \triangleq \omega_b/2\pi$ is set equal to the loop bandwidth B_L and $B_L T$ is fixed with B_L = 500 Hz and $1/T$ = 216 ksps. Also plotted in dashed lines on this figure are several curves corresponding to selection of the lock detector threshold based upon the loop being far out of lock. This is equivalent to ignoring the beat note noise and assuming that the total variance of the integrate-and-dump output is identical both under lock and out-of-lock conditions. Clearly, from (23), the significance of the beat note noise diminishes as the integration time T_i increases. This fact bears out on Figure 2 by comparing the solid and dashed curves corresponding to the same value of T_i/T.

REFERENCE:

1. M. K. Simon and W. C. Lindsey. "Optimum Performance of Suppressed Carrier Receivers with Costas Loop Tracking," IEEE Transactions on Communications, Vol. COM-25, No. 2, February 1977, pp. 215-227.

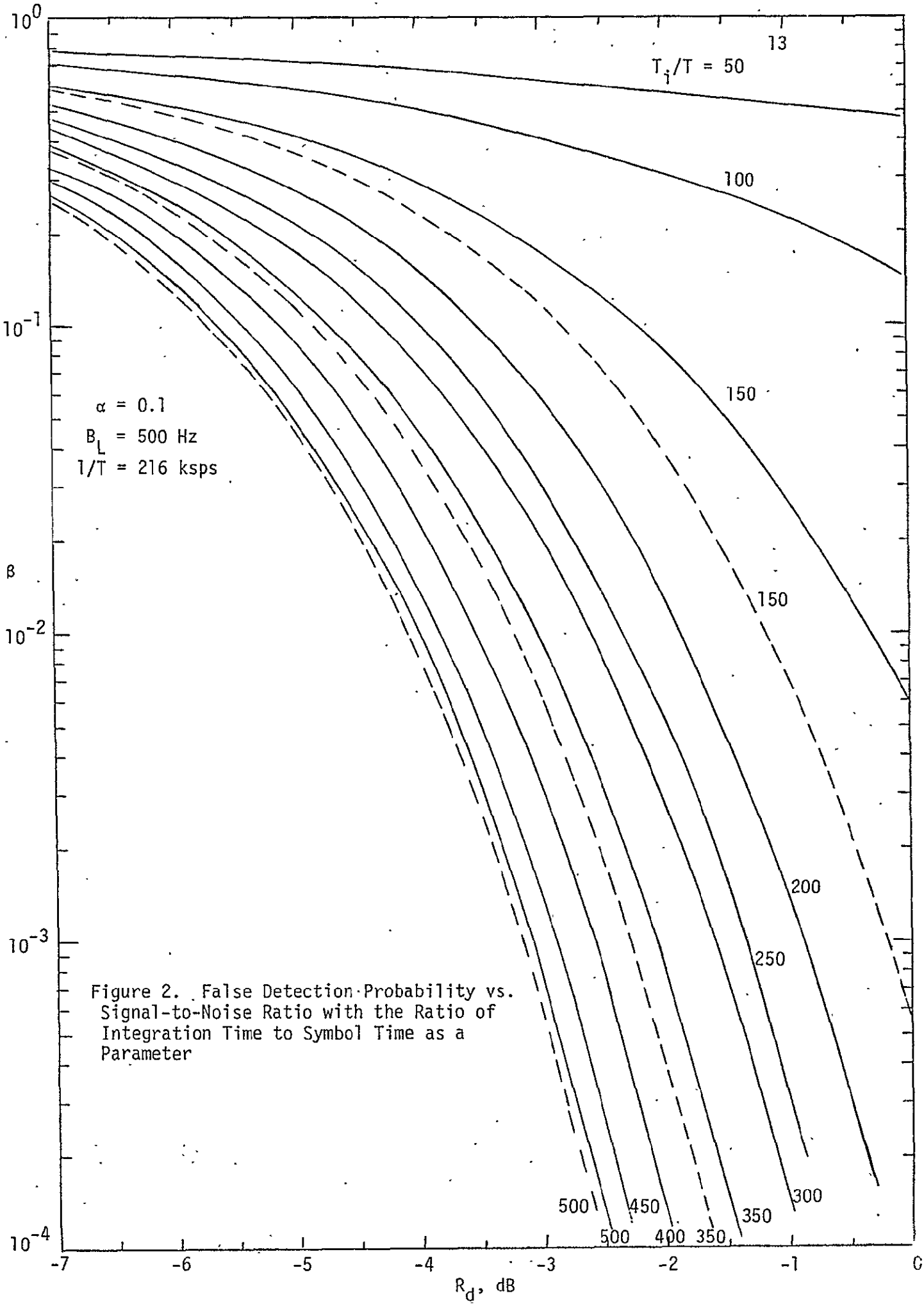

Figure 2. False Detection Probability vs. Signal-to-Noise Ratio with the Ratio of Integration Time to Symbol Time as a Parameter

APPENDIX G

AN ANALYSIS OF THE POWER DIVISION STRUCTURE OF A BANDPASS HARDLIMITED THREE-CHANNEL SIGNAL WITH SINUSOIDAL SUBCARRIERS

APPENDIX G

AN ANALYSIS OF THE POWER DIVISION STRUCTURE OF A BANDPASS HARDLIMITED THREE-CHANNEL SIGNAL WITH SINUSOIDAL SUBCARRIERS

by

Marvin K. Simon

INTRODUCTION

Phase modulation (PM) mode 1 of the Space Shuttle Orbiter (SSO) Ku-band downlink provides for simultaneous transmission of three asynchronous data channels of information. Since the three data channels, which have widely different data rates and power allocations, require independent clocks, phase-multiplexing techniques are advantageous over time-division and frequency-division multiplexing, particularly when the data rates to be reclocked are high, and intermodulation products must be avoided in the face of restricted bandwidths.

One such phase-multiplexing technique uses quadrature carriers and subcarriers and has been shown [1, Appendix A] to have potential implementation advantages over both a conventional PM approach (all three data channels phase modulated on a single carrier) and a three-channel interplex approach [2]. The technique referred to above has been variously called quadrature multiplex [3], dual QPSK [4,5] and QPSK/QPSK [6].

In its original form (see Figure 1), the two lower data rate signals were biphase modulated onto quadrature squarewave subcarriers. This composite signal was then amplitude modulated onto a quadrature carrier and summed with the high rate channel which was biphase modulated onto the in-phase carrier.

A recent performance evaluation on a test link configuration of dual QPSK at scaled-down bit rates and bandwidths was conducted in the System Design Evaluation Area (SDEA) of the Electronic Systems Test Laboratory (ESTL) at the NASA/Johnson Space Center. The results of these tests [5] indicated among other things that when sinewave subcarriers were used in place of squarewave subcarriers, the small signal limiter suppression of the lowest rate channel (approximately 1.5 dB when squarewave subcarriers were employed) [1, Appendix C; 7] had virtually disappeared. Since the absence of small signal suppression in

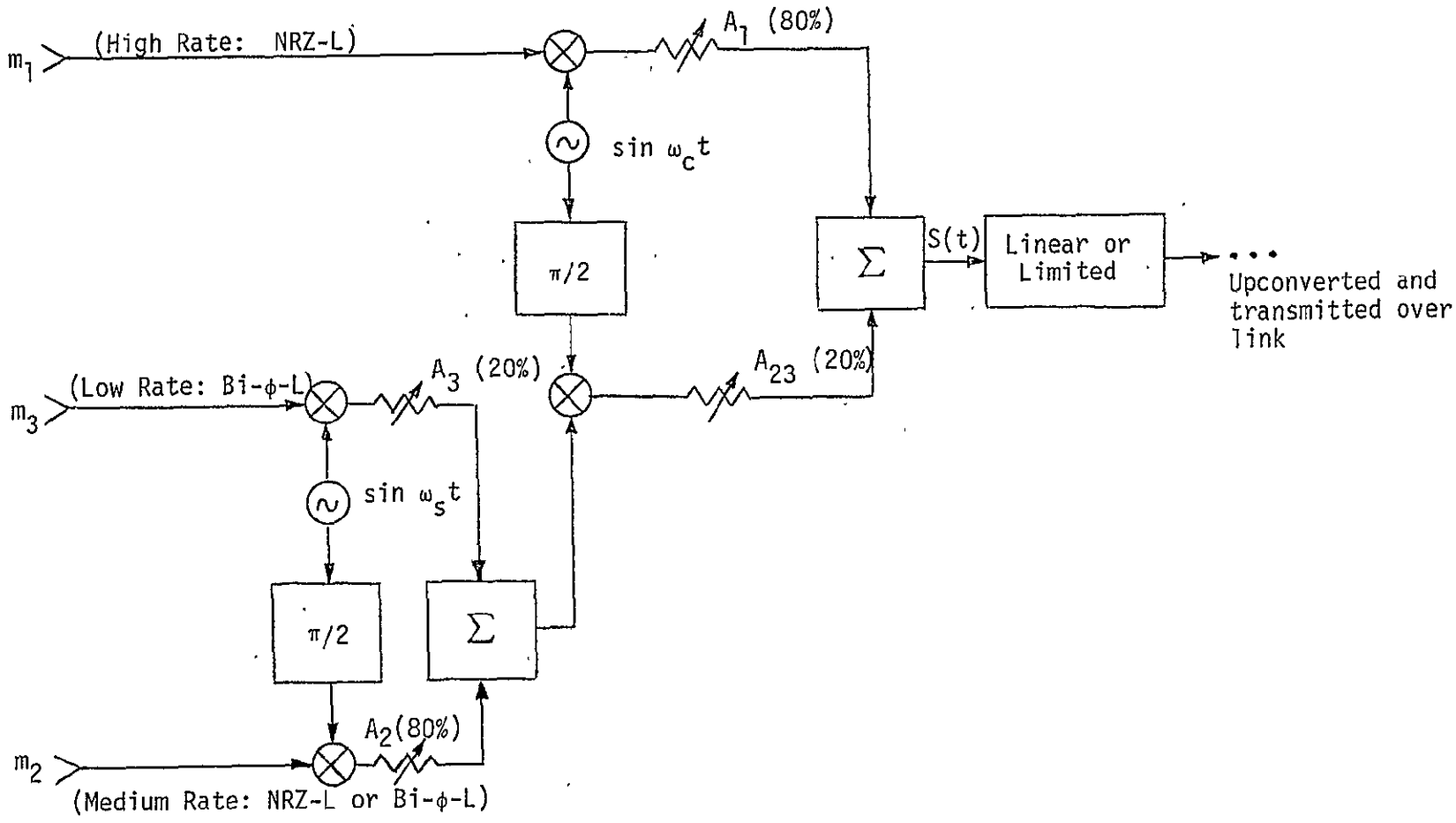

Figure 1. Dual QPSK Configuration

comparison to previous low rate channel squarewave subcarrier results was one of the more interesting results of the tests, the question was raised as to whether this particular phenomenon could be verified analytically. This report attempts to answer this question by presenting an exact characterization of the dual QPSK signal with quadrature sinusoidal subcarriers after it has passed through a bandpass (hard) limiter. This work represents an extension of previous results of the author [1, Appendix C] for the saturated dual QPSK signal with squarewave subcarriers.

Another phase-multiplexing technique referred to as modified interplex [2,6] is derived from a modulation scheme originally introduced at the Jet Propulsion Laboratory and called interplex modulation [8]. This configuration is illustrated in Figure 2, and differs from dual QPSK primarily in the fact that the two lower rate channels are not in phase quadrature. Rather, the medium rate signal alone is biphase modulated on a subcarrier with cross coupling effectively minimized by choosing the subcarrier frequency sufficiently far removed from the low rate baseband signal. Theoretical analyses of this configuration with a squarewave subcarrier and in both the presence and absence of bandpass limiting are given in [2] and [6]. As before, one could easily replace the squarewave subcarrier with a sinewave signal. The power division structure of the modified interplex signal with sinusoidal subcarrier after passing through a bandpass limiter will also be derived in this report.

POWER DIVISION ANALYSIS OF BANDPASS LIMITED DUAL QPSK SIGNAL

The signal generated by the modulator of Figure 1 is

$$s(t) = \sqrt{2}\,\{C(t)\cos\omega_c t + S(t)\sin\omega_c t\} \tag{1}$$

where

$$C(t) = \sqrt{2P_2}\,m_2(t)\sin\omega_s t + \sqrt{2P_3}\,m_3(t)\cos\omega_s t$$

$$S(t) = \sqrt{P_1}\,m_1(t)\,. \tag{2}$$

In (1) and (2), ω_c and ω_s denote the carrier and subcarrier radian frequencies, respectively, and $m_i(t)$; $i = 1,2,3$; are the data modulations in order of decreasing data rate, i.e., $m_1(t)$ is the 100 Msps convolutionally

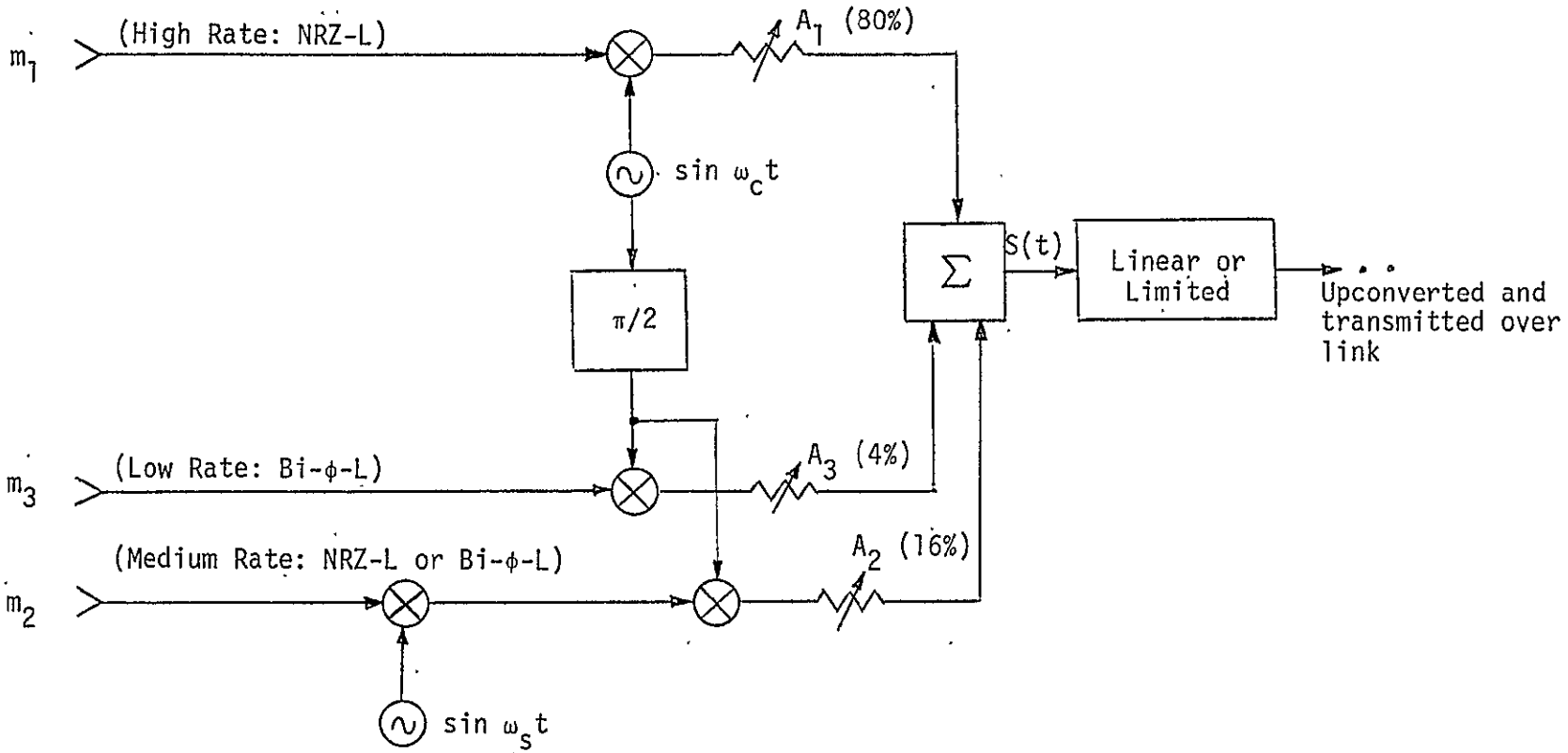

Figure 2. Modified Interplex Configuration

coded data and $m_3(t)$ is the 192 kbps operational data, with respective powers P_1, P_2, and P_3. Letting $P_T = P_1 + P_2 + P_3$ denote the total power, then

$$\eta_1 \triangleq \frac{P_1}{P_T} = 0.8$$

$$\eta_2 \triangleq \frac{P_2}{P_T} = 0.16 \tag{3}$$

$$\eta_3 \triangleq \frac{P_3}{P_T} = 0.04 \ .$$

Rewriting (1) in polar coordinates gives

$$s(t) = \sqrt{2}\, V(t) \sin\left(\omega_c t + \phi(t)\right) \tag{4}$$

where

$$V(t) = \sqrt{C^2(t) + S^2(t)}$$

$$\phi(t) = \tan^{-1} \frac{C(t)}{S(t)} \ . \tag{5}$$

Because of AM to PM conversion which takes place in the power amplifier and possibly in the TDRS repeater, we consider the effects on the signal of (4) of first passing it through a bandpass hardlimiter, thus producing a constant envelope signal. Specifically, passing $s(t)$ of (4) through such a bandpass limiter preserves the phase $\phi(t)$ and produces as its first zone output the signal

$$z_1(t) = \sqrt{2P} \sin\left(\omega_c t + \phi(t)\right) \ , \tag{6}$$

where P is the total power in the first zone. Alternately, in terms of in-phase and quadrature components, (5) can be rewritten as

$$z_1(t) = \sqrt{2P}\left[\frac{S(t)}{V(t)} \sin \omega_c t + \frac{C(t)}{V(t)} \cos \omega_c t\right] \ . \tag{7}$$

Substituting (2) into (5), and using the definitions of (3) gives

$$V(t) =$$

$$\sqrt{P_1 m_1^2(t) + 2P_2 m_2^2(t) \sin^2 \omega_s t + 2P_3 m_3^2(t) \cos^2 \omega_s t + 4\sqrt{P_2 P_3}\, m_2(t) m_3(t) \sin \omega_s t \cos \omega_s t} \tag{8}$$

Since $m_i(t)$; $i = 1,2,3$; are ± 1 digital modulations, (8) simplifies to

$$V(t) = \sqrt{P_T \left[1 - (\eta_2 - \eta_3) \cos 2\omega_s t + 2\sqrt{\eta_2 \eta_3}\, m_2(t)\, m_3(t) \sin 2\omega_s t\right]} \tag{9}$$

Taking the reciprocal of (9), we get

$$\frac{1}{V(t)} = \frac{1}{\sqrt{P_T[1 - (\eta_2 - \eta_3) \cos 2\omega_s t]}} \times \frac{1}{\sqrt{1 + X(t)\, m_2(t)\, m_3(t)}} \tag{10}$$

where

$$X(t) = \frac{2\sqrt{\eta_2 \eta_3} \sin 2\omega_s t}{1 - (\eta_2 - \eta_3) \cos 2\omega_s t} . \tag{11}$$

For any value of t, we can bound $X^2(t)$ by

$$X^2(t) = \frac{4\eta_2 \eta_3 \sin^2 2\omega_s t}{[1 - (\eta_2 - \eta_3) \cos 2\omega_s t]^2} < \frac{4\,\eta_2\,\eta_3}{[1 - (\eta_2 - \eta_3)]^2} . \tag{12}$$

Using the values of η_2 and η_3 of (3) gives

$$X^2(t) < \frac{4(.16)(.04)}{[1 - (.12)]^2} = 0.033 . \tag{13}$$

Since, from (13), $X^2(t) < 1$, we can expand the second square root in (10) in a convergent power series, viz.,

$$\begin{aligned} \frac{1}{\sqrt{1 + X(t)\, m_2(t)\, m_3(t)}} = 1 &- \frac{1}{2} X(t)\, m_2(t)\, m_3(t) \\ &+ \frac{1\times 3}{2\times 4} X^2(t)\, m_2^2(t)\, m_3^2(t) \\ &- \frac{1\times 3\times 5}{2\times 4\times 6} X^3(t)\, m_2^3(t)\, m_3^3(t) \\ &+ \cdots\cdots \end{aligned} \tag{14}$$

Again, since $m_2(t)$ and $m_3(t)$ are ±1 digital modulations, the power series of (14) can be expressed as the sum of two series, viz.,

$$\frac{1}{\sqrt{1 + X(t)\, m_2(t)\, m_3(t)}} = \sum_{n=0}^{\infty} \frac{(4n-1)!!}{(4n)!!} X^{2n}(t) - \left[\sum_{n=0}^{\infty} \frac{(4n+1)!!}{(4n+2)!!} X^{2n+1}(t)\right] m_2(t)\, m_3(t)$$

$$\triangleq C_1(t) - C_2(t)\, m_2(t)\, m_3(t) \,. \tag{15}$$

Fortunately, the power series for $C_1(t)$ and $C_2(t)$ can be expressed in closed form with the results

$$C_1(t) = \frac{1}{2}\left[\frac{1}{\sqrt{1 + X(t)}} + \frac{1}{\sqrt{1 - X(t)}}\right]$$

$$C_2(t) = \frac{1}{2}\left[\frac{1}{\sqrt{1 - X(t)}} - \frac{1}{\sqrt{1 + X(t)}}\right]. \tag{16}$$

Substituting (11) in (16) and simplifying gives

$$C_1(t) = \frac{\sqrt{1 - (n_2 - n_3)\cos 2\omega_s t}}{2}\left[\frac{1}{\sqrt{1 - (n_2 - n_3)\cos 2\omega_s t + 2\sqrt{n_2 n_3}\sin 2\omega_s t}} + \frac{1}{\sqrt{1 - (n_2 - n_3)\cos 2\omega_s t - 2\sqrt{n_2 n_3}\sin 2\omega_s t}}\right]$$

$$C_2(t) = \frac{\sqrt{1 - (n_2 - n_3)\cos 2\omega_s t}}{2}\left[\frac{1}{\sqrt{1 - (n_2 - n_3)\cos 2\omega_s t - 2\sqrt{n_2 n_3}\sin 2\omega_s t}} - \frac{1}{\sqrt{1 - (n_2 - n_3)\cos 2\omega_s t + 2\sqrt{n_2 n_3}\sin 2\omega_s t}}\right] \tag{17}$$

Comparing the expressions in brackets in (17) with (9), we can rewrite (17) as

$$C_1(t) = \frac{\sqrt{1-(\eta_2-\eta_3)\cos 2\omega_s t}}{2}\left[\frac{1}{\sqrt{\eta_1+(\sqrt{2\eta_2}\sin\omega_s t+\sqrt{2\eta_3}\cos\omega_s t)^2}} + \frac{1}{\sqrt{\eta_1+(\sqrt{2\eta_2}\sin\omega_s t-\sqrt{2\eta_3}\cos\omega_s t)^2}}\right]$$

$$= \sqrt{1-(\eta_2-\eta_3)\cos 2\omega_s t}\; D_1(t)$$

$$C_2(t) = \frac{\sqrt{1-(\eta_2-\eta_3)\cos 2\omega_s t}}{2}\left[\frac{1}{\sqrt{\eta_1+(\sqrt{2\eta_2}\sin\omega_s t-\sqrt{2\eta_3}\cos\omega_s t)^2}} - \frac{1}{\sqrt{\eta_1+(\sqrt{2\eta_2}\sin\omega_s t+\sqrt{2\eta_3}\cos\omega_s t)^2}}\right]$$

$$= \sqrt{1-(\eta_2-\eta_3)\cos 2\omega_s t}\; D_2(t) \qquad (18)$$

where

$$D_1(t) = \frac{1}{2\sqrt{\eta_1+2(\eta_2+\eta_3)\sin^2(\omega_s t+\alpha)}} + \frac{1}{2\sqrt{\eta_1+2(\eta_2+\eta_3)\sin^2(\omega_s t-\alpha)}}$$

$$D_2(t) = \frac{1}{2\sqrt{\eta_1+2(\eta_2+\eta_3)\sin^2(\omega_s t-\alpha)}} - \frac{1}{2\sqrt{\eta_1+2(\eta_2+\eta_3)\sin^2(\omega_s t+\alpha)}} \qquad (19)$$

with

$$\alpha \triangleq \tan^{-1}\sqrt{\eta_3/\eta_2}\,. \qquad (20)$$

Combining (10), (15), and (18), we get the simplified result

$$\frac{1}{V(t)} = \frac{1}{\sqrt{P_T}}\left[D_1(t) - D_2(t)\,m_2(t)\,m_3(t)\right]. \qquad (21)$$

Finally, substituting (21) into (7) and making use of the definitions of C(t) and S(t) as given in (2), we get an expression for the bandpass limiter output:

$$z_1(t) = \sqrt{2P/P_T}\left\{\sqrt{P_1}\, m_1(t) D_1(t) \sin \omega_c t - \sqrt{P_1}\, D_2(t) m_1(t) m_2(t) m_3(t) \sin \omega_c t \right.$$
$$+ [\sqrt{2P_2}\, D_1(t) \sin \omega_s t - \sqrt{2P_3}\, D_2(t) \cos \omega_s t]\, m_2(t) \cos \omega_c t$$
$$\left. + [\sqrt{2P_3}\, D_1(t) \cos \omega_s t - \sqrt{2P_2}\, D_2(t) \sin \omega_s t]\, m_3(t) \cos \omega_c t\right\} \tag{22}$$

or

$$z_1(t) = \sqrt{2P/P_T}\left\{\sqrt{P_1}\, m_1(t) D_1(t) \sin \omega_c t - \sqrt{P_1}\, D_2(t) m_1(t) m_2(t) m_3(t) \sin \omega_c t \right.$$
$$+ \left[\sqrt{2P_2}\, m_2(t)\, E_2(t) \sin [\omega_s t - \beta(t)]\right.$$
$$\left.\left. + \sqrt{2P_3}\, m_3(t)\, E_3(t) \cos [\omega_s t + \beta(t)]\right] \cos \omega_c t\right\} \tag{23}$$

where

$$E_2(t) \triangleq \sqrt{D_1^2(t) + (n_3/n_2)\, D_2^2(t)}$$
$$E_3(t) \triangleq \sqrt{D_1^2(t) + (n_2/n_3)\, D_2^2(t)}$$
$$\beta(t) \triangleq \tan^{-1}\left(\sqrt{\frac{n_3}{n_2}}\, \frac{D_2(t)}{D_1(t)}\right) \tag{24}$$

Several interesting conclusions can be deduced from (23). First, we observe that, contrary to the squarewave subcarrier case, the various data components out of the bandpass limiter are not simply reduced in power by fixed (constant) limiter suppression factors proportional to the input power apportionment (see Eq. (C-11) of Reference 1, Appendix C). Rather, each data component (including the cross-modulation component) is amplitude-modulated and, in addition, the two lower rate channels are

phase-modulated by waveforms which are periodic at twice the subcarrier frequency. Figures 3 through 5 plot $D_1(t)$, $D_2(t)$, and $\beta_1(t)$ versus $2\omega_s t$ over one period. The corresponding curves for $E_2(t)$ and $E_3(t)$ are virtually identical numerically to that of $D_1(t)$ versus $2\omega_s t$.* Thus, for all intents and purposes, we shall assume that Figure 2 is also representative of $E_2(t)$ and $E_3(t)$ versus $2\omega_s t$. Second, all of the phase and amplitude modulations are somewhat sinusoidal in behavior. Finally, and most important of all, the peak-to-peak excursion of the amplitude modulation $D_1(t)$ [also $E_2(t)$ and $E_3(t)$] relative to unity (the unmodulated amplitude of the data signals) is quite small and thus it appears that each data channel suffers essentially no limiter suppression. Furthermore, the phase modulation $\beta_1(t)$ has a peak value of about 0.04 radians or 2.3 degrees, which has an insignificant effect on performance degradation.

POWER DIVISION ANALYSIS OF BANDPASS LIMITED MODIFIED INTERPLEX SIGNAL

Corresponding to Figure 2, the signal at the input of the bandpass limiter is also given by (1) with, however,

$$\begin{aligned} C(t) &= \sqrt{2P_2}\, m_2(t) \sin \omega_s t + \sqrt{P_3}\, m_3(t) \\ S(t) &= \sqrt{P_1}\, m_1(t) \end{aligned} \tag{25}$$

Note that (25) differs from (2) in that the lowest rate baseband signal is not placed on a subcarrier. The envelope $V(t)$ of the modified interplex signal prior to bandpass limiting is now given by

$$\begin{aligned} V(t) &= \sqrt{C^2(t) + S^2(t)} \\ &= \sqrt{P_1 m_1^2(t) + 2P_2 m_2^2(t) \sin^2 \omega_s t + P_3 m_3^2(t) + 2\sqrt{2P_2P_3}\, m_2(t)\, m_3(t) \sin \omega_s t} \\ &= \sqrt{P_T [1 - \eta_2 \cos 2\omega_s t + 2\sqrt{2\eta_2\eta_3}\, m_2(t)\, m_3(t) \sin \omega_s t]} \end{aligned} \tag{26}$$

and its reciprocal by

---

*The maximum discrepancy between $D_1(t)$ and either $E_2(t)$ or $E_3(t)$ over one period of the waveforms is in the third decimal place.

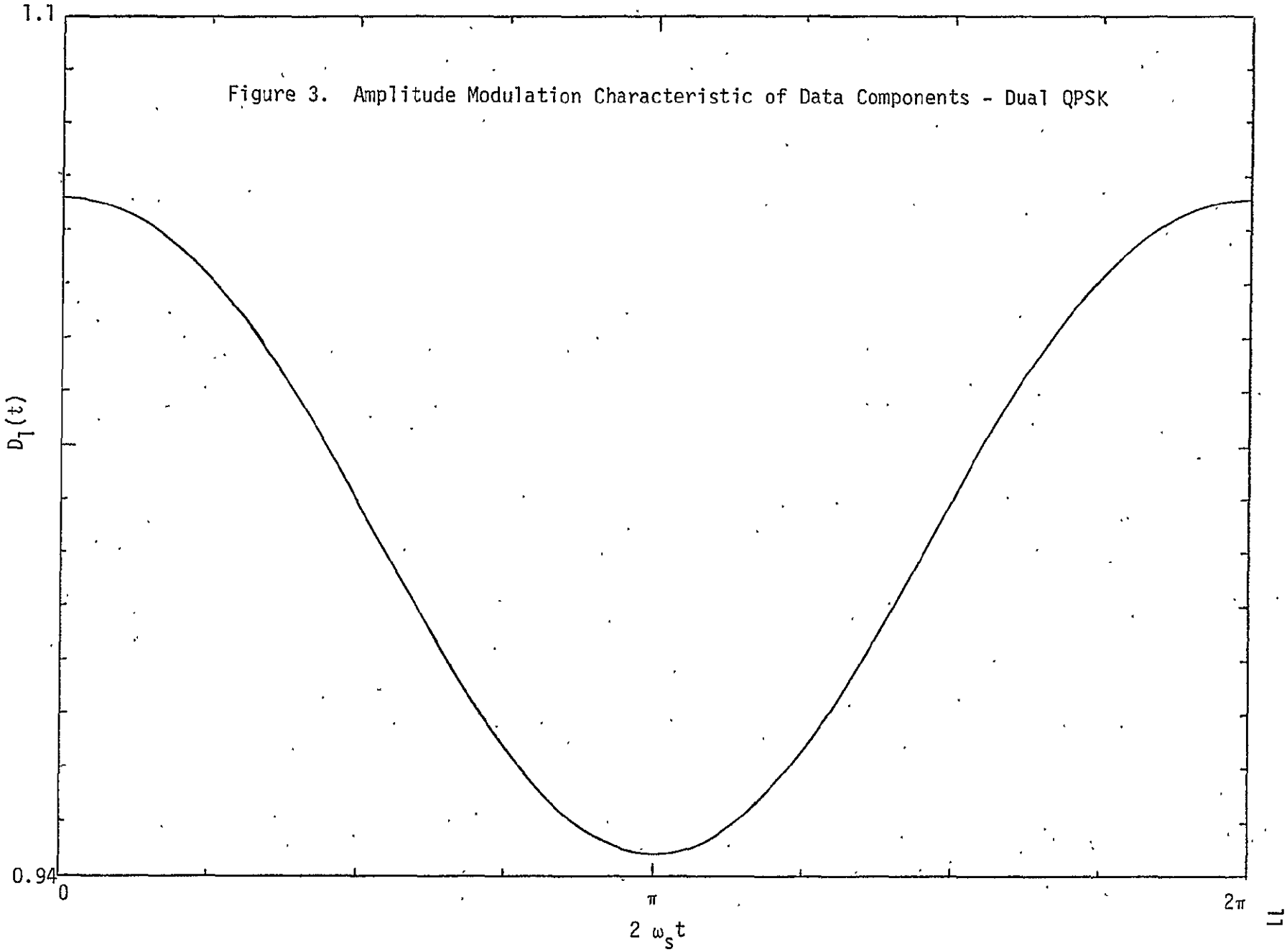

Figure 3. Amplitude Modulation Characteristic of Data Components - Dual QPSK

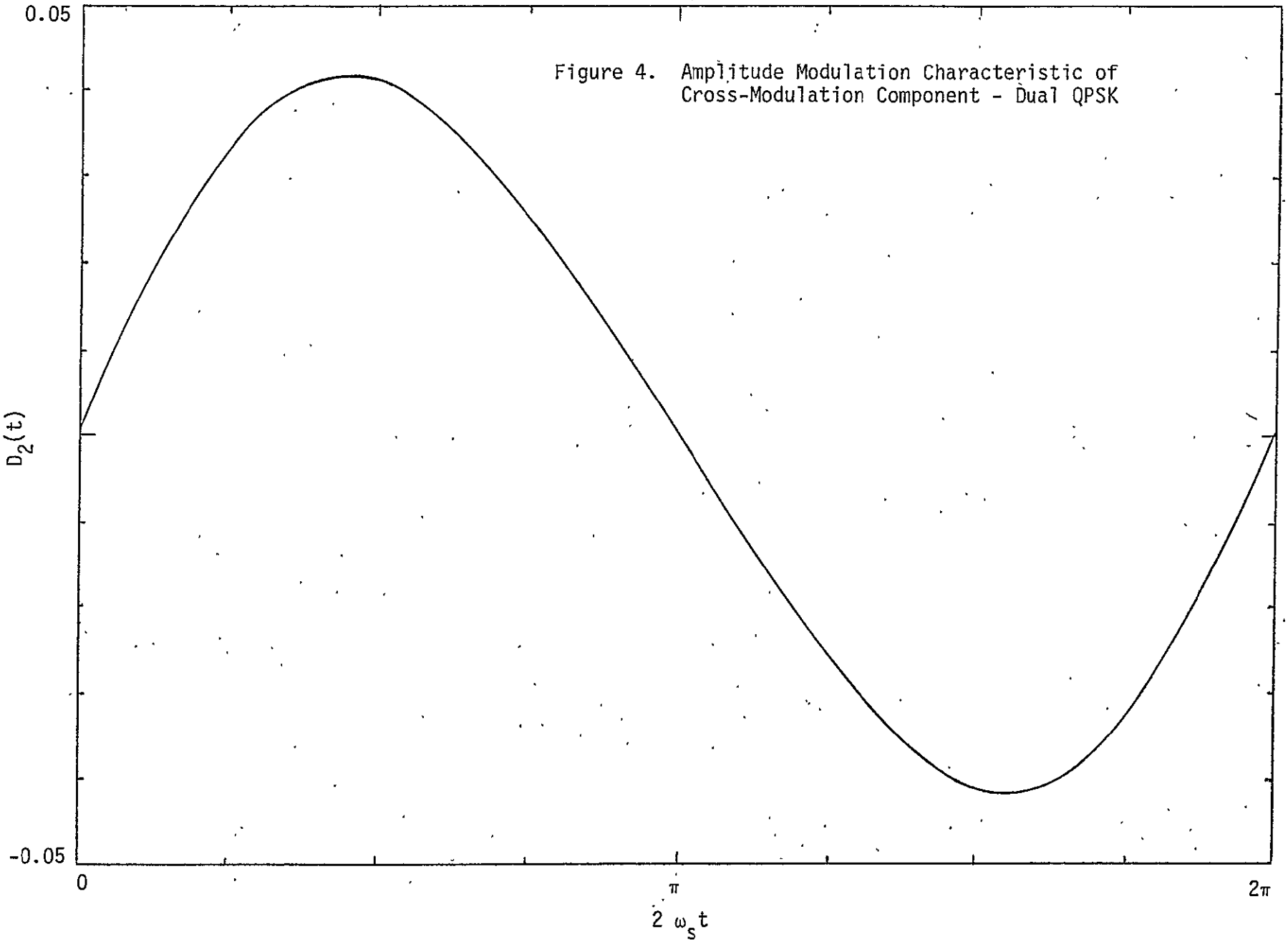

Figure 4. Amplitude Modulation Characteristic of Cross-Modulation Component - Dual QPSK

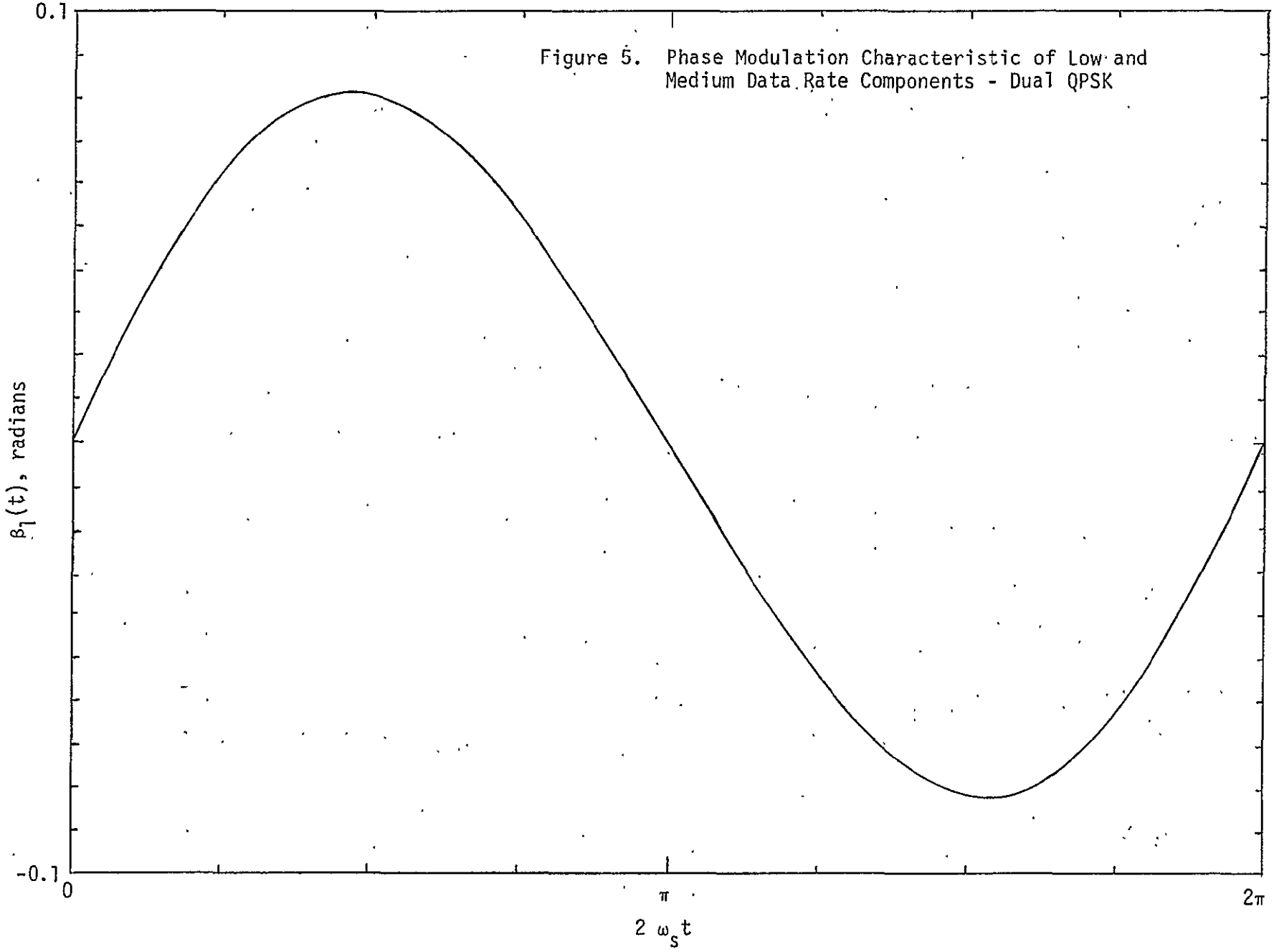

Figure 5. Phase Modulation Characteristic of Low and Medium Data Rate Components - Dual QPSK

$$\frac{1}{V(t)} = \frac{1}{\sqrt{P_T(1 - \eta_2 \cos 2\omega_s t)}} \times \frac{1}{\sqrt{1 + X(t)\, m_2(t)\, m_3(t)}} \tag{27}$$

where now

$$X(t) \triangleq \frac{2\sqrt{2\eta_2\eta_3} \sin \omega_s t}{1 - \eta_2 \cos 2\omega_s t} . \tag{28}$$

Since for the values of η_i; $i = 1,2,3$; as given in (3), $X^2(t)$ is less than unity, then following an approach similar to that leading up to (22), one can show that, for the modified interplex signal, the output of the band-pass limiter is

$$\begin{aligned} z_1(t) = \sqrt{\frac{2P}{P_T}} \Big\{ & \sqrt{P_1}\, D_1'(t)\, m_1(t) \sin \omega_c t - \sqrt{P_1}\, D_2'(t)\, m_1(t)\, m_2(t)\, m_3(t) \sin \omega_c t \\ & + \left[\sqrt{2P_2}\, D_1'(t) \sin \omega_s t - \sqrt{P_3}\, D_2'(t)\right] m_2(t) \cos \omega_c t \\ & + \left[\sqrt{P_3}\, D_1'(t) - \sqrt{2P_2}\, D_2'(t) \sin \omega_s t\right] m_3(t) \cos \omega_c t \Big\} . \end{aligned} \tag{29}$$

or, alternately,

$$\begin{aligned} z_1(t) = \sqrt{\frac{2P}{P_T}} \Big\{ & \sqrt{P_1}\, D_1'(t)\, m_1(t) \sin \omega_c t - \sqrt{P_1}\, D_2'(t)\, m_1(t)\, m_2(t)\, m_3(t) \sin \omega_c t \\ & + \sqrt{2P_2} \left[D_1'(t)\, m_2(t) \sin \omega_s t - D_2'(t)\, m_3(t) \sin \omega_s t\right] \cos \omega_c t \\ & + \sqrt{P_3} \left[D_1'(t)\, m_3(t) - D_2'(t)\, m_2(t)\right] \cos \omega_c t \Big\} \end{aligned} \tag{30}$$

where

$$D_1'(t) \triangleq \frac{1}{2\sqrt{\eta_1 + (\sqrt{2\eta_2} \sin \omega_s t + \sqrt{\eta_3})^2}} + \frac{1}{2\sqrt{\eta_1 + (\sqrt{2\eta_2} \sin \omega_s t - \sqrt{\eta_3})^2}}$$

$$D_2'(t) \triangleq \frac{1}{2\sqrt{\eta_1 + (\sqrt{2\eta_2} \sin \omega_s t - \sqrt{\eta_3})^2}} - \frac{1}{2\sqrt{\eta_1 + (\sqrt{2\eta_2} \sin \omega_s t + \sqrt{\eta_3})^2}} \tag{31}$$

Figures 6 and 7 illustrate $D_1'(t)$ versus $2\omega_s t$ and $D_2'(t)$ versus $\omega_s t$ over one period. Comparing these figures with Figures 3 and 4, we observe the similarity between $D_1(t)$ and $D_1'(t)$; however, $D_2'(t)$ is somewhat different in shape than $D_2(t)$, about twice the amplitude, and half the frequency. We also note that, unlike the dual QPSK case where the two lower rate channels are both amplitude and phase modulated, here in the modified interplex configuration, each of the two lower rate channels is amplitude modulated by $D_1'(t)$ and, in addition, perturbed by a crosstalk component from the other low rate channel with amplitude proportional to $D_2'(t)$. Since the peak of $D_2'(t)$ is greater than 10 dB down from the average value of $D_1'(t)$, we once again have the appearance of no limiter suppression.

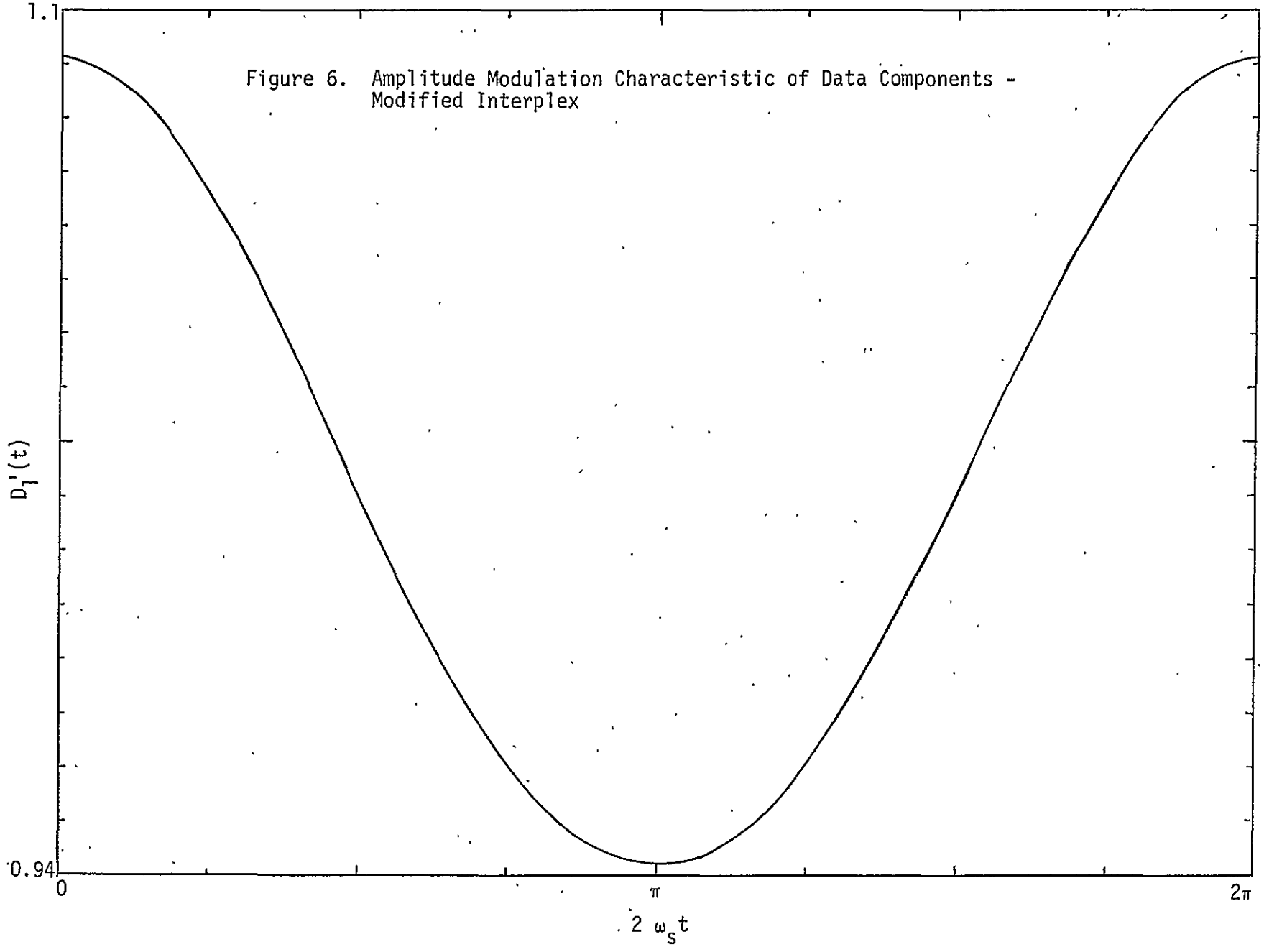

Figure 6. Amplitude Modulation Characteristic of Data Components - Modified Interplex

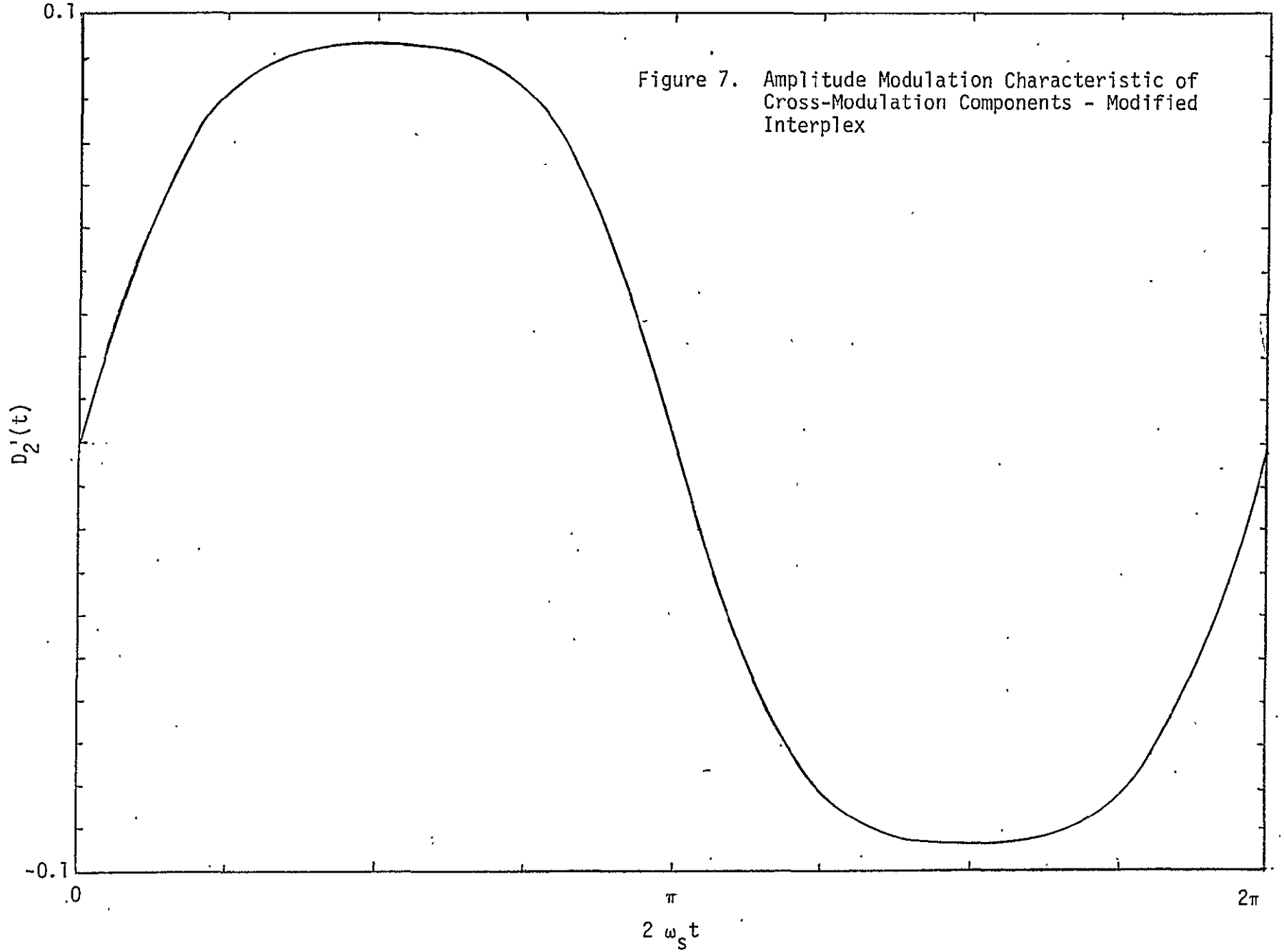

Figure 7. Amplitude Modulation Characteristic of Cross-Modulation Components - Modified Interplex

REFERENCES

1. Huth, G., et al. Integrated Source and Channel Encoded Digital Communication System Design Study - Final Report, Axiomatix Report No. R7607-3, July 31, 1976.

2. Udalov, S. "Feasibility Study of an Interplex Modulation System for the Orbiter's Ku-Band Link," Axiomatix Report No. R7410-5, October 7, 1974.

3. Cartier, D., et al. Shuttle Communications Design Study - Final Report, DRL No. T-975, Magnavox Co., March 31, 1975.

4. Tu, K. "Performance Analysis of the Proposed Three Channel Quadrature Modulation System," Lockheed Electronics Co., Inc., February 1976.

5. Kallas, R. A. "System Design Evaluation Report, Shuttle Ku-Band, PM Mode 1, Scaled Bit Rate Tests," Lockheed Electronics Co., Inc., September 1976.

6. Ku-Band Signal Design Study for Shuttle/TDRSS, Fourth Monthly Progress Report, Motorola, Inc., March 1976.

7. Lindsey, W. C. "Power Division Analysis of a Three Channel Unbalanced QPSK Signal Out of a Bandpass Limiter," LinCom Corp., TR No. 04-7604-8, April 1976.

8. Butman, S., and Timor, U. "Interplex - An Efficient Two-Channel Telemetry System for Space Exploration," JPL Space Programs Summary 37-62, Vol. III, February 1970.